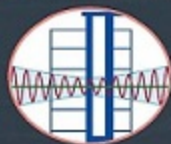# 2021
NCREE Research

Programs and Accomplishments

National Center for Research on Earthquake Engineering
National Applied Research Laboratories

Contents

NCREE

Seismic Requirements for the Framing below the Base of Building Structures

Yuan-Tao Weng[1] and Gee-Jin Yu[2]

翁元滔 [1]、於積瑨 [2]

Abstract

The current design requirements for the seismic design of buildings below the base include the strength of the vertical frame, and the relevant design requirements for appropriately performing the ductility design of such frames, or the capacity design of the ultimate shear force of the upper structure. There is no clear and consistent procedure as to check whether the requirements can ensure that serious damage will not occur. In this study, aiming at the seismic design requirements of the frame below the base surface, a clear and specific design program revision plan is proposed. The seismic design requirements of the frame below the base tend to be more reasonable, consistent, and comprehensive.

Keywords: framing below the base, ultimate shear force, vertical elements

Introduction

The seismic design requirements for structures below the building base are mainly presented in Section 6.2.11 of the current seismic design code in Taiwan [ABRI, 2011]:

Provision:

The design strength and stiffness of the frame between the base and the foundation shall not be lower than those of the superstructure. The special provisions on the ductility of reinforced concrete structures and steel structures shall also apply to the members that transmit seismic forces from the base to the foundation. The ultimate shear force generated above the base can also be used as a lateral force, which can be applied to the base instead; however, the vertical members should still be provided with tight stirrups according to the relevant regulations on ductility.

Commentary:

The basement structure between the base and the foundation has a high stiffness outer wall, which makes it difficult for its beams and columns to yield . Therefore, it should be allowed to be included in a ductility design; however, its strength should be sufficient, and the ground layer should be used. The ultimate shear force is designed to keep the basement structure elastic in the event of a major earthquake. For example, the design of the ground beam should withstand the ultimate floor shear force of the ground floor or the internal force caused by 1.4 times the design seismic force. When the stress method is used for design, it is permissible not to carry out the toughness design. If the shear force transmission of the first floor plan fails, or the exterior wall of the basement is damaged, the ductility design of the basement members will be effective, and the engineer should make appropriate judgments to determine the best way to design the basement members.

The provisions and explanations of this specification refer to the content of SEAOC 1999-108.2.10 [SEAOC, 1999]. The main spirit of the design is that the stiffness and strength of the framework below the base surface must be sufficient to withstand the full development of the superstructure's nonlinear behavior. Therefore, the design strength and stiffness of the frame below the base should not be lower than that of the superstructure, and if the design of the frame below the base is based on the design seismic force, all its components must comply with the structural design specifications. Special provisions for seismic design: if the design is based on the ultimate shear force generated above the base level or the internal force caused by 1.4 times the design seismic force, the ductility design is not

required; however, the reinforced concrete vertical members must still be provided with tight hoop stirrups.

However, the following points remain to be clarified with regard to the provisions and explanations in this section:

1. How much higher strength and stiffness must the frame design below the base surface have than the superstructure to ensure that the superstructure can fully exert its toughness capacity?

2. The strength and stiffness of the frame design below the base level must be higher than the inspection method of the superstructure, which should be based on the comparison of the lateral stiffness and strength of the two adjacent floors above and below the base level.

3. If the frame below the base surface is designed with toughness, can it withstand the axial force and bending moment transmitted from the superstructure to ensure that the superstructure can fully exert its ductility capacity?

4. The frame below the base has very little lateral deformation due to its high stiffness outer wall; that is, it is difficult to ensure ductility requirements. Is it necessary to carry out ductility design?

5. The ultimate shear force is only applied to the base, and the overturning moment caused by transverse force is not considered and the axial force and bending moment requirements of vertical members are underestimated.

6. At present, the estimation methods of ultimate shear force often used in engineering are not consistent.

Other Relevant Provision Contents

1999 SEAOC Bluebook

108.2.10 *Framing Below the Base.* The strength and stiffness of the framing between the base and the foundation shall not be less than those of the superstructure. The special detailing requirements of UBC 97 Chapters 19 and 22, as appropriate, shall apply to columns supporting discontinuous lateral force-resisting elements and to SMRF, IMRF, EBF, STMF, and MMRWF system elements below the base that are required to transmit the forces resulting from lateral loads to the foundation.

C108.2.10 *Framing Below the Base.* The objective of this section is to ensure that the structural system below the base has adequate ductility and capacity to develop the forces and deformations induced by the structure above. Without such

requirements, there is a possibility of major damage. For buildings utilizing special moment-resisting frames, braced frames, or shear wall systems, the framing from the base to the foundation must have the same degree of special detailing or have significantly greater capacity than the framing above the base. Consideration should be given to development of the full capacity of the framing above the base. Columns supporting special moment-resisting frames should have the same details as the columns above the base level; and the beams of these frames at the base level should have the same details as the beams above the base. Shear walls continuing below the base should have the same boundary element details as the wall element immediately above the base. Columns below the base supporting discontinuous shear walls or braced frames are subject to the load, and the detail requirements are presented in Section 105.8.2.2. Overturning effects must be carried into the foundations, and the structural elements of the foundation should have the strength to develop either the capacity of the supported elements or the maximum forces that would occur in the fully yielded structural system. (See Commentary of

Chapter 3 for further discussion of the foundation and related soil conditions.)

ASCE/SEI 7-22

12.4.3.2 Capacity-Limited Horizontal Seismic Load Effect Where capacity-limited design is required by the material reference document, the seismic load effect, including overstrength, shall be calculated with the capacity-limited horizontal seismic load effect, Ecl, substituted for Emh in the load combinations of Section 2.3.6 and Section 2.4.5.

C12.4.3.2 Capacity-Limited Horizontal Seismic Load Effect The standard permits the horizontal seismic load effect, including overstrength, to be calculated directly using actual member sizes and expected material properties, where it can be determined that yielding of other elements in the structure limits the force that can be delivered to the element in question. When calculated this way, the horizontal seismic load effect including overstrength is termed the capacity-limited seismic load effect, E_{cl}.

As an example, the axial force in a column of a moment resisting frame results from the shear forces in the beams that connect to this column. The axial forces caused by seismic loads need not be taken as greater than the sum of the shear forces in these beams at the development of a full structural mechanism, considering the probable strength of the materials and strain hardening effects. For frames controlled by beam hinge-type mechanisms, these shear forces would typically be calculated as $2M_{pr}/L_h$, where M_{pr} is the probable flexural strength of the beam considering expected material properties and strain hardening, and L_h is the distance between plastic hinge locations. Both ACI 318 (2019)

and AISC 341 (2022) require that beams in special moment frames (SMFs) be designed for shear calculated in this manner, and both standards include many other requirements that represent the capacity-limited seismic load effect, E_{cl}, instead of the use of a factor approximating overstrength. This design approach is sometimes termed "capacity design." In this design method, the capacity (expected strength) of one or more elements is used to generate the demand (required strength) for other elements, because the yielding of the former limits the forces delivered to the latter. In this context, the capacity of the yielding element is its expected or mean anticipated strength, considering potential variation in material yield strength and strain-hardening effects. When calculating the capacity of elements for this purpose, expected member strengths should not be reduced by strength reduction or resistance factors, φ.

Amendment Scheme for Seismic Design Requirements of Frames below Base Level

In Section 6.2.11 of the Building Seismic Code (ABRI, 2011) for the design requirements for the structure below the base, the following points must be clarified and adjusted:

1. If the design of the frame below the base level uses the ultimate shear force generated above the base to ensure that its strength and stiffness is higher than those of the superstructure, the ultimate shear force is generally 1.8–2.3 times the total design earthquake transverse force, and the basement structure between the base surface and the foundation has a high stiffness outer wall, and there is no need for toughness. Compared with the upper structure, the internal force caused by the lateral force of the vertical members below the base surface is lower, so if the base surface. The design strength and stiffness of the following vertical members cannot be lower than those of the vertical members connected above the base surface. It is necessary to pay attention to whether the strength of the vertical members connected up and down the base layer are too different. At this time, the frame below the base surface seems to have no… Although it is necessary to carry out toughness design, it is still necessary to consider the relevant inspection requirements such as the gathering members and the force transmission path of the floor slab in order to effectively ensure that the superstructure can effectively exert the toughness and that the vertical members will not cause axial damage.

2. If the ductility design is adopted for the frame below the base surface, it must be carried out on the premise that the design strength and stiffness of the frame below the base surface must not be lower than those of the superstructure. In this case, the design seismic force can be used to adjust the

structure below the base surface design; that is, at least the vertical members must still meet the seismic design requirements of their structural design specifications.

3. Because of the high stiffness of the outer wall of the frame below the base surface, the lateral deformation is very small; that is, it is difficult to have toughness requirements. Therefore, this study suggests that the strength and stiffness of the frame below the base surface should not be lower than those for the superstructure. The design total transverse force of the superstructure can be used to design the frame below the base level; however, at least the vertical members must comply with the special requirements for the seismic design of the structural design code, and the beam members can be considered without ductility. However, the aggregate members in the frame and the shear force transmission path of the floor plan still need to be checked.

4. The ultimate shear force can be estimated in accordance with the provisions of Section 2.17 of the current building seismic code, or a nonlinear static thrust analysis is performed, and the base shear force value corresponding to the lateral thrust building and its ductile capacity shall prevail.

Based on the above considerations, it is suggested to modify the seismic design requirements of the frame below the base as follows:

Provision:

For the framework between the base surface and the foundation, the ultimate shear strength of the floor above the base surface and 1.4 times the design seismic force are considered, and the internal force caused by the two is larger, and the strength design is carried out. At this time, if the design strength of the vertical member below the base surface is… For vertical members whose stiffness is not lower than that of the base surface, the design strength may be calculated on the basis of the design seismic force, and it is ensured that the special requirements for seismic design of the corresponding structural codes are met.

Commentary:

The structure of the basement between the base and the foundation has a high stiffness outer wall, and there is no need for ductility design. Therefore, the frame below the base surface must be designed with strength; however, its strength must be sufficient to support the structure above the base surface and fully develop its nonlinear behavior. The corresponding seismic load is increased, which allows the frame below the base surface to be designed with the internal force caused by the ultimate shear strength of the structure above the base surface and $1.4\alpha_y$ times the

design seismic force, whichever is greater. The frame does not need to meet the special requirements for seismic design of the corresponding structural code.

Compared with the superstructure, the internal force of the vertical member below the base surface caused by the lateral force is relatively low. Therefore, if the vertical member below the base has been designed for the aforementioned strength, its design strength and stiffness are not lower than those connected to the base surface. For vertical members, the minimum total seismic transverse force may be used to calculate their design strength; however, the vertical members must meet the special requirements for seismic design of the corresponding structural code.

Conclusions

This study clarifies the principles and procedures for ductile design or capacity design in the seismic design requirements of the structure below the base level of the building. Considering that the structure below the base level has no obvious ductility requirements, the strength of its vertical members should be considered in the design. Therefore, in this study, it is suggested that if the design of the frame below the base level is carried out with the design seismic force of the upper structure, not only its strength and stiffness should not be lower than those of the upper structure but also its vertical members must meet the seismic resistance of each structural code. The design specifically stipulates that it can have sufficient member strength and ductility to ensure that the superstructure can effectively develop its ductility; if the ultimate shear strength above the base level and $1.4\alpha y$ times the design seismic force are considered, the strength design can be directly carried out. However, regardless of what design procedure is adopted, considering the effect of non-structural walls and other factors, the design of the frame below the base level still needs to check the requirements of the aggregated members and the shear force transmission path of the floor slab.

In the US building design code, the superstructure and the frame below the base level are regarded as different structural systems. In other words, the frame below the base level is regarded as a structural system with low ductility capacity, and its seismic force reduction coefficient is small, making it… The design seismic force is greater than its superstructure, and its vertical members must be designed for capacity.

References

Architecture Buildings Research Institute (ABRI), 2011. *Recommended Provisions for Building Seismic Regulations*, Taipei (in Chinese).

Structural Engineers Association of California (SEAOC). (1999). "Recommended Lateral Force Requirements and Commentary," *7th Edition*, Seismology Committee, Structural Engineers Association of California, Sacramento, California.

American Society of Civil Engineers (ASCE/SEI 7-22). (2022). "Minimum Design Loads and Associated Criteria for Buildings and Other Structures." *ASCE 7-22*, American Society of Civil Engineers, USA.

ACI (American Concrete Institute). 2019. Building code requirements for structural concrete and commentary. ACI 318-14/19, 318R-14/19. Farmington Hills, MI: ACI.

AISC (American Institute of Steel Construction). 2022. Seismic provisions for structural steel buildings. AISC 341-10. Chicago: AISC.

The Scaling Procedure of the Recorded Ground Motions for Seismic Analysis of Base-Isolated Buildings

Wen-Yu Jean[1] and Hsun-Jen Liu[2]

簡文郁 [1]、劉勛仁 [1]

Abstract

The objective of this study is to provide some guidelines for the selection and scaling of real records for bi-directional analysis of base-isolated buildings in Taiwan. The geometric mean component of response spectrum is selected as the preferred definition of the horizontal component when bi-directional analysis is carried out. A 24-storey base-isolated RC building located in Tainan city is selected as the study case. The comparisons show that the selection and scaling requirements specified in the TBC may obtain a very conservative results for recorded ground motion records. Due to some shortages of the PSHA procedures, the design spectrum provided by code is probably not able to represent some features of ground hazard of extreme earthquake at the site. A ground motion recorded from near on-site damaging-earthquake is also recommended for the study case as an extreme damage assessment of the structure.

Keywords: Taiwan Building Code (TBC), response time-history analysis (RHA), ground motion selection and scaling, pulse-like ground motion

Introduction

Estimation of the seismic safety to a structure requires assessment of both the seismic hazard and the structural response due to the earthquake. However, the inconsistencies of definitions of the horizontal spectral component between the seismic hazard assessment and structural analysis have been very common in engineering practices. [Baker, and Cornell, 2006]. The nonlinear response history analysis (RHA) is now a common engineering practice to estimate seismic demands for performance assessment and seismic design of complex structural systems including base-isolated buildings, high-rise structures. Three types of the signals are usually used for the inputs of RHA in engineering practices: (1) artificial waveforms; (2) recorded ground motion records; and (3) simulated accelerograms.

Most seismic design code allows employment of all three kinds of accelerograms listed above as the inputs for seismic structural analysis. In the last two decades, the real accelerograms are becoming the most attractive option to get unbiased estimations of the seismic demand. The purpose of time-history analysis for design is to successfully predict the unbiased seismic demand with relatively limited variation in results. Earthquake records selected for RHAs often need to be scaled to a seismic hazard level considered. The basic features of selecting and scaling of ground motion records for dynamic analysis are consistency, sufficiency, and efficiency.

The selections of ground motion record have to reflect both the seismic hazard and the shallow geology of the area under study, they also have to consider the record-to-record variability. The seismic design codes also provide some basic requirements of selecting and scaling of ground motion record sets, which are sufficient and efficient to produce reliable median estimates of the structural response.

Scaling Requirements as per Codes

A review of code provisions regarding selection and scaling of ground motions for RHA revealed that the guidelines provided by international seismic codes are frequently inconsistent or are lacking transparency regarding the underlying assumptions [Beyer & Bommer, 2007]. For example, the ASCE 7-16 used the maximum direction spectrum to define the design response spectrum. However, the SRSS of bi-direction

---

[1] Research Fellow, National Center for Research on Earthquake Engineering
[2] Assistant Researcher, National Center for Research on Earthquake Engineering

spectrum component was used in the procedures of ground motion selection for the RHA of base-isolated buildings. The comparisons of the international Seismic Design Codes also reveal that the period ranges of interest for checking the fitness of spectral shape are also significantly different. The period range over which matching of design spectrum and the scaled spectrum of the records required by the seismic design code can be expressed as $[T]=[T_{min}, T_{max}] = [\alpha_1 \cdot T_1 , \alpha_2 \cdot T_1]$ for traditional buildings linear or nonlinear RHA. T_1 is the fundamental period of the structure. The factors of (α_1, α_2) are significantly different in the international codes, e.g., (0.2, 1.5) is required in EC8, FEMA 368, and ASCE 7-16; (0.4, 1.3) is required in NZS.

Full agreement of commonly accepted selection and scaling criteria of recorded ground motion records has not yet been reached.

The Spectral Component

The geometric mean spectral ordinates were used to develop the GMPEs, then, the uniform hazard spectral maps were derived through the PSHA, and adopted by the TBC. The geometric mean component of response spectrum is, therefore, selected as the preferred definition of the horizontal component when bi-directional analysis is carried out. Both components of a selected record should be scaled by the same factor, to match their geometric mean spectrum to the target spectrum over the period range. The orientation of the two horizontal components as recorded is used for the selection of single direction ground motion.

The Database for GM Selection

The three most important selection parameters to select ground motions consistent with the hazard are magnitude (M), source-to-site distance (R), and site class. The parameters-(M, R) bins are gained from the de-aggregation of the PSHA on the PE of the specified design-basis ground motion. Based on the design spectral shapes and site conditions, the Taiwan recorded ground-motion database for structural RHA has been established in a previous study. A brief summary of the ground motion properties is provided, which provides a few metadata fields for each selected ground motion. A more complete set of information is available from the project website (http://seaport.ncree.org/inmost/).

Period Range for Scaling

The period ranges of interest, $[T]=[T_{min}, T_{max}]$, for checking the fitness of spectral shape are different in the seismic design codes. This insistency may result in different sets of ground motion and the corresponding scaling factors. The period ranges of interest, $[T]$, required in selected seismic design codes (TBC-2011, ASCE 7-16, NZS-2019, and NBC-2015) for base-isolated buildings are compared and listed in Table 1.

The effective period (T_e or T_M) of the base-isolated structure at the maximum displacement is key factor in the seismic design procedures, and has a significant effects on the structural response subjected to an earthquake. Most seismic design codes use the effective period to define the period ranges for ground motion selection and scaling. As shown in Table 1, the period ranges of interest are extended beyond effective period to recognize that the tangent-stiffness based period near maximum displacement may be associated with a period significantly longer than the secant-stiffness-based period. On the other hand, the NBC-2015 use the post-yield stiffness of the isolation system to define the period range of interest, and is likely to have a larger range of period.

Scaling Procedure

Because of the limitations of the existing earthquake ground motion records, it is necessary and useful to scale the records to make seismograms consistent with a target ground motion for structural

Table 1: the comparisons of period range of interest, [T], required in Seismic Design Code for base-isolated buildings.

Code	period range: $[T]=[T_{min}, T_{max}]$	Notes
TBC-2011	$[0.2 \cdot T_e , 1.5 \cdot T_e]$	T_e : The effective period of the isolated structure at the maximum displacement.
ASCE 7-16	$[0.75 \cdot T_{M1}{}^{*1} , 1.25 \cdot T_{M2}]$	T_{M1}, T_{M2} : The effective period, at the maximum displacement, determined using upper- and lower-bound isolation system properties, respectively.
NZS-2019	$[\min .(0.4T_{eff,L}, T_{1,elastic}), 1.2T_{eff,U}]$	T_{eff} : Effective period of isolated structure; $T_{1,elastic}$: the fundamental period for the isolated system during elastic phase response of the isolators.
NBC-2015	$[0.2 \cdot T_1 , 1.5 \cdot T_1]$	T_1 : the period of the isolated structure, determined using the post-yield stiffness of the isolation system.

Note 1: the requirement of T_{min} is replaced by ASCE 7-22, it is now the same as the case for traditional buildings linear or nonlinear RHA.

design and evaluation. The intensity-based scaling methods preserve the original non-stationary characteristics of the ground motion record and only modify its amplitude. There are many intensity-based scaling procedures have been proposed for the RHA in previous researches [Kalkan & Celebi, 2009; Huang, et al., 2011]. There are two main requirements per current international codes on the selection and scaling for ground motion records: (1) the shape matching criterion, and (2) the 90% criterion.

The shape matching criterion requires that the response spectrum of the record should be as similar as possible to the target. In other words, the average of the logarithm of the acceleration response spectrum of ground record should match the average of the logarithm of the target spectrum over the specified period range, [T]. For record j, the error, Err_{ij}, of the spectral shape at period $T_i \in [T]$ is defined as,

$$Err_{ij} = Err(T_i) = Ln[S_{a,target}(T_i)] - Ln[S_{a,record\_j}(T_i)] \quad (1)$$

and,

$$\overline{Err_j} = \frac{1}{N}\sum_{i=1}^{N} Err_{ij} \quad (2)$$

where, N is the number of records required by the code. The scaling factor of the record j is assigned as $\exp(\overline{Err_j})$, and the fitness index will be σ_{Errj}^2. A two-step scaling procedure is adopted in this study.

Step 1: according to the fitness index, σ_{Errj}^2, N-records are selected, and each one with the scaling factor of $f_{1j} = \exp(\overline{Err_j})$. The shape matching criterion will be satisfied for every individual record and/or for the N-record group (the average spectrum of the N-records).

Step 2: the extra requirement, the 90% criterion, should be applied to make sure that no significant energy drop occurred at any period within the specified period range. This will confirm that the spectrum of the scaled record does not underestimate the code spectrum, with a 10% tolerance. Another scale factor $f_2 \geq 1.0$ must be applied in this step.

The final scaling factor for the j-th record will be $f_j=f_{1j} * f_2$. In most international seismic design code, the 90% criterion is applied to the average spectrum of the N-records, and make an identical group scale factor f_2 for all the N-records. However, the TBC requests that the 90% criterion must be applied to each individual record.

Case Study

A 24-storey base-isolated RC building located in Tainan city is selected as the study case. The site condition, V_{s30}=214.8 m/s, is classified as the S2 site per TBC (or the NEHRP site class "D"). This is not a near-fault site. The important design parameters of the isolator system are summarized in Table 2. The effective period of the seismically isolated structure at design displacement D_D, is estimated as T_e=4.349 s. The period of the isolated structure determined using the post-yield stiffness, K_D, of the isolation system is estimated as T_1=5.48 s. As shown in Table 1, the period ranges of interest required by different seismic design codes for this study case are compared in Figure 1. The period range defined by the NBC-code is much wider than that defined by the ASCE 7-16 code. The variation of the nominal design parameters of the isolator is assumed to be 15% in total for calculating the property modification factors and period range for ASCE 7-16 code.

The total of seven pairs of ground motion records, as suggested by the code, is selected and scaled for nonlinear RHA in this case study. The records are selected from the Taiwan recorded ground-motion database, the (M, R)-bin can reflect the hazard on the PE of the design-basis earthquake. In order to take into account the record-to-record variability, an additional criterion is adopted to limit the number of records to two selected from any single event.

The geometric mean spectra of scaled records compared with the target spectrum are shown in Figure 2, as per TBC-code and ASCE 7-16 code, respectively. The spectra of the original records are also shown for reference. Following the scaling requirements of the TBC-code, the intensities of the scaled record set are 60% higher than those following the ASCE 7-16 code. The TBC-code requests that the 90% criterion must be applied to each individual record, and, could result unnecessarily conservative assessment of the seismic hazard. Similar procedures and results for one-directional ground motion selection and scaling are also conducted in this study.

Table 2: the important characteristics of the isolator system of the study case.

parameters		value
Yielding strength	F_y	801.1 tf
	Q_D	729.24 tf
Initial stiffness	K_1	40055.16 tf/m
Post-yielding stiffness	K_D	3593.16 tf/m
Design displacement	D_D	0.345 m
Effective stiffness at D_D	K_e	5706.9 tf/m
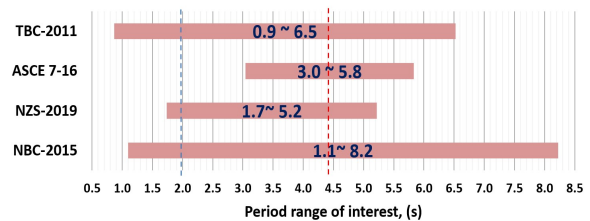
Figure 1. the comparison of period ranges of interest using different Seismic Design Code for the study case.
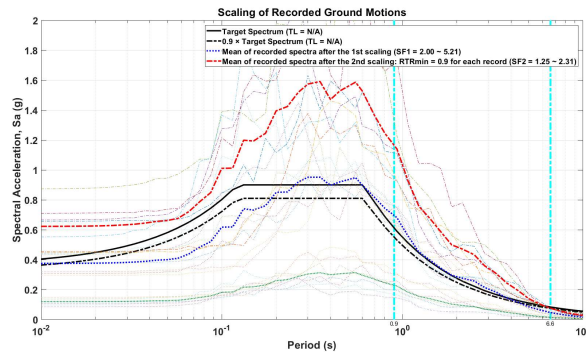
(a)TBC
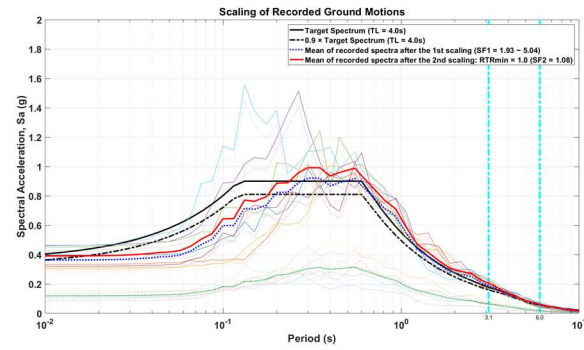
(b) ASCE/SEI 7-16

Figure 2. The comparisons of the RSs of scaled GM-records with the target spectrum (MCE)

Site-Specific Consideration

Due to some shortages of the PSHA procedures, the design spectrum provided by code is probably not able to represent some features of ground hazard of extreme earthquake at the site. One or two ground motions recorded from near on-site historical damaging-earthquake are also suggested as an extreme damage assessment case of the structure using the RHA.

The $M_w6.4$ Meinong earthquake occurred in 2016 and caused significant damage in and around Tainan city (117 deaths). Many strong motion stations near the study site recorded the pulse-like ground motion data. These ground motions contain pulse components of energy that could have a large destructiveness to the long-period structures, e.g., base-isolated buildings. The records of CHY064 and CHY116 of the TSMIP during the $M_w6.4$ event are selected and scaled for the RHA of the case study. The EW-components of these two records have high V/A-values of 0.284s and 0.252s. These high V/A-values reveal the long period energy contents of the ground motion, which is relating to the features of pulse-like ground motion. The geometric mean spectra of scaled records compared with the target spectrum are shown in Figure 3, in a similar way. The period range specified by the TBC-code is used in the scaling procedure for the

pulse-like ground motion records. The lower bound of period range, T_{min}, is based on the TBC-code and fell on the constant spectral acceleration domain of the target spectrum. Based on the geo-mean spectra component, the scaling procedure is, then, likely to be constrained on the constant Sa domain of the target spectrum. The features of the far-field-ground-motion portion can be scaled appropriately, so as those of the pulse-like-ground-motion portion.

Conclusions

The geo-mean spectra component is adopted in the ground motion selection and scaling for the real record. A single scale factor is applied to the two-components of ground motion, which can be applied for evaluation of the seismic demands and performances under the design-basis level earthquakes (DBE and MCE) for the target site. However, there exist a significant difference in intensity between the two components. Considering of different direction of the scaled ground motion pairs to the structure is highly recommended for the RHA to take into account the difference in intensity between two components of the real records.

Figure 3. The comparisons of the RS of GM-record (CHY064) collected from 2016 Meinong $M_L6.6$ ($M_w6.4$) earthquake with the target spectrum (MCE)

References

Beyer, Katrin & Bommer, Julian. (2007). Selection and Scaling of Real Accelerograms for Bi-Directional Loading: A Review of Current Practice and Code Provisions. Journal of Earthquake Engineering. 11. 10.1080/13632460701280013.

Kalkan, Erol & Celebi, Mehmet. (2009). Assessment of ASCE-7 Ground Motion Scaling Method Using Computer Model of Instrumented High-Rise Building. ATC and SEI Conference on Improving the Seismic Performance of Existing Buildings and Other Structures:905-915. 10.1061/41084(364)82.

Huang, Yin-Nan, Andrew S. Whittaker; Nicolas Luco, and Ronald O. Hamburger, 2011. Scaling Earthquake Ground Motions for Performance-Based Assessment of Buildings, Journal of Structural Engineering, Vol. 137, No. 3, DOI: 10.1061/(ASCE)ST.1943-541X.0000155.

Seismic Analysis of a Vertically Irregular Building Collapsed on a Shake Table

Jui-Liang Lin[1] Wen-Hui Chen[1] Fu-Pei Hsiao[1] Yuan-Tao Weng[1] Wen-Cheng Shen[1] Pu-Wen Weng[1] Shu-Hsien Chao[1] Lap-Loi Chung[1] and Shyh-Jiann Hwang[1]

林瑞良[1]、陳雯惠[1]、蕭輔沛[1] 翁元滔[1] 沈文成[1] 翁樸文[1] 趙書賢[1] 鍾立來[1] 黃世建[1]

Abstract

A 7-story reinforced concrete building with a soft bottom story and plan-asymmetry in one horizontal direction was collapsed on a shake table by generating bi-directional near-fault ground motions. The numerical model of the 7-story building is introduced and verified through comparison with the experimental results. The hysteretic models of the verified numerical model are calibrated according to static cyclic component tests. To assume the condition that the static cyclic component tests are not available, the hysteretic models of some critical structural components are intentionally altered. Three additional numerical models of the building, which serve as the distorted numerical models, are obtained from the combinations of the altered hysteretic models. Incremental dynamic analyses (IDA) are applied to the four numerical models of the building (i.e., one verified model and three distorted models). Comparing the IDA results of the four numerical models helps to elucidate the effect of the hysteretic models on the full range of the seismic responses (i.e., from elastic response to total collapse) of the building.

Keywords: seismic analysis, vertically irregular building, shaking table, hysteretic model

Introduction

Hysteretic models can be categorized into two types depending on whether the hysteretic loops are piecewise linear or smooth: a polygonal hysteretic model (PHM) [1] or a smooth hysteretic model (SHM) [2]. Regarding PHMs, Takeda et al. [1] proposed a model with a trilinear backbone curve, whose first segment represents the state of uncracked concrete. Unloading stiffness deterioration was also considered in this model. For SHMs, the Bouc–Wen model [2] has a smooth change in stiffness that realistically reflects the features of hysteretic loops.

The abovementioned hysteretic models [1, 2] are sophisticated and versatile, facilitating the application of nonlinear response history analysis (NRHA) to various structures. However, regardless of the hysteretic model, the selection and justification of the values of the parameters of hysteretic models remain challenging for NRHA. These parameters can be calibrated using the hysteretic loops obtained from static cyclic tests of the structural components under investigation. For example, the deterioration parameters of the hysteretic models proposed by Ibarra et al. [3] were calibrated from component tests performed on materials including steel, reinforced concrete (RC), and plywood. It was remarked that further research is required to establish consistent methods for assessing the deterioration parameters [3]. When the hysteretic loops of component tests are not available for calibration, engineering judgment seems to be the only alternative for deciding the values of the parameters. As a result, it is highly likely that the results of NRHA on a structure fluctuate when different sets of parameter values for the hysteretic models are adopted.

The effect of hysteretic models on the seismic performance of structures has been extensively investigated. For example, Huang and Foutch [4] investigated the effects of five types of hysteresis on the drift limit for global collapse of 3-, 9-, and 20-story steel moment frames. They concluded that strength degradation has a more significant impact on the global drift limit compared with stiffness degradation and pinching [4]. Owing to the scarcity of shake tables with sufficient long-stroke and high-velocity

---

[1] National Center for Research on Earthquake Engineering, Taiwan, R.O.C.

capacities to reproduce near-fault ground motion records, there is a demand to validate numerical models of complete buildings subjected to near-fault ground motions through shaking table tests. A blind contest for predicting the seismic response of a 1:2 scale 7-story RC building was held by Taiwan's National Center for Research on Earthquake Engineering (NCREE) in 2018 (Figures 1 and 2).

The present study first demonstrates the ability of the numerical model to simulate the seismic responses of the 7-story building, varying from slightly yielding to completely collapsed. Second, the verified parameter values of the hysteretic models used for the 7-story building are intentionally altered to simulate cases when the hysteretic loops of the component tests used for calibration are not accessible. Using the hysteretic models with the verified parameter values as benchmarks, the effects of hysteretic models on the seismic evaluation of the 7-story building are examined.
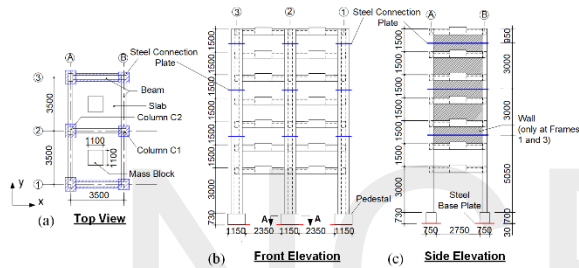
Figure 1. (a) Top view, (b) front elevation, and (c) side elevation of the 7-story building.
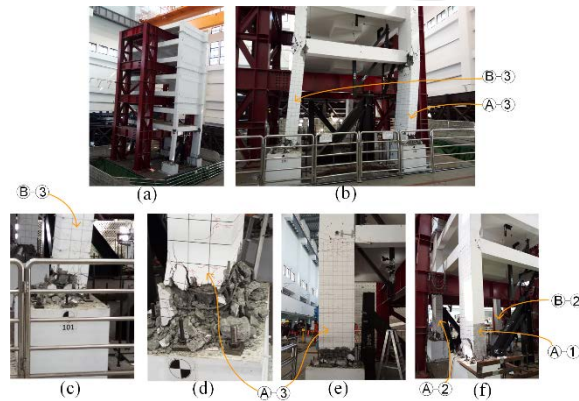
Figure 2. Collapse of the 7-story building under the CHY063_200% event: (a) full model, (b) close-up photograph of the bottom two stories, damage at the bottom of (c) Column C1 located at B-3 and (d) Column C2 located at A-3, (e) Column C2 located at A-3 as viewed perpendicularly to the long side of the column, and (f) perspective from Column C2 located at A-1 toward Column C1 located at B-2.

Shaking Table Test

The 7-story building was tested on the shake table

using five simulated seismic events (Table 1). The first seismic event is the 70%-scaled ground motion record of Station CHY015 during the 1999 Chi-Chi earthquake. The second to fifth seismic events are the ground motion record of Station CHY063 during the 2016 Meinong earthquake with scaling factors of 50%, 100%, 150%, and 200%, respectively. The two selected ground motion records, denoted as CHY015 and CHY063, are far-field and near-fault ground motion records, respectively. Figure 3 shows the acceleration histories of the two selected ground motion records, in which the time scales are multiplied by $1/\sqrt{2}$ according to the theory of dimensional analysis. The east–west, north–south, and up–down (denoted as EW, NS, and UD) components of each generated seismic event were simultaneously applied in the x-, y-, and z-directions of the building model.

Table 1. Peak accelerations of the five shaking events.

Event No.	Ground motion	exerted PGA in $x/y/z$ directions (m/s^2)	Duration (s)
1	CHY015_70%	1.16/1.18/0.26	200
2	CHY063_50%	2.30/1.14/0.81	90
3	CHY063_100%	4.60/2.26/1.72	90
4	CHY063_150%	7.01/3.46/2.54	90
5	CHY063_200%	9.09/5.19/3.28	90
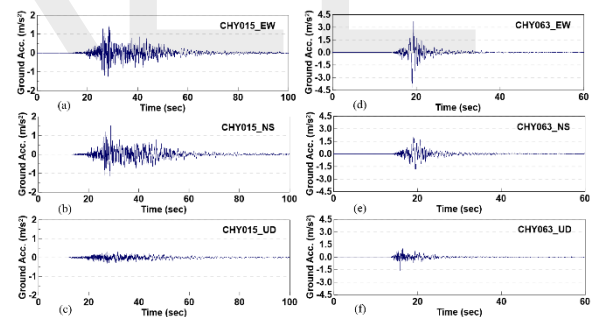
Figure 3. (a) EW, (b) NS, and (c) UD components of the acceleration history of CHY015, and the (d) EW, (e) NS, and (f) UD components of the acceleration history of CHY063.

Numerical Simulation

Based on the results of the component test and shaking table test, a calibrated numerical model was constructed and verified. Beam–column elements with concentrated plastic hinges at the two ends of the elements were used to simulate the beams and columns of the 7-story building model. A degrading material model featuring stiffness deterioration, strength deterioration, and pinching was used for the columns. A bilinear material model was used for the beams. The material models are combined with the section

properties of beams and columns to define the overall force–deformation relationship of a cross section of a beam–column element. Moreover, because most deformation was expected to be concentrated at the soft bottom story, panel elements with a linear elastic material model were used to simulate the walls. The floor slabs were modeled as rigid diaphragms with lumped masses. Rayleigh damping was applied with a damping ratio of 5% for the first two vibration modes to simulate the inherent damping of the building model. The vibration periods of the first and the second modes were found to be 0.72 s and 0.64 s, respectively. In addition, the first mode is purely x-translational, whereas the second mode is coupled y-translation and rotation.

Figures 4c and 4f indicate that the x- and y-directional peak interstory drifts of the first story under the CHY063_150% shaking were 6.5% rad and 1.1% rad, respectively. The peak values of the interstory drifts imply that the building model underwent significantly inelastic excursions in the x-direction and yielded moderately in the y-direction. According to the results of component tests, a drift of 6.5% rad means that the first-story columns have exceeded their peak strength and entered into a negative-stiffness softening state. The x-directional seismic responses are satisfactorily simulated until 22 s. After 22 s, the experimental seismic responses decayed much more slowly than the analytical results. For the y-directional responses, the numerical model is capable of estimating the amplitudes and times of the occurrence of peak responses. Nevertheless, the residual displacement in the y-direction was not well simulated. This verified numerical model is further exploited to investigate the effects of hysteretic models on the seismic evaluations of the building subjected to the near-fault ground motion CHY063.
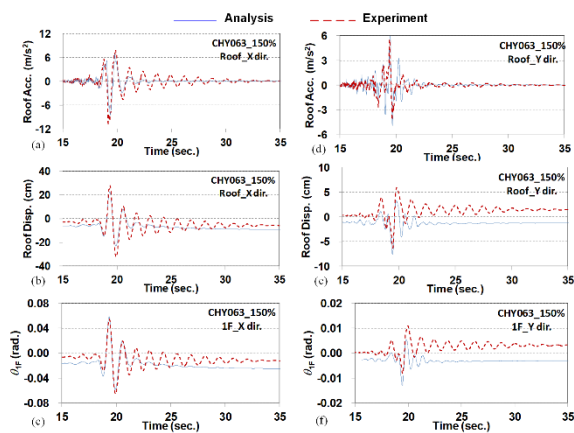
Figure 4. Histories of the x-directional (a) roof acceleration, (b) roof displacement, and (c) the first story interstory drift of the 7-story building under CHY063-150% shaking. Figs. (d), (e), and (f) are the y-directional counterparts of (a), (b), and (c).

Effects of Hysteretic Models

In addition to using the verified numerical model as the benchmark model (denoted as Case O), this study considers three hypothetical cases (denoted as Case I, II, and III). Figures 5a to 5d illustrate the combinations of the hysteretic models of columns and beam-to-column joints used in Cases O, I, II, and III, respectively. In Figure 5, the blue plots are the original (calibrated) hysteretic models and the orange plots are the hypothetical hysteretic models.
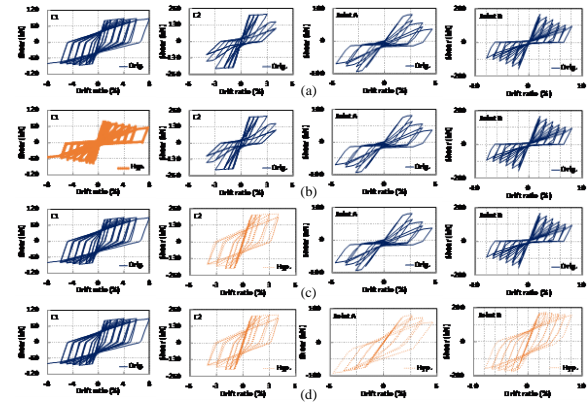
Figure 5. Arrangements of the hysteretic models adopted in Cases (a) O, (b) I, (c) II, and (d) III.

Figure 6a shows the x-directional inter-story drifts at the two edges of the first story (denoted as $\theta_{x,1F,edge}$), in which the two edges correspond to Column C2 at A-3 (denoted as A3) and Column C2 at A-1 (denoted as A1). As the building is symmetrical in the x-direction, the drift responses at the two edges (A3 and A1) are almost identical when the building is elastic, regardless of the hysteretic model used (Figure 6a). Nevertheless, as $S_a(T_1, 5\%)$ is approximately equal to or slightly greater than 0.5 g, the eight lines shown in Figure 6a start bifurcating. The eight lines essentially divide into two groups, one of which contains the four cases of Column C2 at A-3, and the other the four cases of Column C2 at A-1 (Figure 6a). In addition, the drift demands of the former group (Column C2 at A-3) are generally greater than those of the latter group (Column C2 at A-1). This phenomenon implies that the bifurcation of the eight lines (Figure 6a) results from not only the different hysteretic models but also the plan-asymmetry in the y-direction. Furthermore, given the aforementioned division of the drifts into two groups, the x-directional drifts seem to be more affected by the y-directional plan-asymmetry than by the hysteretic models. This observation underscores the complicated seismic characteristics of asymmetric-plan buildings subjected to bi-directional ground motions. Moreover, the magnitudes of the x-directional drift demands from great to small in each group is Case I, Case O, Case II, and Case III; this reasonably reflects the arrangements of the hysteretic models (Figure 5).

Figure 6b shows the y-directional interstory drifts at the two edges of the first story (denoted as $\theta_{y,1F,edge}$), in which the two edges correspond to Column C2 at A-3 (denoted as A3) and Column C1 at B-3 (denoted as B3). As the building is asymmetrical in the y-direction, the drift responses at the two edges (A3 and B3) are substantially different regardless of whether the building is elastic or inelastic (Figure 6b). In addition, because Column Line A is the stiff side in terms of the y-directional plan-asymmetry, whereas Column Line B is the flexible side, the y-directional drift demand of Column C2 at A-3 is significantly less than that of Column C1 at B-3 (Figure 6b). For Column C1 at B-3, the magnitude of the y-directional drift demand from great to small is Case I, Case o, Case II, and Case III, which is identical to the observations for the x-directional drift demands (Figure 6a).
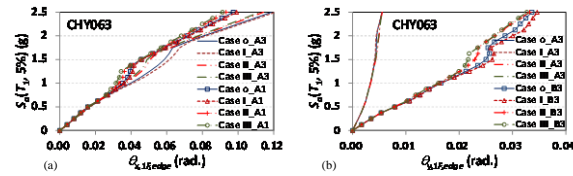
Figure 6. (a) x-directional and (b) y-directional interstory drifts at the corresponding two edges of the first story for Cases O, I, II, and III under various seismic intensities.

Figures 7a and b respectively illustrate the x- and y-directional hysteretic loops of Case o subjected to CHY063 with $S_a(T_1, 5\%) = 2.5$ g. The four plots in each of Figures 7a and b, from left to right, are the hysteretic loops of Column C2 at A-3, Column C1 at B-3, the beam–column joint at A-3, and the beam–column joint at B-3. The counterparts of Cases I, II, and III are illustrated in Figures 7c-d, e-f, and g-h, respectively.

Conclusions

This experimental and numerical study tackled three challenging issues: the replication of near-fault ground motions using a shake table, shaking and numerically simulating a vertically and horizontally irregular building model until its collapse, and consideration of the effect of bi-directional earthquakes. While these issues have been individually and intensively examined by the earthquake engineering community, they have been rarely studied together because of the scarcity of shake tables with a long-stroke, high-velocity capacity. This study addressed these challenges in a single experiment, which may reflect the actual complex conditions imposed on a large number of building structures.
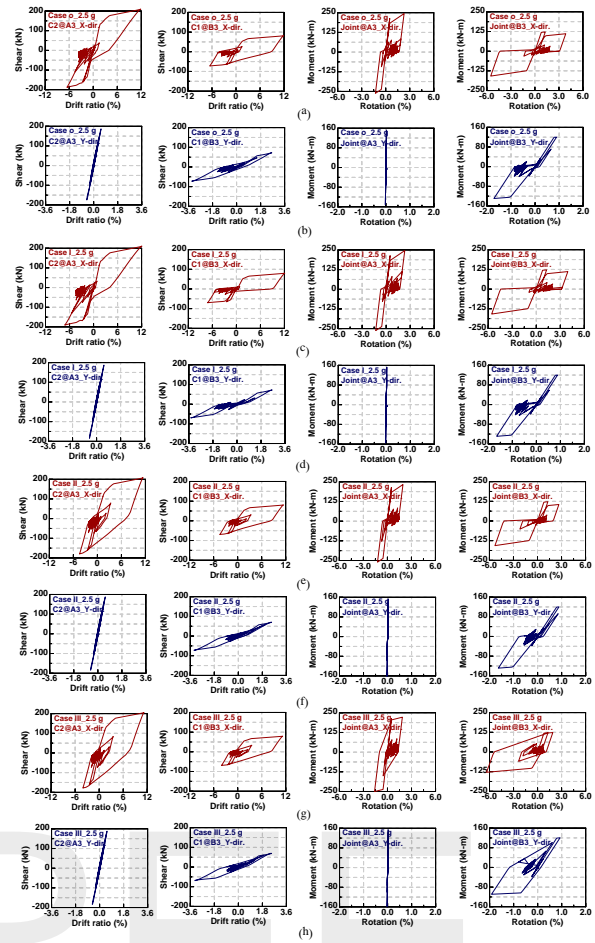
Figure 7. Hysteretic loops of the building under CHY063 with $S_a(T_1, 5\%) = 2.5$ g for Case o in the (a) x- and (b) y-directions, Case I in the (c) x- and (d) y-directions, Case II in the (e) x- and (f) y-directions, and Case III in the (g) x- and (h) y-directions.

References

Takeda, T., Sozen, M.A., and Nielson, N. N. (1970), "Reinforced concrete response to simulated earthquakes", ASCE *Journal of the Structural Division*, 96, 2557–2573.

Wen, Y. K. (1976), "Method for random vibration of hysteretic systems", ASCE *Journal of the Engineering Mechanics Division*, 112, 249–263.

Ibarra, L. F., Medina, R. A., and Krawinkler, H. (2005), "Hysteretic models that incorporate strength and stiffness deterioration", *Earthquake Eng Struct. Dyn*, 34, 1489–1511.

Huang, A., and Foutch, D. A. (2009), "Effect of hysteresis type on drift limit for global collapse of moment frame structures under seismic loads", *Journal of Earthquake Engineering*, 13, 939–964.

In-plane Experimental Study on an Attached RC Frame Using High Strength Anchor Bolts

T.C. Chiou[1]   L.L. Chung[2]   J.F. Liang[3]   Y.C. Lai[4]   J.L. Li[5]   K. Den.[5]

邱聰智[1]   鍾立來[2]   梁瀞方[3]   賴昱志[4]   李梓綸[5]   鄧凱文[5]

Abstract

Attaching external reinforced concrete (RC) frames to existing buildings not only enhances the seismic capacity of existing structures but also reduces the interruption in the use of buildings during retrofitting. The mechanisms of force transmission between the interface of attached and existing frames are significant in design technology. Therefore, improvement in the confidence of connections is essential during construction. This study proposes using high strength anchor bolts for connection instead of adhesive rebar, as this can improve the quality control of connection. Three frame tests, a prototype RC fame, an attached RC frame using an adhesive rebar connection, and an attached RC frame using an anchor bolt connection, are reported. Comparison of the connections using adhesive rebar and anchor bolts is discussed. Testing results indicate that the lateral strength of the retrofitted frames is significantly increased and the deformation capacity is also improved when the frame is attached using anchor bolts rather than adhesive rebar connections.

Keywords: seismic retrofit, reinforced concrete frame, adhesive rebar, anchor bolt, existing building

Introduction

Seismic retrofit of existing public school buildings has been implemented in the past decade in Taiwan. Most of the public school buildings were retrofitted by reinforced concrete (RC) jacketing columns, wing walls, RC walls etc. These traditional retrofitting schemes can be conducted on school buildings because the schools have summer and winter vacations. However, many existing buildings, such as hospitals, factories, and residential buildings, cannot lose functionality for two to three months for retrofitting. Attaching external RC frames to existing buildings can not only enhance the seismic capacity of existing structures but also reduce the interruption to the use of buildings during the retrofitting.

Attaching external RC frames to the outside of existing buildings has been widely applied to schools in Japan. Takeda et al. (2013) adopted a new RC slab for connection between the attached and existing frames by adhesive rebar. However, the construction quality control may be an issue in Taiwan. This study proposes attaching new RC frames to the existing frames without a connecting slab. The interface between the attached new beams and existing beams is connected by high strength anchor bolts. The construction procedure is simplified to drilling holes in the existing RC beams, placing the high strength anchor bolts in the holes, reserving a suitable embedded length of bolts in the steel cages of the new attached beam, and finally casting the concrete of the newly attached beam. No cleaning holes and injection of adhesive paste are required. This can significantly improve the construction quality of connections.

This study conducted cyclic loading tests on three RC frames, a prototype RC frame, an attached RC frame using an adhesive rebar connection, and an attached RC frame using anchor bolt connections, in the structural laboratory of National Center for Research on Earthquake Engineering (NCREE) in Taiwan. Different connections for the interface between the attached beam and existing beam are clarified and discussed in conjunction with the experiments. In the following sections, the retrofitting

design and test program, results of cyclic loading tests, analysis and comparison of testing results, and conclusions are reported.

Retrofitting Design and Test Program

The tests were conducted in the Multi-Axial Testing System (MATS) in NCREE. The specimens simulated the existing school building frames at a scale of 0.45 due to the limitation of MATS. The attached external frame was designed with higher lateral stiffness and strength than the existing frame. Therefore, the new frame will develop its ultimate strength under a small deformation while the existing frame would still remain in the elastic range, as shown in Figure 1.

To test the effectiveness of retrofitting using an external frame, a prototype existing frame and an attached external frame were designed for investigating the behavior. The dimensions of the test frames are shown in Figure 2, and detailed sections of the frames are shown in Figure 3. To test the connection between the beam interfaces, the external frame attached with high strength anchor bolts and with adhesive rebar were tested. The connection details of the beam interfaces are illustrated in Figure 4.
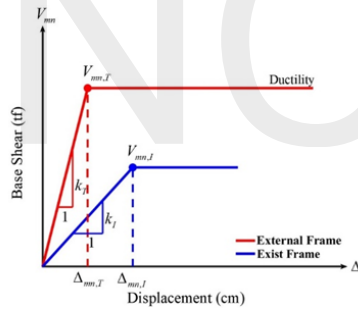
Figure 1. Design concept of retrofit by external frame
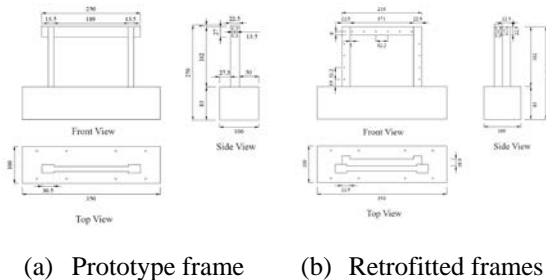
(a) Prototype frame (b) Retrofitted frames

Figure 2. Dimensions of prototype and retrofitted RC frames

(a) Column section of prototype frame (b) Beam section of prototype frame

(c) Column section of retrofitted frames (d) Beam section of retrofitted frames
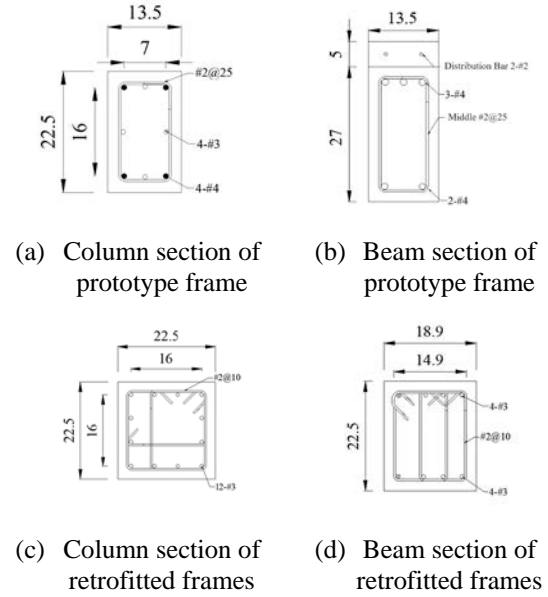
Figure 3. Detailed sections of prototype and retrofitted RC frames

(a) Adhesive rebar (b) Anchor bolts
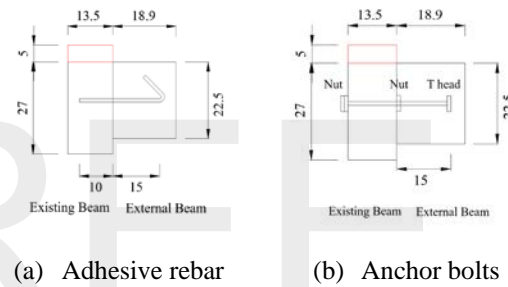
Figure 4. Different connections of prototype and retrofitted RC frames

Cyclic Loading Tests

The existing prototype frame is abbreviated as PT, the external frame attached with high strength anchor bolts as AB, and the external frame attached with adhesive rebar as PB. The material properties are reported in Tables 1 and 2.

The tested behavior of specimen PT is summarized as follows. The frame remained elastic while the inter-story drift ratio was less than $\pm 0.5\%$. The ultimate lateral strength occurred when the inter story drift ratio reached $\pm 1.5\%$, and the ultimate lateral strength was 4.84 tf and 5.39 tf, respectively. The cracking pattern at the ultimate lateral strength is shown in Figure 5. Above 2.0% inter story drift ratio, the lateral strength slowly decreased. The test was terminated at the first cycle of 5.0% inter story drift ratio due to loss of axial loading capacity of the columns; at this point the lateral strength decreased to 2.05 tf. The hysteresis loop of lateral strength versus displacement of specimen PT is shown in Figure 6.

The behavior of specimen AB is as follows. Frame AB remained elastic while the inter story drift ratio was below $\pm 0.5\%$. The ultimate lateral strength was reached when the inter story drift ratio reached $\pm 3.0\%$, and it was 13.84 tf and 11.41 tf, respectively. The cracking pattern at the ultimate lateral strength is shown in Figure 7. Above 4.0% inter story drift ratio, the lateral strength slowly decreased. The test was terminated at the second cycle of 10% inter story drift ratio due the loss of axial loading capacity of the columns, and the residual lateral strength was only 2.02 tf. The hysteresis loop of lateral strength versus displacement of specimen AB is shown in Figure 8.

The behavior of the specimen PB is as follows. BP remained elastic below $\pm 0.375\%$ inter story drift ratio. The ultimate lateral strength was reached when the inter story drift ratio reached $\pm 1.5\%$ and was 14.23 tf and 12.93 tf, respectively. Significant flexural cracks occurred in the columns of the existing frame, and. the cracking pattern at the ultimate lateral strength is shown in Figure 9. After 2.0% inter story drift ratio, the lateral strength decreased significantly. The test was terminated at the first cycle of 8.0% inter story drift ratio due to loss in the axial loading capacity of the columns, and the residual lateral strength was only 6.72 tf. The hysteresis loop of lateral strength versus displacement of the specimen PB is shown in Figure 10.

Table 1. Compressive strength of concrete

f_c' (kgf/cm^2)	PT	AB	PB
Existing frames	356	419	421
Attached frames	-	452	427

Table 2. Tensile strength of rebar

f_y (kgf/cm^2)	Existing frames	Attached frames
#2	3647	3647
#3	3632	4490
#4	3466	-
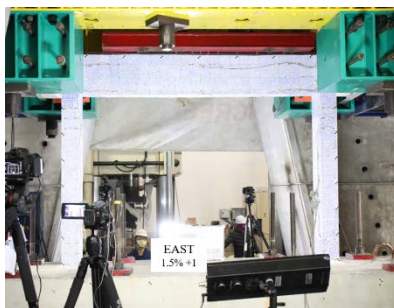
Figure 5. Cracking pattern of specimen PT at the ultimate lateral strength.
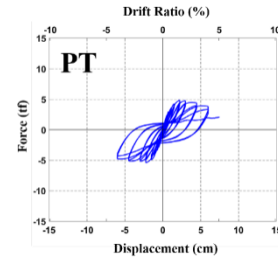
Figure 6. Hysteresis loop of lateral strength versus displacement of specimen PT.
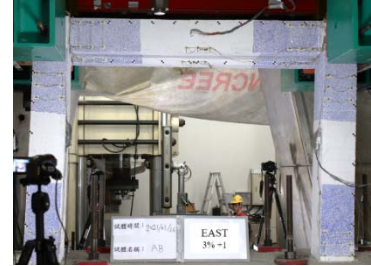
Figure 7. Cracking pattern of specimen AB at the ultimate lateral strength.
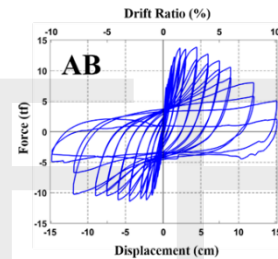
Figure 8. Hysteresis loop of lateral strength versus displacement of specimen AB.
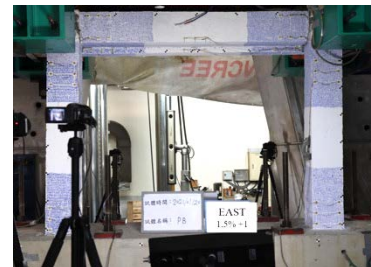
Figure 9. Cracking pattern of specimen PB at the ultimate lateral strength.
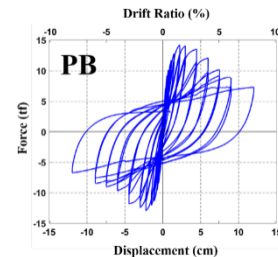
Figure 10. Hysteresis loop of lateral strength versus displacement of specimen PB.

Analysis and Comparison of Test Results

Comparison of the ultimate lateral strength of the three specimens is shown in Table 3. The test results indicate that the ultimate lateral strength of the retrofitted frames was significantly increased, with strength values more than double that of the prototype frame.

Comparing the anchoring effect using the different connections indicates that the lateral force was well transmitted between the interface of the existing and new beams by both the anchor bolts and the adhesive rebar. However, the beam connection with high strength anchor bolts (specimen AB) could retain its post strength toughness more effectively than the connection with adhesive rebar (specimen PB), as shown in Figure 11.

Table 3. Comparison of ultimate lateral strength of the three specimens.

$V_{max.}$ $(tonf)$	ultimate lateral strength	$\frac{V_{max.}}{V_{max.}^{PT}}$
PT	5.39	1.0
AB	13.84	2.57
PB	13.12	2.43
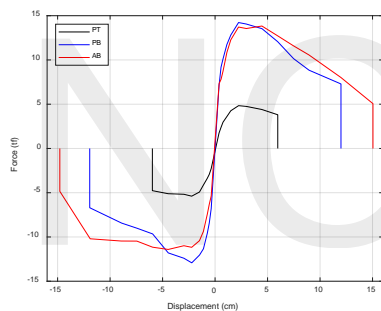
Figure 11. Envelopes of the hysteresis loops of the three specimens.

Conclusions

The study conducted cyclic loading tests of three RC frames, a prototype existing RC frame, an attached RC frame using an adhesive rebar connection, and an attached RC frame using an anchor bolt connection. Based on the test results, the following conclusions can be drawn.

1. Retrofitting frames with attached external frames significantly increases the ultimate lateral strength, with strength values more than double that of the prototype frame.

2. Retrofitted frames with attached external frames have increased deformation capacity, with values more than double or triple that of the prototype frame.

3. Both the proposed connection using high strength anchor bolts and that using adhesive rebar transmit the lateral force between the interface of the existing and new beams well.

4. The proposed beam connection using high strength anchor bolts performs better with regard to post strength toughness than that using adhesive rebar.

References

Liang, J.-F. (2021) "Retrofitting Method by Connecting External Reinforced Concrete Frame with High-Strength Anchor Bolts"master thesis, dept. of civil engineering, NTU.

Japan Building Disaster Prevention Association, "ollection of seismic reinforcement construction method" 2008.

伊藤宰、辻聖晃、吉富信太、竹脇出,「アウトフレーム連結制振耐震補強のための連結ダンパーの合理的決定法,日本建築学会構造系論文集,第 74 巻,第 636 號,273-218,2009。

辻聖晃、中川大輔、吉富信太、竹脇出,「アウトフレーム型連結制振構法におけるアウトフレーム及び連結ダンパーの応答低減比マップを用いた設計法」,日本建築学会構造系論文集,第 75 巻,第 648 號,337-346,2010。

Kiyoji Takeda, Kyoya Tanaka, Toshiaki Someya, Asao Sakuda, and Yoshiteru Ohno, "Seismic retrofit of reinforced concrete buildings in Japan using external precast, prestressed concrete frame", PCI Journal, pp.41-61, 2013.

Lin, S.-S., Lai, Y.C., Lai, T., Chung, L.-L., Huang, G.-L., Tseng, C.-C. (2009), "seismic Retrofit by External Reinforced Concrete Frames – Using School Building of HOU-JIA Junior High School as Example" Journal of Institute of Structural Engineering, Vol. 31. No4. pp.19-37, 2009.

Lai, Y.-C., Lin, S.-H., Chung, L.-L., Tseng, C.-C., Huang, G.-L. and Lai, T. (2018). "Experimental study on retrofit with external reinforced concrete frame and its application on seismic retrofit of hospital", Journal of Chinese Institute of Civil and Hydraulic Engineering, Vol. 30. No. 1. pp. 61-72, 2018.

Chiou, T.-C., Chung, L.-L., Tu, Y.-C., Lai, Y.-C., Tseng, C.-C. Weng, P.-W., Chuang, M.-C., Yeh, Y.-K., Li, C.-H., Lin, M.-L, Wang, J.-X., Shen, W.-C., Hsiao, F.-P., Xue, Q., Hwang, S.-J. (2020), "Technical Hand Book for Taiwan Earthquake Assessment and Strengthening of Structures by Pushover Analysis (TEASPA4.0)", National Center for Research on Earthquake Engineering, report number：NCREE-20-005, Taipei, 2020.

Flexural-Shear Behavior of Existing Reinforced Concrete Columns under High Axial Load and Varying Axial Load

Wen-Cheng Shen[1] Pu-Wen Weng[2] Yi-An Li[3] and Ling-Chun Chen[4]

沈文成[1]　翁樸文[2]　李翼安[3]　陳翎鈞[4]

Abstract

Many old existing mid- to high-rise reinforced concrete buildings do not meet the requirements of current seismic codes and are vulnerable to damage in earthquakes. The damaged column is found to be controlled by flexural-shear failure. When the ground columns of mid- to high-rise buildings are subjected to an earthquake force, the axial load varies between tension and high compression in the edge columns owing to the overturning moment effect. The main goal of this research is to study the seismic shear strength and deformation capacity of flexural-shear critical columns under high axial load and varying axial load.

This research conducts an experimental study on six full-scale column specimens with cross-sectional dimensions of 500 mm × 500 mm subjected to quasi-static cyclic loading under constant high axial load and varying axial load. The design parameters were the spacing of transverse reinforcement and the magnitude and type of applied axial load. Test results indicate that the higher the applied axial load, the faster the degradation of strength and stiffness.

Keywords: flexural-shear, high axial load, full-scale, reinforced concrete column

Introduction

Reinforced concrete (RC) structures are the major building system in Taiwan. Due to high population density in the metropolitan area, construction of high-rise residential buildings is a necessity. The lower-story columns of a high-rise building cause extremely high axial load. Earthquake reconnaissance reports show that RC columns of old existing buildings are vulnerable to earthquakes because the transverse reinforcement is widely spaced [1]. RC columns with insufficient transverse reinforcement could be dominated by flexural-shear failure [2]. The strength and stiffness of the structure severely degrade due to shear failure after the flexural strength.

Although many experimental studies have been conducted to investigate the seismic behavior of RC columns, they focused on low-rise RC buildings. Moreover, in existing experimental studies, the structures were mostly subjected to a lower axial load [3]. Test results under high axial load are limited, leading to insufficient data. The present study elucidates the flexural-shear behavior of a column under high axial load and varying axial load. Moreover, the test results can be used for developing the backbone curve and hysteretic loop models of RC columns.

Specimen Design

All the column specimens were designed with 500 mm × 500 mm square cross sections. The clear height of specimens was 2000 mm, with each specimen having a constant height-to-depth ratio of 4.0. Figure 1 shows the elevation and rebar layout of each column.

The nomenclature of the specimens is as follows: letters "R" and "V" denote the specimens under constant and varying axial loads, respectively; letters "D" and "N" denote the specimens with 100 mm and 200 mm spacing, respectively; numbers "4" and "6" denote the specimens with applied constant axial load

---

ratios ($P/A_gf'_c$) of 0.4 and 0.6, respectively.
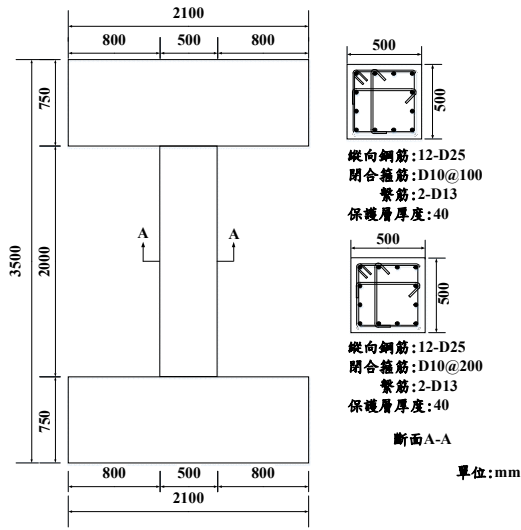
Figure 1. Elevation view and rebar layout

The longitudinal reinforcement consisted of 12-D25 with a measured yield strength of 468 MPa. The corresponding longitudinal reinforcement ratio was 2.43%. The D10 and D13 rebars were used for stirrups with 135-degree hooks and crossties with 90-135 degree hooks, respectively. The measured yield strengths of D10 and D13 transverse reinforcement were 456 and 468 MPa, respectively. The spacings of transverse reinforcement were 100 and 200 mm, respectively. Hence, the corresponding transverse reinforcement ratios were 0.54% and 0.27%, respectively. The measured compressive strengths of concrete ranged from 22.0 to 25.2 MPa on the day of tests. Specimens RD4 and RN4 were subjected to an axial load ratio of 0.4, while specimens RD6 and RN6 were subjected to an axial load ratio of 0.6. As for the rest of specimens, varying axial load ratios were applied. The design parameters and material properties of specimens are listed in Tables 1 and 2.

Table 1. Design Parameters

Specimen	Longitudinal rebar	Transverse rebar	$\frac{P}{A_gf'_c}$
RD4		Stirrup: D10 Crosstie: D13 $\rho_t = 0.54\%$	0.40
RD6			0.60
VD	12-D25 $\rho_\ell = 2.43\%$		Varying
RN4		Stirrup: D10 Crosstie: D13 $\rho_t = 0.27\%$	0.40
RN4			0.60
VN			Varying

Table 2. Material Properties

Specimen	$f_{y\ell}$ (MPa)	f_{yt} (MPa)	f'_c (MPa)
RD4			24.8
RD6			25.2
VD	468 (D25)	456 (D10) 468 (D13)	24.6
RN4			22.0
RN6			24.4
VN			24.9

Not only constant axial load but also varying axial load was chosen to investigate the flexural-shear behavior of column specimens. Two actuators were added to supply the vertical load to simulate the axial load of the edge column of mid- to high-rise RC buildings under earthquakes. The concept of varying axial load was adopted from Hassan [4]; the test results are compared with those of specimens subjected to constant axial load.

Test Setup

Tests were conducted using the Multi-Axial Testing System (MATS) at the National Center for Research on Earthquake Engineering. The specimens were subjected to constant and varying axial loading in conjunction with double-curvature cyclic loading. The lateral cyclic loading was based on the ACI test guideline [5]. The initial drift ratio was 0.25% in the linear elastic response range. The lateral drift ratio was increased by 1.25 to 1.5 times of the previous one. The load cycles were repeated three times at each drift ratio. The loading protocol is shown in Fig. 2.
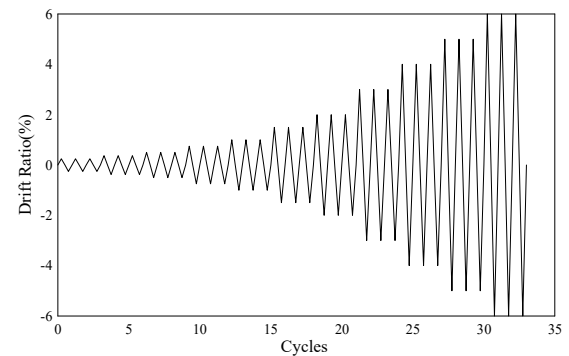
Figure 2. Loading protocol

Test Result

Figure 3 shows the crack pattern of specimens at peak load. When specimens were subjected to a larger drift level, some inclined cracks developed and became enlarged when they propagated closer to the top and bottom of specimens. The peak strengths of four specimens under constant axial load were reached

at 1.00% drift ratio, whereas the peak strengths of two specimens under varying axial load were reached at 0.75% and 1.00% drift ratios. Severe spalling of concrete was observed at the final stage of loading.

| RN4 | RN6 | VN | RD4 | RD6 | VD |
| @-1.00% | @1.00% | @0.75% | @-1.00% | @-1.00% | @1.50% |
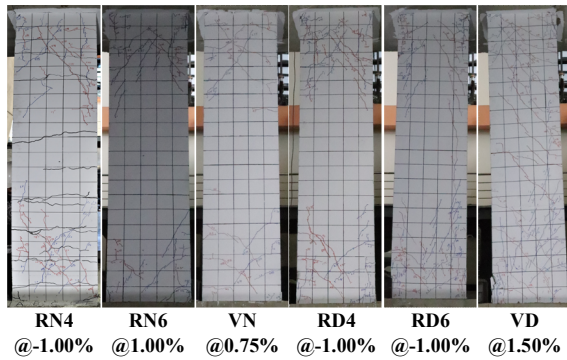
Figure 3. Crack pattern at peak load

Hysteretic Response

Figure 4 shows the relationship between lateral force and drift ratio for each specimen, in which the P-Δ effect has been removed. The drift ratio was calculated by dividing the lateral displacement by the clear height. The envelope curve was obtained by connecting the peak values of hysteresis loops of the first cycle, as shown in Fig. 4. The comparison of envelope curves of each specimen is shown in Fig. 5.

After the peak strength, most specimens showed a significant loss of strength and stiffness during cyclic loading. Specimen RD6 experienced the maximum strength in the positive and negative directions among the four specimens under constant high axial load. Meanwhile, no significant differences were observed on the maximum strength in the positive and negative directions of the two specimens under varying axial load.
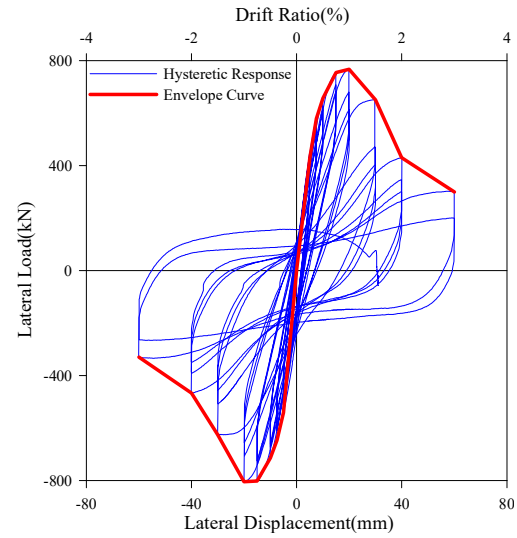
(b) Specimen RD6
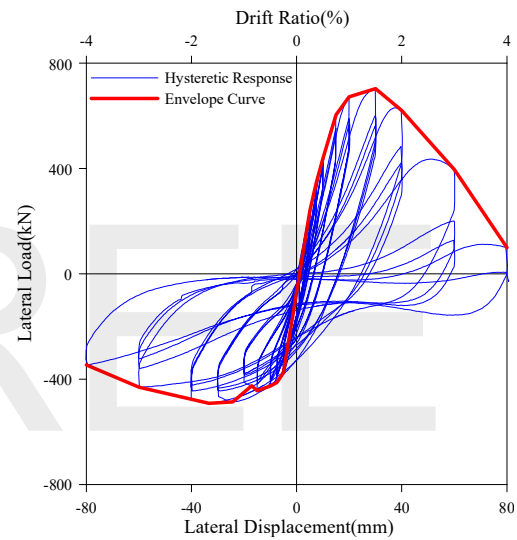
(c) Specimen VD
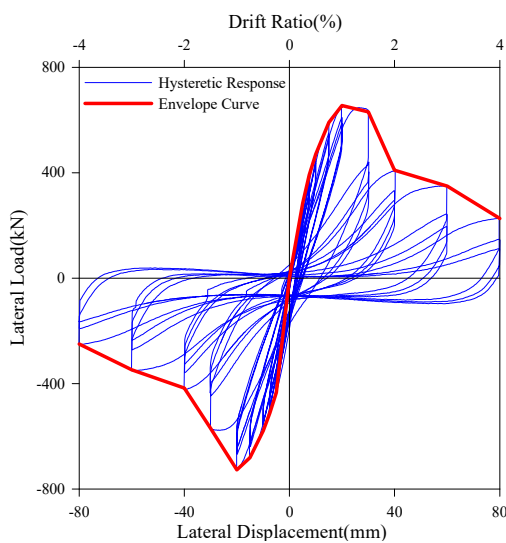
(a) Specimen RD4
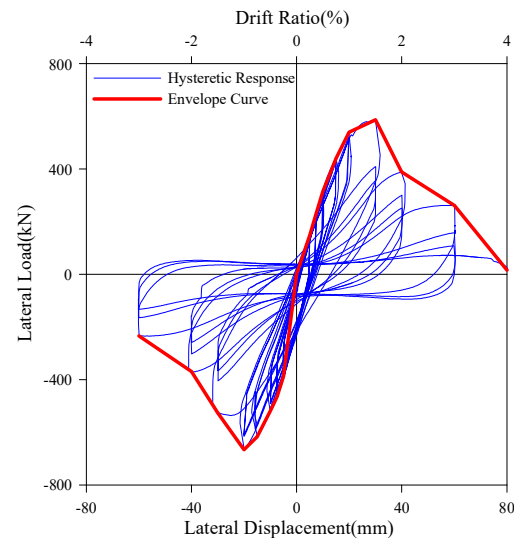
(d) Specimen RN4
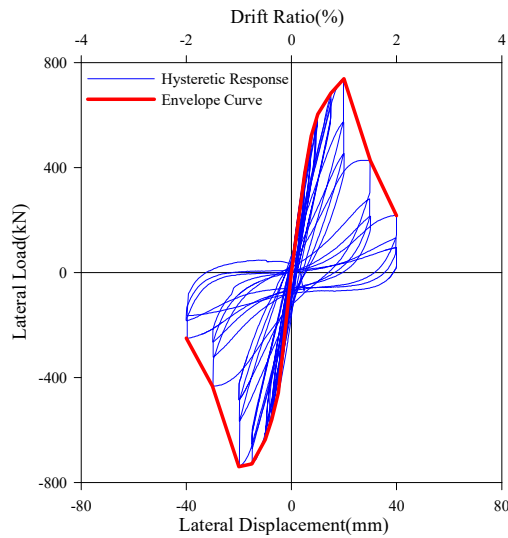
(e) Specimen RN6
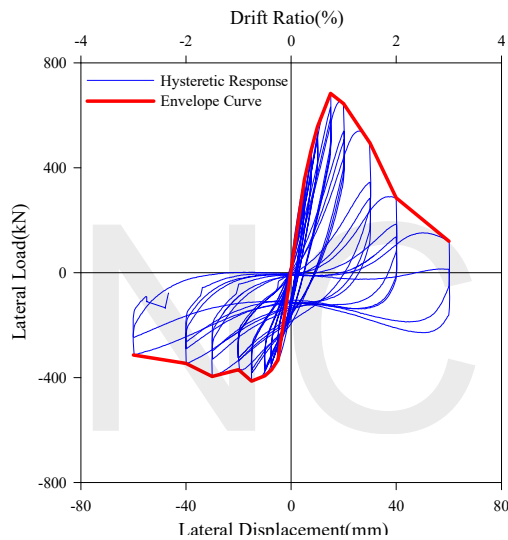
(f) Specimen VN

Figure 4. Hysteretic response and envelope curve
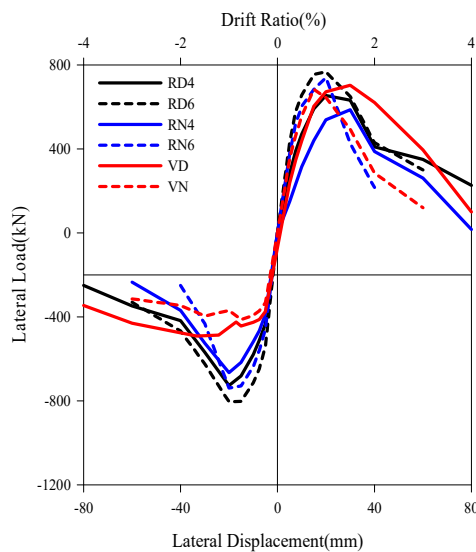
Figure 5. Comparison of envelope curves

Conclusions

In this study, cyclic tests were conducted on critical column specimens. The test parameters were the amount of transverse reinforcement and the magnitude and type of applied axial load. Based on experimental observations, the following conclusions are drawn:

(1) The hysteretic response of specimens RD4 and RN4 were similar; however, the ductility of specimen RD4 was better than that of specimen RN4.

(2) For specimens RD6 and RN6, the strength and stiffness of specimen RN6 dropped dramatically after the peak strength.

(3) The maximum strength of specimen RN6 was greater than that of specimen RN4; however, the deformation capacity of specimen RN6 was lower than that of RN4.

(4) For specimens under varying axial load, the deformation behavior of specimen VD was better than that of specimen VN.

(5) When specimen with lower amount of transverse reinforcement was subjected to high axial load, the strength degraded rapidly and the seismic performance was poor.

References

Wang R. Z. et al., (2018), "Reconnaissance Report of Seismic Damages Caused by the 6 February 2018 Earthquake, Hualien, Taiwan, NCREE Technical Report, NCREE-2018-005, Taipei.

Elwood, K. J., and Moehle, J. P., (2005), "Drift Capacity of Reinforced Concrete Column with Light Transverse Reinforcement," Earthquake Spectra, Vol.21, No.1, pp71-89.

Hsiao F. P. et al., (2013), "Technology Handbook for Seismic Evaluation and Retrofit of School Buildings - Third Edition," NCREE Technical Report, NCREE-18-023, Taipei.

Hassan, W. M., (2011), "Analytical and Experimental Investigation of Seismic Vulnerability of Beam-Column Joints without Transverse Reinforcement in Concrete Buildings," PhD Dissertation, University of California, Berkeley.

ACI (American Concrete Institute), (2013), "Guide for Testing Reinforced Concrete Structural Elements under Slowly Applied Simulated Seismic Loads (ACI 374.2R-13)," ACI Committee 374, Farmington Hills, MI, 18 pp.

Taiwan Earthquake Assessment of Reinforced Concrete Structures Using Dynamic Analysis

Pu-Wen Weng[1], Wen-Cheng Shen[2], Chia-Chen Lin[3], Fu-Pei Hsiao[4], Ren-Jie Tsai[5],
Yu-Cheng Hsu[5], Te-Kuang Chow[3], Hsun-Jen Liu[2], Yuan-Tao Weng[1], and Wen-Yu Chien[4]

翁樸文 [1]、沈文成 [2]、林佳蓁 [3]、蕭輔沛 [4]、蔡仁傑 [5]、
徐侑呈 [5]、周德光 [3]、劉勛仁 [2]、翁元滔 [1]、簡文郁 [4]

Abstract

The Meinong earthquake struck southern Taiwan in the early morning of February 6, 2016. Two years later, a major earthquake also occurred in the Hualien area at midnight on February 6, 2018. Several mid-to high-rise buildings collapsed after each event. Some of those collapsed buildings caused severe casualties. The damage modes of such buildings can be summarized as follows: the presence of a soft and weak first story, a lack of redundancy, and a lack of lateral reinforcement. Results of the investigation of such buildings are used in conjunction with the earthquake duration screening database recently recommended by the National Center for Research on Earthquake Engineering to propose a set of easy-to-implement non-linear dynamic analysis methods, designated as the "Non-linear dynamic analysis methods for seismic evaluation of reinforced concrete structures in Taiwan" (Taiwan Earthquake Assessment for Structures by Dynamic Analysis), as a standard reference for domestic and foreign industry, academia, and research circles. It is hoped that it can effectively remove doubts concerning the poor earthquake resistance of existing buildings and serve as a basis for subsequent improvement.

Keywords: non-linear dynamic analysis, mid-to high-rise buildings, damage investigation, seismic assessment methods

Introduction

Due to a large number of residents in mid-to high-rise buildings, earthquake disasters that affect these buildings, such as building collapse and other damage, should be a subject of serious concern. An appropriate seismic evaluation method for such buildings is urgently needed as a basis for screening in engineering practice.

Current evaluation methods are mostly carried out using nonlinear pushover analysis, which is accurate for low-rise buildings, but its defect is that the methods cannot be used to predict the effect of the higher vibration modes of mid-to high-rise buildings. It is also a deterministic method, which fails to consider the uncertain factors regarding the seismic load, the analysis method, and construction errors. In light of this, the National Center for Research on Earthquake Engineering (NCREE) recommended a reasonable probabilistic collapse assessment method for mid-to high-rise buildings (Hsieh et al., 2018). The assessment process refers to the collapse fragility assessment (CFA) of FEMA P-58 and incremental dynamic analysis (IDA) is used to consider the nonlinear dynamic responses of mid-to high-rise buildings during strong earthquakes and account for the uncertainty of the seismic load. This method estimates the structural response using nonlinear dynamic analysis and employs a probabilistic seismic assessment framework to take into account the many uncertainties involved in the analysis. The collapse criteria refer to the American Society of Civil Engineers (ASCE) 41-13 and the Tall Building Initiative (TBI) recommended standards for avoiding collapse and damage, to formulate clear judgment criteria. This method is used to assess the seismic

capacity of buildings and can avoid the analysis limitations of nonlinear pushover analysis for buildings with significant torsional or high modal effects. However, a large number of analysis operations must be performed and so it is more suitable for use in important facilities with high seismic performance requirements.

For the needs of more general building types, this paper proposes an easy-to-implement nonlinear dynamic analysis method with the input motion selection database recently proposed by the National Earthquake Center, named the "Taiwan Earthquake Assessment for RC Structures by Dynamic Analysis" (TEASDA). It is to be used as a common reference for domestic and foreign industry and university research centers, and it is hoped that it can effectively remove any doubts concerning the insufficient seismic capacity of existing buildings and serve as a basis for subsequent improvement of building seismic capacity.

Ground Motion Selection

In the current draft revision of the seismic code for buildings, at least three horizontal seismic records consistent with the design response spectrum are required for the ground motion input selection of the dynamic analysis method. The ground motion should be able to accurately reflect the design base earthquake of the site (or the maximum considered earthquake). If more than seven horizontal seismic records consistent with the design response spectrum are used, the structure may be designed using the average of the analysis results. For any horizontal seismic record, its response spectrum with a 5% damping ratio should be calculated. At the same time, the seismic records should be adjusted so that the spectral acceleration value at any point within the period range 0.2-1.5 T_1 is not lower than 90% of the design spectral acceleration value, and the average value within this period range is not lower than the average of the design spectral acceleration value, where T_1 is the fundamental natural period of the building in the direction under consideration.

To enable engineers to conduct design checks and seismic assessments following the relevant requirements of the seismic code when conducting dynamic analyses, the NCREE built a database of "Recorded Ground Motion Selection for Generic Sites" (Liu et al., 2020). At present, the Platform "Input Motion Selection for Taiwan" (Figure 1) has been preliminarily constructed for general earthquake areas in Taiwan and the Taipei Basin (excluding the near-fault area). This platform can assist in the selection of earthquake records for design verification.

Figure 1. The platform of input motion selection for Taiwan (http://seaport.ncree.org/inmost/)

After the ground motion selection is completed, the intensity must be adjusted according to the provisions of the current seismic code on dynamic analysis. According to the research of Malhotra (2003), it is suggested that the limit of the adjustment ratio of earthquake intensity should not exceed 4.0 and 6.0 in an earthquake regression period of 475 years and 2500 years, respectively. The Canadian National Building Code (NBC) Interpretation J, Appendix 4.2 recommends that the earthquake intensity adjustment ratio should be between 0.5 and 4.0. If the selected earthquake record cannot meet this criterion, it is suggested that the natural earthquake records be used to make artificial earthquakes. The number of artificial earthquakes should not exceed one-third of the ground motions used for design verification. In addition, if a sufficient number of earthquake records cannot be found in the database, other seismic record databases are available (such as the ground motion database of the Pacific Earthquake Engineering Research Center (PEER) in the United States, https://ngawest2.berkeley.edu/site) from which suitable ground motions can be selected.

Member Behavior and Simulation

Engineers often use structural analysis packaged software such as ETABS and SAP2000 to perform pushover analysis or nonlinear dynamic analysis of reinforced concrete (RC) structures. Most of these analysis software products are mainly composed of members and nodes to form a model of the structure and are combined with nonlinear hinge settings to simulate the nonlinear behavior of structural members, such as its columns, beams, and RC walls. Therefore, it is necessary to understand the nonlinear behavior of such structural members, before assigning them suitable nonlinear hinge properties and positions to simulate their behavior.

3.1 RC columns

When an RC column is subjected to both axial and lateral loads, it has three failure modes: shear failure, flexure-shear failure, and flexural failure. For shear failure column members, the oblique shear cracks are usually distributed at both ends of the column. Li et al. (2019) found that the deformation

capacity of the shear-dominated column was not as conservative as expected and suggested a model presenting the lateral load-displacement curve. When a column has sufficient stirrups, its column shear strength will be higher than its flexural strength, and its failure mode will tend toward flexural behavior. Assuming that the longitudinal reinforcement does not undergo strain hardening, the lateral load strength remains constant. Until the column has a flexural failure mode such as a longitudinal reinforcement fracture, buckling, or the crushing of confined concrete, its lateral load strength will decrease, but its axial load capacity will not be lost immediately.

Since the position of the inflection point of the column will change during the nonlinear reaction of the frame, the failure mode of the column cannot be specified before the analysis. Therefore, when setting the nonlinear hinges of the column member, it is necessary to set the moment nonlinear hinges at both ends of the column. The moment nonlinear hinge is used to simulate the moment-rotation relationship of the column. The shear nonlinear hinge is set in the middle of the column to simulate the shear-displacement relationship of the column, as shown in Figure 2.
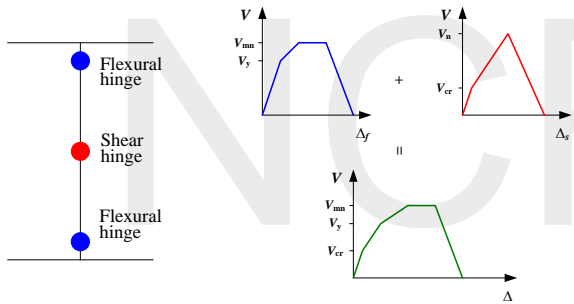
Figure 2. The simulation of a column (nonlinear hinge)

3.2 RC beams

In the case of a cracked section, the flexural stiffness of the beam is generally expressed as $0.35E_c I_g$, where E_c is the modulus of elasticity of the concrete and I_g is the moment of inertia of the total section. Considering that the beams of an existing reinforced concrete structure are often connected with the floor slab to form T-beams, the seismic capacity of the beams is improved. Therefore, the behavior and the section stiffness of the T-beams should also be considered in the beam simulation. The nonlinear behavior of RC beams can be based on the nonlinear hinge that comes from the load-displacement curve of RC members suggested by ASCE/SEI 41-13.

3.3 RC walls

Weng et al. (2017) suggested that a trilinear analysis model should be used to simulate the relationship between the shear force and lateral displacement of RC walls with a height-to-length ratio less than two, as shown in Figure 3. This analysis model includes the cracking point, strength point, and collapse point. Before the concrete cracks, the RC wall remains elastic and has high lateral stiffness. After the concrete cracks, its lateral stiffness begins to reduce, and this first turning point is the cracking point. When the concrete cracks, the crack pattern in the RC wall develops and accumulates rapidly, accompanied by a large amount of shear deformation and finally concrete crushing damage occurs. This is the second turning point, namely the strength point. After shear failure occurs, its stiffness and shear strength decrease rapidly, and eventually the RC wall loses its ability to carry the lateral load, which is the collapse point. The analytical model simulates this behavior by a negative slope.
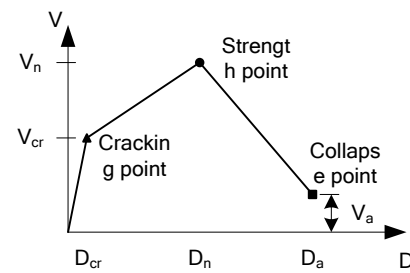
Figure 3. The lateral load-displacement curve of a wall

Hysteresis Model of the Structural Members

The nonlinear dynamic analysis contains repeated loading. For the nonlinear plastic hinge of the structural members, its hysteresis behavior must be clearly defined, including the characteristics of unloading and reloading. An appropriate hysteresis model must be selected to describe the energy dissipation behavior of different structural members. This study proposes to use the Pivot hysteresis model for the RC column, in which the force-displacement curve points to specific reference points (P1~P4, PP2, and PP4) during unloading and reloading. These reference points are called "pivot points" and defining these pivot points by parameters α and β can describe the hysteresis behavior of nonlinear plastic hinges (Figure 4). Since the hysteresis behavior of the RC column has different properties due to its failure mode, Ling (2019) suggested that the two parameters can be calculated according to the following equations:

$$\alpha = a \times \left(\frac{N}{A_g f_c'} \right)^b \times \left(\frac{\rho_\ell f_{y\ell}}{f_c'} \right)^c \times \left(\frac{\rho_t f_{yt}}{f_c'} \right)^d + e \leq 10 \quad \text{...(1)}$$

$$\beta = a \times \left(\frac{N}{A_g f_c'} \right)^b \times \left(\frac{\rho_\ell f_{y\ell}}{f_c'} \right)^c \times \left(\frac{\rho_t f_{yt}}{f_c'} \right)^d + e \leq 1 \quad \text{…(2)}$$

where N is the axial load, A_g is the gross area of

concrete section, f_c' is the specified compressive strength of concrete, ρ_ℓ and ρ_t is the ratio of area of longitudinal steel and transverse steel, $f_{y\ell}$ and f_{yt} is the specified yield strength of steel.

The five parameters a, b, c, d, and e were adopted from the work of Ling (2019) and were substituted into the above equations to calculate α and β. In addition, it is recommended to use the Takeda hysteresis model for the flexural-plastic hinges and shear-plastic hinges of RC beams and RC shear walls.
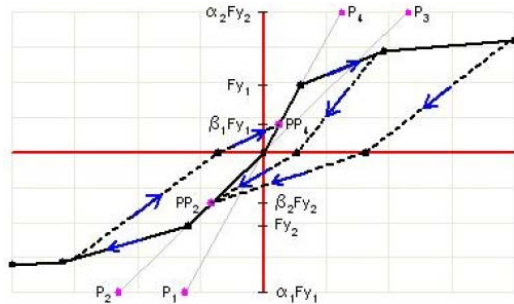
Figure 4. Pivot hysteresis model in ETABS (CSI, 2018)

Seismic Performance

Regarding the implementation of the earthquake resistance assessment and reinforcement plan of the Executive Yuan, the regulations on earthquake seismic evaluation, and retrofitting standards, a building can also be evaluated using its performance target point as the verification for earthquake resistance to ensure that the building is within the 475 years return period earthquake, which is the performance level to be achieved under design seismic forces. In line with this benchmark, the proposed performance targets are divided into overall and member component criteria, which are described below.

Overall criteria: The technology handbook for seismic evaluation and the retrofit of school buildings should be referred to in order to define the seismic performance target of the structure. For an importance factor I = 1.25 structure, it is recommended that the maximum inter-story drift angle of any floor should not exceed 2%. For an importance factor I = 1.5 structure, the building should be required to have a higher performance level, so it is stipulated that the maximum inter-story drift angle of any floor should not be greater than 1.0%. For a structure of importance factor I = 1.0, the maximum inter-story drift angle of any floor should not be greater than 2.5%.

Member component criteria: To avoid serious damage to the vertical structural members, which may lead to the collapse of the entire structure, the performance criteria adopted for the members should be such that the vertical load-carrying members should not suffer axial damage or completely lose lateral strength.

Conclusions

Mid-to high-rise buildings have a high population density. When disaster strikes such a building, the effect on human life and damage to property is much greater compared with low-rise buildings. The 0206 Hualien earthquake in 2018 was a moderate earthquake with a magnitude of 6.0 on the Richter scale, but it also caused the collapse of four mid-to high-rise buildings. It is thus evident that the earthquake resistance problems of existing mid-to high-rise buildings have never been effectively solved. In order to effectively solve the above-mentioned problems, this paper proposes an easy-to-implement nonlinear dynamic analysis method for the reference of domestic and foreign industry, academia, and researchers, in the hope of more effectively clarifying the seismic capacity of existing buildings and thereby removing doubt. This could form the basis for subsequent improvement of building earthquake resistance.

References

CSI, (2018) "ETABS： Extended 3D analysis of building systems, nonlinear version 2018," Computer and Structures, Inc., Berkeley, California.

Hsieh W. H., Lu L. Y., Hsiao, F. P., Tang, Y. S., and Huang, Y. N., (2018) "Probabilistic assessment of seismic performance and collapse risk for mid-rise buildings," Structural engineering, Chinese Society of Structural Engineering, Vol. 33, No. 2, pp. 89-120. (in Chinese)

Li, Y. A., Weng, P. W., and Hwang, S. J., (2019) "Seismic performance of RC intermediate short columns failed in shear," ACI structural journal, Vol. 116, No. 3, May. 2019, pp. 195-206.

Liu, H. J., Chien, W. Y. and Chang, Y. W., (2020) "A study on recorded ground motion selection for generic sites in Taiwan," The fifteenth national conference on structural engineering/ The fifth national conference on earthquake engineering, paper No. 143, 2-4 September, Tainan, Taiwan. (in Chinese)

Ling, Y. C., (2019) "A study on hysteresis modeling of reinforced concrete columns," master thesis, National Taiwan University, Taipei, pp. 118. (in Chinese)

Malhotra, P. K., (2003) "Strong-motion records for site-specific analysis," Earthquake spectra, Vol. 19, No. 3, pp. 557–578.

Weng, P. W., Li Y. A., Tu Y. S., and Hwang S. J., (2017) "Prediction of the Lateral Load-Displacement Curves for Reinforced Concrete Squat Walls Failing in Shear," Journal of Structural Engineering, ASCE, Vol. 143, No. 10.

Experimental Study on Seismic Performance of Innovative Reinforced-Concrete Coupling Beams

Min-Lang Lin,[1] Chao-Hsun Huang,[2] and Min-Chin Lin[3]

林敏郎 [1]、黃昭勳 [2]、林敏沁 [3]

Abstract

Short-span reinforced-concrete (RC) coupling beams are prone to shear failure and slip failure of the main steel bars. Therefore, this study proposes two schemes to improve the seismic performance of traditional coupling beams with straight-through main reinforcement. In the first scheme, a sheet steel plate is placed inside the traditional coupling beam to increase the shear strength. In the second scheme, the traditional coupling beam is cladded with additional reinforcement and concrete, but leaving a gap at the ends of the coupling beam such that the end portions have the same dimensions as the original dimensions. The cladded RC can only improve the shear strength of the original beam section and the bond strength of the main steel bar but not the moment strength of the original beam section. The test results show that the two schemes exhibit good ductility performance, and neither shear failure nor main steel bar splitting failure occurs. Plastic hinges occur for both specimens at the ends of the beams; this suggests the ideal flexural failure mode, thus meeting the expected behavior.

Keywords: coupling beam, shear plate, shear capacity, shear demand, bond strength, bond demand, double-layer stirrup.

Introduction

A coupling beam is an important member of the ductile reinforced-concrete (RC) shear wall system. In the current Taiwan Civil 401 [1] and ACI 318 [2] design codes, coupling beams with a span-to-depth ratio of less than 2 and shear requirements must be configured with diagonal reinforcement. However, it is very difficult to apply diagonal reinforcement in an actual construction site.

According to previous research results, the traditional coupling beam with straight-through reinforcement has a bending moment capacity similar to that of the diagonally reinforced beam but lower ductility performance. Embedding steel plates in a traditional straight reinforced coupling beam can increase the shear strength of the beam and delay its degradation. This may in turn improve the ductility of the beam. Therefore, traditional straight reinforced coupling beams composited with steel plates may exhibit good seismic performance and can address the problem of difficult construction of diagonal steel bars.

In this study, cyclic loading tests were conducted on high-strength RC coupling beams embedded with steel plates for shear walls to evaluate the behavioral response of the coupling beams. Furthermore, the proposed steel plate and beam composite and steel plate end anchor design theory were verified.

It was observed that the embedded steel plate increases the beam's shear capacity. However, it also increases the bending moment capacity, which in turn increases the beam shear requirements. To reduce the increase in the bending moment capacity of the beam caused by the embedded steel plate, the embedded steel plate needs to be partially cut off in the plastic hinge zone of the beam.

Specimen Design

An experiment to simulate the behavior of a coupling beam under the action of seismic force was conducted in the reaction wall and strong floor test area at the National Center for Research on Earthquake Engineering. The simulation causes double curvature deformation of the testing frame. To accommodate the limitations of the test structure, a beam section of 30

[1] Research Fellow, National Center for Research on Earthquake Engineering
[2] Associate Professor, National Taipei University of Technology
[3] Master, National Taipei University of Technology

cm × 50 cm with a length of 100 cm was selected. In this study, Ci-Hong Chen[3] CB20SW1 was adopted as the standard specimen, and two coupling beam specimens with a span–depth ratio of 2 were designed and constructed.

CB2-1 and CB2-2 are test specimens embedded in comb-shaped cutting steel plates, with Ci-Hong Chen[3] CB20SW3 as the model, having a beam section of 30 cm × 50 cm, beam lengths 100 cm and 150 cm, and span–depth ratios of 2 and 3, respectively. The two test body reinforcement configurations are as follows: twelve straight-through main ribs #6-SD420, transverse tie reinforcements #4-SD420, and stirrups #3-SD420, with a 10 cm spacing; six boundary column main ribs #7-SD420, and stirrups #3-SD420, with a 6 cm spacing. Concrete strength is 42 MPa. This test mainly aimed to reduce the number of main reinforcements and the spacing of the stirrups as well as increase the reinforcement as the main variables.

CB2-2 has an enlarged middle section of 45 cm × 65 cm and the standard section of 30 cm × 50 cm is retained at 5 cm in front of and behind the beam section in both ends.

The reinforcement configuration for CB2-2 is the same as that for the CB20SW1 specimen: six straight-through rebars #8-SD420, transverse reinforcements #4-SD420, and stirrups #3-SD420, with a 10 cm spacing. Then, a second layer of stirrups and tie ribs is inserted in the middle section to observe whether in the later stage of the experiment, the damage of shear force and grip wrap can be effectively avoided, and, as a result, the specimen's ductility performance can be improved.

Table 1. Specimen design parameters.
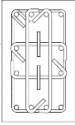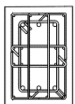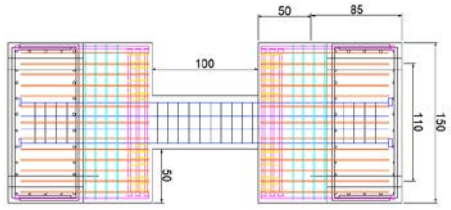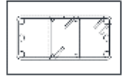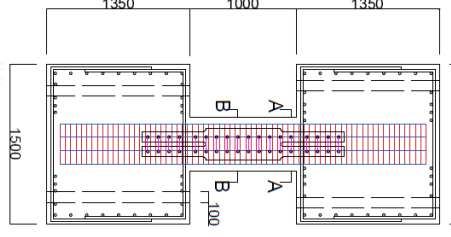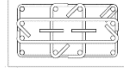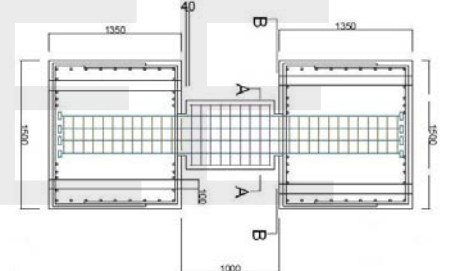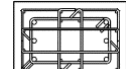
Specimen	Section	Steel plate ratio	Steel plate thickness	Steel plate anchor length
CB2-1		1.33%	t = 1.0 cm (cut 50%)	45 cm

Specimen	Section	original	Expanded section
CB20SW1		30 cm × 50 cm	-
CB2-2		30 cm × 50 cm	45 cm × 65 cm

Table 2. Specimen size chart (mm).

CB20SW1	
CB2-1	Section A-A Section B-B
CB2-2	Section B-B Section A-A

Test Setup and Cyclic Loading Tests

This test simulates the double curvature deformation of the specimen when it is subjected to a seismic force. An L-shaped steel frame and two vertical MTS actuators were used to ensure that the upper foundation did not rotate during the test. Two horizontal MTS actuators were used to apply a progressively increasing displacement to the test specimen. The test setup for the test is shown in Figure 1.

Figure 1. Test setup.

To simulate the repetitive characteristics of earthquakes, this test referred to the loading protocol of ACI 374.1-05. A total of two loops were performed for each displacement load. The lateral displacement increments were 0.25%, 0.375%, 0.5%, 0.75%, 1%, 1.5%, 2%, 3%, 4%, 5%, 6%, 8%, and 10%, respectively, as shown in Figure 2.
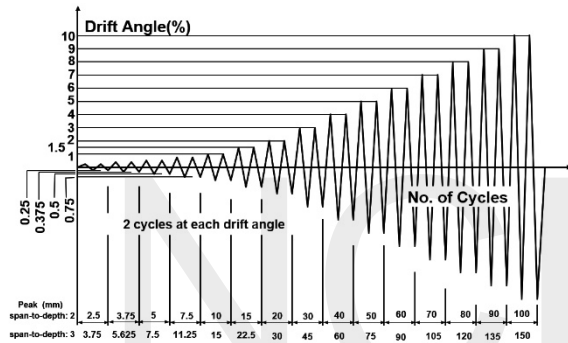
Figure 2. Test protocol.

Test Results

Figure 3 shows the load and displacement hysteresis cycles of each specimen. The extremum of the first cycle of each interlayer displacement is plotted as an envelope, and the ultimate interlayer displacement of each specimen is calculated, as shown in Figure 4. Table 3 lists the initial strength value of each specimen, and Figure 5 shows the failure of each specimen.

The ultimate interlayer displacement of the standard specimen CB20SW1 is only 2.22% (negative), which implies that the displacement toughness of the coupling beam with traditional reinforcement is poor and the energy dissipation ability is the worst.

For cutting steel plate specimens, the part with span–depth ratio 2 is compared with the Ci-Hong Chen[3] standard specimen CB20SW1 and cutting steel plate CB20SW3. Specimen SW3 has a maximum strength point of approximately 2% interlayer displacement and a maximum lateral force of 760.8 kN; CB2-1 has a maximum strength of 3%, which is similar to that of CB20SW3 (approximately 4%) and approximately 40% higher than the maximum lateral

force of the standard specimen. From the perspective of the ultimate interlayer displacement, the steel plate specimen CB2-1 was configured to be approximately 2.46 times higher than the standard specimen and approximately 1.73 times higher than CB20SW3 and the cumulative dissipation energy when 7% interlayer displacement is reached is 1.5 times that of the CB20SW3. After the standard specimen is configured with the steel plate, the cladded part must be considered so that with the increase in the lateral force, the strength of the specimen does not decay rapidly in the later stage, thereby fully taking advantage of the ability of the steel plate.

For the cladded concrete specimen, CB20SW1 was used as the prototype to cover the concrete in the middle section of the beam to increase the shear strength while the shear demand remains unchanged. The maximum lateral force of CB2-2 is approximately 1.5 times that of CB20SW1 at 861 kN; its displacement capacity is 5.81%, which is approximately 2.1 times that of the standard specimen; the cumulative dissipation energy of CB2-2 when 5% interlayer displacement is reached is approximately 2.25 times that of CB20SW1, and the maximum lateral force increase results in an increase in accumulated dissipative energy. The above analysis results indicate that the configuration of double-layer stirrup-cladded concrete in the middle section of the beam can effectively improve its interlayer displacement and increase the maximum lateral force as well as the accumulated energy.

The intensity decay of each specimen shows that, among all specimens, CB20SW1 has the maximum strength before the interlayer displacement of 3%, and there is no obvious attenuation; Furthermore, rapid decay in the standard specimen strength is observed after the interlayer displacement of 4%. Below, the configuration of the cutting steel plate specimen and the cladded concrete specimen is maintained at the maximum lateral force strength of more than 80%, with the decay in the later stage being relatively less. It can be seen that the initial strength of the CB2-1 steel plate with 50% of the cutting area of the comb-shaped steel plate is the initial stiffness of the CB2-2-coated concrete specimen, which is 81.1 kN/mm; it is approximately 3% lower than that of the standard specimen 0.6%. This indicates that irrespective of whether CB2 is placed in steel plates or cladded on concrete, the initial stiffness is relatively unaffected.

Table 3. Initial stiffness of specimens.

Specimen	Initial stiffness (kN/mm)			
	+	-	Average	Increase
CB20SW1	82.4	81.1	81.7	-
CB2-1	85.8	83.6	84.7	+3.0%
CB2-2	82.9	79.3	81.1	−0.6%

The deformation of CB20SW1 mainly occurs in the beam body, which is shear force deformation, while the boundary structure remains intact. The deformation of CB20SW3 occurs in the beam body, where it is curved deformation in the early stage and grip wrapping deformation in the later stage. Deformation of the CB2-1 and CB2-2 specimens occurs at the junction of the beam and foundation, while the core concrete remains intact. Plastic hinges are generated at the end of the beam, which is a flexural failure.
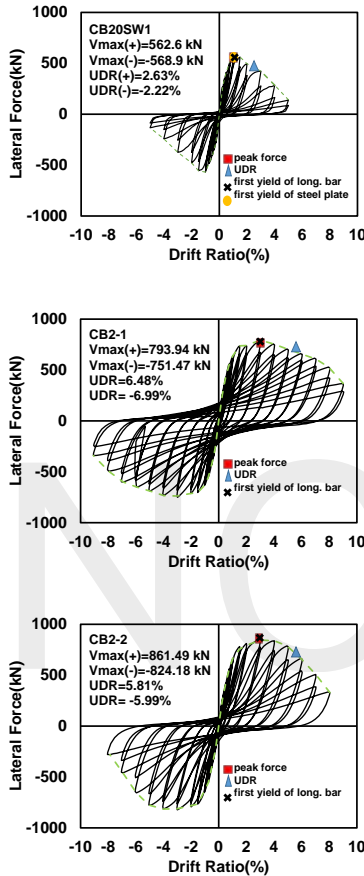
Figure 3. Hysteretic loops of specimens.
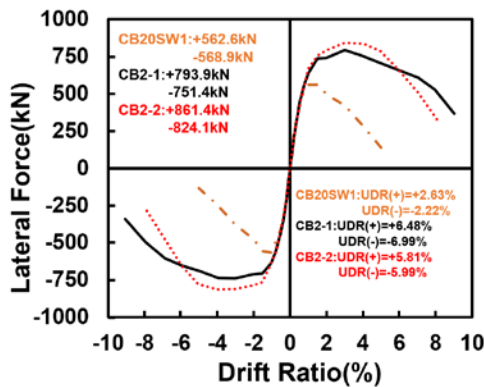
Figure 4. Envelope curves of specimens.

CB20SW1

CB2-1   CB2-2

Figure 5. Failure mode of specimens

Conclusions

In this study, two reinforced-concrete (RC) coupling beam specimens with a span–depth ratio of 2 were designed and tested. The test results revealed that plastic hinges were generated on the specimens mainly at the end of the beam, which is an ideal flexural failure. Good ductility performance was observed for the specimens used in the two design schemes. The comprehensive experimental results confirmed that the proposed RC coupling beam schemes have good seismic performance and can be used for engineering applications in practice.

References

1. Chinese Society of Civil and Hydraulic Engineering, "Concrete Design Codes and Explanations (Civil Engineering 401-100)", 2011.

2. ACI Committee 318, Building Code Requirements for Structural Concrete (ACI 318-19) and Commentary (ACI 318R-14), American Concrete Institute, Farmington Hills, 2019.

3. Min-Lang Lin, Shan-Chun Yang(2014) "Study on Seismic Behavior for High Strength Reinforced Concrete Coupling Beams of Shear Walls" NCREE, Taipei.

4. Min-Lang Lin, Chao-Hsun Huang, Sung-Yi Yang and Ci-Hong Chen(2019), "Study on Seismic Behavior for Steel-Plate-Embedded Reinforced-Concrete Coupling Beams of Shear Walls" NCREE, Taipei.

5. ACI Committee 374, Acceptance Criteria for Moment Frames Based on Structural Testing and Commentary, American Concrete Institute, Farmington Hills, 2013.

Research on the Application of a Fiber Section Model in ETABS

Te-Kuang Chow [1] and Yu-Fang Liu [2]

周德光 [1]、劉郁芳 [2]

Abstract

Using ETABS software, the nonlinear hinge is replaced with the fiber section to explore and simulate the backbone curve of TEASPA's RC component. The fiber section model has the function of mutual control of axial force and bending moment and free setting of hysteresis loop rules. Herein, the analysis results of the fiber section model and the nonlinear hinge model are compared using the three- and seven-story structures of the South Laboratory of the NCREE. The analysis results show that the nonlinear dynamic analysis of the overall structure based on the fiber section model is efficient and feasible. The results of nonlinear hinge and fiber section models are compared with experimental values. The results confirm that the fiber section model can reflect the axial force and bending moment of PM interaction. The convergence of the descend of the fiber section model is better than that of the nonlinear hinge model. Hence, the fiber section model can be used in nonlinear dynamic analysis and can compensate for the shortcomings of PM nonlinear hinges in ETABS that cannot freely set the hysteresis behavior. The analysis results of the three-story and seven-story structures with the fiber section model of the TEASPA method are consistent with the experimental values to a certain degree. The fiber section model is suitable for use in the seismic evaluation program for weak ground-floor buildings and mid- and high-rise buildings.

Keywords: detailed seismic evaluation, fiber section model, nonlinear hinge model, TEASPA

Introduction

At present, the detailed evaluation method of TEASPA earthquake resistance commonly used by engineers in Taiwan [1,2] adopts TEASPA's nonlinear model of a concrete structure and nonlinear lateral push analysis to obtain the capacity curve of the building structure, that is, to establish the relationship curve of the structural base shear force and the roof displacement. Then, based on the performance requirements of the building, the performance target point is set on the capacity curve, and the Capacity Spectrum Method [3] is used to determine the performance target earthquake with the roof displacement response of the performance target point. The performance target design earthquake is presented in terms of the seismic response spectrum and the maximum surface acceleration during the earthquake. A performance target earthquake greater than the 475

design earthquake implies that the building has sufficient earthquake resistance; otherwise, the building needs to strengthen its earthquake resistance. TEASPA2.0 [4] uses the M3 nonlinear hinge. After TEASPA3.1 version [5], this was replaced with the PM nonlinear hinge with mutual axial force and bending moment, which also lifted the limit on the number of floors and obtained certification from the Construction and Construction Administration. China still uses nonlinear static lateral thrust analysis for the seismic evaluation of mid-to-high-rise buildings. However, the higher the floor, the higher the error of the analysis. It is necessary to check the seismic performance of the building with nonlinear dynamic analysis; however, general software packages cannot freely set the hysteresis energy dissipation mode of PM nonlinear hinges. Therefore, this study explores replacing nonlinear hinges with fiber sections and simulating the spine curve of TEASPA's RC members,

which has mutual axial force and bending moments. Further, the function of the hysteresis energy dissipation mode is freely set.

The fiber section model was established for the three- and seven-story frame specimens of the southern laboratory of the National Center for Research on Earthquake Engineering (NCREE) [6], based on the single-column lateral thrust analysis as a benchmark. The cross-section model adopts the TEASPA seismic evaluation program developed by the NCREE. The resulting fiber cross-section model can fully conform to the TEASPA's nonlinear model. The three- and seven-story structures of the fiber section model are used to perform nonlinear dynamic analysis to obtain the overall structural response. The results of the experiments, nonlinear hinges, and fiber section models are compared, based on the fiber section obtained by TEASPA. For the model, the analysis results of the three- and seven-story structures show a certain degree of accuracy with the experimental values. This paper adopts the recommendations of the second edition of the Technical Manual of NCREE [4] to set the bending moment of the nonlinear hinges of the member, and the nonlinear dynamic analysis is performed with the package software ETABS [7].

Fiber Section Model

The fiber element model, also known as the section discrete element, is the most detailed analysis model in the nonlinear analysis of reinforced concrete frame structures and is close to the actual structural force performance. It has a wide range of applications; its principle is to divide the component into several sections longitudinally. The deformation of a certain section in the middle of each section represents the deformation of the section. The section is divided into several concrete and reinforcing steel fibers. The force state of the fiber element is only one-dimensional. Strain, through the integration of each sub-block or layer along the section to obtain the generalized stiffness relationship between the internal force of the section and the corresponding deformation, and then the stiffness matrix of the component element is obtained.

ETABS provides a beam–column fiber section model [7]. For the beam fiber section model, the fiber division in only one direction of the section is considered. Therefore, only unidirectional compression and bending interaction (PM) can be considered, and section torsion, shear force, and out-of-plane bending are assumed to be elastic. This model is used for simulating the unidirectional nonlinear bending of the beam section. As for the column fiber section model, the fiber division is considered in two directions; therefore, the bidirectional compression and bending interaction (PMM) can be considered, assuming the same cross-section torsion and shear to be elastic. This

model is mainly used for double-bending simulation of the column cross-section.

In ETABS, first, the nonlinear stress–strain curve (for material fiber) and the corresponding hysteresis model are defined, and then, the column or beam section reinforcement of the required fiber section is defined. Further, the ETABS program is used according to the set fracture of the surface, and its reinforcement can automatically generate fiber section hinges and automatically distribute fiber hinges on the section. This type of fiber hinge is Fiber P-M2-M3, which describes the relationship between force and the deformation of the member and the relationship between the stress and strain of the material. Therefore, the mutual relationship between the axial force and the bending moment and the construction of hysteresis energy dissipation behavior can be realized simultaneously. Theoretically, the fiber element model has higher accuracy and is especially suitable for situations where the axial force changes greatly, such as mid- and high-rise buildings; however, its disadvantage is the larger workload, which requires considerably more calculation time.

Single Column Test

The NCREE produced two reinforced concrete three-dimensional structure specimens with nonductile reinforcement for three- and seven-story buildings. The first floor is high, the first and second floors have only columns without any walls, and the floors above the third floor. Reinforced concrete walls are installed on the two outer sides of the short direction to highlight the characteristics of the weak ground floor and to explore the seismic performance of typical composite mid-to-high-rise buildings in Taiwan under the action of near-fault earthquakes. Before conducting three- and seven-story shaking table experiments, the mechanical properties of structural members need to be understood. Therefore, two-pillar member specimens are prepared with the same cross-sectional dimensions and steel bar configuration, and repeated load tests are conducted using the multi-axial testing system (MATS) of the Taipei Laboratory of the National Center for Seismology [6]. The two column components of the single-column specimens are A-column (30 cm × 30 cm) and B-column (30 cm × 75 cm). The nonlinear hinge model and the fiber cross-sectional model of the single-pillar specimens are compared as follows. Figure 1 shows the comparison of the lateral capacity curve of the fiber section model of A-pillar and the hysteresis loop of the single-column test, and Figure 2 shows the comparison of the lateral capacity curve of the fiber section model of the B-pillar and the hysteresis loop of the single-column test. The fiber model is extremely close to the test values irrespective of whether in the capacity curve or the hysteresis loop.
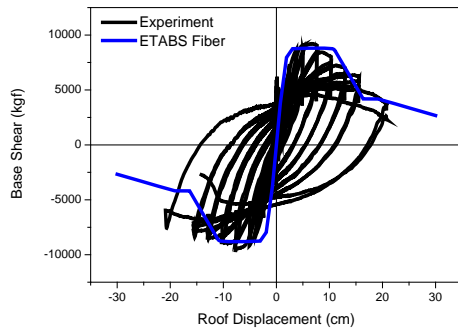
Figure 1. Comparison of A-column capacity curve of the single-column Specimen with the test value hysteresis curve
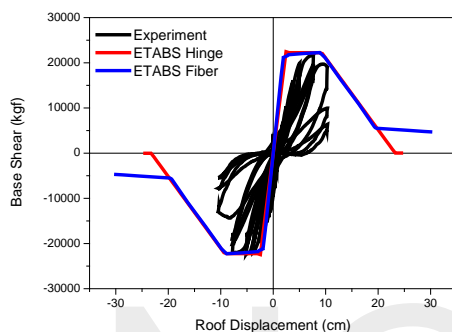
Figure 2. Comparison of B-column capacity curve of the single-column specimen with the test value hysteresis curve

Three-Story Structure Test

The NCREE produced a three-story nonductile reinforced concrete three-dimensional structure specimen [4]. The first floor is high, the first and second floors have only columns without any walls, and the third floor is in the short direction. Reinforced concrete walls are set on the outside to highlight the characteristics of the weak ground floor and to explore the seismic performance of typical high-rise buildings in Taiwan under the action of near-fault earthquakes. The southern laboratory of the National Earthquake Center officially conducted public seismic tests on the three-story test specimen [6]. Four groups of tests were conducted: the 0728 TCU052_350gal near-field earthquake and 0728 CHY047_420gal far-field earthquake on July 28, 2006, and 0809 TCU052_800gal and 0809 TCU052_1000gal on August 9, 2006. The peak ground acceleration (PGA) value mentioned after the earthquake record name is the set target value, and the actual shaking table output is slightly different. The seismic chronological analysis sequence of the frame specimen, except for the three-story frame specimen, was set. In addition to its own weight, the earthquake duration analysis was performed first with 0809TCU052_800gal and 0809TCU052_1000gal. Then, the post-earthquake test body was used as the prototype test body, and four sets of seismic tests were officially conducted

continuously [11]. For the nonlinear hinge model and fiber section model of the three-story structure specimen, the input seismic sequence described in the previous section is followed, and PERFPRM-3D is used to achieve the nonlinear hinge model and fiber section model of the three-story structure. Comparison of the roof displacement histories from the two models are compared for the small earthquake TCU052_350gal and the large earthquake TCU052_1000gal, as shown in Figure 3 and Figure 4, respectively.
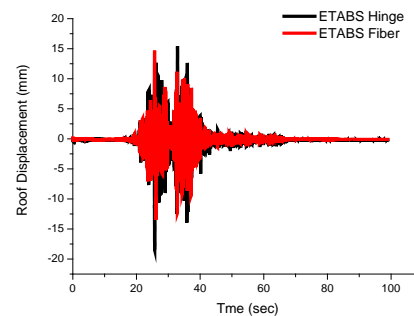
Figure 3. TCU052_350gal roof displacement comparison
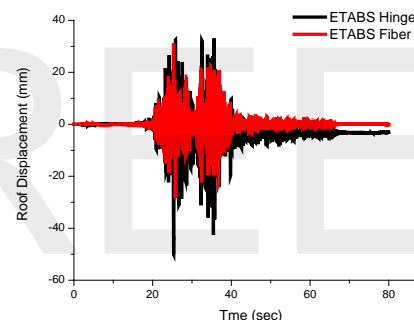
Figure 4. TCU052_1000gal roof displacement comparison

Seven-Story Structure Test

The NCREE assembled the seven-story structure test body and conducted follow-up related tests. For further details, refer to the blind test analysis test [12] of the reinforced concrete three-dimensional frame specimen of the seven-story building with nonductile reinforcement. The earthquake duration and maximum surface PGA [12] of the CHY015 and CHY063 stations set by the test were used. The sequence of earthquake duration analysis was set as follows: In addition to its own weight, the sequence of earthquake duration input is CHY015_70%, CHY063_50%, CHY063_100%, CHY063_150%, and CHY063_200%; CHY015 is a remote earthquake, while CHY063 is a near-field earthquake. PERFPRM-3D was used to perform the nonlinear dynamic analysis on the nonlinear hinge model and fiber section model of the seven-story structure. The roof displacement histories of the analysis values of the two models are compared for the small earthquake CHY015_70% and the large earthquake CHY063_150,

as shown in Figure 5 and Figure 6, respectively.
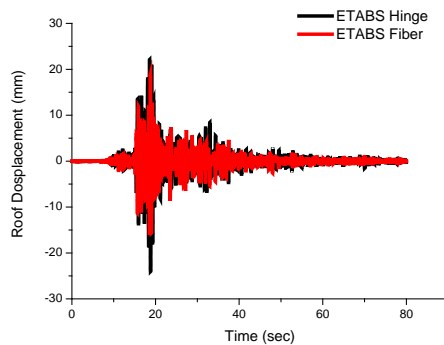
Figure 5. CHY015_70% roof displacement comparison
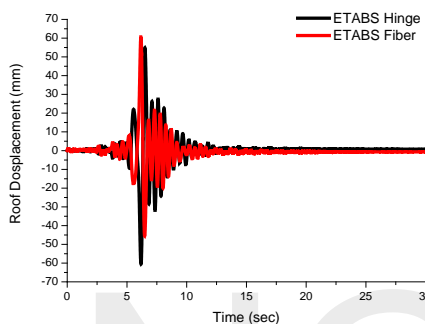
Figure 6. CHY015_150% roof displacement comparison

Conclusions

In this paper, based on the lateral push analysis of the fiber section model of two curvature columns A and B and the TEASPA bending moment nonlinear hinge model, the material parameters of the fiber section model were adjusted such that the capacity curves of the two are consistent. Then, the fiber cross-section model of the B-column and the three-story building and the seven-story building structures were used separately for nonlinear dynamic analysis based on the selected far-field and near-field seismic records. The acceleration, displacement, and floor center of each floor were analyzed. The interlayer displacement angle was compared with the experimental values of the nonlinear hinge and fiber section models to discuss the rationality and accuracy of the compared fiber section model. The following conclusions can be drawn from the comprehensive analysis results:

1. The fiber cross-section model ratio of the single-column specimen is extremely close to the test data whether it is the spine curve or the hysteresis loop.

2. The analysis results of the nonlinear hinge model and the fiber section model of the three- and seven-story structures are consistent in the medium and small earthquakes. When a large near-field earthquake is applied, the analysis results begin to show obvious differences. The analysis results of the hinge model and the fiber section model are still close to the test.

3. The fiber section describes the relationship between the force and deformation of the component and the relationship between the stress and strain of the material. It can consider the mutual control of axial force and bending moment and construct hysteresis energy dissipation behavior simultaneously. It has high accuracy and is suitable for situations with large axial force changes such as medium- and high-rise buildings. The software package ETABS, commonly used in the industry and in this study, automatically generates the fiber of the column section. Hence, it is a convenient and accurate method for both academic research and engineering practice cases.

References

1. Seismic Evaluation of Reinforced Concrete Structure with Pushover Analysis，NCREE-09-015，Taipei，2009。

2. Technology Handbook for Seismic Evaluation and Retrofit of School Buildings Third Edition，NCREE-13-023，Taipei，2013。

3. Applied Technology Council (ATC), ATC-40 Seismic Evaluation and Retrofit of Concrete Buildings, prepared by the Applied Technology Council, Redwood City, Calif., 1996.

4. Technology Handbook for Seismic Evaluation and Retrofit of School Buildings Second Edition，NCREE-09-023，Taipei，2009。

5. Taiwan Earthquake Assessment for Structures by Pushover Analysis (TEASPA V3.1) 」，NCREE-18-015，Taipei，2018。

6. Shaking TbaleTests, Instrumental Technology, Structural Identification and Nponlinear Dyanmic Analysis of a 3-story RC Frame Specimen，NCREE-19-004，Taipei，2019。

7. CSI, *ETABS: Integrated Building Design Software, Version 2016*, Computers and Structures, Inc., Berkeley, California, 2016.

8. Technology Handbook for Seismic Evaluation and Retrofit of School Buildings，NCREE-08-023，Taipei，2008。

9. Laura N Lowes., and Carson Baker, Recommendations for Modeling the Nonlinear Response of Slender Reinforced Concrete Walls Using PERFORM-3D, SEAOC 2016 .

10. Priestley, M.J.N., Seible, F. and Calvi, M., Seismic Design and Retrofit of Bridges, Wiley & Sons, New York, 1996.

11. Nonlinear Dynamic Analysis Research Based on TEASPA Fiber Section Model，NCREE-20-012，Taipei，2020。

12. Blind Analysis Contest on a 7-story Reinforced Concrete Building under Near-fault Earthquakes 2018~2019, Taiwan Tainan https://www.ncree.org/conference/index.aspx?n=C2 0180501A0

A Preliminary Study of the Data Science Method Applied to the Long-term Monitoring of Bridges

Chun-Chung Chen[1], Bo-Han Lee[2], Chi-Rung Jiang[3] and Sheng-Yuan Siao[3]

陳俊仲 [1]、李柏翰 [2]、江奇融 [3]、蕭勝元 [3]

Abstract

Artificial intelligence and extensive data analysis technologies have been gradually developed in many fields, and their benefits and market demand in the industry are becoming more and more apparent. This article briefly describes a preliminary research framework for applying data science methods to long-term bridge monitoring technology. Using integrated field inspection or test data, we can conduct data analysis research and extract critical information from structural monitoring data. The extracted sensing parameters can lighten the burden on the long-term monitoring system and construct a representative data science model that incorporates data science monitoring and management thinking. Combined with an economic sensing system, it enables bridge maintenance authorities to improve the efficiency of bridge maintenance management operations under the restraints imposed by limited maintenance resources. Furthermore, it allows the collection time of on-site bridge monitoring data to be extended in accordance with the demands of bridge service life.

Keywords: Data science, Bridge structure, long-term monitoring

Introduction

Bridges provide essential infrastructure required to maintain a sustainable level of transportation within a society. In response to the successful developments in information technology, many advanced countries have been gradually investing management resources into important bridge structures, installing long-term on-site bridge monitoring systems, and also conducting research into structural health diagnosis technology applications and related subjects. The number of bridges set up for long-term monitoring has increased. The number of sensors installed in each monitored bridge is also growing, and so the amount of collected long-term bridge monitoring data is enormous. The current bridge long-term monitoring technology needs to be improved to use the data to increase the effectiveness of the long-term monitoring system. Many unique bridges, such as landscape suspension bridges, cable-stayed bridges, and extradosed bridges have been built to meet the needs of traffic, road transportation, and regional economic development. Many bridges have been set up with long-term monitoring systems to collect field data on the structural condition of the bridges, especially cable-stayed and extradosed bridges.

The processing tools of the data science methods can be divided into three categories with regard to bridge monitoring parameters: structural analysis, data regression, and structural condition classification, as shown in Figure 1. Figure 2 shows the scientific monitoring and management framework for the bridge data proposed in this study. For the long-term in situ monitoring operation of bridges, the work items usually include planning and construction of the monitoring system, the construction of structural finite analysis models, and the collection and analysis of long-term monitoring data. However, it is challenging to adopt a single finite analysis model to estimate the output response of the local bridge structure using analytical methods because the input conditions of the local bridge environment or the external influences on the structural response of the bridge are dynamic systems and because the structural field test data are included in the long-term monitoring operation.

For the implementation of bridge life-cycle management monitoring, the actual structural responses can be obtained through field test data

collection so that the analysis model better represents the primary structural characteristics. However, the structural properties of the bridge may change over its service life, and it is still a great challenge for a constructed analytical model to appropriately correct for these changes.

Figure 1. Data science analysis methods for bridge monitoring parameter categories.
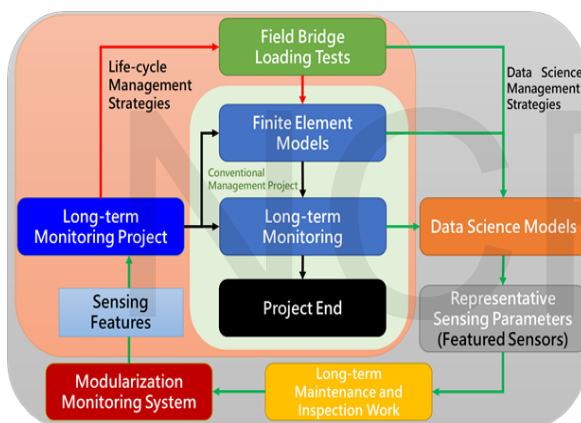
Figure 2. Data science monitoring and management thinking framework for bridges.

Challenges of Monitoring Data Analysis

The essential software and hardware structure for long-term monitoring systems of bridges includes four significant functions: data sensing, data transmission, data storage, and data processing. Therefore, the monitoring system must effectively integrate precise and reliable hardware and software to robustly provide complete monitoring records for data processing. The infrastructure of the monitoring system can improve the decision-making confidence of management authorities, enhance the efficiency of maintenance operations, and effectively reduce full life-cycle costs and the operational risks of structures. With the development of information technology, the number of sensors and the types of sensing items configured in the monitoring system are increasing, resulting in a more complex system integration. Consequently, the

amount of information collected at remote servers or in cloud databases is becoming greater and greater. The specific techniques employed include the application of big data analysis techniques to overcome the problem of vast and overwhelming monitoring data, the use of credible data science methods to supplement the monitoring and evaluation of information when it is insufficient, and the adoption of crucial and optimal system configuration structures to improve the economic efficiency of the monitoring system. From a data science approach, it is very challenging to handle the massive amount of data involved in the monitoring system and also to consider the data diversity and immediacy in order to analyze, retrieve, integrate, search, share, store, convert, visualize, query, and secure these data.

Data Science Monitoring

In recent years, Taiwan has introduced the concept of full life-cycle management to bridge maintenance operations. The monitoring system is built during the construction of a new bridge to ensure the quality of the engineering design and construction and to record the initial bridge structure system characteristics through in-situ testing for subsequent long-term monitoring system data collection. The two main objectives of deploying a long-term bridge monitoring system are to assess the structural safety of a bridge in its current condition and to investigate its durability over its service life.

Traditionally, the technical approach has been to conduct tests on the bridge in situ and collect data for feedback to a finite element or other numerical analysis models, together with structural long-term inspection operation records. However, the long-term monitoring system still has an execution limitation in its application to bridges due to the reliance of the monitoring system on the long-term maintenance operation of the software and hardware needed to ensure regular operation with limited resources. It is not an easy task for management to build the monitoring system into the bridge in a flexible manner or after completing the monitoring data collection task, and it can be similarly difficult to decide on the appropriate scale of the monitoring system or on whether to withdraw from data collection.

Through proper data science methods the long-term monitoring data of bridges can be analyzed scientifically. It is expected that more specific monitoring purposes will be recommended, and that long-term monitoring data can be extracted to monitor critical aspects of a bridge. Furthermore, the structural components representing the actual bridge characteristics can be identified, which can be used as a reference for the timing decision of bridge long-term monitoring system construction planning and system scale adjustment.

Monitoring Data Model Framework

A long-term monitoring system has a considerable construction cost and follow-up maintenance cost in the initial stage. In practice, an existing bridge monitoring project results in long-term monitoring data collection interruption and withdrawal, often due to the constraints of maintenance resources. Therefore, this study proposes a data science analysis method for existing long-term monitoring system data analysis, screening essential sensor items after the monitoring system completes the initial stage of data collection. This data science model can maintain dynamic data correction and incorporates a feedback mechanism. Figure 3 illustrates the contents and projects involved in the construction of this model and the continued development of methods and processes for each project to feed into the development of long-term bridge monitoring technology.
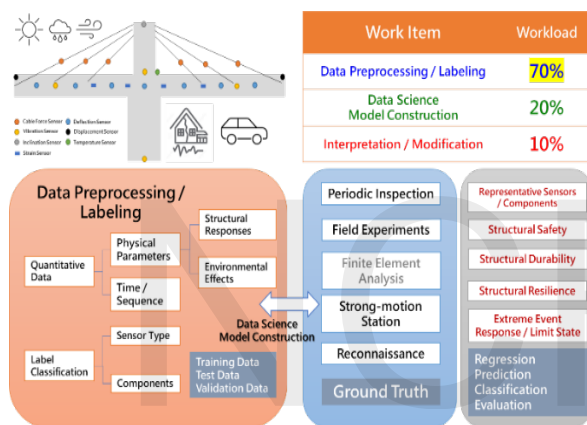
Figure 3. Data science model construction content and items for bridge monitoring.

The highest technical workload when applying data science methods is estimated to be at least 70% related to the complexity of the data analyzed and processed and also to the amount of raw data. In order to develop a long-term bridge monitoring data analysis model properly, this study has to use various data models and consists of three stages. The first stage is data pre-processing and classification labeling. The second stage is the construction of the data science analysis model. In this stage, there are many development resources available for implementation due to the universality of open-source programs and tools; however, custom models are still needed depending on the characteristics of the field data. Therefore, an examination of the results of the analysis and model tuning comprise the third stage of this construction process.

Laboratory Experiments of Loading Tests

The planned analysis process and study details are shown in Figure 4. Using the bridge long-term field monitoring system and the load test on experimental specimens returns a considerable amount of measurement data. This study verified the scientific analysis measurements using these data. On-site monitoring data mainly use the environmental temperature change as an input parameter and match vehicle load test results. The laboratory load test can accurately show applied load values and loading positions and conditions and can measure the precise response of structural specimens. In addition to the traditional finite element analysis method that uses the structural model for analytical solutions, load tests can also be analyzed using structural influence line theory to obtain an analytical solution for the corresponding load condition.

The structural analysis model and test measurement data can be compared. Data science methods can be used to perform regression calculations and classification analyses. The sorting and screening data are required to formulate functional studies for monitoring and measurement data and define representative measurement parameters corresponding to safety. A quantitative index process that assesses bridge safety and disaster prevention can then be developed.
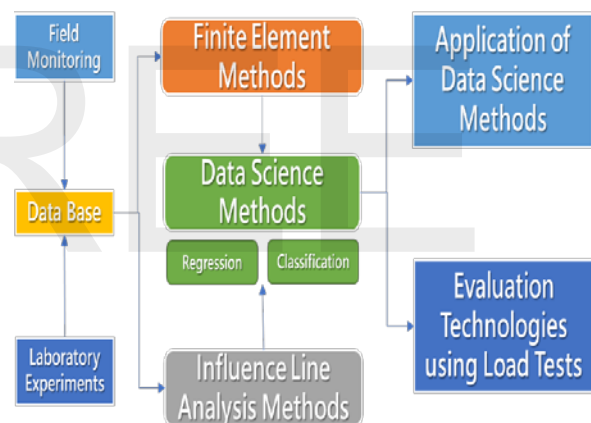
Figure 4. The research analysis process and the studied content.
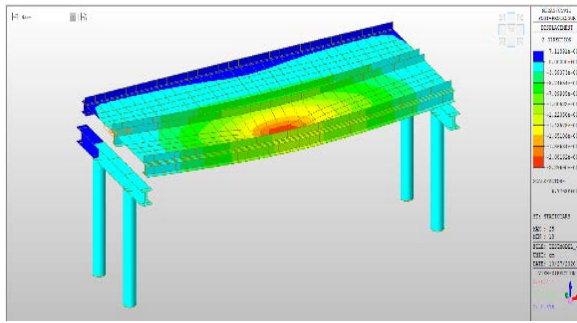
Figure 5. Load test landslide lane and the structural analysis model.

The data science analysis model can be examined and trained to develop a framework applicable to the bridge monitoring field by collecting and analyzing the test data. The current measurement parameters of the laboratory experiments include loading car speed, structural displacements, and component strains, and with the mounting of related structural damping elements such as tuned mass dampers, the structural loading characteristics can be analyzed. The importance and correlation of each measurement parameter can be further explored, The data science method can thus be applied to extract critical monitoring data and make recommendations for adjusting the monitoring measurement project.

Conclusions

This study evaluates the application of data science methods to long-term bridge monitoring data and relevant field inspection or test data. The purpose is to extract critical information from the structural monitoring feedback to ease the long-term monitoring system because constructing a representative data science model combined with a more economical monitoring system will help authorities expand the benefits of the monitoring system and refine life-cycle maintenance behavior. The contents and projects involved in construction of the data science model for bridge monitoring data will continue to develop methods and processes for each project and provide feedback to the research and development of long-term bridge monitoring technology in the field. In addition, the data science analysis will be beneficial for exploring the basic specifications and standards of the monitoring system, which can be used as a reference for developing technical manuals or guidelines for bridge monitoring. This study also anticipates the combination of the technical development of strong seismic monitoring stations for domestic infrastructure with the provision of feedback to the research and development of structural system health diagnosis and safety assessment technologies in order to provide sustainable disaster prevention services.

This study also proposed an innovative experimental platform for evaluating bridge structures using load tests. A series of flatcar load tests were conducted, and data science methods were applied to the test data to assess bridge structure safety. The feasibility of the dynamic load test was demonstrated in a laboratory.

This study aimed to collect large amounts of data using experiments or field projects to select and discuss the applicability of the data science models. For old bridges or bridges with unique structural systems, the field load test is a practical method to assess structural safety in detail. With the increasing trend in artificial intelligence analysis, much data from field monitoring, inspection, or experiments can be obtained and transformed for evaluation via scientific data analysis methods. We are now moving toward intelligent decision-making in bridge disaster prevention and management, ensuring bridge service safety during the bridge life-cycle, achieving complete life-cycle management and maintenance, improving bridge disaster prevention technology, and implementing business applications.

References

Cremona, C. and Santos, J., "Structural Health Monitoring as a Big-Data Problem," Structural Engineering International, 2018, 28:3, pp. 243-254.

System Identification on the Modal Parameters of the Main Girder of an Extradosed Bridge

Zheng-Kuan Lee[1], Hsiao-Hui Hung[2] and Chia-Chuan Hsu[3]

李政寬 [1]、洪曉慧 [2]、許家銓 [3]

Abstract

A newly constructed extradosed bridge on provincial highway No. 61 is located in Yongan Fishing Port, Taoyuan. Fiber optic accelerometers are installed on its main girder. In this study, signal processing techniques are applied to analyze the natural vibration frequencies and the associated mode shapes of the bridge structure; they are then compared with the numerical analysis of the structural design. The research results show that the first mode identified from the collected data is quite similar to that of the structural design. Therefore, the proposed signal process technique is a feasible method for in situ bridge vibration signal.

Keywords: system identification, signal processing, modal analysis, optic fiber sensing

Introduction

A newly constructed extradosed bridge, WH10A, located in Yongan Fishing Port (Figure 1) is one of the characteristic bridges of provincial highway No. 61, Taiwan. The bridge is a single leaning tower with asymmetrical external pre-stressed cables. It was completed in early 2018 and opened to the public on May 19. Due to its specialty, the National Center for Research on Earthquake Engineering (NCREE) was entrusted with the health monitoring project by the bridge owner. Along with the main girder, fiber optic accelerometers were installed inside the box girder. This study aims to analyze its dynamic behavior from the data collected by the fiber optic accelerometers. In addition, the analyzed modal parameters are compared with those from the design.

Modal Analysis of the Design Structure

Based on the design blueprint, from the natural vibration analysis by Midas Civil, the first and second mode shapes of WH10A bridge are illustrated in Figure 2.

Layout of the Optic Fiber Accelerometers on the Girder

The bridge is an asymmetrical bridge with a single leaning tower. The north and south spans are 70 m and 90 m long, respectively. Inside the girder, three fiber optic accelerometers are deployed with equal intervals in each span, as shown in Figure 3 and Figure 4. Symbol N represents the north span, symbol S represents the south span.

Figure 1. Location and appearance of WH10A extradosed bridge

Figure 2. The first mode shape and the second mode shape, with the associated natural frequencies, from the structural analysis by Midas Civil

[1] Research Fellow, National Center for Research on Earthquake Engineering
[2] Associated Research Fellow, National Center for Research on Earthquake Engineering
[3] Assistant Research Fellow, National Center for Research on Earthquake Engineering
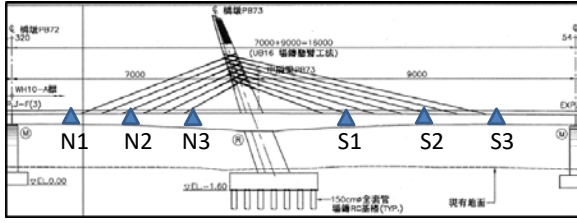
Figure 3. Layout of the optic fiber accelerometers on the main girder

Figure 4. Installation of the optic fiber accelerometer on the main girder

Signal Processing Applied for Modal Analysis

Consider two sets of time series x[n] and y[n] with $0 \leq n < N$. Appling discrete Fourier transform (DFT) for x[n] and y[n], as shown in Equations (1) and (2), the X[k] and Y[k] frequency spectra are obtained, with $0 \leq k < N$.

$$X[k] = \sum_{n=0}^{N-1} e^{-j\frac{2\pi nk}{N}} x[n] \qquad (1)$$

$$Y[k] = \sum_{n=0}^{N-1} e^{-j\frac{2\pi nk}{N}} y[n] \qquad (2)$$

Since both X[k] and Y[k] are complex numbers, Equations (3) and (4) separate their real part and imaginary part, respectively.

$$X[k] = Re(X[k]) + Im(X[k]) \cdot j \qquad (3)$$

$$Y[k] = Re(Y[k]) + Im(Y[k]) \cdot j \qquad (4)$$

Let us define Z[k] as follows:

$$Z[k] = Re(X[k]) \times Re(Y[k]) + Im(X[k]) \times Im(Y[k]) \quad (5)$$

Z[k] amplifies those spectra of X[k] and Y[k] with the same dominant frequencies, the same phase, or opposite phase. Z[k] could be a handy method for modal analysis.

Signal Analysis for the Collected Data

At 13:11 on October 24, 2021, an earthquake with magnitude 6.5 occurred in Yilan County, Taiwan; it shook the WH10A extradosed bridge with local intensity 4, according to the Center Weather Report. At 13:06 and 13:16, before and after the quake, respectively, two text files with 1 minute collected signals were applied for the modal analysis.

Among N1, N2, N3, S1, S2, and S3, the vibration at S3 is expected to be the largest. Therefore, S3 is assumed to be in a positive phase for all modes, and whether N1, N2, N3, S1, and S2 are in the positive or negative phase depends on the analysis results according to Equations (1)–(5). If the result is positive, they have the same phase as S3, and if the result is negative, they have the opposite phase to S3. Figures 5–7 show the analysis results obtained using Equation (5), and Tables 1 and 2 summarize the findings on those figures.

To have a better understanding, Table 2 is visualized and shown as Figures 8 and 9. The above analysis indicates the following: (1) For the first mode, the two text files at 13:06 and 13:16 before and after the quake, respectively, possess almost the same modal parameters, and the associated mode shape is very similar to the analytical result from Midas. (2) For the second mode, the text file at 13:16 after the quake shows similar mode shape with the analytical result from Midas.

Conclusions

Regarding structure dynamics, the conventional discrete Fourier transform method for acceleration data not only lacks the phase information between spatial points but also faces difficulty when selecting the natural frequency in the "multi-extremum zone" of the spectrum. The proposed signal processing technique can quickly calculate the vibration parameters of bridges, including natural frequency as well as mode shapes. The case study demonstrates that the identified parameters are reasonably close to those from the numerical model.

References

Ray W. Clough and Joseph Penzien (2003) "Dynamics of Structures", 3rd Edition, Computers & Structures Inc., California, USA.
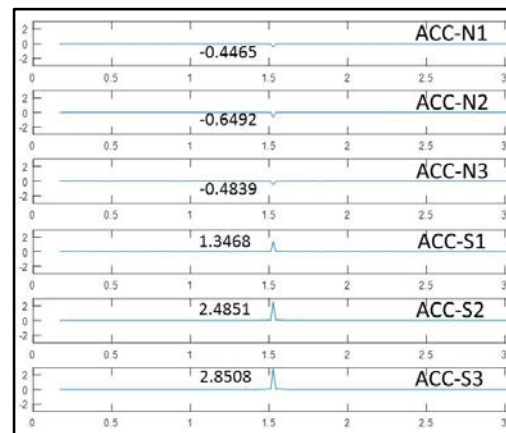
Figure 5. Amplitude and phase for the first mode between the six stations before the earthquake. The horizontal axis represents frequency (Hz) and the vertical axis represents the amplitude and phase.
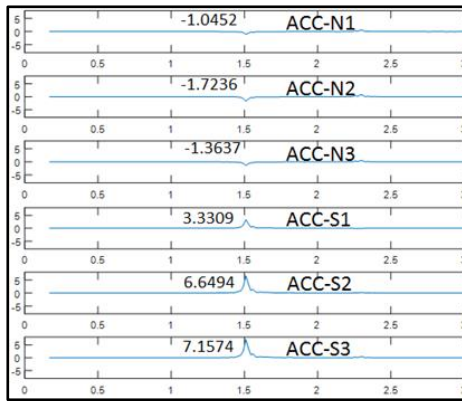
Figure 6. Amplitude and phase for the first mode between the six stations after the earthquake.
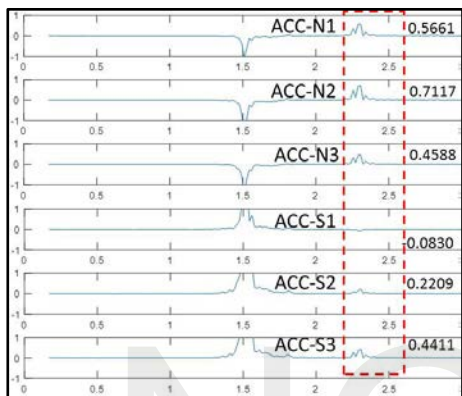
Figure 7. Amplitude and phase for the second mode between the six stations after the earthquake.

Table 1 Comparison of the frequency and mode shape for the first mode. The amplitude ratio of S3 is normalized as 1.

Midas analysis	f1(Hz)	Phase	Amplitude ratio
N1	1.44	-	0.1522
N2	1.44	-	0.1957
N3	1.44	-	0.1087
S1	1.44	+	0.4130
S2	1.44	+	0.9348
S3	1.44	+	1.0000

Before the earthquake	f1(Hz)	Phase	Amplitude ratio
N1	1.527	-	0.1566
N2	1.527	-	0.2277
N3	1.527	-	0.1697
S1	1.527	+	0.4724
S2	1.527	+	0.8717
S3	1.527	+	1.0000

After the earthquake	f1(Hz)	Phase	Amplitude ratio
N1	1.511	-	0.1460
N2	1.511	-	0.2408
N3	1.511	-	0.1905
S1	1.511	+	0.4654
S2	1.511	+	0.9290
S3	1.511	+	1.0000

Table 2 Comparison of the frequency and mode shape for the second mode. The amplitude ratio of S3 is normalized as 1.

Midas analysis	f1(Hz)	Phase	Amplitude ratio
N1	2.35	+	1.9512
N2	2.35	+	1.9512
N3	2.35	+	0.7805
S1	2.35	-	0.2195
S2	2.35	+	0.4878
S3	2.35	+	1.0000

Before the earthquake	f2(Hz)	Phase	Amplitude ratio
N1			
N2			
N3	The second mode signal is too weak to be identified.		
S1			
S2			
S3			

After the earthquake	f2(Hz)	Phase	Amplitude ratio
N1	2.305	+	1.2834
N2	2.305	+	1.6135
N3	2.305	+	1.0401
S1	2.305	-	0.1882
S2	2.305	+	0.5008
S3	2.305	+	1.0000
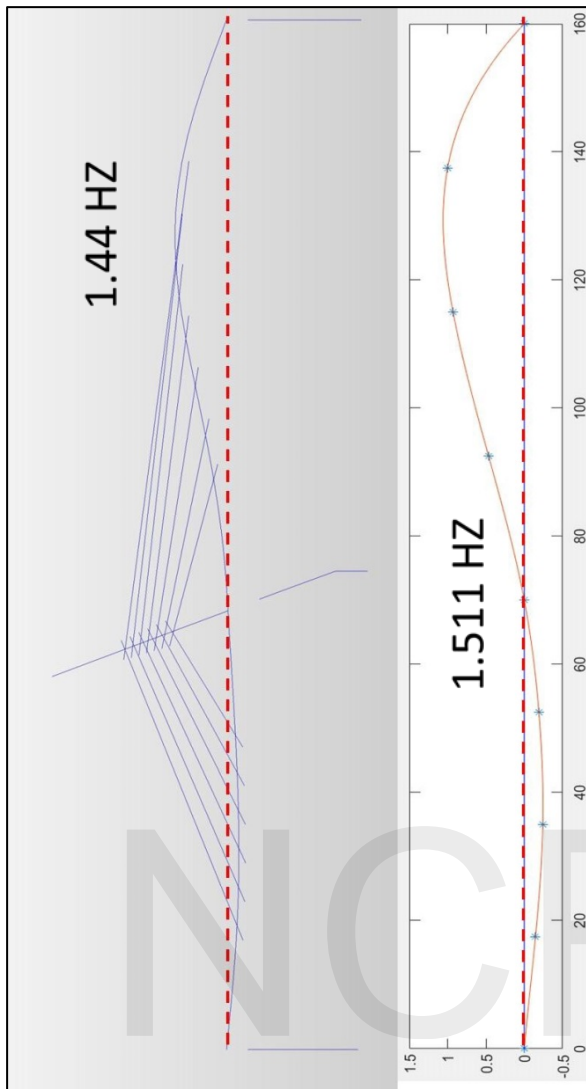
Figure 8. Comparison of the frequency and mode shape for the first mode. The amplitude ratio of S3 is normalized as 1.
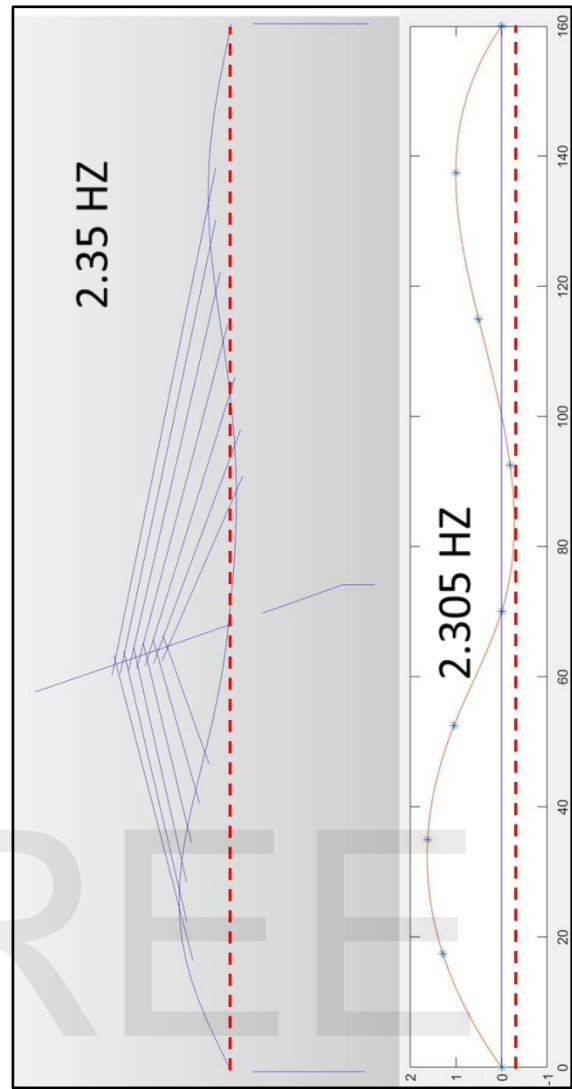
Figure 9. Comparison of the frequency and mode shape for the second mode. The amplitude ratio of S3 is normalized as 1.

Enhancement of the Structural Seismic Performance of Low-Rise Buildings using a Displacement-Dependent Tuned Mass Damper

Bo-Han Lee[1], Chun-Chung Chen[2], Sheng-Yuan Siao[3], Chi-Rung Jiang[4], Fang-Yao Yeh[5]

李柏翰 [1]、陳俊仲 [2]、蕭勝元 [3]、江奇融 [4]、葉芳耀 [5]

Abstract

Tuned mass dampers are used to reduce the vibration of high-rise buildings caused by wind disturbance. Specifically, the displacement-dependent tuned mass damper (DTMD) is an effective vibration energy absorber that is connected to a primary structure to reduce its vibration response under harmonic and external force disturbances. Its natural frequency is adjusted to be close to the fundamental vibration frequency of the primary structure. This leads to an antiphase resonance that dissipates the external force-induced disturbance energy. Several studies have proposed different optimization design objective functions and developed active and semi-active tuned mass damping systems to improve control efficiency significantly. Therefore, we considered a reasonable mass and an objective function using a simplified degree-of-freedom structural model (DTMD and primary structure) to derive an optimized design method and evaluated the feasibility of the structural reinforcement through numerical analysis of the tuned mass damper and shaking table tests. The fundamental retrofit design process used in this study can facilitate the development of a specialized tuning mass damper that can be used in practical engineering applications, such as improving the seismic resistance of ancient and low-rise buildings.

Keywords: Tuned mass damper, seismic performance, shaking table test

Introduction

Many studies have applied the tuned mass damper (TMD) concept in the seismic design of civil structures. Housner G.W. *et al.* proposed developing structural control devices and algorithms for the passive control of nonlinear systems, concentrating on energy-saving methods and hardware to handle the strong inputs [1]. The primary structural system was subjected to harmonic excitation of the fixed acceleration and displacement amplitudes without damping. The theoretical formulae of the optimal TMD damping ratio and the primary structure's frequency ratio under the minimum steady-state response were derived [2]. Warburton derived the optimal TMD design formula for the damping of a single-degree-of-freedom (SDOF) system in a primary structural system subjected to harmonic external and white noise random excitation; however, structural systems experience damping effects; therefore, the effect of structural damping needs to be considered for optimal TMD design [3]. Therefore, Warburton used the value method to investigate the behavior of a primary structural system with damping. The TMD design parameters were optimized, and a chart was created for practical design reference [4, 5]. Tsai and Lin used the curve-fitting method to confirm the optimized TMD design parameter formula [6].

Sadek *et al.* used the state space method to derive theoretical formulas for optimal TMD frequency and damping ratios under the condition that for the main structure that contains the TMD, the first two modes have the most extensive and almost equal damping ratios. Numerical analysis proved that an increase in the mass ratio results in a smaller design frequency

ratio and a larger design damping ratio.

The objective function of TMD design is to optimize the dynamic characteristics [7]. For general TMD parameter design, when the primary structural system is subjected to harmonic excitations, the formula or regression chart obtained in the linear elastic phase is still considered applicable. TMD system design based on the harmonization of external excitations can reduce the response of the primary structure.

In the formulated design procedure, the TMD mass required is determined on the basis of the concept that the damping factor loss is equal to the additional equivalent damping factor introduced by a TMD [8]. Kaneko K describes the passive control method of the TMD for reducing seismic response in reinforced concrete buildings. The displacement-dependent optimal tuning ratios of linear TMDs for nonlinear responses were formulated to reduce the seismic response for a wide range of solid ground motion levels [9].

This study explores the application of a displacement-dependent TMD (DTMD) to enhance structural seismic performance. To evaluate the feasibility of such an enhancement, shaking table tests were conducted to compare the responses of a two-story bare frame with and without displacement-type tuned mass dampers. The duration of the test earthquake was decided considering different peak ground accelerations (PGAs) and seismic characteristics.

In recent years, many studies have focused on structural components and materials, particularly on low floors that undergo long-term aging and deterioration and thus, affect structural safety. Designing reinforcements to improve earthquake resistance is a common countermeasure for this problem. The earthquake resistance of a degraded structure can be enhanced by improving its strength, increasing the damping ratio, and extending the primary vibration period.

Shaking table test

This section describes the test specimens, DTMD mechanism design, input seismic excitations, and measurement details of the shaking table tests. The numerical analysis is also discussed, including comparisons of the displacement responses, inter-story drifts, and acceleration responses of the test specimens. The reduction in the dynamic responses of the specimens with DTMDs under different input seismic excitations is explored. Conclusions and suggestions regarding the feasibility of DTMDs for the enhancement of structural seismic performance are presented.

The long-stroke high-velocity seismic simulation shaking table used for the tests has a plane size of 8 m × 8 m, a mass of 92,000 kg, a maximum load of 250,000 kg, and four pressure actuators on each axis. The shaking table could simulate seismic responses for six degrees of freedom along three axes. The maximum displacements of the shaking table were ±100 cm, ±100 cm, and ±40 cm in the longitudinal direction (X), lateral direction (Y), and vertical direction (Z), respectively. The maximum accelerations of the empty table surface in the X, Y, and Z directions were ±2.5 g, ±2.5 g, and ±3.0 g, respectively.

As per the shaking table specifications, the existing two-story steel frame of the National Center of Research on Earthquake Engineering (NCREE) in Taiwan was selected as the test specimen. The specimen with a DTMD (DTMD specimen) was compared with the specimen without a DTMD (bare specimen). Each floor of the test frame was 3500 mm long, 3500 mm wide, and 3000 mm high. The cross-section of the column member of the test specimen was H-shaped steel with dimensions 340 mm × 250 mm × 9 mm × 14 mm; the beam cross-section was C-shaped steel with dimensions 300 mm × 90 mm × 12 mm; and the girder cross-section was H-shaped steel with dimensions 340 mm × 250 mm × 9 mm × 14 mm. The steel that was used satisfied the following specifications: SN490B (equivalent to A572) and SN400B (equivalent to A36).
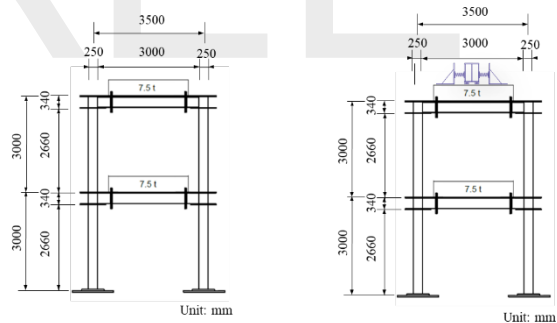
(a) Bare specimen   (b) DTMD specimen
Figure 1. Elevations of the test specimens

Displacement-dependent tuned mass damper

The equations of motion that govern the response of a structure when it is subjected to ground excitation can be expressed as follows:

$$M\ddot{u}(t) + C\dot{u}(t) + Ku(t) = -MR\ddot{u}_g(t) \qquad (1)$$

$$\begin{bmatrix} m_p & 0 \\ 0 & m_t \end{bmatrix}\ddot{u}(t) + \begin{bmatrix} c_p + c_t & -c_t \\ -c_t & c_t \end{bmatrix}\dot{u}(t) + \begin{bmatrix} k_p + k_t & -k_t \\ -k_t & k_t \end{bmatrix}u(t) = -\begin{bmatrix} m_p & 0 \\ 0 & m_t \end{bmatrix}\begin{Bmatrix} 1 \\ 1 \end{Bmatrix}\ddot{u}_g(t)$$

where M, C, and K are the mass, damping, and stiffness matrices of the structure, respectively; $\ddot{u}(t)$,

$\dot{u}(t)$, and $u(t)$ are the acceleration, velocity, and displacement vectors, respectively, of the structure relative to the ground; R is the influence coefficient vector, which represents the displacement vector; $\ddot{u}_g(t)$ is the acceleration of the input ground motion; m_p is the effective mass of primary structure; k_p is the elastic stiffness of the primary structure; and c_p is the damping coefficient of the primary structure.

As illustrated in Figure 2, the DTMD consists of a mass m_t, which slides relative to the primary structure and is attached to it through a spring with stiffness k_t and a friction support with coefficient c_t. The parameters of the DTMD are its tuning, mass, and damping ratios. The tuning ratio f depends on the balance of the fundamental frequency of the DTMD ω_t with that of the primary structure ω_p. Thus, the dynamic characteristics of the linear system are as follows:

$$\omega_t = \sqrt{\frac{k_t}{m_t}} \tag{2}$$

$$\xi_t = \frac{c_t}{2m_t\omega_t} \tag{3}$$

$$\omega_p = \sqrt{\frac{k_p}{m_p+m_t}} \tag{4}$$

$$\xi_p = \frac{c_p}{2m_p\omega_p} \tag{5}$$

where ω_t and ξ_t are the apparent circular frequency and damping ratio of the DTMD, respectively; the corresponding circular frequency ω_p is defined assuming m_p and k_p for the primary structure; and ξ_p is the damping ratio of the primary structure.
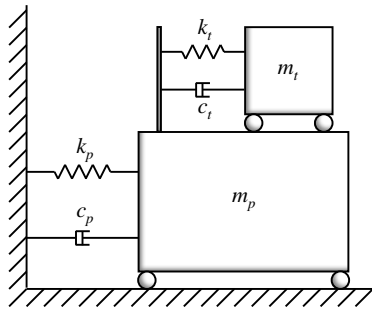
Figure 2. Tuned mass damper mounted on the primary structure

For a linear DTMD, an optimal tuning ratio f^{opt} and an optimal damping ratio ξ_t^{opt} are expressed in the following form:

$$f^{opt} = \frac{\sqrt{1-\bar{\mu}/2}}{1+\bar{\mu}}, \ \bar{\mu} = \psi^2 \frac{m_t}{m_p} \tag{6}$$

$$\xi_t^{opt} = \frac{1}{2}\sqrt{\frac{\bar{\mu}(1-\bar{\mu}/4)}{(1+\bar{\mu})(1-\bar{\mu}/2)}} \tag{7}$$

$$\frac{\phi^T M r}{\phi^T M \phi}\phi = (\psi)^T, \ r = (1,1,\cdots,1)^T \tag{8}$$

where Ψ is the participation vector on the top floor, the modal vector ϕ is considering a structure with a DTMD, and M is the corresponding mass matrix.

The remaining design parameter is the coefficient friction α_a, which needs to be tuned to obtain the optimal hysteretic damping in the DTMD. For convenience, a standardized coefficient $\bar{\alpha}$ is defined in the following form:

$$\bar{\alpha} = \frac{\alpha_a}{\alpha_b} \tag{9}$$

For linear elastic structures, a base shear coefficient of the controlled structure replaces the parameter α_b and is defined in the following form, where Q_b and g are the peak base shear and gravity acceleration, and S_a is the spectral acceleration for specified ground motion:

$$\alpha_b = \frac{\max_t Q_b(t)}{(m_p+m_t)g} \approx \frac{S_a(\omega_p,\xi_p)}{g} \tag{10}$$

For nonlinear structures, the parameter α_b is defined in the following form:

$$\alpha_b = \frac{Q_y}{(m_p+m_t)g} \tag{11}$$

where Q_y is the maximum shear strength of the simplified lumped-mass structure model and the optimal coefficient $\bar{\alpha}$ is approximately equal to 0.25 using numerical optimizations based on a time history analysis:

$$\bar{\alpha}^{opt} \approx 0.25 \tag{12}$$

With the aforementioned experimental and numerical verification, a preliminary design procedure of the DTMD approach is provided based on the simplified lumped-mass structure model, as presented in Figure 3. Under the objective function of minimizing the structural base shear, a numerical model was developed using the SAP2000 software for the time-history analysis using TMD properties and checking whether the structural response reduction and TMD deformation were acceptable. If the response reduction is insufficient, the TMD mass should be increased, and if it does not satisfy the constraint, the damping coefficient should be increased. Then, the time history analysis should be performed again. In the range of alpha 0.2–0.25, the

anti-phase difference motion between the TMD and the controlled structure was more noticeable when the external force was applied. Therefore, the seismic response of the controlled structure can be decreased based on the anti-phase motion. In a nonlinear system, a value is sensitive to the frequency ratio between the TMD and the controlled structure. Therefore, the $\bar{\alpha}^{opt}$ was calculated using the time-history analysis results of the seismic response.
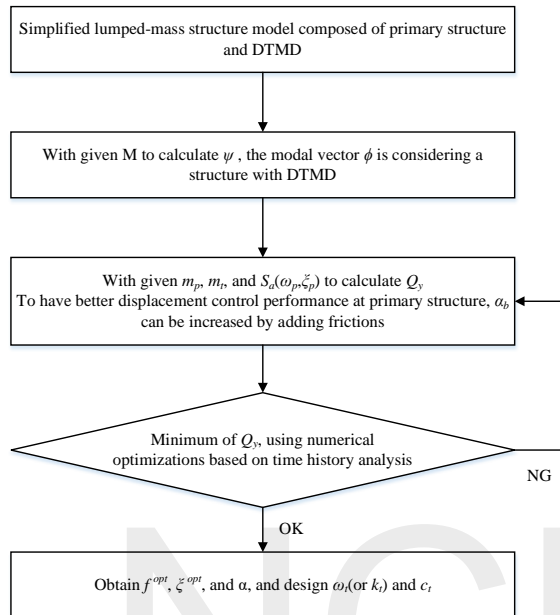
Figure 3. Design procedure of the proposed DTMD

Conclusions

We considered different PGAs and seismic excitations for a two-story scaling test specimen to verify the reduction in structural responses achieved using a DTMD. In previous studies, TMDs have been used for the wind-resistant design of high-rise buildings. In this study, the use of DTMDs was proposed to improve the seismic performance of ancient and low-rise buildings with insufficient seismic resistance. This design method provides a buffer solution for ancient and low-rise buildings that have not yet undergone urban renewal, ensuring safety during strong earthquakes. A two-story steel structure was used to simulate a low-rise RC building for the shaking table test, and the maximum responses in the positive and negative directions for the bare and DTMD specimens during the earthquake excitation experience were observed. The test results showed that a DTMD can effectively reduce the structure's response. Furthermore, the strokes of the DTMD in the positive and negative directions during the seismic excitations were less than the design value of 50 mm, indicating that the structure's stability and response reduction are representative.

In summary, a DTMD, which produces an antiphase resonance to dissipate external force disturbance energy, enhances structural seismic performance. The test results revealed that the test specimen equipped with a DTMD did not exhibit a significantly reduced inter-story drift ratio. The reduction in the acceleration response of the DTMD specimen could be increased beyond 10% using a properly designed DTMD mechanism and parameters. Moreover, the use of compression springs to provide stiffness and friction supports to provide energy dissipation is a feasible method. Thus, the modularly designed mass, compression springs, and friction supports together could form a viable mechanism to enhance structural seismic performance.

References

[1] Housner GW, Bergman LA, Caughey TK, Chassiakos AG, Claus RO, Masri SF, Skelton RE, Soong TT, Spencer Jr. BF, Yao JTP. Structural control: past, present and future. J Eng Mech - ASCE 1997;123(9):897–971.

[2] Den Hartog JP. Mechanical vibrations. 4th ed. New York: McGraw-Hill; 1956.

[3] Warburton GB. Optimal absorber parameters for various combinations of response and excitation parameters. Earthq Eng Struct Dyn 1982;10(3):381-401.

[4] Warburton GB, Ayorinde EO. Optimum absorber parameters for simple systems. Earthq Eng Struct Dyn 1980;8(3):197-217.

[5] Warburton GB. Optimum absorber parameters for minimizing vibration response. Earthq Eng Struct Dyn 1981;9(3):251-62.

[6] Tsai HC, Lin GC. Optimum tuned-mass dampers for minimizing steady-state response of support-excited and damped systems. Earthq Eng Struct Dyn 1993;22(11):957-73.

[7] Sadek F, Mohraz B, Taylor AW, Chung RM. A method of estimating the parameters of tuned mass dampers for seismic applications. Earthq Eng Struct Dyn 1997;26(6):617-35.

[8] Kaneko K. Optimal design method of tuned mass damper effective in reducing overall bending vibration in steel buildings with inter story dampers. J Struct Constr Eng Trans AIJ 2017;82(737):1003-12.

[9] Kaneko K, Takahashi K, Zhang KW, Chen TW, Lee BH and Chen CC. Nonlinear response analysis-based control performance diagrams for TMDs mounted on reinforced concrete buildings. Japan Association for Earthquake Engineering (JAEE) 2021;21(4):34-48.

Development of Advanced Bridge Information System (II)

Kuang-Wu Chou[1] and Chia-Chuan Hsu[2]

周光武 [1]、許家銓 [2]

Abstract

This study is to develop a system that can perform bridge structural analysis on the web. To support such analysis, we build this system's infrastructure this year, which comprises an efficient back-end system and a responsive front-end system. The JavaScript framework Angular is used to provide the front-end system with a responsive web user interface. The computer graphics engine WebGL is utilized to render 3D structural models in the canvas of this web user interface. A simple example demonstrates that the document-oriented database technology MongoDB can straightforwardly describe and efficiently store a structural model. The back-end technology Node.js works smoothly with the MongoDB database, providing the front-end system with a web application programming interface. Through this interface, the back-end system can feed the front-end with data of a structural model.

Keywords: C++, JavaScript, TypeScript, MongoDB, Angular, Node.js, WebGL

Introduction

Developers prefer to create native desktop applications instead of applications of other types such as console and web applications. This is because desktop applications provide users with rich and diverse native graphical user interfaces (GUI) while the others seem unable. Nevertheless, recently, popular and powerful desktop applications like Atom, Visual Studio Code, Microsoft Teams, and Facebook Messenger were developed with the web technologies supported by a famous framework Electron. They offer native GUIs for Windows, macOS, and Linux. And Their being developed with the same source code suffices to make them cross-platform.

Web technologies keep developing and get improved so fast that we cannot ignore them. While most of numerical analysis software are developed with desktop application technologies other than web technologies, this study intends to examine if developing numerical analysis software could benefit from applying web technologies.

As a procedure of numerical analysis, finite element analysis or structural analysis is essential to simulate bridge mechanical behaviors and to examine the health of existing bridges. Thus this study aims at developing a system that can perform structural analysis of bridges on the web. This system will be implemented as a web application, which never needs users to install and frequently update it while desktop applications need both. Besides, Electron can easily transform this web application into a desktop application without modifying the code of this web application.

Before implementing structural analysis into this web system, this year we build this system's infrastructure comprising a back-end system and a front-end system. This infrastructure should support this web system to effectively manipulate and display structural models, to offer users responsive interface, and to perform time-consuming computations. This infrastructure is described in the following. A minimal example is also given to demonstrate how this web system's prototype works.

System Infrastructure

The client-server architecture is applied to develop this web system. This means that this system comprises a back-end system and a front-end system. The two subsystems are illustrated as follows.

Back-end system

The back-end system takes charge of providing

[1] Associate Researcher, National Center for Research on Earthquake Engineering
[2] Assistant Researcher, National Center for Research on Earthquake Engineering

clients with the resources it manages. One important resource is the front-end system, which is described later.

Another important resource the back-end manages and provides is data of structural models. To effectively manage structural model data, the back-end utilizes a MongoDB database to store the data. This database stores data in documents. Documents are more flexible than fixed rows and columns, which traditional, relational SQL databases utilize to manage data (MongoDB 2022). In addition, the way of describing documents in MongoDB fits how a structural model is defined by finite element software. This is demonstrated in the next section (System Prototype Demonstration).

Able to directly manipulate the database of structural models, the back-end is supposed to perform numerical analysis on these models and thus should have corresponding analysis modules for the back-end to invoke. These modules will be implemented in C++, ensuring that those analyses can be efficiently executed. Nevertheless, we consider that these C++ modules may be called by not only the back-end, but also the front-end. That is, our system might let users choose which end to perform analysis.

The back-end is implemented as a web API (Application Programming Interface) for any front-end program or system to call. To fulfil the tasks mentioned above, the web API is supposed to provide manipulation and analysis on structural models.

The web API is implemented by utilizing a cross-platform back-end web technology: Node.js. It is a JavaScript runtime that is built and runs on Chrome's V8 JavaScript engine (OpenJS Foundation 2022; Wikipedia 2022). Node.js enables using the programming language JavaScript to develop and run back-end systems. This means we can use JavaScript to create both the front-end and the back-end systems.

The API of Node.js suffices to do many things like creating web APIs and using databases (especially MongoDB databases). To simplify our codes and ensure the stability and reliability of our web systems, we use a framework for building Node.js web applications: Express. Express is minimal and flexible, treated as the de facto standard server framework for Node.js.

Node.js offers transparent ways for a JavaScript module to call C++ modules. More importantly, the C++ modules can run asynchronously in a Node.js application without blocking this application's main thread. This means that a Node.js application can run time-consuming tasks and respond to user requests at the same time. That is why this study chooses Node.js to examine if structural analyses that likely consume much CPU time may run along with web applications.

Front-end system

The front-end system provides this web system's GUI. This GUI helps clients send requests on structural model data to the back-end system. To build a responsive web GUI that feels like a native desktop GUI, this study adopts the SPA (Single Page Application) approach. This approach prevails over the "traditional" MPA (Multiple Page Application) approach. At the client side, SPA retrieves the single web page only once from the server. After that, according to user requests, SPA will send data to the server or get data from the server to update the content of this page. Under such pattern of communication between clients and the server, the server takes charge of only receiving and providing data that users concern about. That is why we design the back-end system as a web API, which provides user with manipulation on structural model data.

There are JavaScript frameworks or libraries for building SPAs. Three mainstream ones are Facebook's React, Google's Angular, and Vue. Currently, this study adopts Angular because it is a full-featured framework and because its programming language is Typescript that we prefer to utilize. Typescript is a strict syntactical superset of JavaScript. Typescript is statically typed so that some errors may be caught in compile time. For dynamically typed JavaScript, compile time never exists to detect errors. Besides, Angular Material is used to design the front-end system's web GUI while Angular Mater supplies high quality UI design components for developing Angular applications.

In addition to offering the web GUI, the front-end system is supposed to show 3D structural models in browsers. To ensure that this system can efficiently display objects in 3D, this study uses a low-level JavaScript API that can command a GPU (Graphics Processing Unit) to draw with minimal overheads. Currently, only two APIs may be utilized: WebGL and WebGPU. Because WebGPU is still a W3C working draft, we adopt WebGL and would try WebGPU which is claimed faster than WebGL.

System Prototype Demonstration

Considering that next year, structural analyses will be implemented and tested on this web system, simple examples detailing for verifying the analysis results are required. Here we borrow Example 5.9 from McGuire et al (2000). This example shows a frame structure that comprises three structural members (See Fig. 1). Each member has its section properties. Fig. 2 shows that the structural model of this frame is defined and stored as a JSON (JavaScript Object Notation) document object in this system's MongoDB database. A JSON object is described with its properties surrounded by two curly braces {}. Each

property is represented by a key-value pair. The JSON object that describes this frame has key "_id", "name", "nodes", "elements", "materials", and "sections". The "name" key has a string value. Each of the key "nodes", "elements", "materials", and "sections" has an array value.

The array value of the key "nodes" has four members each representing a node because this frame has four nodes. As a node, each member is described by an array having three floating-point values that are the node's coordinates.

Since this frame has three elements, the array value of the key "elements" has three members representing these elements, respectively. To sufficiently describe an element, each member is defined as a JSON object owning the property (or key) "nodes" and "section". This property "nodes" describes an element's nodes with an array of node indices. The "section" property has a string value that is the name of a section. A section is also described with a JSON object, as a member of the property "sections" of the root JSON object describing a structural model. Expanded in Fig. 2, the second member of the property "elements" has the property "nodes" containing the index 1 and 2 and the property "section" whose value is "beam". This value is the name of a section object defined in the property "sections" of the root JSON object (Fig. 2 shows the first, expanded section object has a different name "column").
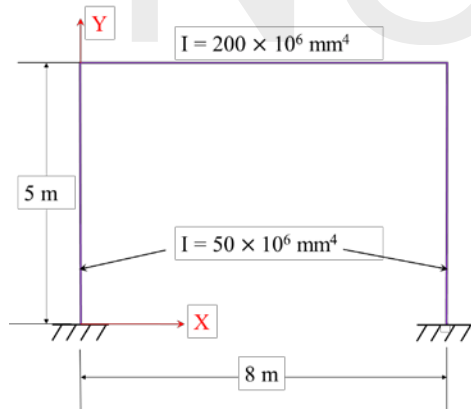
Fig. 1. A simple planar frame

Fig. 3 shows that the web API of this system prototype returns a JSON object almost the same as in Fig. 2 to a Chrome browser. The URL (Uniform Resource Locator) of the web API is http://61.56.6.172:8080/frames/61add2032623b9aa1ac8e9cb. The identifier at the end of this URL matches the value of the property "_id" of the JSON object describing this frame in the MongoDB database. The web API uses this identifier to find a structure model from this database.

Fig. 4-6 show a minimal web application of the

system prototype. In fact, this application calls the web API with the aforementioned URL. Thus this web application gets the model data of this frame from the server. Then this application displays a 3D view of this frame and shows the model data by using the web 3D graphics engine WebGL and Angular Material UI (User Interface) components, respectively.
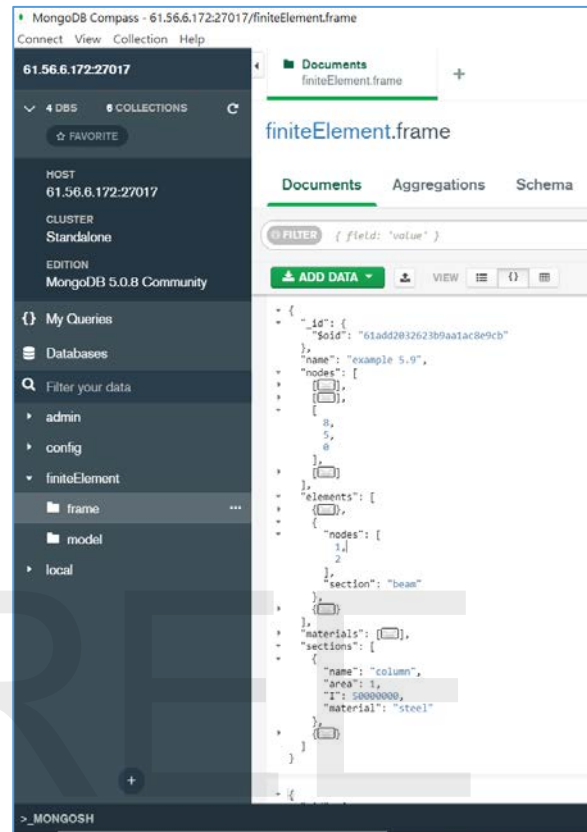
Fig. 2. A MongoDB document that describes the structural model of a planar frame with a JSON object
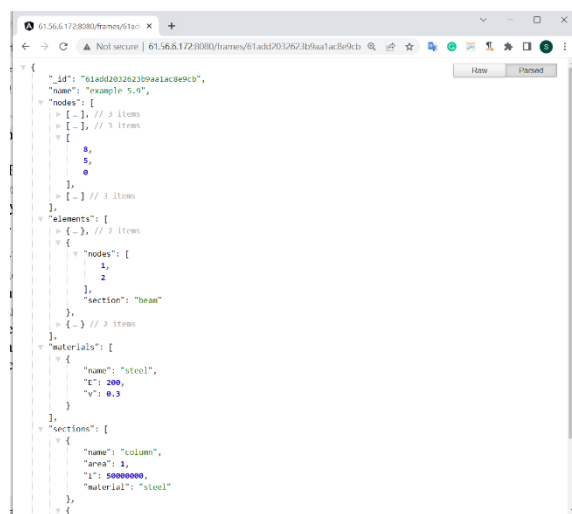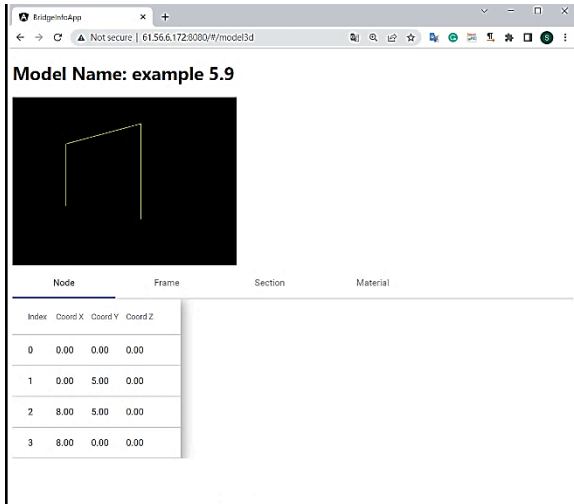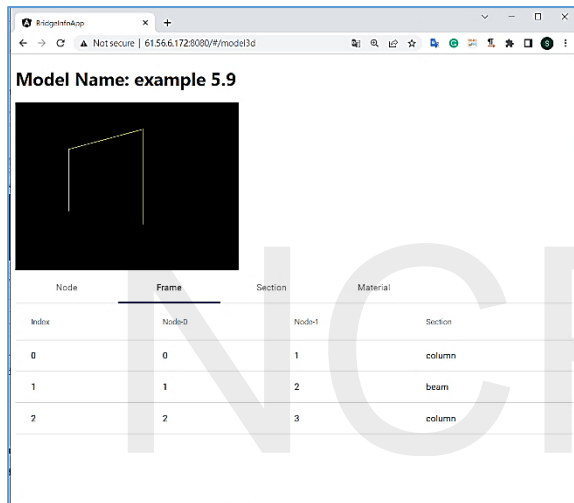
Fig. 3. The web API of the system prototype returns a structural model in JSON format to a Chrome browser
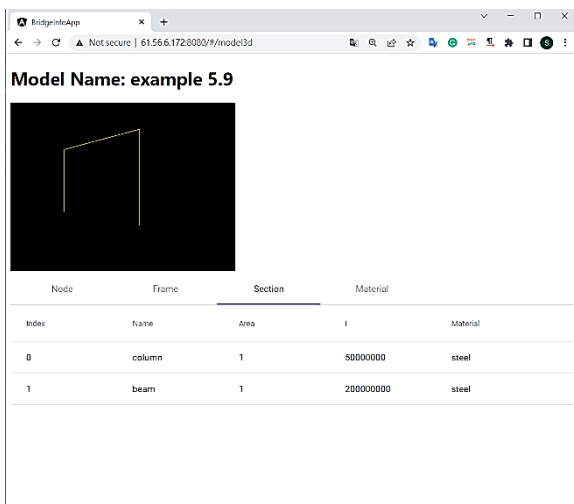
Fig. 4 Node data of a frame model

Fig. 5. Frame element data of a frame model

Fig. 6. Section data of a frame model

Conclusions

This study created a system prototype that provides a web API and a web application. This practice shows that the document-oriented database technology MongoDB can effectively describe, store, and disseminate structural models with JSON document objects.

Utilizing Node.js, we quickly prototyped a web server (the back-end system) in JavaScript. This server may manage the MongoDB database, providing other systems with a web API to access the structural models stored in the database.

The front-end JavaScript framework Angular and its UI design component, Angular Material, suffice to create a responsive UI for the system prototype. By consuming the web API, this UI can show the data that defines a frame model. This practice also shows that Angular can smoothly work with the 3D graphics JavaScript API, WebGL.

Still, this study has crucial tasks to do. First, we need to create data of a large, complex structural model in the MongoDB database. Until then, it is unlikely to examine the design and performance of the system prototype, especially the design of viewing 3D structural models. The second is implementing modules of structural analysis into the Node.js server. This is to examine if such a server can efficiently run structural analysis without blocking its communicating with multiple clients. In addition, this implementation can bring out more functions to be added to the system prototype, helping this prototype become mature.

References

McGuire, W., Gallagher, R. H., and Ziemian, R. D. (2000). "Matrix Structural Analysis, 2nd Edition", Faculty Books. 7.
https://digitalcommons.bucknell.edu/books/7

MongoDB, Inc (2022). "What is a Document Database?". Available from https://www.mongodb.com/document-databases.

OpenJS Foundation (2022). Node.js [Web technology]. Available from https://nodejs.org.

Wikipedia (2022). "Node.js". Available from https://en.wikipedia.org/wiki/Node.js

Experimental Study on the Performance of CFRP Patch Anchors

Fang-Yao Yeh[1], Chi-Rung Jiang[2], Sheng-Yuan Shiao[2], Chun-Chung Chen[3], and Hsiao-Hui Hung[3]

葉芳耀 [1]、江奇融 [2]、蕭勝元 [2]、陳俊仲 [3]、洪曉慧 [3]

Abstract

Carbon fiber-reinforced polymers (CFRP) have been widely used for retrofitting and strengthening concrete structures over the past two decades. Concrete members strengthened by externally bonded CFRP sheets can fail prematurely in debonding between the interface of CFRP and concrete, not allowing full utilization of CFRP tensile strength, in engineering practice. Thus, it is essential to develop an effective and convenient CFRP anchorage system that can be applied to practical engineering. The objective of this research is to study the effect of changing the width and thickness of the CFRP anchorage patches on the tensile strength and effective strain of the FRP reinforcement sheets under the same strengthening conditions. The results indicated that (1) in the CFRP patch anchorage method used in the reinforcing scheme, the effective strain of the CFRP reinforcement sheets under the maximum tensile force is above 0.0038, which can be used as a reference amount for the reinforcing design strain in this scheme. (2) The CFRP patch anchorage method improves the tensile strength and effective strain of the CFRP reinforcement sheets, and increasing the width of the CFRP anchorage patches increases the tensile strength and effective strain of the CFRP reinforcement sheets; however, when the number of plies and fiber area weight (FAW) of the CFRP anchorage patches is increased, the improvement effects on the tensile strength and effective strain of the CFRP reinforcement sheets are not significant.

Keywords: carbon fiber-reinforced polymers, shear strengthening, CFRP patch anchorage method, tensile strength, effective strain

Introduction

In reinforced concrete (RC) members that are shear-strengthened with externally bonded carbon fiber-reinforced polymer (CFRP) sheets, a premature debonding failure mode often occurs in the side-bonding or U-wrapping CFRP schemes. Such interfacial debonding can cause some serious issues, not only because CFRP composites cannot fully exert their high tensile performance but also because the strengthening member will suffer low efficiency and ductility [1].

The on-site bridge, which is the subject of the study, requires shear strengthening owing to its shear crack damage condition. The retrofitting design refers to the AASHTO strengthening specification [2]. CFRP reinforcement sheets and the CFRP patch anchorage method is used for bridge shear strengthening as shown in Figure 1.

Figure 1. Bridge damage conditions and CFRP reinforcement sheets for shear strengthening.

Experimental Program

In this study, the effects of changing the width and thickness (defined as the number of CFRP plies or density of CFRP sheets) of the CFRP anchorage

patches on the tensile strength and effective strain of the CFRP reinforcement sheets were investigated experimentally under the same CFRP strengthening conditions. Table 1 shows the plan of the CFRP patch anchor performance test specimens. The parameters for thickness of reinforcement sheets are 2 plies and 4 plies with a density of 300 g/m² (denoted as FAW300), and width of 50 cm. The parameters for anchor patches are no anchor patch, anchor patches with a width of 50 cm and 75 cm and density of FWA300 and 2 plies, and anchor patches with a width of 50 cm and density with FAW300 and FAW400 and 4 plies.

Table 1 Plan of CFRP patch anchor performance test.

No.	No. of Specimen	CFRP Reinforcement Sheets	CFRP Anchor Patches
1	BM1	FAW300-50-2	-
2	PA1	FAW300-50-2	FAW300-50-2
3	BM2	FAW300-50-4	-
4	PA3	FAW300-50-4	FAW300-50-2
5	PA4	FAW300-50-4	FAW300-75-2
6	PA5	FAW300-50-4	FAW300-50-4
7	PA6	FAW300-50-4	FAW400-50-4

Specimen design

The total length of the concrete specimen and the CFRP anchor patches is 230 cm to meet the requirement of the space limitation for the test machine. For the CFRP anchor patch performance test, taking the specimen number PA1 (Specimen No. 1 of Patch Anchor) as an example, the size of the concrete block is 1600 mm × 850 mm × 354 mm. The design drawing is shown in Figure 2. The free region of the CFRP reinforcement sheets is 1000 mm, and the size of the CFRP anchor patch is 1500 mm × 500 mm. The design diagram is shown in Figure 3.
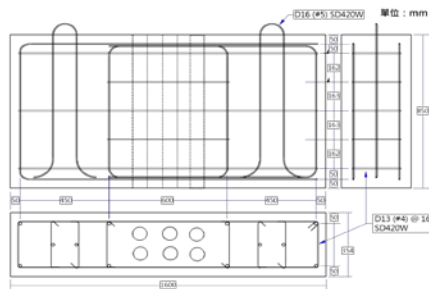
Figure 2. Design drawing of concrete block.
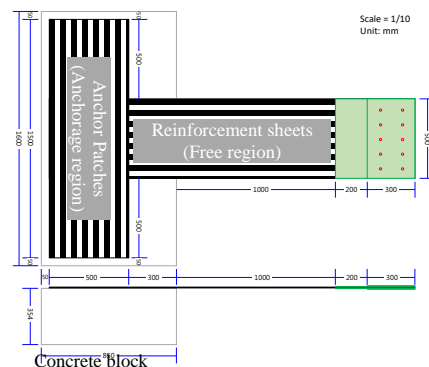
Figure 3. Design diagram of CFRP patch anchor performance test specimen.

Preparation of specimens

The preparation procedure of the CFRP anchor patch performance test specimens includes the following. (1) The surface treatment of the concrete block. (2) Polishing of the surface of the concrete block was polished such that the surface roughness of the concrete conformed to ICRI Guideline No.03732 CSP 2-4 grade (roughness 25-750 μm). (3) Cleaning of the surface of the concrete block by grinding the surface of the concrete block and removing the dust with a brush or a high-pressure air gun. (4) Testing of the moisture content of the concrete block to ensure that the moisture content is lower than 8%. (5) Mixing the primer and epoxy resin and using the mixture at one time within the recommended requirements. (6) Coating of the primer and epoxy resin wherein the primer was evenly coated using brush roller, with the coating range being not smaller than the attachment range of the anchor patches. (7) Using the carbon fiber patch paste as follows: (a) After the unidirectional carbon fiber patch was attached to the resin coated surface, a brush roller or a rubber scraper was used to forcefully push it in the direction of the fiber to infiltrate the resin and remove air bubbles. (b) Paste was applied and left for 30 min. If the fiber was floating or the thread was off, a brush roller or a rubber scraper was used to flatten and correct it. (c) When two or more layers of carbon fibers were pasted on top of each other, steps (a) to (b) were repeated, ensuring that the previous layer of resin was dry to the touch before applying the next layer. Photos of the preparation of test specimen are shown in Figure 4.
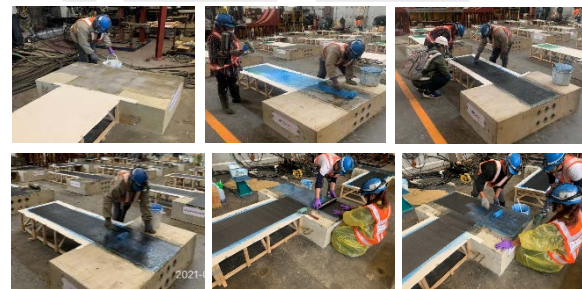
Figure 4. Preparation of performance test specimens.

CFRP patch anchor performance test

The test program adopts the shock absorption and energy dissipation components test system of the National Center for Research on Earthquake Engineering (NCREE). The test system consists of a test frame and a high-performance dynamic hydraulic actuator, and the component test was mainly performed by displacement control. Figure 5 shows the experimental device and the test setup of the test specimen for the performance test of the CFRP anchorage patch system.

Figure 5. Experimental device and test setup.

Measurement configuration

To understand the behavior of the carbon fiber reinforcement sheets and anchor patches during the experiment, a total of six strain gauge measuring lines were arranged on the specimens. The three measuring lines (1-3) were arranged on the free region of CFRP reinforcement sheets. The strain gauge number and position for measurement configuration are shown in the Figure 6.
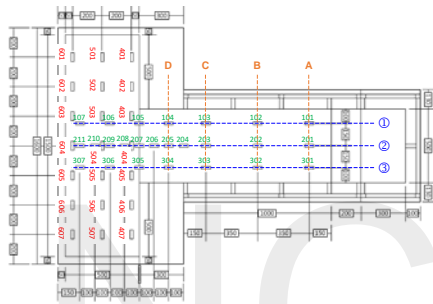
Figure 6. Strain gauge number and position.

Test procedure

The procedure of the anchorage performance test was as follows: (1) The test machine was started and the oil pressure was confirmed to be in a stable state. (2) The actuator was controlled by displacement to make the specimen appear in a state of pre-tension. (3) The actuator of the machine was controlled by displacement, and the displacement increment was set at 1 mm/min. (4) When the tensile force measured by the load cell of the actuator was lower than 30% of the peak tensile force during the test, then an emergency stop of the test was initiated.

Experimental Results and Discussions

Analyses of seven specimens were conducted in this test, and the measurement results of tensile force, displacement and strain were recorded. Figure 7 shows the relationship between the tensile force and the displacement of the anchorage performance test. Among the various specimens, the maximum tensile strength occurred in the PA5 specimen, and the maximum tensile force was 211.81 kN. The minimum tensile strength occurred in the BM1 specimen, and the maximum tensile force was 106.71 kN. Figure 8 shows a photo of the interfacial debonding failure mode of the PA1 specimen. As the tensile force increases, the

interfacial debonding region (red line area) between the carbon fiber sheets and the concrete interface gradually extends from the reinforcement sheets to the anchor patches, and finally breaks instantly.
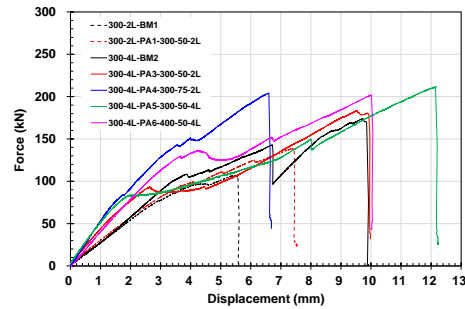
Figure 7. Relationship between the tensile force and the displacement of the anchorage performance test.

Figure 8. Interfacial debonding failure mode of the PA1 specimen.

Strain analysis of CFRP reinforcement sheets

To understand the uniformity of the reinforcement sheets under tensile force, four sections (Lines A-D) were selected for strain comparison. Figure 9 shows the relationship between the strain and the displacement measured by the three strain gauges along Line A of the PA1 specimen. When the displacement was less than 3 mm, the tensile force and strain remained linear. However, when the displacement was greater than 3 mm, the CFRP sheets and concrete interface began to peel and slip, and the tension and strain showed a nonlinear relationship. When the maximum tensile force was 138.57 kN, the strains measured by the strain gauges SG 101, SG 201 and SG 301 were 0.00352, 0.00368 and 0.00358, respectively. The average strain was 0.00359, showing that the strain field of Line A was very uniform.
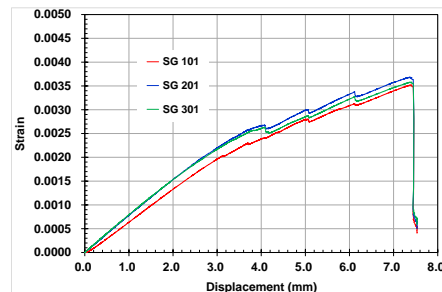
Figure 9. Relationship between the strain and the displacement along Line A of the PA1 specimen.

Force transfer behavior of CFRP

To understand the force transmission behavior of the patch anchorage system under tension,

measurement line 2 of the strain gauge was selected for strain comparison. Figure 10 shows the relationship between the strain and the displacement measured by the seven strain gauges along Line 2 of the PA1 specimen. When the displacement was less than 3 mm, only the three strains (SG 201, SG 202 and SG203) in the free region of the reinforcement sheets had responses and remained linear. When the displacement was close to 3 mm, the SG 205 began to respond, and the force was gradually transmitted to the anchor patches. When the displacement was greater than 4.1 mm, the force is transmitted to the SG 207 position. When the displacement was greater than 6.1 mm, the force was transmitted to the SG 209 position. When the displacement was greater than 7.3 mm, the force was transmitted to the position of SG 211, and the test specimen instantly produced interfacial debonding failure between the carbon fiber sheets and the concrete.
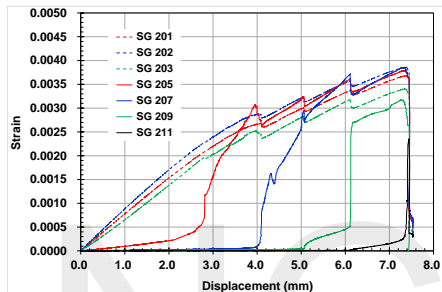
Figure 10. Relationship between the strain and the displacement along Line 2 of the PA1 specimen.

Performance evaluation of CFRP patch anchorage system

The patch anchor performance test adopts a dynamic strain gauge with a sampling rate of 5Hz. When the tensile force reached the peak value, the maximum strain value at the maximum tensile force measured in the free region of the reinforcement sheets and the maximum average strain of the maximum tensile section (Line A, Line B or Line C) were recorded and are shown in Table 2.

Table 2 Results of CFRP patch anchor performance test.

No.	No. of Specimen	CFRP Reinforcement Sheets	CFRP Anchor Patches	Maximum tensile force (kN)	Maximum strain	Maximum average strain
1	BM1	FAW300-50-2	-	106.71	0.0038	0.0036
2	PA1	FAW300-50-2	FAW300-50-2	138.57	0.0041	0.0038
3	BM2	FAW300-50-4	-	173.80	0.0029	0.0024
4	PA3	FAW300-50-4	FAW300-50-2	183.68	0.0042	0.0038
5	PA4	FAW300-50-4	FAW300-75-2	204.25	0.0061	0.0049
6	PA5	FAW300-50-4	FAW300-50-4	211.81	0.0040	0.0031
7	PA6	FAW300-50-4	FAW400-50-4	201.89	0.0038	0.0034

The test results show that the maximum average strain of PA1 and PA3 were 0.0038 and 0.0038, respectively. The research results show that when the CFRP patch anchorage method was used in the on-site strengthening scheme, the effective strain of the CFRP reinforcement sheets under the maximum tensile force of the test was above 0.0038.

A comparison of the test results of PA3 and PA4, shows that the maximum tensile force increased from 183.68 kN to 204.25 kN, an increase of approximately 11.19%; the maximum average strain increased from 0.0038 to 0.0049. The research results show that when using the CFRP patch anchorage method, increasing the width of the CFRP anchorage patch has the effect of improving the tensile strength and effective strain of the CFRP reinforcement sheets.

A comparison of the test results of PA3 and PA5, shows that the maximum tensile force increased from 183.68 kN to 211.81 kN, an increase of approximately 15.31%; however, the maximum average strain decreased from 0.0038 to 0.0031. The research results show that when using the CFRP patch anchorage method, increasing the number of plies of anchor patches has no significant effect on increasing the effective strain of the CFRP reinforcement sheets.

A comparison of the test results of PA5 and PA6, shows that the maximum tensile force decreased from 211.81 kN to 201.89 kN, a decrease of approximately 4.68%; the maximum average strain increased from 0.0031 to 0.0034. The research results show that when using the CFRP patch anchorage method, the effect of increasing the FAW of CFRP anchorage patches on improving the maximum tensile strength and effective strain of the CFRP reinforcement sheets is not significant.

Conclusions

The results of this study showed that (1) when the CFRP patch anchorage method is used in the reinforcing scheme, the effective strain of the CFRP reinforcement sheets under the maximum tensile force is above 0.0038, which can be used as a reference amount for the reinforcing design strain in this scheme. (2) The CFRP patch anchorage method improves the tensile strength and effective strain of the CFRP reinforcement sheets, and increasing the width of the CFRP anchorage patch increases the tensile strength and effective strain of the CFRP reinforcement sheets; however, when the number of plies and fiber area weight of the CFRP anchorage patch is increased, the effect of improving the tensile strength and effective strain of the CFRP reinforcement sheets is not significant.

References

1. Weiwen Li, Wei Liu, Xu Yang, and Feng Xing, "Experimental Study on FRP-to-Concrete Bonded Joints with FRP Sheet Anchor System," Advances in Materials Science and Engineering, March 2020, pp.1-13.

2. AASHTO, Guide Specifications for Design of Bonded FRP Systems for Repair and Strengthening of Concrete Bridge Elements, American Association of State Highway and Transportation Officials, 2012.

Hybrid Simulation of a Seven-story Buckling-restrained Braced Frame Using a Mixed Displacement and Force Control Method for the First-story Beam-to-column Subassembly

Kung-Juin Wang[1], Chung-Che Chou[2], Cheng-Wei Huang[3], Hou-Kuan Shen[3],
Man-Hong Tam[3], Claudio Sepulveda[4], Gilberto Mosqueda[5], and Chia-Ming Uang[5]

王孔君[1]、周中哲[2]、黃丞偉[3]、沈厚寬[3]、覃文康[3]、
Claudio Sepulveda[4]、Gilberto Mosqueda[5]、汪家銘[5]

Abstract

A series of hybrid simulations was performed on a model of a seven-story steel buckling-restrained braced frame (BRBF) with an experimental beam-to-column subassembly. The seismic response of the BRBF is examined considering column axial shortening caused by local buckling at the experimental column base. To achieve a more accurate control and reliable simulation result, displacement control was applied in the lateral direction, with force control for the column axial degree-of-freedom to impose the varying axial load predicted by the simulation in each integration time step. Although the employed computer structural analysis software does not support modeling of local buckling in columns subjected to high axial force and large lateral drift, an innovative approach introducing a fictitious equivalent pull-down force was adopted to enforce the displacement compatibility with the experimental column shortening and the numerical model. Test results confirm that the proposed testing method can account for the measured shortening caused by local buckling of the column in the analysis.

Keywords: hybrid simulation, box-column, column shortening, column buckling, PISA3D, Abaqus, displacement compatibility, force control, mixed-mode control

Introduction

Chou *et al.* (2019, 2020) pointed out that steel box columns under large axial force and large drift can exhibit significant column axial shortening due to local plate buckling at large drifts. Such behavior has not been experimentally investigated using beam-column subassemblies to simulate frame response under earthquake motions. The effects of shortening in the overall frame behavior have also not been studied. This work is aimed at investigating seismic behavior via hybrid simulation (HS).

Hybrid simulation has been widely regarded as an effective testing method to study the dynamic response of structures subjected to dynamic loading. However, HS has its own limitations and challenges (Nakashima 2001). For example, the fidelity of boundary conditions for the specimen can significantly influence the quality of the HS test results. HS can be viewed as a finite element analysis with some elements experimentally simulated in the laboratory. This leads to HS requiring a smaller integration time step size to obtain more accurate (or even converging) results when analyzing stiffer structural models. Moreover, the quality of the HS results could be affected by error-propagation (Shing and Mahin 1983) resulting from actuator control when imposing the target deformation

[1] Principal Engineer, National Center for Research on Earthquake Engineering

[2] Director, National Center for Research on Earthquake Engineering, Professor, Department of Civil Engineering, National Taiwan University

[3] Graduate student, Department of Civil Engineering, National Taiwan University

[4] PhD student, Jacob of School Engineering, University of California, San Diego

[5] Professor, Jacob of School Engineering, University of California, San Diego

on the physical substructure.

This study aims to investigate the seismic behavior of a box column subjected to high axial load and large drift using HS. However, if a column is selected as the physical substructure, HS would be challenging because (1) in the actual laboratory environment it might be difficult to properly impose the required rotational degree-of freedom (DOF), and (2) the displacement-control method might not be able to provide sufficiently accurate control in deforming the column in its axial DOF due to the high stiffness.

Three innovative approaches are used to address these challenges. Firstly, instead of using a single column as the specimen, this study investigates the method of experimentally simulating a single column while using a one-story beam-to-column subassembly as the specimen. Secondly, the force-control method is used to increase the control accuracy for the column axial DOF. Thirdly, the effects of the axial shortening of the column caused by local plate buckling is brought into the finite element simulation by applying a set of fictitious forces in the next integration step to enforce the displacement compatibility in the time-history analysis procedure.

Simulation Model and Test Setup

This experimental project adopted the computer program "Platform for Inelastic Structural Analysis for 3D Systems" (PISA3D) (Lin *et al.* 2009) as the analysis engine for HS tests. The studied seven-story buckling-restrained braced frame (BRBF) is a dual system (Chou *et al.* 2020), which uses built-up box-sections for the right exterior and interior columns and an H-shaped section for the left exterior column. Figure 1 shows a schematic vertical view of the prototype building. This research focuses on the seismic behavior of the first-story interior column (the physical substructure, shown in orange in Figure 1), as well as the system level BRBF seismic response. In addition to the single column, the erected specimen is a subassembly that includes the 1st story column, two half-span 2nd story beams, and the lower half of the 2nd story column. Figure 2 shows the specimen, which corresponds to the portion of the model enclosed in the blue dashed-line box in Figure 1. Although the specimen is a full-scale cruciform subassembly, only the 1st story column is selected as the physical substructure. The other elements in the specimen are considered the boundary conditions for the 1st story column. The actuation system includes four hydraulic actuators: two horizontal actuators at the top of the specimen, with their control targets being the column top horizontal displacement, and two vertical actuators at the mid-span position of the 2nd story beams. In addition, a servo-controllable oil jack system was mounted on the top of the specimen to impose an axial force specified by PISA3D on the specimen during HS.
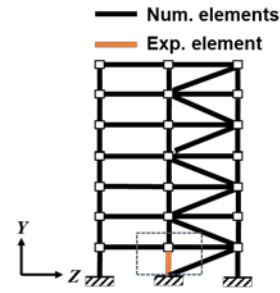
Figure 1. PISA3D models

Figure 2 The beam-column subassembly specimen

High-resolution digital displacement transducers (Temposonics-III) were used to measure the horizontal and vertical displacements of the column top end, which is defined as the lower point of the panel zone. PI gauges were installed to measure the column top rotation. A 3D optical displacement measurement system was used to capture the buckling behavior of the specimen. Strain gauges were used to measure the hysteretic behavior of the beams and column. Two dial gauges were also used to monitor the slip that might occur at the column base.

The control targets of the horizontal actuators are the absolute horizontal displacement calculated by using the real-time measurement of the two Temposonics-III readings. For the vertical actuators, (illustrated in Figure 2), the control target of each vertical actuator is the vertical displacement at the mid-span of the beam, which is assumed to be the average of the vertical displacements of the adjacent column top ends. In other words, the displacement commands are $0.5 \times (u_{y,L}^{lab} + u_{y,M}^{lab})$ and $0.5 \times (u_{y,M}^{lab} + u_{y,R}^{lab})$ for the left and right vertical actuator, respectively, where $u_{y,M}^{lab}$ is the total vertical displacement of the interior column and is measured during HS. Preliminary Abaqus analyses on two models of the left and right beam-column subassembly (illustrated in Figure 3) were conducted to obtain estimated time histories of $u_{y,L}^{lab}$ and $u_{y,R}^{lab}$. The 1st story column top rotation was not controlled in this research since preliminary numerical analysis indicated that with the real boundary condition for the 1st story column, the control approach mentioned above provides reasonably accurate responses of the column top rotation.
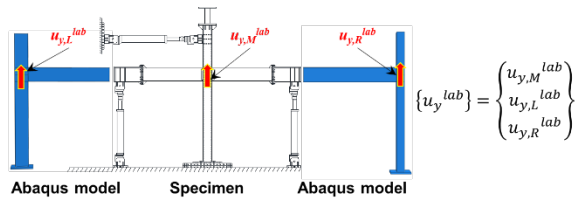
Figure 3 Displacement command for two vertical actuators

Method of Enforcing Displacement Compatibility and HS Implementation

Details of the method used to enforce displacement compatibility with column shortening can be found in Hashemi and Mosqueda (2014) and Sepulveda *et al.* (2022). To apply the experimentally measured and Abaqus-predicted column vertical displacements in PISA3D, a set of fictitious pull-down forces can be calculated from Eq. 1, where [K] is a 3×3 stiffness matrix associated with the vertical DOF u_y and $\{u_y^{bcl}\}$ denotes the vertical displacement vector due to column buckling, which can be calculated from Eq. 2.

$$\{F_{eq}\}_{i+1} = [K]\{u_y^{bcl}\}_i \qquad (1)$$

$$\{u_y^{bcl}\}_i = \{u_y^{lab}\}_i - \{u_y^{ref}\}_i - \{u_y^{geo}\}_i \qquad (2)$$

The subscript i in Eq. 2 is the integration time step index. $\{u_y^{lab}\}$, $\{u_y^{ref}\}$, and $\{u_y^{geo}\}$ denote the total vertical displacement vector, the vertical displacement vector due to gravity and seismic response, and the vertical displacement vector due to geometric constraints, respectively. As shown in Figure 3, $\{u_y^{lab}\}$ is composed of three components: $u_{y,M}^{lab}$ is the measured vertical displacement at the top end of the interior column in the laboratory, and $u_{y,L}^{lab}$ and $u_{y,R}^{lab}$ are the vertical displacements at the top end of the left and right exterior columns, respectively. The latter two are obtained from preliminary Abaqus analysis results. $\{u_y^{ref}\}$ can be obtained by a HS without considering the column shortening effect. For convenience of computation, $\{u_y^{geo}\}$ is set as zero for all the three DOFs since the horizontal displacement of the three column top ends is assumed to be identical. Note that this leads to incorrect vertical displacements of the 1st story columns but the responses (deformation and inernal force) of all the other members in the model remain correct. Theoretically, applying the fictitious force $\{F_{eq}\}_{i+1}$ to the model would force the analysis to include an additional displacement component $\{u_y^{bcl}\}_i$ in the next step if the model remains elastic.

In addition to the ground excitation, the pull-down force $\{F_{eq}\}_{i+1}$ is applied to the model in the time-history analysis by utilizing the experimental elements developed at the National Center for Research on Earthquake Engineering (Wang and Tsai 2015). To use the experimental element, the user firstly

needs to specify the initial stiffness matrix of the experimental element. Then secondly the user needs to specify a specific signal source for the resisting force of each DOF. This signal source can be a real sensor or a set of mathematical formulae in the remote laboratory that provides the restoring force of its associated specimen. Then the element returns the received restoring force when requested by the finite element analysis framework. In other words, if – $\{F_{eq}\}_{i+1}$ is assigned as the restoring force for the experimental elements, it is equivalent to applying the external force $\{F_{eq}\}_{i+1}$ in the analysis. Therefore, to conduct HS using the described mixed displacement and force control method and the described method of enforcing displacement compatibility, it is required to simultaneously run two simulation procedures on two models: the "Reference model" that does not simulate the effects of column buckling, and the "Hybrid simulation model" that does. The "Reference model" is needed to determine $\{u_y^{bcl}\}_i$. The details of the two models are shown in Figure 4. The experimental elements are shown in orange or blue, and the ordinary numerical elements are shown in black. Figure 4 also shows the settings of the initial stiffness of all the experimental elements. Figure 5 shows the software architecture of running two PISA3D analyses for the HS.
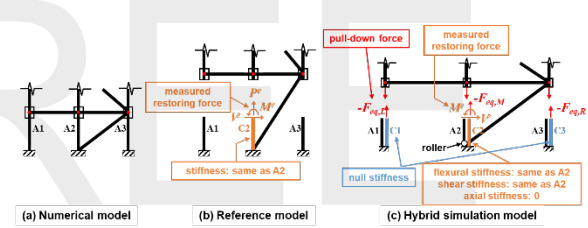
Figure 4. Details of the models used in numerical analysis and hybrid simulation tests
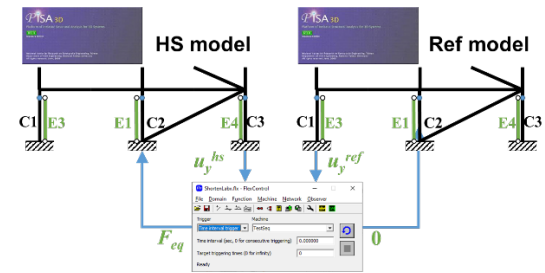
Figure 5 Software architecture of HS

Test Results

A series of HS tests was conducted using the aforementioned testing methods on the seven-story BRBF with increasing intensity of a near-fault ground motion from the 1999 Chi-Chi earthquake. Figure 6 shows local buckling at the column base at the 1st story drift angle of 4%. Figure 7 shows the displacement and rotation responses at the interior column top end. Figure 7(a) shows that both the horizontal

displacements obtained from the analysis for the Reference and HS models are similar and are about 30% larger than the predicted value obtained from the numerical analysis at peak story drift. This suggests that the technique of enforcing displacement compatibility might not be necessary for this building under this excitation. Figure 7(b) shows that the measured vertical displacement agreed well with that calculated in the HS model, indicating that the proposed method for enforcing displacement compatibility is effective.

Figure 6 Local buckling at the column bottom observed at 4% drift ratio

(a) Horizontal displacement history

(b) Vertical displacement history

(c) Rotation history
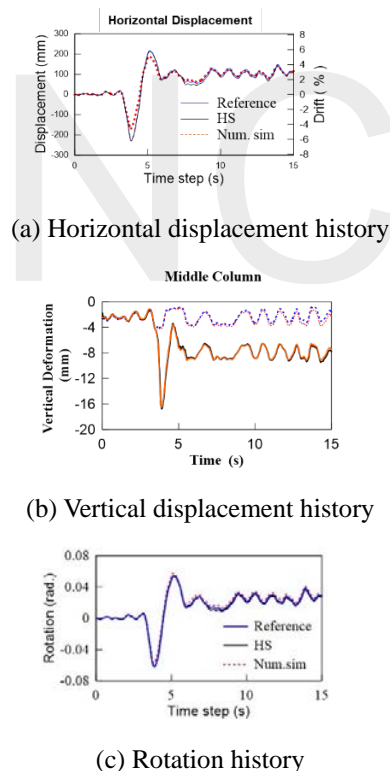
Figure 7. Comparison of the first-story column top end displacement in different models

Conclusions

In this work, an advanced method was employed in hybrid simulation (HS) to achieve reliable simulation results while the effects of column shortening were captured. Test results demonstrate that the proposed mixed displacement and force control method is reliable for applying HS lateral and vertical degrees of freedom (DOFs). The feasibility of enforcing displacement compatibility for the force-controlled DOFs by applying an equivalent fictitious force is confirmed.

References

Chou C. C., Chen G. W., (2020) "Lateral Cyclic Testing and Backbone Curve Development of High-strength Steel Built-up Box Columns under Axial Compression," *Engineering Structures*, 2020, 223, 111147.

Chou C. C., Wu S. C., (2019) "Cyclic Lateral Load Test and Finite Element Analysis of High-strength Concrete-filled Steel Box Columns under High Axial Compression,". *Engineering Structures*, 189, 89-99.

Chou C. C., Lin T. H., Lai Y. C., Xiong H. C., Uang C. M., El-Tawil S., McCormick J. P., Mosqueda G., (2020), "US-Taiwan Collaborative Research on Steel Column through Cyclic Testing of Two-story Subassemblages," *17th World Conference on Earthquake Engineering*, Paper No. C4352 (2i-0213), Sep, 13-18, Sendai, Japan.

Lin B. Z., Chuang M. C., Tsai K. C., (2009), "Object-oriented Development and Application of a Nonlinear Structural Analysis Framework," *Advanced Engineering Software*, 40(1):66-82.

Hashemi, M.J., and Mosqueda, G., (20140, "Innovative Substructuring Technique for Hybrid Simulation of Multi-story Buildings through Collapse," *Earthquake Engineering and Structural Dynamics,* 43(14):2059-2074.

Nakashima M., (2001), "Development and Limitations of Real-time Online (Pseudo-dynamic) Testing," Phil Trans Roy Soc London A. 359(1786):1851-1867.

Shing P., Mahin A., (1983), "Experimental Error Effects in Pseudodynamic Testing," UCB/EERC-83/12, June 1983.

Sepulveda C., Mosqueda G., Uang C. M., Chou C. C., Wang K. J., (2022), "Hybrid Simulation Using Mixed Displacement and Equivalent-force Control to Capture Column Shortening in Frame Structures," (2022), *Proceedings of the 12th National Conference in Earthquake Engineering*, Earthquake Engineering Research Institute, Salt Lake City, UT.

Wang K. J., Tsai K. C., (2015), "A Uniform Method to Integrate Test Equipment for Large-scale Quasi-static Structural Testing," *Proceedings of the 6th International Conference on Advances in Structural Engineering*, University of Illinois, Urbana-Champaign, United States.

Approaches to Improve Force Measurement of a Biaxial Testing System

Chung-Han Yu[1], Wang-Chuen Lin[1], Shiang-Jung Wang[2], Cho-Yen Yang[1]

游忠翰[1]　林旺春[1]　汪向榮[3]　楊卓諺[1]

Abstract

The Biaxial Testing System located in the National Center for Research on Earthquake Engineering's Tainan laboratory features a high testing speed under large compressive loading. The testing system has been employed to conduct many seismic engineering experiments and has enabled significant achievements in research and application. However, since specimen forces are always measured by the differential manometer embedded in actuators, the errors arising from inertia forces and system friction are simultaneously recorded with the actual specimen responses. Moreover, these errors might be significantly increased when small specimens are tested. This study proposes two approaches to effectively reduce the influence of errors: one is indirectly using empirical equations to modify test results and the other is mounting a shear force measurement system on the specimen to directly acquire the response of the specimens.

Keywords: biaxial testing system, testing error, system friction force, inertia force, empirical modification equations, shear force measurement system

Introduction

The Biaxial Testing System (BATS) located in the National Center for Research on Earthquake Engineering's Tainan laboratory can achieve a maximum 60 MN vertical compression force, 4 MN horizontal force, and 1 m/s horizontal velocity. According to recent studies and tests, owing to the large compression load and high horizontal movement velocity, the inertia force and system friction generated from the loading table and actuator connection interface, respectively, are significant. The differential manometers embedded in the actuators are usually used to measure the force responses during tests; these however include the specimen force responses and errors, such as the above-mentioned inertia force and system friction. These errors included in the test data are further enlarged when the specimens have low resistance to horizontal force. To counteract this, this study aims to reduce the influence from errors and increase test accuracy and proposes two approaches: indirectly modifying test results according to empirical equations and directly measuring specimen force responses from a designed measurement system.

Empirical Modification Equations

The empirical modification equations, which can be regressed from a series of sinusoidal and triangular reversal tests, are used to greatly reduce the effects of inertia force and system friction from any test results. To acquire the empirical equations, the process is simply introduced below.

First, under the condition of horizontal movement without vertical loading (Figure 1(a)), the feedback force, $P(t)$, can be expressed as follows:

$$P(t) = F_I(t) + F_F(t) , \qquad (1)$$

where $F_I(t)$ is the system inertia force and $F_F(t)$ is system friction. The latter can be simply defined as:

$$F_F(t) = \mu_{avg} N(t) , \qquad (2)$$

where μ_{avg} is the generalized system average friction coefficient and $N(t)$ is the system vertical loading. For instance, $N(t)$ is equal to the self-weight of the loading table when there is no vertical

loading.

Therefore, a series of triangular reversal tests (with zero acceleration) can be used to regress the average friction coefficient under a zero vertical loading condition. On the other hand, a series of sinusoidal reversal tests, continued from triangular reversal tests, can be used to regress the effective self-weight of the loading table after the average friction coefficient is known.

By using a flat sliding bearing and conducting a series of triangular and sinusoidal tests with various vertical loadings, the average friction coefficients with different vertical loadings can be acquired (Figure 1(b)) according to the following equation:

$$P(t) = F_B(t) + F_I(t) + F_F(t) , \qquad (3)$$

where $F_B(t)$ is the horizontal force of the flat sliding bearing.

The average friction coefficients versus table movement velocity under 0 t and 1000 t vertical loadings (empirical modification equations) are plotted in Figure 2. It is evident that the coefficient varies with different table movement velocities and decreases under vertical loading.
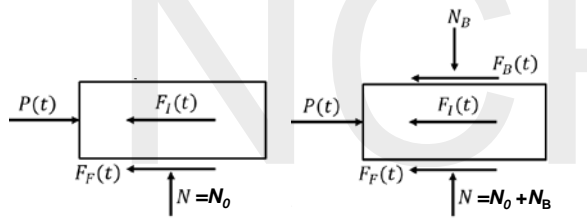
(a) Without vertical loading (b) Under vertical loading
Figure 1. Free body diagram of a loading table.
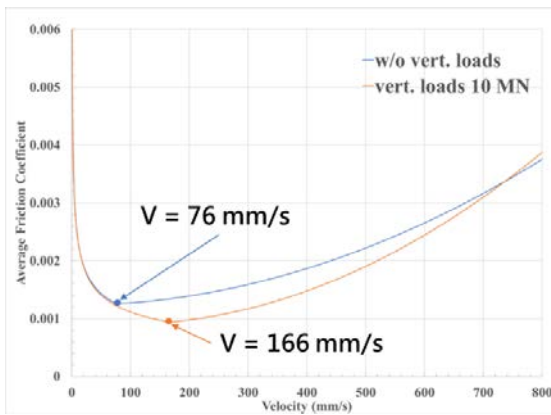
Figure 2. Empirical modification curves of the average friction coefficient.

Shear Force Measurement System

As shown in Figure 3(a), the shear force measurement system comprises a natural rubber bearing (NRB) used to transmit the vertical load applied to the specimen, an intermediate plate used to connect the system with the specimen, a reaction frame fixed at the top of the BATS reaction block, and four prestressed rods used to transmit horizontal force from the specimen to the reaction frame. Therefore, the shear force applied on the specimen is equal to the summation of the changes in force on the four prestressed rods and the NRB. In other words, in the horizontal direction, the specimen is connected in series to the prestressed rods and the NRB.
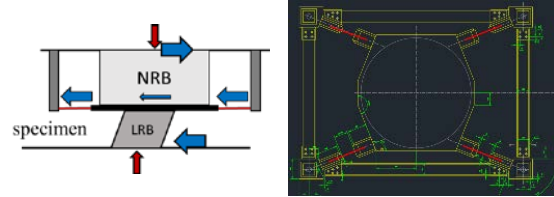
(a) Transmitted force diagram   (b) Plan view of design drawing

Figure 3. The shear force measurement system.

In detail, each pressed rod is pin-connected via laboratory-designed spherical washers at both ends. Near the intermediate plate end, a load cell is connected with the prestressed rod in series to measure the axial force. Based on calculations, the theoretical elastic lateral stiffness of the NRB is approximately 0.95 kN/mm, whereas the summation of axial stiffnesses of the four prestressed rods is approximately 400 kN/mm. This shows that the prestressed rods can take approximately 99.7% of the shear force, which can be precisely measured by the load cells. That means the error arising from the theoretical calculation of the NRB, according to theoretical stiffness and measured deformation, can be ignored.

Finite-element analysis was conducted using the commercial program ANSYS to check in detail the safety and functionality of each component in the measurement system. The finite-element model adopts the following assumptions:

1. The contact surfaces between the bottom side of the reaction block of the BATS and the top side of the NRB, as well as the reaction frame, are assumed to be bounded.

2. The friction coefficient of metal-to-metal slidable contact surfaces, *i.e.*, the spherical washers, is assumed to be 0.2.

3. Because the NRB only has minor deformation and remains in an elastic state during tests, it is simplified as an isotropic cylindrical elastomer, whose Young's modulus and Poisson's ratio are 978.4 MPa and 0.49, respectively.

4. The diameter of the specimen, which is not included in the numerical model, is assumed to be 500 mm. The compression force and shear force, which are 10,000 kN and 200 kN, respectively, are uniformly distributed on the bottom side of the intermediate plate.

5. The pretension force in the four prestressed rods is 120 kN.

The results of the principal stress analysis of the shear force measurement system are shown in Figure 4. The stresses at the intermediate plate and the reaction frame are much smaller than the yielding stress of A36 steel, whereas the stresses at the prestressed rods and their connecting ends concentrates up to approximately 300 MPa, but are still much smaller than the yielding stress of F10T steel. The deformation condition is shown in Figure 5. The maximum deformation (1.0-1.5 mm) of the NRB occurs at the central, owing to the applied compression and shear forces, and the maximum vertical displacement (approximately 2.4 mm upward) occurs near the center of the intermediate plate.
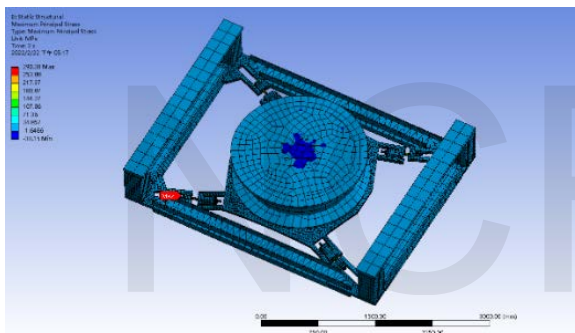
Figure 4. Principal stress distribution.
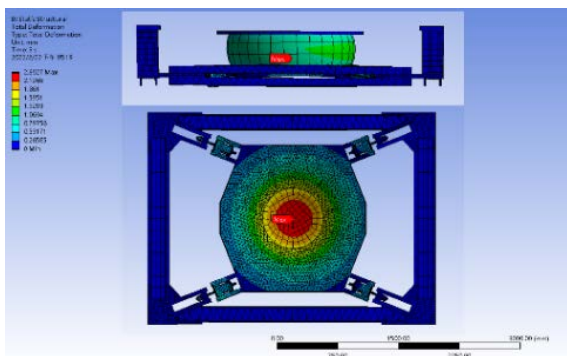
Figure 5. Deformation condition.

To verify the efficiency of the shear force measurement system, a series of practical experiments was conducted on the BATS, as shown in Figure 6. The specimen installed beneath the measurement system is a 500 mm diameter lead rubber bearing (LRB), with a total height of 197 mm and thicknesses of 4.5 mm for single rubber layers and a total rubber layer thickness of 90 mm, respectively. The force at zero displacement,

i.e., the characteristic strength, is 64 kN, and the effective stiffness corresponding to 100% shear strain of rubber is 1.13 kN/mm. The experiment comprised seven four-cycle sinusoidal reversal tests under the same compressive stress of 10 MPa. Of the seven tests, five tests were conducted with the same frequency (0.25 Hz) but different amplitudes (50%, 100%, 150%, 200%, and 250% shear strain of rubber) to observe the influence of different specimen shear forces on the measurement system, and the other two tests were conducted with same amplitude (100% shear strain of rubber) but different frequencies (0.01 Hz and 0.1 Hz) to observe the influence of different loading velocities on the response time of shear force measurement.

Figure 6. The experimental setup.

Two representative test results, Test 3 (100% shear strain of rubber and 0.1 Hz frequency) and Test 7 (250% shear strain of rubber and 0.25 Hz frequency) were chosen to demonstrate the functionality and efficiency of the shear force measurement system. The results are shown in Figure 7; the green curves (469D) are the direct feedback forces from actuators, the blue curves (Sum of LC) are the summation of orientation-modified measurement data from the four load cells installed at the prestressed rods, and the red curves (NRB) are the theoretical forces of the NRB calculated from the measured deformation and theoretical elastic stiffness, where the force in the NRB is only 2% of the prestressed rod. The percentage is slightly larger than the original prediction, but it nevertheless verified the design concept.
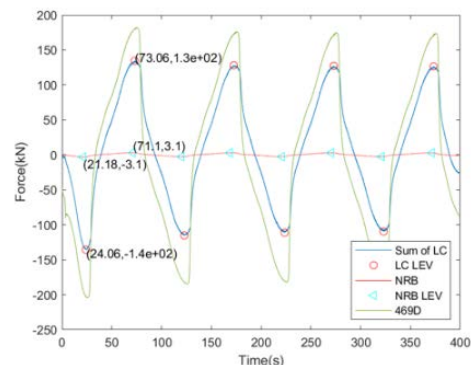
(a) Test 3 (shear strain 100%, frequency 0.1 Hz)
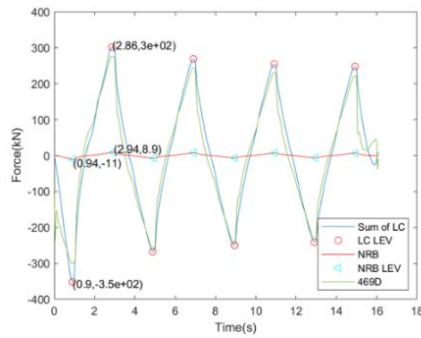
(b) Test 7 (shear strain 250%, frequency 0.25 Hz)

Figure 7. Time history of results for forces.

Likewise, the force–displacement results of Test 3 and Test 7 were chosen to discuss the reasonableness of shear force measurement results and are plotted in Figure 8. In this figure, $F1$ is the direct feedback force from actuators, $F2$ is force $F1$ modified according to the empirical modification equations, and $F3$ is the force measured from the shear force measurement system (including the orientation-modified load cell forces and the theoretically calculated NRB force.)

As observed from Figure 8(a), under low velocity and small shear strain, $F2$ and $F3$ are obviously smaller than $F1$, owing to the deduction of the friction force. However, because the friction coefficient of the modification equations has larger variance under low velocity range, $F2$ is slightly different from $F3$. On the other hand, as shown in Figure 8(b), under high velocity and large shear strain, comparison of $F1$ to $F2$ and $F3$ shows that not only the friction force but also the inertia force is modified, which can be seen from the counterclockwise rotation of the force–displacement behaviors. Furthermore, $F2$ and $F3$ are similar, which mutually verifies the accuracy of the modification equations and measurement system.
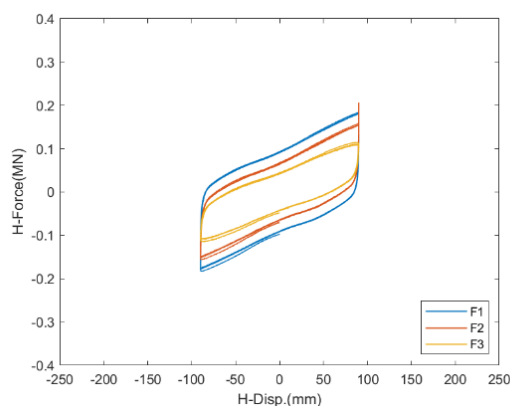
(a) Test 3 (shear strain 100%, frequency 0.1 Hz)
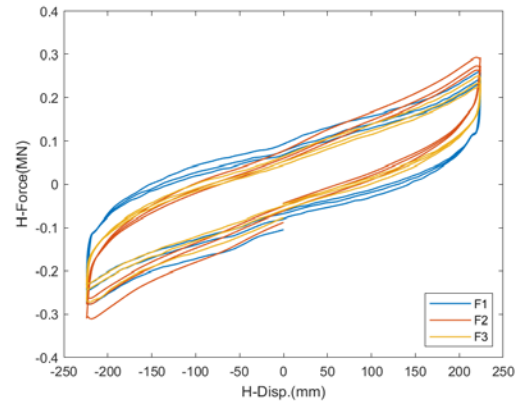
(b) Test 7 (shear strain 250%, frequency 0.25 Hz)

Figure 8. Comparison of hysteresis loops.

Conclusions

This study preliminarily verified the feasibility of both the empirical modification equations and shear force measurement system. Through a practical experiment, the two approaches were found to have greater differences under low velocity and small shear strain, but were mostly consistent under high velocity and large shear strain. However, in practical terms, although the shear force measurement system has higher accuracy, the complex installation process, large space requirement, and limited measurement capacity may reduce the scope of application. Therefore, the ultimate goal of this study is to develop a precise and convenient approach for shear force and inertia force modification. Under this premise, future work will have two aims: 1) to decrease the error of the empirical equations via more testing and verification of the shear force measurement and 2) to increase the measurement capacity of the shear force measurement system under limited installation space.

References

林旺春,劉瓊林,汪向榮,楊卓諺,游忠翰,林晉承,盧煉元,黃震興,張國鎮(2022)，"雙軸向動態試驗系統之基本參數研究與探討"。

Kelly, J.M. (1993). "Earthquake-Resistant Design with Rubber.", Chapter 8.3 p.170-p.174.

J. S. Shortreed, F. Seible, A. Filiatrault and G. Benzoni. (2001). "Characterization and testing of the Caltrans seismic response modification device test system", Phil. Trans. R .Soc. A, 359: 1829-1850.

Experimental Study of Suspended Busway Systems

Wei-Chung Chen[1], Zeng-Wei Zeng[2], Fan-Ru Lin[3], Juin-Fu Chai [4],

Bai-Yi Huang[1], Yu-Ciao Huang[1] and Chao-Yu Tu[1]

陳威中 [1]、曾增維 [2]、林凡茹 [3]、柴駿甫 [4]、黃百誼 [1]、黃昱喬 [1]、涂昭仔 [1]

Abstract

Damage to nonstructural components during past seismic events has been shown to be not only a critical threat to life in extreme cases but has also led to a substantial reduction in the functionality of buildings and other facilities. Suspended busway systems are among the important yet lesser understood nonstructural components of a building for which the current standards provide only limited seismic design guidance due to their heterogeneous and complex construction. In order to understand the dynamic behavior of suspended busway systems, a series of full-scale shaking table tests were conducted at the National Center for Research on Earthquake Engineering Tainan Laboratory. This paper presents details of this experimental study, including the test setup and configurations, the test motions, and the failure patterns of the busway systems observed during the tests.

Keywords: suspended busway systems, cast resin busway, UL busway, shaking table tests, nonstructural components

Introduction

The busway (Fig. 1) is a suspended electrical distribution system that uses copper or aluminum busbars with suitable enclosures and a significant amount of protection to prevent the inside conductors from damage caused by foreign bodies. It has a compact design and the compressed flat conductors can pass through the enclosure. Due to this compact design, busway systems require less space than traditional cable systems do and this is a major advantage when thousands of amperes of electricity need to be transmitted. These systems can also be used in any kind of structure and with any configuration. They are easily modifiable and hence an extra room or building can be easily added, and they also help to facilitate the efficient and safe distribution of lines with junction boxes located where they are required. The data junction boxes can be easily increased in number and changed whenever and wherever this is required. In addition to the convenience and safety factors, there are several other advantages that the busway system has over traditional cable systems and that is the reason they are becoming commonly used in important buildings and facilities.

Figure 1. The suspended busway system

Seismic events have caused damage to suspended busway systems, which have been documented from the 1999 Chi-Chi earthquake in several post-earthquake studies. The reported damage primarily consisted of fractured elements, damaged trapeze systems, joint connection failure, and anchorage failure. Loss of power was shown to be not only a

critical threat to life but also led to a substantial reduction in the functionality of important facilities.

Suspended busway systems are composed of combinations of many discrete components, which makes it difficult to determine the strength capacity of the entire system. In order to understand the seismic performance and the dynamic behavior of busway systems subjected to earthquake induced excitation, a series of full-scale shaking table tests were performed using a long-stroke and high-speed earthquake simulator at the National Center for Research on Earthquake Engineering (NCREE) Tainan Laboratory. This paper presents the test setup, specimen configurations, input test motions, and failure mechanisms of the busway systems observed during the experiments.

Test Setup

A three-story test frame 5 m × 5 m in area and 12.7 m high was mounted on the shaking table at the NCREE Tainan Laboratory for a series of full-scale dynamic tests. The structure is shown in Fig. 2. For the purpose of achieving a larger inter-story drift, an increased mass was added to the floor decks. The weight of the test frame without the busway system was approximately 46t. The dynamic properties of the bare test frame were obtained using transfer functions, Hanning window with 8192 window points from data, calculated from acceleration histories (white noise tests) between the shaking table and the roof center. The fundamental frequencies of the test frame in the two horizontal directions were both 1.1 Hz.

Figure 2. The three-story test frame

In order to measure the response of the test system, various instruments including accelerometers, displacement transducers, and motion capture systems (as summarized in Table 1) were installed in the

shaking table, the test frame, and the busway systems.

Table 1. List of instrumentation

Instrumentation	Quantity
Tri-axial accelerometer (Dytran)	34
Single-axis accelerometer (Setra)	9
Temposonis (MTS)	21
DP-E Displacement Transducer (Tokyo Measuring Instruments Lab.)	8
Motion capture system (Optitrack)	40

Test Busway Configurations

Two types of suspended busway systems were constructed inside the three-story test frame to investigate the influence of various input motions and layout parameters. The first system was the metal sandwich busway system, in which the inner conductor and insulator are protected by a metal shell structure (Fig. 3). The other system was the cast resin busway system (Fig. 4) that uses a mixture of epoxy resin and insulating filler as a shell to protect the inner conductor.
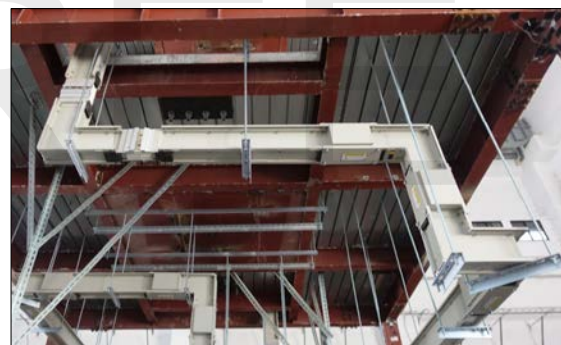
Figure 3. The metal sandwich busway system

Figure 4. The cast resin busway system

Figure 5 shows the test configurations of the suspended busway systems on different floors, which consist of series of line elements joined by different types of connections. A distribution box was installed at the center of the first floor, and two complete UL

busway systems with different configurations were developed from the distribution box through the second floor to the third floor. The primary test parameters of these two systems were the plenum heights which were 1.5m and 3.0m respectively. A portion of a typical cast resin busway system was installed on the second floor. This test specimen was designed to explore the seismic performance of the cast resin busway system and to investigate the effects of different plenum heights at the same time.

Figure 5. The test busway configurations

All of the test busway systems were made in compliance with the current construction methods in Taiwan. The trapeze systems (see Fig. 6(a)) hanging the main runners were placed at intervals of 150 cm, and two types of braced frames were adopted for the busway systems with different plenum heights, as shown in Fig. 6(b, c).

(a)   (b)   (c)
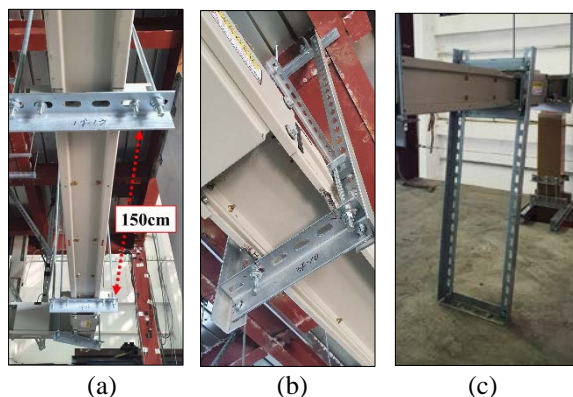
Figure 6. (a) The trapeze systems; (b) suspended braced frame; (c) grounded braced frame

Test Motions

Various input motions were used for different purposes. White noise tests, sine-beat tests, and sine sweep tests were performed to identify the dynamic characteristics of the test busway systems, whereas ground motion tests were implemented to simulate realistic earthquake events. Table 2 summarizes the information of the selected earthquake events, and these events were scaled down to target levels to prevent the test frame from suffering severe structural damage. A conceptual computer model (Fig. 7) was created using SAP2000 to assess the strength capacity of the test frame, which took into account the interaction between the test frame and the busway systems.

Table 2. Description of the test motions

Events	Station	Scaling
Kobe EQ	JMA	20%
	Takatori	20%
	Shin-Osaka	60%
Northridge EQ	Rinali Receiving	20%
	Beverly Hill	30%
Chi-Chi EQ	CHY101	40%
	CHY025	90%
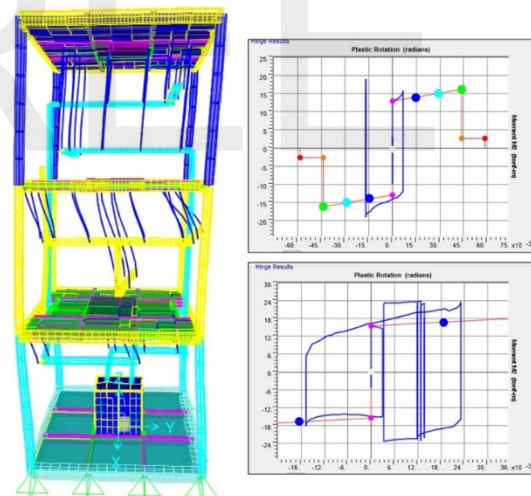
Figure 7. The SAP2000 numerical model

The test busway systems were subjected to incremental base motions, starting from 10% of the target level of each earthquake event until substantial and unrepairable damaged was observed in the test specimens. After each step of each seismic event, the busway systems were visually inspected to record the changes and to document the damage. It was noted that any damage to the test specimens could only be simply repaired, resulting in accumulated damage to the busway system in the subsequent test steps.

Test Results

The test results of the primary failure patterns of the busway systems are presented in this section. Three main failure patterns were identified: (i) failure of the trapeze systems, (ii) failure of the braced frames, and (iii) failure of the line elements.

Failure of the trapeze systems

Slip between the line elements of the busway and the trapeze systems was observed early during the experiment and occurred at a low intensity of the input excitation (peak floor acceleration (PFA) of 250 gal). The failure of one trapeze system resulted in progressively missing vertical supporting and uneven loading distribution on the busway systems, which led to other more severe failure (see Fig. 8).

(a) (b) (c)
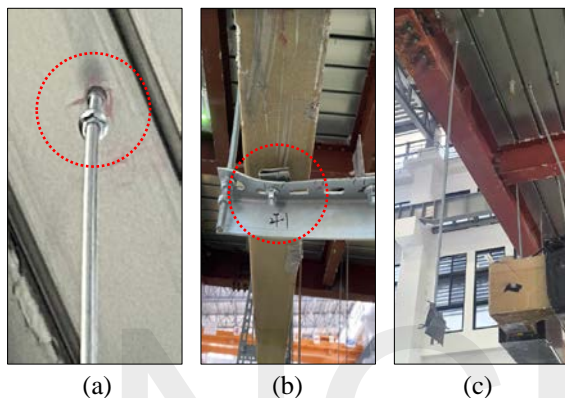
Figure 8. Failure of trapeze systems

Figures 8(a) and (b) show the failure of the trapeze rods and trapeze attachments with a corresponding PFA of 450 gal and 600 gal, respectively. The most serious damage to the trapeze systems was observed when the PFA exceeded 650 gal, as shown in Fig. 8(c).

Failure of the braced frames

Visible deformation of the grounded braced frames (Fig 9(a)) was recorded with a PFA of 300 gal and this caused slip between the line elements of the busway and the braced frames. Eventually the grounded braced frames were pulled out when the PFA exceeded 650 gal, as shown in Fig. 8(b).

(a) (b)
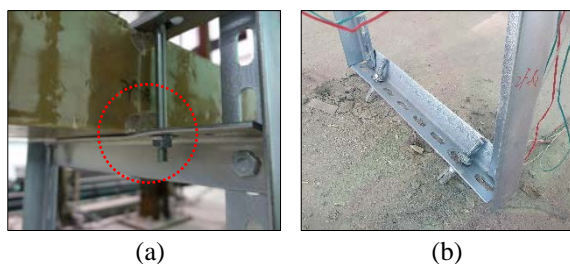
Figure 9. Failure of grounded braced frames

The failure patterns of the suspended braced frames were similar to those of the grounded braced

frames. Visible deformation and complete failure (Fig. 10) were observed with a PFA of 450 gal and 800 gal, respectively.

(a) (b)
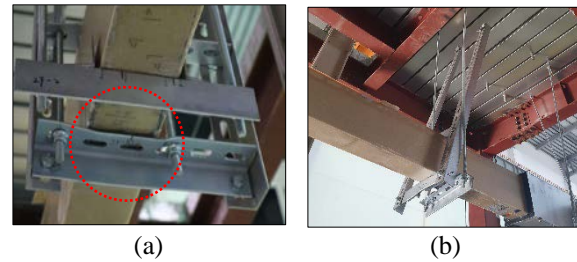
Figure 10. Failure of suspended braced frames

Failure of the line elements

Damage to the line elements (Fig. 11(a)) occurred primarily in the cast resin busway system when the PFA exceeded 200 gal. The worst case resulted in exposure of the conductor and was recorded with a PFA of 650 gal, as shown in Fig. 11(b).

(a) (b)

Figure 11. Failure of line elements

Conclusions

Past earthquakes have demonstrated that damage to suspended busway systems can lead to interruptions to post-earthquake operations of critical facilities. However, the current standards in Taiwan provide limited seismic design guidance for busway systems. This paper presents a full-scale shaking table tests of the busway systems and the observations from the tests.

References

American Society of Civil Engineers (ASCE), 2016, Minimum design loads for buildings and other structures, ASCE/SEI 7- 16, ASCE, Reston, VA.

Federal Emergency Management Agency (FEMA 273). (1997). "NEHRP Guidelines for the Seismic Rehabilitation of Buildings." FEMA 273, Applied Technology Council, Redwood City, CA, USA.

Federal Emergency Management Agency (FEMA 302). (1997). "NEHRP Recommended Provisions for Seismic Regulations for New Buildings and Other Structures: Part 1, Provisions." FEMA 302, Building Seismic Safety Council, Washington, DC, USA.

Seismic or Vibration Testing Requirements for Wind Energy Equipment

Bai-Yi Huang[1], Juin-Fu Chai[2], Fan-Ru Lin[3], Wei-Hung Hsu[1], Tzu-Chieh Chien[4], Zhen-Yu Lin[1] and Chin-Xin Wang[5]

黃百誼[1]、柴駿甫[2]、林凡茹[3]、徐瑋鴻[1]、簡子婕[4]、林震宇[1]、王鑑翔[5]

Abstract

Taiwan has been developing on-shore wind turbines for decades and aims to increase offshore wind power installed capacity owing to the abundant wind resources in the west coast. The first offshore wind farm in Taiwan started commercial operation at the end of 2019, which represents an important milestone of the energy policy transition in Taiwan. However, natural hazards such as typhoons or earthquakes pose constant threat. BSMI Taiwan cooperated with NCREE and announced an amended edition of the national standard CNS 15176-1-2018 on design requirements of wind turbines. The standard includes the seismic design requirements to improve the safety of wind turbine-supporting structures. However, it is also important to verify the seismic safety of the instruments inside the wind turbine or substation. This article reviews the seismic or vibration testing requirements of present design standards or operational documents of wind turbines issued by internationally recognized organizations, such as IEC, DNV GL, or IEEE.

Keywords: Wind turbine, Substation, Seismic qualification, Vibration test

Introduction

At each phase of the life cycle of a wind power plant, namely the development phase, construction phase, and operation phase, relevant inspection or verification need to be conducted in accordance with the specific standards provided by the accreditation body. In addition, prototype certification and component certification require the submission of qualified documents corresponding to the test or acceptance standards for design evaluation or manufacturing evaluation. The standards adopted depend on the accreditation or certification bodies. Commonly, standardization bodies can be classified into international (ISO, IEC, IEEE, etc.), regional (EU, CEN, CENELEC, etc.), or national (BSMI in Taiwan, BSI in Britain, API in the United States, BSH in Germany, NEK and PSA in Norway, etc.). By contrast, classification societies such as ABS in the United States, ClassNK in Japan, and BV and DNV GL have been dedicated to the field of maritime engineering for

a long time and transferred into certification bodies. Therefore, these classification societies established technical standards for ships and offshore structures (Norsk Industri AS, 2020).

This article reviews the requirements for the seismic or vibration testing of wind turbines described in the documents issued by the internationally recognized organizations, such as IEC, DNV GL, or IEEE. These requirements can be used as the reference materials to improve the safety of wind turbine in Taiwan to mitigate seismic hazards. In addition, some of the standards described sampling or testing methods for site investigation or liquefaction resistance, which are also helpful for improving the seismic safety of wind turbines. However, this article focuses on the requirements for shaking table testing.

IEC

The International Electrotechnical Commission

(IEC) is an authoritative international standards organization formed more than a century ago. IEC prepares and publishes a large number of international standards for all electrical, electronic, and related technologies and cooperates with several major standards development organizations, such as ISO, ITU, and IEEE. To facilitate international trade in equipment and services for use in renewable energy sectors, IEC established the IECRE system, which aims to offer a harmonized application around the globe for certification to standards relating to equipment used in solar PV energy, wind energy, and marine energy. The standards applied to wind energy are the IEC 61400 series, which are also the bellwether in the field of wind energy. The design requirement standards issued by the Bureau of Standards, Metrology and Inspection (BSMI, 2018) in Taiwan and some other national standardization organizations are based on IEC 61400-1 and harmonized according to local environmental conditions and needs.

The main IEC relevant standards that cover wind energy generation systems are the IEC 61400 series, which aim to ensure the wind turbines are appropriately engineered against damage from hazards within the planned lifetime. Among this series, the IEC 61400-1 standard specifies the basic design requirements for the subsystems of wind turbines, such as control and protection mechanisms, internal electrical systems, mechanical systems and support structures. It describes the assessment of earthquake conditions, and the seismic load should be carried out according to local codes (IEC, 2019). By contrast, the requirements related to seismic or vibration testing were described in the withdrawn IEC 61400-22, which was replaced with the deliverables for the wind sector (WE-OMC) contained in the IECRE. The IECRE provided the operational document OD-501, which specifies procedures for the type certification scheme, with respect to specific standards and other technical requirements; it is applicable for both onshore and offshore wind turbines and not limited to wind turbines of any particular size or type. The type certification scheme also covers prototype certification, including procedures related to the evaluation of the safety of operating a prototype to enable testing of a new wind turbine type (IECRE, 2018). To reduce the complexity of the certification procedure for the applicant, the document describes procedures for conformity assessment relating to design, testing, and manufacturing. Based on OD-501, the IECRE provided a series of sub-documents that defines the conformity assessment and certification of specified components of wind turbines by renewable energy certification bodies (RECB), which include the blade (OD-501-1), gearbox (OD-501-2), tower (OD-501-3), loads (OD-501-4), control and protection system (OD-501-5), and main electrical components (OD-501-7). Among these sub-documents, the requirements related to seismic or vibration tests are described in OD-501-7, and the applicable standards, scopes of evaluation

for specific electrical components are shown in Table 1 (IECRE, 2019).

Table 1. Design evaluation requirements

component	Standard	Scope of evaluation
Generator	60034 series	• heat-run test results (converter operated, if applicable), • other type/prototype test results, • vibration test results as applicable, • routine test plan, • bearing rating life calculation (ISO 281), • cooling system, • cable connection and interfaces, • installation and environment, • protection and earthing • direct drive generators shall be documented according to an agreed design basis as IEC • 60034 does not account for the special issues related to direct drives systems.
Converter	62477-1 or 61800-4 (if Ur > 1kVa.c.)	• EMC according to IEC 61800-3 or equivalent, • IEC type and routine tests such as protective bonding impedance test, impulse • withstand voltage test, touch current measurement, thermal performance test, etc., • insulation design (including environmental categories according to IEC 60721, • overvoltage categories, clearance and creepage distance, etc.).
Transformer	60076 series	• type and routine tests, • vibration test, • environmental testing, • cooling system, • installation and earthing • protection and monitoring equipment
Switchgear	62271 series	The switchgear arrangement for the main power line between generator and grid and its ratings shall be compared with assumptions made in the design basis. For high-voltage switchgear internal faults testing, pressure relief measures and their possible influence on the installation environment shall be checked in addition.

Among the applicable standards listed in Table 1, there are no environmental test requirements in the IEC 60034 series. The vibration test results should be the vibration measurement results induced by the operation of rotating electrical machines; IEC 60076-16 is the applicable standard for dry-type or liquid-

immersed transformers used in wind turbines. The climatic and environmental test requirements shall follow the service conditions specified in IEC 60076-11 (dry-type transformers), and IEC 60076-11 referred to IEC 60068-3-3 for seismic tests; IEC 62271 series are standards for high-voltage switchgears and controlgears, and the sub-documents IEC 62271-207, -210, and -300 provided the requirements of seismic qualification for high-voltage gas-insulated switchgear assemblies, metal enclosed and solid-insulation enclosed switchgear and controlgear assemblies, and alternating current circuit breakers, respectively. These standards referred to the IEC 60068 series for seismic or vibration testing procedures; no environmental testing requirement is described in IEC 62477-1 and 61800-4 (which was replaced by IEC 61800-2) for converters.

DNV (formerly DNV GL)

Det Norske Veritas (DNV) and Germanischer Lloyd (GL) are both long-established classification societies, and they merged in 2013. They had accumulated maritime engineering experience for more than a century and delivered classification, certification, and advisory services for relevant industries. Recently, DNV had built a complete set of standards and recommended practices for wind power plants, including turbines, bottom-fixed and floating support structures, cables, and offshore substations. Therefore, DNV and IEC are the leading organizations that have published the most extensive documents related to offshore wind turbines. Nowadays, not only offshore but also onshore wind power assets are included in the scope of the certification service provided by DNV, which are shown in Figure 1 and 2.
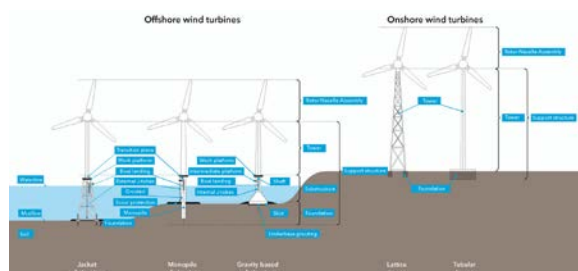
Figure 1. Definition of offshore and onshore wind turbine components (DNV GL, 2015)
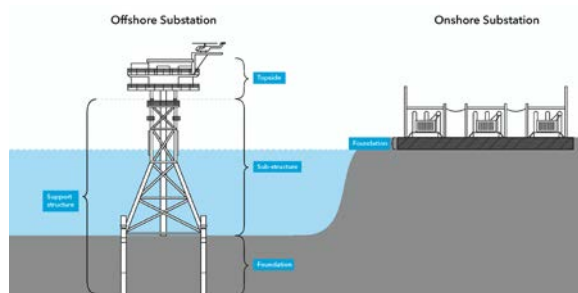
Figure 2. Definition of offshore and onshore substation components (DNV GL, 2015)

The service document system is organized according to a three-level document hierarchy. Service specification (SE) provides principles and procedures related to certification and verification services and presents the scope and extent DNV GL's services. Standard (ST) issued as neutral technical standards to enable their use by national authorities, as international codes and as company or project specifications without reference to DNV GL's services. Recommended practices (RP) provide DNV GL's interpretation of safe engineering practice for general use by the industry (DNV GL, 2018).

DNVGL-ST-0145 (2020) provides design requirements for offshore substations, including structural design, electrical design, among others. Major electrical equipment shall comply with the corresponding requirements, such as IEC 62271-203 (high voltage switchgear), IEC 62271-200 (medium voltage switchgear), IEC 62271 series (switchgear in general), IEC 60076 series (transformer in general), IEC 60076-15 (gas insulated transformers), and IEC 60099-4 (surge arresters). Most of the standards referred to IEC 60068 series as the seismic or vibration testing method as well.

DNVGL-ST-0076 (2015) provides design principles and technical requirements for electrical installations in onshore or offshore wind turbines. It states in Chapter 11 that the electrical equipment for measurement and control use and its accessories for wind turbine applications shall comply with the part of IEC 60068 series, and the parameters of the tests required for a specific product shall be determined on a case-by-case basis depending on the product and its use. Further, the standards referred for fire hazard (IEC 60695) and laser products (IEC 60825-1) require vibration tests in accordance with IEC 60068-2-6.

Although DNVGL-RP-0585 (2021) is a recommended practice for seismic design of wind farms and focuses on site investigation and soil dynamic analysis, seismic qualification for components is not required in the document. As an internal summary, the design or certification requirements for wind turbines issued by DNV basically refer to other international standards or specifications because DNV and GL were formerly classification societies. In terms of electronic or electrical equipment, IEC 60068 series refers to vibration tests or seismic qualification.

Other organizations

The standards related to wind turbines issued independently by the International Organization for Standardization (ISO) include the blade coating inspection series (ISO 19392), mechanical vibration (ISO 10816-21:2015), and condition monitoring and diagnostics of wind turbines (ISO 16079), etc., and the

joint standard IEC 61400-4:2012 for gearboxes with IEC. Although there are no relevant standards particularly for seismic design or testing of offshore or onshore wind turbines. However, some seismic design requirements for offshore wind turbine-supporting structures given by other specifications, such as DNV-OS-J101, referred to ISO 19901-2 as the basis for offshore structural design methods, although there is no description on vibration or seismic testing as well.

The standards related to wind turbines issued independently by the Institute of Electrical and Electronics Engineers (IEEE) include personnel safety (IEEE Std 2760-2020), acoustic noise measurement techniques (IEEE Std 2400-2016), or technical supervision codes for rotor systems (IEEE Std 1834-2019), and the joint standard IEC/IEEE 60076-16-2018 for transformers with IEC. In the aspect of electrical power systems applied to offshore facilities, IEEE provided IEEE Std 1662 (IEEE, 2016) for power electronics (PE), which referred to IEC 60068-2-6 as the basis of the vibration test method. Furthermore, for the PE installed in seismic active areas and emergency standby power systems, it is suggested in IEEE Std 1662 to withstand physical shocks and multi-axis accelerations as specified in the International Building Code (IBC) or other applicable local building codes. IBC states in Section 1705.14.2 that the nonstructural components shall be qualified by analysis, testing, or experience data specified in Section 13.2.1 of ASCE 7 (ICC, 2021), and ASCE 7 in Section 13.2.6 required that the seismic qualification shall be in accordance with the nationally recognized testing standard procedure, such as ICC-ES AC156 (ASCE, 2022). In addition, IEEE Std 693-2018 is the authoritative standard for the seismic design of onshore substation.

Conclusions

This article reviewed the design requirements or project certification specifications for wind turbines. In the aspect of improving the structural integrity and reliability, the effect of earthquakes is usually taken into consideration for the load combination with other environmental conditions, such as wind, waves, and currents, during the structure design phase. However, an earthquake is considered as a regional hazard; therefore, the relevant requirement should be given by the local seismic code. Most of the reviewed specifications lay stress on site inspection to identify the earthquake or liquefaction hazards. There are not too many detailed instructions on the seismic qualification of equipment. Further, to identify the practical measures, this article reviewed the relevant standards specified or referred in the guidance documents or standards. It turns out that the standards of the specified equipment or component provide the testing requirements or acceptance criteria and refer to other standards for detailed testing or qualifying procedures. Commonly, the environmental test

methods referred by the standards are IEC 60068 series, especially the IEC 60068-2-6 for the sinusoidal vibration test method and IEC 60068-3-3 for the seismic test method. These standards provided the method to conduct the seismic or vibration tests; however, no specific testing parameters are given. It is necessary to determine the suitable parameters based on the local seismic and structural characteristics through analysis or simulation.

References

Norsk Industri AS. (2020). Overview of offshore wind standards and certification requirements in selected countries (Report No.: 2020-1194, Rev. 01). DNV GL.

BSMI. (2018). Wind turbines − Part 1: Design requirements (CNS 15176-1).

IEC. (2019). Wind energy generation systems - Part 1: Design requirements (IEC 61400-1).

IECRE. (2018). Type and Component Certification Scheme (OD-501).

IECRE. (2019). Conformity assessment and certification of Main Electrical Components by RECB (OD-501-7).

DNV GL. (2015). Design of electrical installations for wind turbines (DNVGL-ST-0076).

DNV GL. (2018). Certification of floating wind turbines (DNVGL-SE-0422).

DNV GL. (2020). Offshore substations (DNVGL-ST-0145).

DNV GL. (2021). Seismic design of wind power plants (DNVGL-RP-0585).

DNV GL. (2014). Design of Offshore Wind Turbine Structures (DNV-OS-J101).

DNV GL. (2015). Project certification of wind power plants (DNVGL-SE-0190)

IEEE. (2016). IEEE Recommended Practice for the Design and Application of Power Electronics in Electrical Power Systems (IEEE Std 1662-2016).

International Code Council. (2021) International Building Code (IBC).

American Society of Civil Engineers. (2022). Minimum Design Loads and Associated Criteria for Buildings and Other Structures (ASCE/SEI 7-22).

Parametric Analyses of Strength–Energy Dissipating Hybrid Seismic Stud Columns

Sheng-Jhih Jhuang[1], Ker-Chun Lin[2], Kai-Ning Chi[1], Chen-Wei Syu[3], and Chui-Hsin Chen[4]

莊勝智 [1]、林克強 [2]、紀凱甯 [1]、許宸唯 [3]、陳垂欣 [4]

Abstract

In past cases of applying seismic stud columns (SSC) to structures, Japanese design procedures are often adopted that considered SSCs solely as dampers. In order to achieve the design purpose of dampers, a nonlinear energy-dissipation capability is developed with as little deformation as possible. Energy dissipation is provided by the web of the H beam, which is expected to develop shear yielding. According to Taiwanese design codes, these energy-dissipating SSCs should not be considered as part of the seismic-force-resisting system. In this study, the SSC's shear yielding strength, the lateral stiffness of the SSC segment, and the rotational stiffness of the connecting beams are established based on the results of finite-element analyses and by considering parameters of SSC section size, material strength, SSC height, and length of the SSC dissipating core. By combining the concept of an interstory drift requirement in the code, this paper proposes a new concept for designing hybrid-type SSCs by controlling the SSC yielding displacement. Based on comprehensive analysis results, recommendations for limit equations of the flange to core web thickness ratio and the core height to SSC height ratio of 0.2–0.6 are proposed for stable shear yielding performance of SSCs.

Keywords: seismic stud column, shear strength, yielding displacement

Foreword

As Taiwan is situated in the Circum-Pacific seismic belt, it is highly prone to high-intensity earthquakes occurring fairly frequently. After the Chi-Chi earthquake, in view of the fact that earthquakes cause serious damage to buildings and pose a great threat to life and property, various shock-absorbing and energy-dissipating elements have been developed and applied to buildings in Taiwan to improve their seismic performance and enhance comfort. In response to different requirements of seismic performance and structural design, an increasing variety of energy-dissipation elements have emerged, of which the seismic stud column (SSC) is one type.

The SSC is a short column arranged in the middle of the span between two structural columns and only one story height. In general, in the design of SSC, the shear force and bending moment caused by horizontal seismic force are mainly considered and not the axial force acting on the SSC. The SSC together with a moment-resisting frame can resist the seismic force, and the SSC acts as a structural fuse that controls horizontal displacements of the structure. According to the current design of the energy-dissipating SSC, it cannot be regarded as a member that participates in strengthening the structural system because the SSC enters the yield phase very early in order to meet the displacement requirements of the seismic code. Under a statutory seismic force, the SSC remains elastic, provides strength, and controls lateral deformation. However, when the seismic force exceeds the statutory seismic force, the SSC enters a yield phase and facilitates energy-dissipation damping. This study aims to design a hybrid-type SSC that can contribute to the strength and stiffness of a frame during application.

Analytical Model

To avoid premature failure of nonstructural members, which affects the usability and safety of buildings, the relative lateral interstory drift of structures under moderate and small earthquakes is limited to 0.005 rad. According to the design principle that the structure must maintain elastic behavior under medium and small earthquakes, a frame meeting this displacement limit is considered to have met the strength design considerations for medium and small earthquake forces. This study achieves the member strength requirements by controlling the interstory

---

[1] Research Assistant Fellow, National Center for Research on Earthquake Engineering
[2] Research Fellow, National Center for Research on Earthquake Engineering
[3] Master, Department of Civil Engineering, National Yang Ming Chiao Tung University
[4] Associate Professor, Department of Civil Engineering, National Yang Ming Chiao Tung University.

drift of the SSC. To control the deformation of the SSC during yielding, the lateral elastic stiffness and shear yield strength of the SSC in the frame need to be accurately estimated. The lateral elastic stiffness can be divided into two components: the lateral stiffness of the SSC and the elastic rotational stiffness of the top and bottom boundary beams at the connections. Considering the rotation of the boundary beam and assuming this beam as a rigid body with the deformation mechanism in the depth of the beam, the interstory drift can be expressed by:

$$\theta_s^* = \rho(\frac{V_e}{k_{SSC}H_{SSC}}) + \frac{\Sigma(V_e H_s)}{k_{\theta b}} \quad (1)$$

The interstory drift of a structure under seismic force specified by the displacement limit of the code is the limit θ_u of the yielding interstory drift of the SSC, that is, $\theta_s^* \geq \theta_u$.

For subsequent analysis and research, two finite-element analysis models are established in this study to explore the stiffness and strength of the SSC. The first type is the SSC model with both ends fixed (hereinafter referred to as SSC-f). The model is shown in Figure 1. For the material settings of this model, only the web material of the core segment is set to its minimum yield strength, while the other materials are set to remain elastic. The following four design parameters are varied for the analysis: (1) the ratio of height of the core segment to that of the whole segment is 0.1-0.9; (2) the depths of the SSC are set to 400 mm and 800 mm; (3) the flange thickness, t_f, is 15-30 mm; and (4) the web thickness of the core segment, t_{wc}, is 8-24 mm. A lateral displacement is given to the top of the SSC in the analysis such that the core segment begins to shear yield. The stiffness of the SSC is calculated analytically from the linear elastic results of the relationship between the shear of the SSC and the lateral displacement; this will be compared with the estimated value. Furthermore, from the analytical value of yield strength under nonlinear conditions, the initial yield coefficient (λ) of shear force under each parameter combination can be calculated.
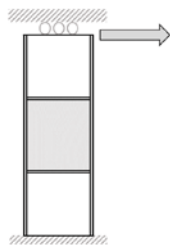
Fig. 1 SSC model with both ends fixed.

The second model type is a cross-frame model with boundary beams; they can be categorized as a cross-frame model including a boundary beam with fixed top and bottom ends (hereinafter BB-f, as shown in Figure 2(a)) and a cross-frame model including a boundary beam and structural columns (hereinafter

BB-c, as shown in Figure 2(b)). Both models contain boundary beams with half the height of the SSC segment above and below the boundary beam. The sections of the SSC at the top and bottom connected to the boundary beam are identical. The boundary beam of the BB-c model is connected to the two structural columns, and the column height above and below the boundary beam is half the floor height. A minimum yield strength is set for the web material of the SSC core segment; the web of the connection between the SSC and the boundary beam is set as a rigid body, while the rest of the materials are set to remain as elastic. The variable parameters are as follows: (1) the depth of the SSC (d) is set to 400 mm and 800 mm and (2) the depth of the boundary beam (d_b) is 400-1000 mm. Assuming half the height of the SSC is an inflection point, one unit of the opposite horizontal force is applied to the top and bottom SSCs during the analysis. The rotational stiffness can be calculated from the rotational angle of the boundary beam, and it is compared with the estimated value.
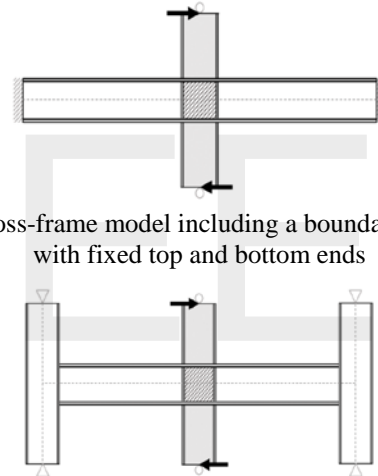
(a) Cross-frame model including a boundary beam with fixed top and bottom ends

(b) Cross-frame model including a boundary beam and structural columns

Fig. 2 Cross-frame model with boundary beams.

To estimate the lateral stiffness of the SSC, the equivalent single-member method proposed by Hsu *et al*. (2017) is used. Assuming that the shear force in the SSC is a constant value and the bending moment changes linearly, the overall stiffness of the member originally composed of multiple sections is expressed as the equivalent member of a single section and the contributions of shear force and flexural deformation are considered simultaneously. The rotational stiffness of the boundary beam is derived from the bending moment caused by the SSC shear force at the center of the boundary beam, and it is assumed that no displacement or rotation occurs at the beam-to-column connection. To obtain an accurate stiffness estimation, in addition to the deflection deformation in the beam, the contribution of the shear deformation (Orosz, 1970) is also taken into account by the energy method.

Analysis Results and Discussion

1. Stiffness

SSC-f model

In the comparison of stiffness of the SSC, the lateral stiffness estimated by the equivalent member method is compared with the analysis results for the SSC-f model, and the stiffness error e_{k1} is calculated. When the flange thickness t_f is 15 mm and 30 mm, the changes in the length ratio of the core segment and the ratio of the web thickness of the connecting segment to the core segment are as shown in Figures 3(a) and (b), respectively. The value of e_{k1} is affected by t_f, d, and γ_{Av}. The smaller the value of d or t_f, the higher the inaccuracy of stiffness estimation. By contrast, the estimates with γ_{Av} equal to 1.0-1.2 are closest to the analytical values and are less affected by the flange thickness. As γ_{Av} increases, the error decreases. When the flange thickness is 15 mm, the partial error curves for γ_{Av} equal to 2.0 and 3.0 are lower than -10%. The parameter ranges that do not meet the ±10% error are approximately $t_f \leq 20$, $\gamma_{Av} \geq 2.0$, and $d \leq 0.6$, which may be applied in the actual design and application. To increase the accuracy of the yielding displacement estimation of the SSC, a stiffness adjustment coefficient m_k (such as Equation (2)) is determined to adjust the stiffness k_{eq} estimated by the equivalent member method. The relationship between the adjusted stiffness k_{SSC} and the adjustment coefficient m_k is given by:

$$m_k = [0.005(\gamma_{Av} - 1)(40 - t_f)(0.9 - \delta) + 1] \geq 1.0 \quad (2)$$

and:

$$k_{SSC} = m_k k_{eq} \quad (3)$$
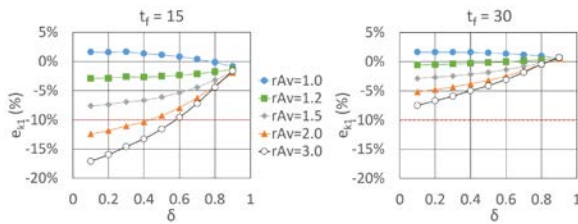
Fig. 3 Error distributions of the unadjusted stiffness estimate of the SSC.

The distributions of the adjusted stiffness error e_{k1} are shown in Figure 4. It can be seen that the adjusted errors are all within ±5%.
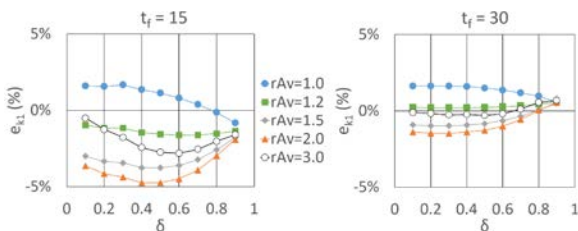
Fig. 4 Error distributions of the adjusted stiffness estimate of the SSC.

BB-f and BB-c models

The rotational stiffness of the boundary beam is obtained in the analysis of BB-f and BB-c models. The estimated stiffness $k_{\theta b(pred.)}$ is compared with the analytical value to calculate the estimated error. Table 1 shows the changes in stiffness and their errors under varying SSC depths d and structural column depths d_b, where $k_{\theta b(anal.)f}$ and $k_{\theta b(anal.)c}$ are the stiffness analysis values of BB-f and BB-c models, respectively, and e_{k2}^f and e_{k2}^c are their errors, respectively. It can be seen that the estimated value is quite consistent with the analytical value of the BB-f model with the same assumed boundary conditions, and the errors are all positive and within 10%. It is also consistent with the analytical value of the BB-c model under actual boundary conditions, and the maximum error is only 17.2 %. Based on the overestimation of stiffness, the consideration of yielding displacement is conservative. This study concludes that the original stiffness calculation formula can be used to estimate the rotational stiffness of the boundary beam.

Table 1 Comparison of estimated and analytical rotational stiffnesses of boundary beams.

d (mm)	d_b (mm)	$k_{\theta b(pred.)}$	$k_{\theta b(anal.)}^f$	e_{k2}^f	$k_{\theta b(anal.)}^c$	e_{k2}^c
400	400	234013	213003	9.9%	199737	17.2%
	1000	1610784	1586914	1.5%	1438746	12.0%
800	400	266749	248078	7.5%	230461	15.7%
	1000	1807363	1815591	-0.5%	1626101	11.1%

2. Strength

The yielding shear force and λ value under different parameter combinations can be obtained from the SSC-f model. Figure 5 shows the change in the λ value when the web thickness of the core segment equals 16 mm. The λ value is almost constant within the 'stable interval' of the certain height ratio δ of the core segment. When δ is greater than a certain limit, the shear force decreases because of the increase in the deflection effect of the web in the core segment. In addition, in the array analysis, λ has a sudden increase when $\delta = 0.1$. To stabilize the web shear force yielding in the core segment and avoid the deflection effect, the minimum δ of the SSC is 0.2. The acceptable λ is set as the λ corresponding to $\delta = 0.2$, and the slippage is not more than 0.02; the allowable analytical values are indicated by the solid points in the figure. Figure 6 shows the acceptable maximum δ as δ^M at two SSC depths and the change in $\gamma_t = t_f / t_{wc}$. This figure shows the increase in γ_t of the SSC, which can increase the allowable length ratio of the core segment. Furthermore, linear regression is performed on δ^M under different d values to obtain the allowable

δ^M under specific γ_t values and d values, as given by:

$$\delta^M = \frac{\gamma_t}{5} + \frac{3d}{8000} + 0.05 \tag{4}$$

In other words, if δ and d of the SSC are known, then the allowable minimum γ_t is calculated by:

$$\gamma_t^m = 5\left(\delta - \frac{3d}{8000}\right) - 0.25 \tag{5}$$
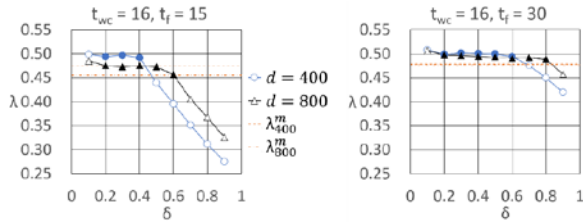
Fig. 5 Analysis values of the shear initial yielding coefficient.
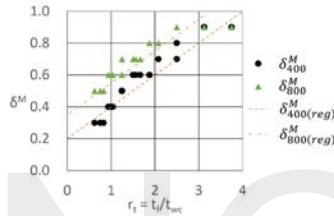
Fig. 6 Allowable maximum length ratio distribution of the core segment.

Table 2 Variation of $\bar{\lambda}$ with the thickness of the flange and web of the core segment.

		t_{wc}				
		8	12	16	20	24
t_f	15	0.493	0.483	0.471	0.467	0.462
	20	0.502	0.491	0.481	0.475	0.471
	25	0.508	0.497	0.489	0.484	0.476
	30	0.513	0.5	0.493	0.488	0.484

From the analysis results, the effect of SSC depth on λ is only within 0.02 and can be ignored, so the average of $\bar{\lambda}$ in the stable interval when d = 800 mm is taken as $\bar{\lambda}$. The variation of $\bar{\lambda}$ with the flange thickness t_f and web thickness t_{wc} of the core segment is listed in Table 2. As the thickness ratio γ_t decreases, the $\bar{\lambda}$ value also tends to decrease. Owing to conservative considerations, the four combinations with γ_t approximately 1.0 in the parameter combination (gray items in Table 2) are used as the benchmark, and the average of $\bar{\lambda}$ of the four combinations is taken as the initial shear force yielding coefficient of the SSC $\lambda \approx 0.48$. The shear yielding strength of the SSC is $V_e = 0.48 F_{yc} A_{vc}$. When the web of the core segment is yielding, the flanges of the SSC also provide lateral strength. The yield strength suggested in this paper is higher than the yield strength $0.4 F_y A_v$ of the commonly used initial steel plate. Compared with the results of this study, within the range of design parameters in this analysis, the shear

initial yielding strength obtained by considering the contribution of the flange will be approximately 1.16-1.28 times higher than the theoretical shear strength of the steel plate.

Conclusions

This study proposed design method assumptions for a hybrid type of seismic stud column (SSC) and attempted to perform stiffness verification and strength analysis of the SSC based on the displacement limit of the code. The analysis results showed that the stiffness of the SSC calculated from the equivalent stiffness was overestimated when γ_t is large or δ is small. The stiffness error can be corrected by the stiffness adjustment coefficient and controlled within ±5%. The rotational stiffness of the connected beam derived from the boundary conditions assuming fixed beam ends was reasonably accurate. In the analysis results for yield strength, it was found that when the ratio γ_t of the web thickness to the flange thickness was small, the web of the energy dissipation segment that was originally expected to exhibit shear yield may instead undergo flexural yielding, resulting in strength decrease. This study proposed the minimum limit of γ_t to avoid deflection of the web of the core segment in the section design with the SSC depth of 400-800 mm and a thickness ratio of the flange to the core segment web of 0.625-3.75. In addition, this study suggested the appropriate length ratio range of the SSC to be 0.2-0.6. From the results of finite-element analysis, it was recommended to adopt $V_e = 0.48 F_{yc} A_{vc}$ to estimate the yielding strength of the shear yielding-type SSC, wherein the shear yielding strength of the SSC obtained by considering the contribution of the flange will be approximately 1.16-1.28 times higher than the theoretical shear strength of the steel plate.

The structural interstory drift (for a conservative value 0.005 rad) under a specified seismic force generated based on displacement limits of the code is used as the requirement of the yielding interstory drift of the SSC. Combined with the estimation of stiffness and strength, $\theta_s^* \geq \theta_u$ can be used to successfully analyze the strength requirements of the SSC in the preliminary design stage.

References

Construction and Planning Agency, Ministry of the Interior (2011), "Seismic Design Specifications and Commentary of Buildings".

Hsu, C. H., Li, C. H., Chin, P. Y., and Tsai, K. C. (2017), "Seismic Design and Analysis of Steel Frame with Steel Panel Dampers", Structural Engineering, Volume 32, Issue 2, Pages 5~34.

Ivan Orosz (1970), "Simplified Method for Calculating Shear Deflections of Beams", U.S.D.A Forest Service Research Note.

Structural Vibration Monitoring of Offshore Wind Turbines in Taiwan

Kung-Chun Lu,[1*] James Chang,[1] Yu-Shu Kuo,[2] Wei-Chen Tseng,[2] Harris Lee,[3] Yu-Chieh Wang,[4] Hao Chang[4]

盧恭君 [1*]、張心寧 [1]、郭玉樹 [2]、曾韋禎 [2]、李宏道 [3]、王昱傑 [4]、張皓 [4]

Abstract

Monopile foundations with grout connections have been widely used for the supporting structures of offshore wind turbines. However, the offshore wind power industry has recently found that the existing design method for the tower transition piece may cause the tower structure to collapse. This implies that the structural characteristics and behavior of the transition piece are greatly affected by the performance and safety (life) of the supporting structure of offshore wind turbines. This study is part of the second phase of the National Energy Project (NEP-II) and investigates the issues of structural behavior and fault features of the transition piece on the Swancor offshore wind turbine, which is located in the outer sea area of the Longfeng Port, Miaoli. Vibration response monitoring of the supporting structure of the offshore wind turbine is accompanied by signal analysis to obtain the structural behavior and then understand the damage mechanism. Furthermore, the study reviews literature from countries with advanced wind energy development, organizes the research results related to the transition piece, and applies them to this study. In this paper, an example of vibration response monitoring of an offshore wind turbine is introduced, the structural description and damage of the transition piece are elucidated, and related literature is reviewed.

Keywords: Offshore wind turbine, transition piece, grout.

Introduction

Monopile (MP) foundations with grouted connections (GC) are widely used not only in the oil and gas industry but also in the supporting structures of wind turbines. They provide an efficient solution for joining the pile driven into the seabed and the sub-part of the supporting structure. However, since late 2009, unexpected settlements of the transition piece (TP) relative to the MP have been reported in many of the plain-pipe GCs for offshore wind turbine generators constructed before 2010. This has increased the likelihood of loss of operation and structural failure and resulted in extensive remedial work to relieve such GCs from accumulating damage. This would have a direct impact on the performance of offshore wind turbines in the future in Taiwan. Therefore, timely detection of these problems is vital.

From the aspect of structural health monitoring (SHM), the loss of functionality of GCs can be detected theoretically. However, research related to this specific area is limited. In this study, methods and strategies based on continuous identification of natural frequencies and transfer functions of the wind turbine structure are proposed for estimating the loss of functionality of GCs.

This study briefly presents a literature review, investigates the mechanics of GCs, and conceptually describes the development of the proposed method for monitoring the robustness of GCs.

Monitoring System

With the increasing demand for wind power, the effective management of wind turbines in service lays the foundation for abundant and uninterrupted energy supply from wind. An integral SHM system for

[1] National Center for Research on Earthquake Engineering
[2] Department of Hydraulic and Ocean Engineering, National Cheng Kung University
[3] Formosa 1 Wind Power Co. Ltd.
[4] System Access Company Ltd.

offshore wind turbines was proposed by Rolfes *et al.* (2007), who also introduced the concept of safety monitoring for support structures of wind turbines.

The offshore wind turbine on which the team performs instrumentations is located at the Longfen Port, Miaoli, and has an MP foundation with a GC. Further details about the sensing system, sensor instrumentation, measurements, and the time signal are as follows.

The sensing system, supported by SystemAccess, consists of a data logger set that includes a controller module (CANFX/L-DCB8) and a DAQ module (CANSASflex-DCB8). CANFX/L-DCB8 is a real-time embedded system that coordinates all peripherals and the DAQ module. CANSAflex-DCB8 is an 8-channel DAQ module with a measurement circuit and sensor powering system. The sampling rate was software adjustable and was set to 200 Hz in this study. The controller and DAQ modules were connected to serve as a data logger, as shown in **Figure 1**.

Figure 1a. Data logger (controller).

Figure 1b. Data logger (DAQ module).

The vibration transducer is a MEMS accelerometer (SDI2210-002), which is a high-gain accelerometer with a small package and requiring 8–32 V DC power supply. A total of seven accelerometers were applied in this measurement. A biaxial inclination sensor (CR2101), which is a digital sensor communicating via CAN Bus, and the setup of seven accelerometers are shown in **Figure 2** and **Figure 3**, respectively. All the above equipment was adopted as the structural monitoring system of the

wind turbine to detect the structural vibration responses of the TP and layout of the support structure of the wind turbine.

The entire sensing system is coordinated with the controller, offering the functions of data storage and communication. The equipment used in this study is listed in **Table 1**.

Figure 2. Accelerometer and tilt sensor.

To identify the modal parameters and to investigate the tower motion and the interactions between the soil and foundation in the future, the measurements were instrumented at each location to record the responses of the whole structure.
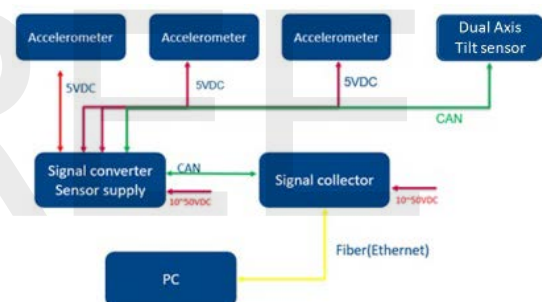
Figure 4. Framework of the monitoring system.
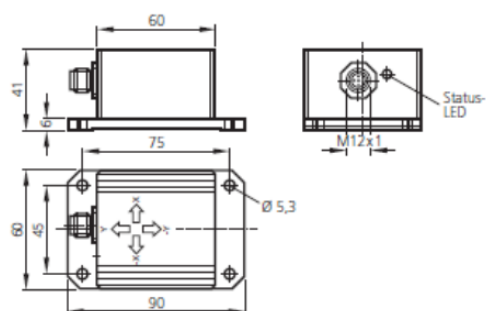
Figure 3. Schematic of the tilt sensor and sensing direction.

The entire system framework is shown in **Figure 4**, including sensors (accelerometers and tilt sensor), the data logger (controller and DAQ modules), and the monitoring screen (PC). Based on this application scenario, the accelerometers were powered by the data logger with 5 V DC; the tilt sensor was a digital sensor

with a CAN Bus in which data transmission and powering are achieved with the data logger. The two modules of the data logger, *i.e.*, controller and DAQ, were powered by the site resources with 10–50 V DC, and the feedback was recorded via the Internet through a fiber wire. A PC is linked and data are downloaded through the Internet with host server software (IMC Link and IMC Studio).

Table1. equipment list		
Items	Equipment name	Number of instruments
1	Data collection host BUSFX-2	1
2	Analog signal processing module CANFX/L-DCB8-350	1
3	Single axis high precision accelerometer SDI 2210-002	7
4	Two-axis high precision tilt meter CR2101	1
5	Server side: data receiving software	1 set
6	Server end: data receiving equipment (installation space, power, network routing owner)	1 set

The sensor layout depends on the structure's dynamic physical and vibration features. The objective was to focus on the damage features of the GC, and the layout concept used to achieve this objective. The details of the sensor layout are described as below.

Figure 5 shows the overall measurement configurations. Along the tower in the vertical direction, three elevations are selected to be monitored: the top of the tower, called the platform; the first working plate, which is approximately 2.8 m from the top; and the bottom of the tower, which is 14.8 m from the top.

at the top of the tower, dual-axis accelerations were detected by two accelerometers installed here.

At the first working plate, both a dual-axis tilt sensor and a data logger were installed here with a power supply of 110–240 V AC and internet (fiber).

At the bottom of the tower, this position is the connection of the TP and MP, also called GC. The vibrations of both the TP and MP were detected, with tri-axial vibration on the MP and bi-axial vibration on the TP. The vertical-axis vibration was added to detect the tilt of the MP.

Investigation of Grout Connections

The GC, which transfers the bending moments from the TP to the MP, is a crucial linkage component in offshore applications. The interface behavior of the GC is numerically modeled using a finite-element method (Kim *et al*., 2014), which shows that the maximum deformation of the GC takes place at the bottom of the pile because of the yielding of the pile.

The environmental scenarios, including load characteristics (Tziavos, 2006), and ambient conditions (Schaumann, 2017) can affect the damage behavior of the GC. The scour and grout damage were well introduced by Gupta (2015), who particularly modeled elastomeric bearings as a retrofit measure to provide a foundation with a high load-carrying capacity in the vertical direction.
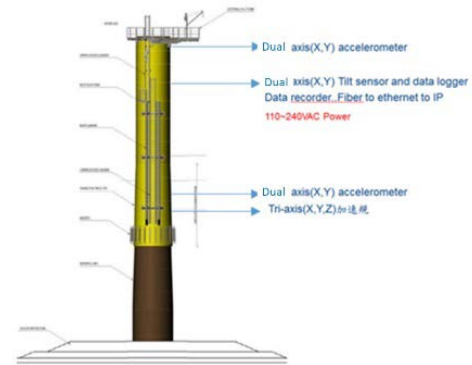
Figure 5. Measurement configuration.

Moreover, to achieve a more robust platform foundation, considerable research has been conducted to clarify the mechanism of GCs through experimental tests during the 1970s to 1980s, especially for offshore engineering structures. The work mainly focused on the effect of crucial parameters of GCs and associated structural components, such as the grout strength, shear-key height and spacing, ratio of diameter to thickness of the piles, outer sleeves, and grout annulus, on the ultimate capacity of the connection. A typical design of an energy converter with a height of 80 m and capacity of 80 GW/year is shown in **Figure 6**. The experimental testing can be grouped into four categories (Dallyn, 2015): static axial loading, pre-stress, dynamic axial loading, and bending/gapping. However, the quantification of the performance of the GCs does not necessarily indicate an understanding of the potential loss of functionality of a GC in offshore applications.
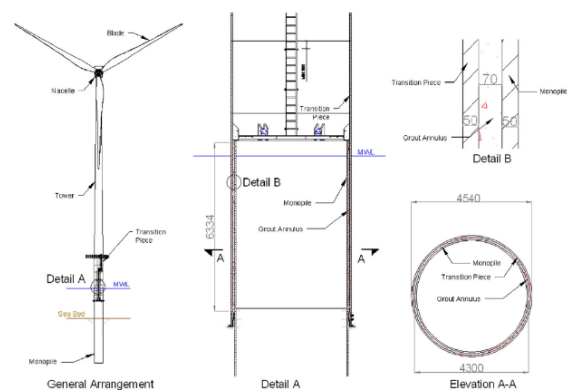
Figure 6. Typical design of grouted connections for an offshore wind turbine.

A recent review of technical literature related to the behavior of GCs has highlighted a paucity of research in this area, with historical experimental testing on GCs predominately focusing on the above-mentioned four categories. From the viewpoint of SHM, although comprehending the intrinsic mechanism of GCs and the pattern of loads acting on structures is important, studies should first prioritize conceiving a method to retrieve the fundamental parameters of the offshore wind turbine, such as natural frequencies and vibration modes, from the measurement data. The following section broadly addresses the issue.

Conclusions

The study conducted the following:

(1) Established a structural health monitoring system on an offshore wind turbine;

(2) Presented an overview of the research on grout connections; and

(3) Proposed methods and strategies for evaluating the GC performance.

This project is still in process and the concepts in this study should be verified in the future. Accordingly, the future works are as follows:

1. Evaluation of the proposed method;

2. Verification of the vibration monitoring system; and

3. Realization of the behavior of grout connections on the basis of monitored data.

References

Ki-Du Kim, International Journal of STEEL STRUCTRES, "Interface Behavior of Grouted Connection on Monopile Wind Turbine Offshore Structure," Jan. 13, 2014.

Tziavos, "Grouted connections on offshore wind turbines," Research at Birmingham, May 2016.

Peter Schaumann, 14th Deep Sea Offshore Wind R&D Conference, "Fatigue behavior of grouted connections at different ambient conditions and loading scenarios," Jan. 2017.

Shashank GUPTA, SECED 2015 conference, "Condition monitoring of offshore wind turbines with scour and grout damage in monopole foundations," July 2015.

Paul Dallyn, Structures, "Experimental testing of grouted connections for offshore substructures: a critical review," Mar. 2015.

Michael Link, Proceedings of the 9th International Conference on Structural Dynamics, "Structural health monitoring of the mono-pile foundation structure of an offshore wind turbine." 2014.

R Rolfes, S Zerbst, G Haake, J Reetz, J P Lynch. Integral SHM-system for offshore wind turbines using smart wireless sensors. Proceedings of the 6th International Workshop on Structural Health Monitoring, Stanford, CA, September 11-13, 2007.

Seismic Behavior of High-Strength Kernel-confined Columns Under High Axial Load

Ker-Chun Lin[1], Jun-Kai Huang[2], Kai-Ning Chi[3] and Sheng-Jhih Jhuang[3]

林克強 [1]、黃竣楷 [2]、紀凱甯 [3]、莊勝智 [3]

Abstract

This paper examined a kernel-confined (KC) column for which some of the longitudinal reinforcements that are conventionally placed around the outer periphery of the column section were moved to the kernel confined concrete of the inner region. This is referred to as a kernel confined bar and its seismic performance of KC column under a high axial load was investigated. Six high-strength RC column specimens with a cross section of 600 mm × 600 mm were carried out experimentally. The design strength of the concrete, f_c', was 70 MPa and the longitudinal and transverse reinforcements used SD 550 W and SD 790 steels, respectively. Key design parameters included the quantity and position of the kernel confined bars, overall position, and the quantity and strength of the transverse reinforcement. Test strength results showed that the maximum testing flexural strengths for all specimens were larger than the flexural strengths of the ACI model. An average value of the ratios of the maximum testing flexural strength to ACI model strength was 1.25 for all specimens. Nevertheless, according to the strength results analyzed using the XTRACT software, a good prediction was acquired and the average value of the ratios was 0.99. Based on the specimen deformation analysis results, the amount of confined transverse reinforcement required by ACI 318-19 and controlled by the equation considering a high axial load, $0.5f_c'A_g$, resulted in a column that had an interstory drift angle capacity of 3% radian.

Keywords: high-strength RC column, kernel confined bar, high axial load, deformation capacity.

1. Introduction

Traditionally, a reinforced concrete (RC) column places its longitudinal reinforcements on the periphery of its column section to maximize its flexural strength capacity. For RC moderate- and high-rise buildings, a column on a lower story usually accumulates a tremendous self-weight from the building, and so a large amount of longitudinal reinforcement is required to resist the axial load. This can result in excessively close placement of such longitudinal reinforcements, potentially reducing the workability of pouring concrete and increasing the difficulty of installing longitudinal reinforcements for intersected beams. Under high axial loads and seismic loading reversals, the longitudinal reinforcements on the periphery of a column section can easily buckle after the column cover peels out and the column strength further degrades (Elwood *et al*., 2009). To reduce the buckling effect of the longitudinal reinforcements on the periphery of the column section, some of the longitudinal reinforcements could be moved to the kernel confined core of the column, known as a "kernel-confined (KC) bar", which is expected to prevent buckling or else to decrease the effect of the strength degradation as a result of buckling. Use of KC bars in a column can reduce the number of longitudinal reinforcements on its periphery, facilitate the quality of concrete pouring, and delay the strength degradation of the column from longitudinal reinforcement buckling. Herein, an RC column that contains KC bars is referred to as a "KC column" and the seismic performance of a high-strength KC column subjected to a high constant axial load is investigated.

According to the current Concrete Structures Design Code in Taiwan (CPAMI 2019) and ACI 318-11 (ACI 2011), the confined transverse reinforcement ratio, $R_t (= A_{sh}/sb_c)$ shall satisfy the larger of either EQ (1) or EQ (2).

$$R_{t,(a)} = 0.3\frac{f_c'}{f_{yt}}\left(\frac{A_g}{A_{ch}}-1\right) \qquad (1)$$

$$R_{t,(b)} = 0.09\frac{f_c'}{f_{yt}} \qquad (2)$$

These requirements for the confined transverse reinforcement ratio do not consider the unfavorable effects of an RC column with a high axial load and high-strength concrete. When a column is subjected to an axial load that exceeds $0.3f_c'A_g$, a lateral drift ratio of 3% radian may not necessarily be achieved. According to the ACI 318-14 and -19 Codes, a further requirement, EQ (3), must be met for a confined transverse reinforcement ratio for a column considering the effects of high-strength concrete and high axial load added to acquire the expected deformation capacity of an interstory drift angle of 3% radian.

$$R_{t,(c)} = 0.2\, k_f k_n \frac{P_u}{f_{yt}A_{ch}} \qquad (3)$$

here, $k_f = f_c'/175 + 0.6 \geq 1.0$

$$k_n = \frac{n_l}{n_l - 2}$$

where all variable definitions refer to the ACI 318-16 and -19 Codes. When the design strength of concrete is larger than 70 MPa or the design axial load exceeds $0.3A_g f_c'$, the transverse confined reinforcement demand is controlled by Eq. (3).

2.   Experimental Plan

In this research, six column specimens made of high-strength RC material and under a high axial load of $0.5f_{ca}'A_g$ were studied to investigate the lateral seismic performance of KC columns, where f_{ca}' is the actual compressive strength of concrete and A_g is cross section of the column. The design compressive strength of the concrete was 70 MPa and the longitudinal and transverse reinforcements used SD 550W and SD 790 (USD 785 from Tokyo Tekko Company, Japan), respectively.

2.1 Specimen Design

All design dimensions of the six reinforced concrete specimens were identical. The cross section and height of each specimen were 600 mm × 600 mm and 1800 mm, respectively, and the ratio of the height to width was 3:1. Each specimen had equally spaced transverse reinforcement along its whole length. The main design parameters included the contain ratio of the KC bars to the entirety of the longitudinal reinforcement and the amount of transverse reinforcement. Each specimen name consisted of eight letters composed of four sub-groups with two letters in each pairing. The first two letters of the first sub-group were "NC" or "TC", indicating "meeting" or "not meeting" the requirements for confined reinforcement of ACI 318-14 (and -19), respectively. The second sub-group, K0, K2, K3, and K4, indicated that the total sectional areas of the KC bars were zero, 20%, 28%, and 40% of the cross-sectional area, respectively. The two letters of the third pairing indicated the spacing of the transverse reinforcement by S8 or S9, corresponding to 80 or 95 mm, respectively, as per the confinement requirements of the ACI 318-14 or -19 Codes. The last two letters indicated the testing constant axial load and was "P5" for each specimen, i.e., 50% of the actual concrete axial strength of each column, $0.5f_{ca}'A_g$, was applied. The transverse confined reinforcements for each layer consisted of one hoop and many crossties of which one end was a 135° hook and the other end was a 90° hook. The testing axial load exceeded $0.3f_c'A_g$ for all specimens, and so their required confinement reinforcements were controlled by Eq. (3). The design parameters and results and placements of the longitudinal and transverse reinforcements for all specimens are shown in Table 1.

Table 1 Specimen design parameters

		NCK0S8P5	NCK3S8P5	NCK2S8P5	NCK4S8P5	TCK4S9P5	TCK0S8P5
Section type							
f_{ca}' (MPa)		70					
Longitudinal	Grade	SD 550					
	Periphery Reinforcements	20-#8	20-#8	16-#8	12-#8	12-#8	20-#8
	Kernel Reinforcements	0	4-#11	4-#8	4-#11	4-#11	0
	R_{KC}	0%	28%	20%	40%	40%	0%
	Longitudinal ratio ρ	2.82%	3.95%	2.82%	2.82%	2.82%	2.82%
Transverse	size and spacing	#4@80	#4@80	#5@80	#5@80	#5@95	#5@80
		#4@80	#4@80	#4@80	#5@80	#5@95	#5@80
	f_{yt} (MPa)	690	690	690	690	790	690
	R_t	1.83%	1.83%	1.87%	1.91%	1.61%	1.91%
	$R_{t,(a)}$	1.01%	1.01%	1.01%	1.01%	0.88%	1.01%
	$R_{t,(b)}$	0.91%	0.91%	0.91%	0.91%	0.80%	0.91%
	$R_{t,(c)}$	1.62%	1.62%	1.69%	1.80%	1.57%	1.80%

2.2 Experimental Setup and Procedure

All columns were tested under the high axial load of $0.5 f_{ca}' A_g$ and were subjected to cyclic loading to simulate a double curvature deformation condition. The Multi-Axial Testing System (MATS) testing facility was used, and the test setup is shown in Figure 1. During the entire testing procedure, a series of axial loading procedures based on force control were conducted as shown in Figure 2 before applying the lateral cyclic loads. The lateral cyclic loads were applied continuously and followed the loading procedure shown in Figure 3 under the fixed axial load of $0.5 f_{ca}' A_g$, where the actual strength of the concrete, f_{ca}', on the testing day for each specimen is presented in Table 2. The lateral cyclic loads were applied using the displacement control procedure. The displacement, Δ, were obtained based on the multiplication of the drift ratio, shown in Figure 3, with column height, h.

Figure 1. Experiment Setup
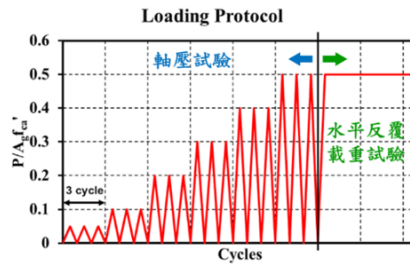
Figure 2. Loading history of the axial load
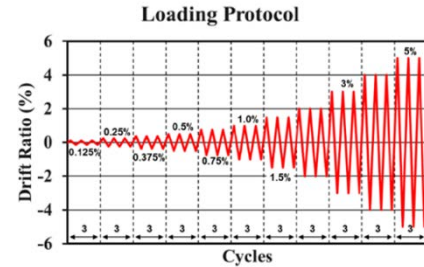
Figure 3. Loading history of lateral cyclic displacement
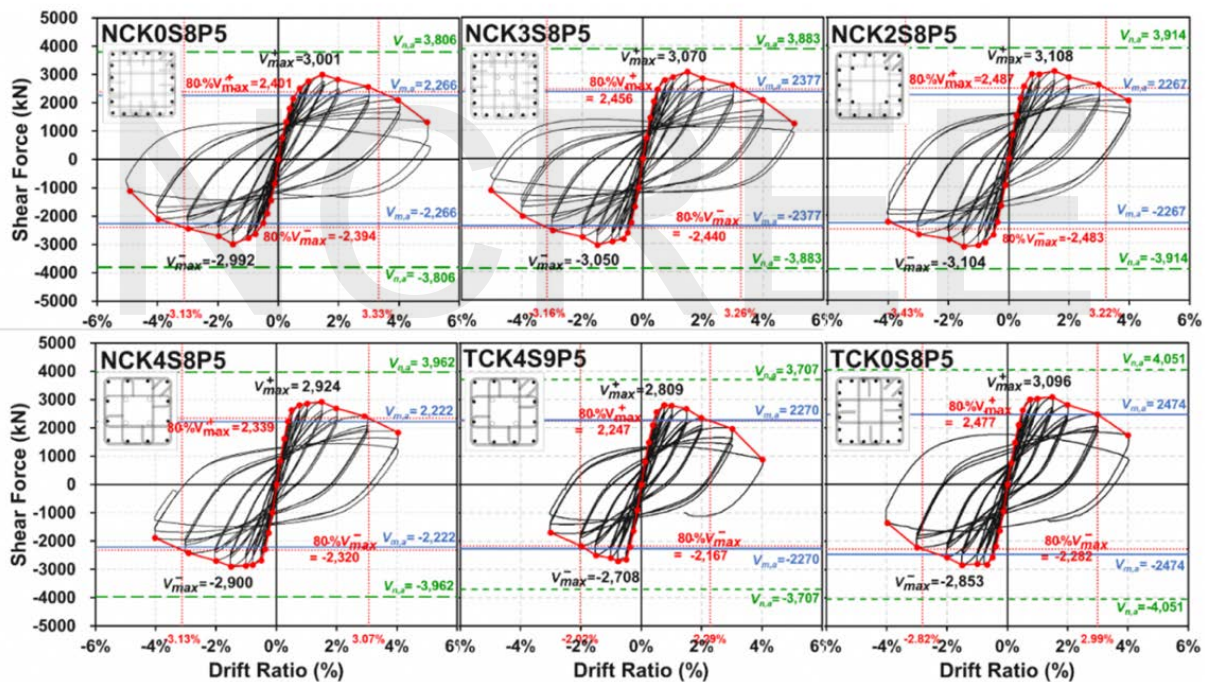
Figure 4. Hysteretic loop curves between column shear and interstory drift angle for all specimens

Table 2 Comparison between test and theoretical shear strengths for all specimens

	f_{ca}' (MPa)	(1) $V_{max,avg}$ (kN)	(2) $V_{m,a(e)}$ (kN)	(3) $V_{m,x(e)}$ (kN)	$\dfrac{(1)}{(2)}$	$\dfrac{(1)}{(3)}$
NCK0S8P5	74.7	2997	2346	3126	1.28	0.96
NCK3S8P5	79.4	3060	2440	3202	1.25	0.96
NCK2S8P5	78.3	3106	2346	3092	1.32	1.01
NCK4S8P5	78.3	2912	2264	2827	1.29	1.03
TCK4S9P5	84.3	2759	2332	2664	1.18	1.04
TCK0S8P5	84.8	2975	2547	3080	1.17	0.97
				Avg	1.25	0.99

3. Test Results and Discussion

3.1 Results of the Material Tests

The actual strength of the concrete of each specimen was tested on the testing day and is shown in Table 2. The tested strengths of the longitudinal reinforcements for #8 and #11 of SD 550W were 554 and 587 MPa, respectively. The actual strengths of 856 and 824 MPa were obtained, respectively, for #4 and #5 of SD 790 for the transverse reinforcements.

3.2 Strength Capacity

Figure 4 shows the testing hysteretic loops between shear response and interstory drift angle for all specimens. According to the test results, the five specimens, NCK0S8P5, NCK3S8P5, NCK2S8P5, NCK4S8P5, and TCK0S8P5, developed their maximum shear strength on two positive and negative directions at the peak drift angle of 1.5% radian cycle, except for Specimen TCK4S9P5, for which its maximum shear strength occurred at the peak drift angle of 0.75% radian cycle. Figure 4 indicates that all testing hysteretic loops are relatively full and do not display a significant pinching phenomenon. The testing maximum shear strengths of all specimens exceeded their shear strengths computed based on the actual material strengths, $V_{mn,a}$, but did not exceed their nominal shear strengths, $V_{n,a}$.

Table 2 shows the maximum average shear, $V_{max,avg}$, in the positive and negative directions, and the theoretic shears of $V_{m,a(e)}$ and $V_{m,x(e)}$ corresponding to the flexural strengths from ACI and the XTRACT models, respectively, for each specimen. The average value of the $V_{max,avg}$ to $V_{m,a(e)}$ ratios for all specimens was 1.25 and the average value of the $V_{max,avg}$ to $V_{m,x(e)}$ ratios was 0.99.

3.3 Deformation Capacity

A deformation capacity of $DR_{80\%}$ was selected as the basis of the assessment. The $DR_{80\%}$ was defined as the deformation angle that was in the enveloped curve as the strength passed over the maximum strength and dropped to 80% of its maximum strength. The test results indicated that the deformation angle capacities, $DR_{80\%}$, were 3.23%, 3.21%, 3.33%, and 3.10% radian for Specimens NCK0S8P5, NCK3S8P5, NCK2S8P5, and NCK4S8P5, respectively. The assessment criterion of the interstory drift angle was whether it exceeded 3% radian. The deformation angle capacities of Specimens TCK4S9P5 and TCK0S8P5 were respectively 2.16% and 2.91% radian, i.e., less than 3%. The reasons for Specimens TCK4S9P5 and TCK0S8P5 having deformation capacities below 3% radian are possibly their actual concrete strength f_{ca}' was 20% larger than the nominal concrete

strength f_c', shown in Table 2, and the provided confined reinforcements that corresponded to only 0.5 $f_c'A_g$, $R_{t(c)}$, were not sufficient for 3% radian under the axial load of 0.5 $f_{ca}'A_g$.

4. Conclusion and Recommendations

The following conclusions were drawn:

1. The experimental results showed that the maximum shear responses of the column specimens were under their shear capacities. The figures of the shear and deformation relation for all specimens were relatively plump and no obvious pinching phenomena were observed.

2. The predicted flexural strengths using the XTRACT software can obtain accurate results with an average error of 1%. The predicted flexural strengths using the ACI model underestimated specimen strength by an average of 25%.

3. Under the 0.5 $f_{ca}'A_g$ high axial load, the deformation and strength capacities for the KC column specimens with 20% to 40% KC bar approximated to those for Specimen NCK0S8P5, the conventional column without the KC bar. It was found that providing the confined reinforcement of $R_{t,(c)}$ was a feasible way to enable a column member to achieve a 3% radian lateral deformation angle. Therefore, as long as a column member has $R_{t,(c)}$ of the confined reinforcements, some of the closer longitudinal bars on the periphery of a conventional column are able to move to the kernel region to alleviate the issue of too closely spaced longitudinal reinforcement, reducing the numbers of tie bar and enhancing the ability to pour concrete.

References

ACI Committee 318 (2011, 2014, 2019), Building Code Requirements for Structural Concrete and Commentary, American Concrete Institute (ACI), Farmington Hills.

CPAMI, 2019, Design Code for Structural Concrete, Construction and Planning Agency, Ministry of the Interior, Taipei, Taiwan.

Elwood KJ, Maffei J, Riederer KA, Telleen K (2009) "Improving column confinement; Part 2: proposed new provisions for the ACI 318 building code," Concrete International, 31(12):41-48.

Mechanical Properties of Commonly Used Headed Bars in Taiwan and Development of Test Equipment

Kai-Ning Chi,[1] Ker-Chun Lin,[2] Sheng-Jhih Jhuang,[1] and Chen-Yu Ou[3]

紀凱甯 [1]、林克強 [2]、莊勝智 [1]、歐宸宇 [3]

Abstract

Past research results have confirmed that headed bars have good anchoring performance in concrete and can effectively replace traditional standard hooks as end anchors. However, although headed bars have been widely used in construction projects, there are no relevant domestic test methods and acceptance standards. The purpose of this research is not only to discuss the mechanical properties of commonly used headed bars, but also to develop a set of open-type test equipment. By means of finite-element analysis, the force mechanism of the test equipment and its optimization are developed. In a discussion of the mechanical properties of headed bars, it is suggested that the strength, slip, and elongation should be considered in tests to ensure that headed bars meet the specified mechanical properties of bars. In the production of test equipment, in order to improve the usability and convenience, the strength of steel is improved through heat treatment processing, and magnetic adjustable parts are used. These are easily installed and tested by a single person, which takes approximately 20 minutes from installation to completion of the test. According to the test results, the strength and elongation of the bars meet the specified mechanical properties if they conform to the manufacturing procedure. Observation of the degree of slip during the headed bar tests shows that the welded type exhibits no slip, the screw welded type has no more than 0.1 mm slip, the rolling type has 0.1–0.2 mm of slip, the threaded sleeve type with a non-slip nut has a maximum 0.3 mm of slip, and slip of the threaded sleeve type without the non-slip nut exceeds 0.9 mm.

Keywords: headed bar, test equipment, slip, welded type, threaded sleeve type.

Introduction

The end bars of traditional reinforced-concrete members are anchored by hooks; examples are longitudinal bars at the ends of column members anchored to the foundation and top beams, shear wall bars, and beam bars in the beam–column joint area. However, the reinforcement configuration in the joint area can often be congested. When a traditional standard hook is used for anchoring, it will not only cause difficulties in reinforcement configuration and binding, but also affects the quality of concrete pouring. Using headed bars for anchorage can not only shorten the embedded length of bars, but also relieve congestion in the joint area and improve the quality of concrete pouring.

In 2008, the American Concrete Institute ACI 318 specification first proposed design recommendations for headed bars in tension. Based on test results of Shao et al. (2016) on headed bars, the American Society for Testing and Materials specification (ASTM A970, 2018) revised the definition and limitations of the HA-level head-end dimensions. The ACI development length formula of headed bars was also revised (ACI 318-19, 2019), which means that it is more valid in practical application.

The Taiwan Concrete Institute formulated the 'Specification for Headed Steel Bars for Concrete Reinforcement' in 2014 (TCI, 2014) with reference to the recommendations of the Japan Society of Civil Engineers (Japan Concrete Institute, 2007). The test procedures and the performance evaluation criteria for strength and slip were recently revised by the Chinese Institute of Civil and Hydraulic Engineering in 2021. However, there is no test method standard for headed bars in Taiwan. If headed bars are to be widely used in the future, then it is necessary to strictly define their relevant mechanical properties and formulate relevant test methods and performance evaluation standards.

In terms of current usage in Taiwan, the commonly used types of headed bars are divided into

three categories: welded type, rolling type, and threaded sleeve type, as detailed in Table 1. Depending on the condition that the bars develop the expected required strength, there is no doubt about the relative slip of the welded type where the end plate is directly welded to the steel bar (which is zero), while all other types have a risk of relative slip. In order to obtain reliable mechanical properties for headed bars, it is necessary to develop a standard test method and to develop a reasonable and accurate test device.

Table 1. Types of headed bars.

Welded	Threaded			Sleeve
Welding friction	Threaded welding	Threaded rolling	Threaded restraint	Mortar (coupling) sleeve

Equipment Design and Analysis

In order to simulate the pressure-bearing effect of a headed bar in concrete, the test setup is as shown in Figure 1. The installation space for the extensometer is narrow and its erection is difficult and time-consuming when the end plate is not flat. On average, it takes approximately an hour to set up a specimen, so it is difficult to perform the test accurately and efficiently.

Figure 1. Photographs and diagram of test equipment and aspect to be improved.

This research improves the test device in response to the above problems. Its characteristics are as follows. (1) Focusing on operation by a single person, the equipment is designed to be open (rather than sealed) in order to mitigate congestion in the installation space. (2) A seat and the end plate are designed to be fixed to each other, and the extension steel piece is used to make the extensometer easy to erect and quickly insert into the setup to improve efficiency. (3) Pressure-bearing supports corresponding to different types of head plate are designed to improve measurement accuracy. The design of the device in this study is divided into three parts: the main frame, pressure-bearing seat, and extensometer holder. The setup is designed to be tested with SD 690-D39 steel bars.

(1) The main frame consists of an upper screw, an upper plate, four connecting screws, and a lower plate, as shown in Figure 2. The upper screw is fixed with the upper plate by means of screw threads, while the upper plate and the lower plate are connected by four connecting screws, and

the upper part is fixed by penetrating the upper plate and using nuts for fixing. In addition, the lower plate is designed as a U-shaped slot so that the specimen can be directly placed, erected, and taken out, and a shallow slot opens in the center to facilitate installation.

(2) The fixed seat device on the extensometer is shown in Figure 3. For the fixed seat, a separate design is adopted, with the seat fixed on the top of the anchor head with three-point bolts and a magnetic extension steel plate used to adsorb it on the fixed seat. The fixed seat device under the extensometer is shown in Figure 4, and it also has a separate design. The fixed seat is fixed to the end of the bars with four-point bolts, the extension steel plates are welded on both sides, and the extension steel plates are fixed on both sides of the fixed seat by strong magnets, which greatly improves the installation efficiency.

(3) The transfer pressure-bearing seat device is shown in Figure 5. The pressure-bearing seat is designed with a fixed outer diameter, and a central hole is opened for different types of headed bars, so that the bearing surface of the anchoring head can be supported on the pressure-bearing seat so as to be fixed with the lower plate.

Combining the above four parts, the new test device designed in this study is shown in Figure 6 and is an open device. During the erection process, the device and the measuring instrument do not interfere with each other and the measuring points of the instrument are clearly visible, which improves the overall test efficiency and reliability. The setup is suitable for a single person to perform tests.
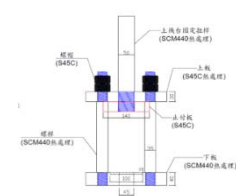
Actual photograph   Design sketch
Figure 2. The main frame setup.

Figure 3. Device on the extensometer.

Figure 4. Device under the extensometer.

Figure 5. Transfer pressure-bearing seat.

Figure 6. Test setup.

This study simulates the actual force mechanism of the test device, and uses finite-element analysis software to check the force of the device, as shown in Figure 7. There are three parameter settings for the contact surfaces at the device connections: (1) the contact surfaces between the transfer pressure-bearing seat, the device, and the headed bar are frictional; (2) the headed bar passes through the pressure-bearing seat and the device without friction; and (3) the other connections are set as combined forms. The analysis results show that the maximum stress is concentrated at the edge of the transfer bearing seat, and it can be applied to the design strength range of the setup, as shown in Figure 8.
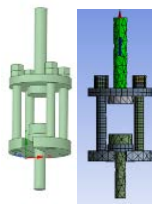
Figure 7. Device model.
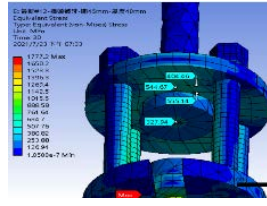
Figure 8. FEM results.

Experimental Plan

In this study, tests were carried out on the more common types of headed bars in Taiwan (Table 1), welded type, screw type, and threaded sleeve type. The welded type is mainly in the form of friction welding; the screw type is subdivided into welding, rolling and limited slip; and the threaded sleeve type is based on the mortar sleeve type.

In the Specification for Headed Steel Bars for Concrete Reinforcement for uniaxial tensile tests, the loading procedure is 0 to $0.95P_y$ and then unloading to $0.02P_y$. After measuring the residual slip between the anchor head and the reinforcing bar (rebar), the tensile force was applied until the specimen fractured. The residual slippage of the headed bar should not be greater than 0.3 mm. In the Construction Specification for Civil Works 401-110 specification, the test procedure is similar to the above, but the upper limit of loading is reduced to $0.67P_y$. The upper limits of the loading program of the tensile test were $0.95P_y$ and $0.70P_y$, and both were unloaded to $0.02P_y$ in order to measure the residual slip. The test loading process is shown in Figure 9.

The nominal diameter of the bar tested in this study exceeded 25 mm. According to the Chinese National Standard CNS 2112 (CNS, 1995), a rod-shaped No. 14A test piece was used in this case. The test method refers to the CNS 2111 (CNS, 1996) ASTM A370 method, which uses five times the nominal diameter of the bar and 8 inches (200 mm) as the gauge length measurement. A schematic diagram of the setup is shown in Figure 10.
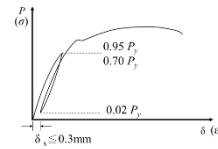
P_y: The specified yield strength of test bars.

δ_s : Residual slippage when loaded to the upper limit of specified loading, and then unloaded to $0.02P_y$.

Figure 9. Loading protocol.
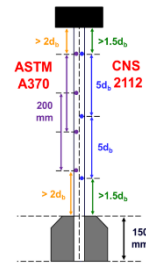
Figure 10. Gauge length of test bars.

Test Results

In the tensile strength part of the experiment, the test results show that the actual tensile strength of the specimen was greater than the corresponding standard tensile strength of all types of headed bars, and the actual tensile strength f_{ua} was greater than $1.25f_y$, as shown in Figure 11. For the residual slip part of the experiment, when the welded and screw-type headed bars were tested with the upper limits of loading ($0.70P_y$ and $0.95P_y$), the slip was controlled within 0.3 mm and there was almost no slippage of the welded type. The maximum slip value of the screw welded type was no more than 0.1 mm, and that of the rolling type was 0.1–0.2 mm. The results are shown in Figure 12. Since the sleeve-type headed bar uses mortar as the grouting material, the relative slip between the two is somewhat doubtful. However, the data show that the residual slip of product B meets the requirements. The residual slippage of product C did not meet the allowable limit because there was no nut for counteracting action. The results are detailed in Figure 13.

In terms of fracture elongation, the failure modes of this test were divided into three categories: rebar fracture (BF), head fracture (HF), and rebar pullout (PO). The results show that, if the failure mode was rebar fracture and the break occurred along the gauge length, the elongation meets the specified value. In contrast, if the failure mode was head fracture or rebar pullout, then most of the headed bars cannot reach the specified elongation.
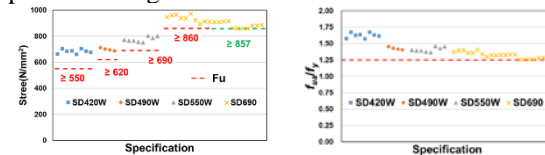
Figure 11. Results of tensile testing.
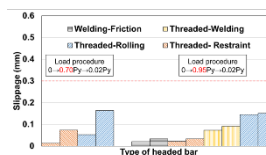
Figure 12. Slip of welded and screw type headed bars.
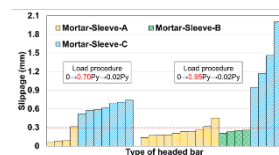
Figure 13. Slip of threaded sleeve type headed bar.

Figure 14 shows the tensile properties of the headed bars. For the welded type, the curves of strength and slip between loading and unloading are basically completely matched, indicating that there is no doubt about the slip of the two materials. For the screw type, although the bars were processed with friction welding and the fixed area of the anchor head was still connected with a thin thread, the strength and sliding curves during the unloading process did not fit with those of the loading process, so there was slippage.

The rolling type headed bars behaved differently from the friction welding type. In the initial loading stage, the strength and sliding curves first plateaued and then rose. The pitch was larger than that of the thin thread friction welding type, so a larger amount of slip resulted. The limited-slip type was the same as the rolling type, and only the counter-bolts were added for reinforcement, so that the threads are more closely connected and the initial loading stage was different from that of the rolling type bars. The tooth type bars had the same plateau as the sliding type bars.

For the threaded-sleeve type bars, the gaps between the rips were filled with mortar during grouting, and although the strength and sliding curves during the initial stage of test loading rose rapidly, the mortar was easily damaged after being stressed. Finally, the mortar was crushes and this caused slip between the expansion head and the rebar.
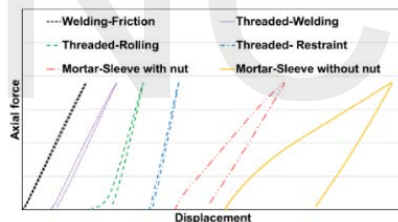
Figure 14. Slip characteristics of various types of headed bars.

Conclusions

1. The test setup adopted an open-type design to improve the erection efficiency of equipment and instruments. The single-person operation time was shortened from 90 minutes per group to 20 minutes.

2. The test results showed that the same results can be obtained when $0.7P_y$ and $0.95P_y$ are used as the upper limits of loading in the uniaxial tensile tests for three types of headed bars: welded, screw, and threaded sleeve. The threaded sleeve type with an anti-slip nut can effectively control the residual slip.

3. If the failure mode of the headed bar is anchor head slip or fracture outside the gauge length, then the fracture elongation cannot be effectively measured, so it is recommended to consider uniform elongation.

4. It is recommended that the upper limit of the loading protocol for the uniaxial tensile test be set to $0.95P_y$. The allowable value of the slip is 0.3 mm.

5. It is recommended that the tensile test of the headed bars should include three verification properties: tensile strength, slippage, and elongation.

References

ACI Committee 318 (2019), Building Code Requirements for Structural Concrete and Commentary (ACI 318-19/318R-19), American Concrete Institute (ACI), Farmington Hills, Mich.

Shao, Y., Darwin, D., O'Reilly, M., Lequesne, R. D., Ghimire, K., and Hano, M. (2016), "Anchorage of Conventional and High-Strength Headed Reinforcing Bars," SM Report No. 117, University of Kansas Center for Research, Lawrence, KS, Aug., 234 pp.

The Bureau of Standards, Metrology and Inspection (BSMI) (1996), "Method of Tensile Test for Metallic Materials," CNS 2111 G2013, Taiwan.

The Bureau of Standards, Metrology and Inspection (BSMI) (1995), "Test pieces for tensile test for metallic materials," CNS 2112 G2014, Taiwan.

Chinese Institute of Civil and Hydraulic Engineering (2021), "Specification and Interpretation of Concrete Engineering Design (Civil 401-110)," Taiwan.

Japan Society of Civil Engineers (2007), "鉄筋継手-定着指針", Tokyo, Japan.

Seismic Performance Evaluation of an Embankment Using a Pseudo-static Analysis Method

Chih-Chieh Lu[1], Kuan-Yu Chen[2], and Jin-Hung Hwang[3]

盧志杰 [1]、陳冠羽 [2]、黃俊鴻 [3]

Abstract

River embankments are important water conservancy facilities designed to prevent flooding; however, due to cost limitations, their design and construction quality are generally unreliable, and the seismic performance is usually poor. In the past, there have been many cases of river embankments having been damaged by earthquakes in seismically active areas, especially those located in areas with soil liquefaction potential. This shows that the earthquake-resistant safety of river embankments is a major earthquake engineering issue that must be faced. Therefore, this study refers to the experience of other countries in implementing seismic safety assessment of river embankments and proposes a pseudo-static analysis for embankments located in liquefaction potential areas. The proposed seismic evaluation procedure is illustrated with examples and its versatility is demonstrated.

Keywords: embankment, soil liquefaction, performance, seismic

Introduction

River embankments are rarely designed taking seismic performance into full consideration as their primary role is as a water conservancy facility to prevent flooding. Due to cost limitations they are usually made of existing river bed materials and simply piled up, making the construction quality of the embankments relatively unreliable. Moreover, in soft ground, such as areas close to river outlets, the compaction of the embankments is less likely to be carefully controlled in order to avoid subsidence of the ground due to consolidation or compaction of the foundation. Therefore, the seismic performance of the river embankment is usually poor and it is easily damaged by earthquake shaking.

There are many actual cases of embankments that have been damaged by ground shaking, including the 1995 Kobe earthquake, the 2011 Great East Japan earthquake, and the 2018 Hokkaido earthquake in Japan (Public Construction Commission, 2000; River Embankment Earthquake-Resistant Measures Emergency Review Committee, 2011; Sasaki et al., 2012) and the 1999 Chichi earthquake and 2016 Meinong earthquake in Taiwan (Public Construction

Commission, 2000; Tsai et al., 2017). There are many large-scale deformation cases, in which the amount of subsidence exceeded three meters. Many of these occurred in old river channels and estuary alluvial fans where soil liquefaction is likely to occur. As such, it has been found that many embankments have been seriously damaged due to soil liquefaction. Based on a summary by the River Embankment Earthquake-Resistant Measures Emergency Review Committee (2011), in addition to the damage caused by liquefaction of the foundation ground (which was previously assumed to be the primary form of damage), significant damage has also been caused by liquefaction of the embankment, and this requires special attention.

Based on the lessons learned from the 1995 Kobe earthquake, the 1999 Chichi earthquake, and the 2011 Great East Japan earthquake, it is known to be difficult to restore damaged embankments within the short time interval between the earthquake itself and the rainy season. This is because of the significant number of damage events and their spatial distribution. It is also worth noting that the moment magnitudes of the 2016 Meinong earthquake and the 2018 Hokkaido earthquake were only 6.4 and 6.6, respectively, and the

---

[1] Research Fellow, National Center for Research on Earthquake Engineering
[2] Assistant Research Fellow, National Center for Research on Earthquake Engineering
[3] Professor, Department of Civil Engineering, National Central University

moderate magnitudes of these earthquakes demonstrate just how weak the earthquake resistance of existing embankments is.

In Taiwan, although there have been many cases of river embankments damaged by earthquakes, such as the 1999 Chichi earthquake and the 2016 Meinong earthquake, there are no domestic regulations for the inspection and seismic assessment of river embankments. The goal of this study is to refer to the experience of other countries in implementing a seismic safety assessment of embankments and propose a pseudo-static analysis procedure for the seismic assessment of river embankments suitable for Taiwan's local characteristics. The analysis was validated using a real case, so as to increase its applicability to relevant government units in conducting seismic performance evaluation of critical embankments.

Pseudo-static Analysis

Pseudo-static analysis is one of the suggested detailed seismic evaluation methods for use with river embankments and relies on finite element or finite difference numerical programs to simulate the deformation of the embankment and the foundation stratum after an earthquake. In comparison with dynamic effective stress analysis, the pseudo-static analysis is a relatively simple analysis that considers the self-weight deformation of a river embankment as caused by the effect of soil liquefaction. The concept of the method is shown in Figure 1.
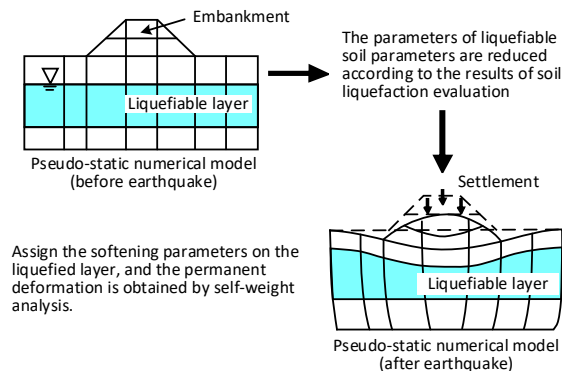
Figure 1. The concept of the pseudo-static analysis

Before conducting the numerical analysis, it is necessary to collect drilling data relevant to the site and the design earthquake data, and then conduct a stress-based simplified procedure, such as the hyperbolic function (HBF) method (Hwang et al., 2021), the National Center for Earthquake Engineering Research (NCEER) method (Youd et al., 2001), the Japan Road Association (JRA) method (JRA, 2017), and the Architectural Institute of Japan (AIJ) method (AIJ, 2001), to identify the stratum that has liquefaction potential. Using the above

information, a numerical model of the river embankment is created to obtain the pre-seismic deformation. After that, the strength and stiffness of the soils with a liquefaction resistance factor (FL) less than 1.0 (based on soil liquefaction evaluation) is then modified to simulate the mechanical behavior of the liquefaction. Regarding the strength of the liquefied soils, the residual shear strength can be assigned according to the methods of Stark and Mesri (1992) and Idriss and Boulanger (2008), who established the relationship between the normalized residual shear strength (S_u/σ_{v0}') and the clean sand equivalence of the corrected SPT blow count (($N_1)_{60cs}$) shown in Figure 2.
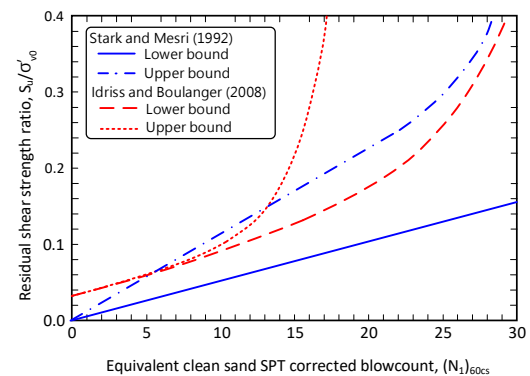
Figure 2. The relationship between S_u/σ_{v0}' and $(N_1)_{60cs}$

Case Study

The river embankment next to the Maoluo River in Nantou City was selected for use as a calculation example. The location of the demonstration site, the seismic station used in this study, and the active fault in this region are shown in Figure 3. The river embankment section suffered significant subsidence during the 1999 Chi-Chi earthquake. Relevant information about this case can be found in the literature because damage investigation and restoration were conducted in this area, making it a suitable demonstration case. This study collected the relevant riverbank, design earthquake, and drilling data, and then conducted a preliminary and detailed seismic evaluation of the river embankment.
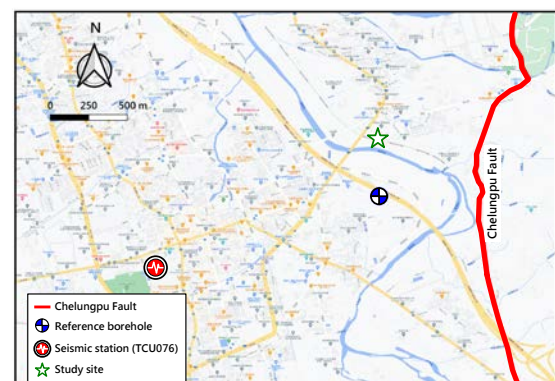
Figure 3. Locality map of the demonstration site

The detailed analysis was conducted on the Maoluo River embankment next to the Nantou Jungong Bridge (Baowei revetment). The geometry of the river embankment was based on actual measurements and a detailed drawing is shown in Figure 4. The considered flood level with a return period of two years (Q2) was at an elevation of 84.89 m (as provided by the Third River Bureau of the Water Resources Administration of the Ministry of Economic Affairs). According to the Ministry of the Interior (MOI, 2011), the horizontal peak ground acceleration (PGA) of this site was 0.3936 g. The moment magnitude (M_w) of the design earthquake was 7.1.
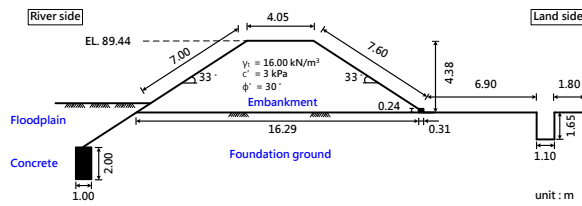
Figure 4. The information of the embankment

The pseudo-static analysis was conducted using the two-dimensional explicit finite difference program FLAC to investigate the deformation and damage of the embankment caused by liquefaction of the foundation soil under the given target earthquake. The analysis section of this study was conducted on the embankment on the side of the Maoluo River. Figure 5 shows the numerical analysis grid of the standard section and the boundary conditions. The number of grid elements was approximately 1900. The size of the grid elements near the embankment was decreased to obtain more accurate analysis results. Those close to the left and right boundaries were larger to save computational time. The left and right boundaries of the model were set with a roller condition that restrained the horizontal displacement to satisfy the subsidence and uplift phenomena when the stratum was deformed; the bottom of the model was set with a roller condition to restrain vertical displacement. The elevation of the ground water tables on the left-side boundary (river side) and right-side boundary (land side) of the model were set according to the Q2 flood level elevation (84.89 m) and the groundwater level observed from the drilling data (elevation 84.09 m), respectively.
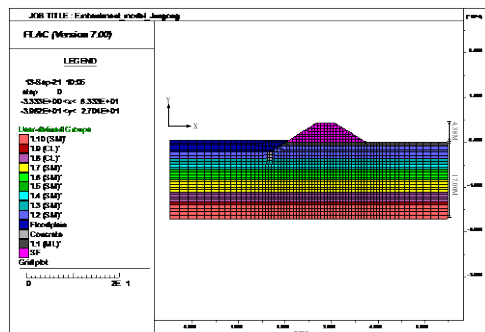
Figure 5. The numerical model of the embankment

The soil parameters of the model are listed in Table 1. The focus of the pseudo-static analysis of river embankment liquefaction is weakening of the liquefied soil parameters. In considering the parameters of the liquefied soil layer, the liquefaction potential of the saturated sandy soil was evaluated first using the stress-based simplified HBF method. Cases with $F_L < 1.0$ were regarded as having soil that will undergo soil liquefaction during the earthquake, and this is indicated the last column in Table 1.

Table 1. The soil parameters of the numerical model

Soil layers	USCS	N-value	γ_t (kN/m³)	c' (kPa)	ϕ' (deg)	G (MPa)	K (MPa)	Liq?
Embankment	SM	10	16.37	3.0	30.0	9.08	27.25	No
Floodplain	SM	10	19.35	1.0	29.1	9.08	27.25	Yes
L1	ML	2	18.60	23.5	0.0	1.75	8.18	No
L2	SM	7	18.81	0.0	26.8	6.36	19.08	Yes
L3	SM	13	19.75	0.0	31.1	11.81	35.43	Yes
L4	SM	4	20.10	0.0	23.9	3.63	10.90	Yes
L5	SM	19	20.28	0.0	34.5	17.26	51.78	No
L6	SM	16	20.28	0.0	32.9	14.53	43.60	Yes
L7	SM	32	21.56	0.0	40.3	29.07	87.20	No
L8	CL	16	20.80	94.2	0.0	13.17	654.00	No
L9	CL	27	20.80	158.9	0.0	22.22	1103.63	No
L10	SM	28	21.58	0.0	38.7	25.43	76.30	No

The numerical analysis was conducted as follows: After the numerical mesh and boundary conditions were established, the soil parameters shown in Table 1 were assigned to the corresponding soil layers. Then, the self-weight balance was carried out to generate the initial stress; the initial stress conditions are those achieved by the numerical analysis model, including the embankment and the foundation, after equilibrium was reached. Before the weakening analysis was carried out, the strength and elastic parameters of the liquefied soils were first updated. The undrained shear strain (S_u) was obtained according to the empirical formula for the relationship between the normalized residual shear strength (S_u/σ_{v0}') and the clean sand equivalence of the corrected SPT blow count ($(N_1)_{60cs}$) suggested by Stark and Mesri (1992) and Idriss and Boulanger (2008). The Young's modulus (E) of the liquefied soils was obtained from the empirical relationship $E/S_u = 300$, and their Poisson's ratio (v) was assumed to be 0.49 to satisfy the undrained condition of the liquefied soils. With E and v, the shear modulus and bulk modulus of the liquefied soil layer were obtained from the theory of elasticity. After updating the liquefied soil parameters in the program, the balance calculation was performed again, and the deformation behavior of the embankment after liquefaction of the foundation soil was found.

The stress balance analysis was conducted as follows: After assigning the weakening parameters in the program, the subsidence increment of the top of the embankment was monitored. The stress balance analysis was continued iteratively until there was no significant further increase in subsidence, which means that the stress state of the whole model had

become stable. Figure 6 shows the final numerical mesh and displacement field generated after assigning the lower bound weakening parameters suggested by Stark and Mesri (1992). From observation of the mesh before and after the weakening analysis, it appears that the subsidence and deformation of the embankment caused the ground on both sides of the embankment toe to be squeezed and uplifted. The mesh deformation mainly occurred in the embankment and in the liquefied layers below the embankment. The subsidence of the embankment with the lower bound weakening parameters suggested by Stark and Mesri (1992) was 1.48 m.

(a) Undeformed (green) and deformed (red) mesh

(b) Displacement field
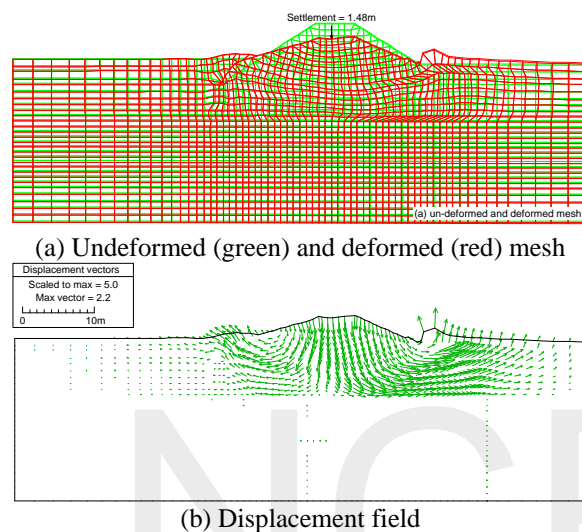
Figure 6. The pseudo-static analysis results of the embankment

Conclusions

This study proposed a practical seismic assessment process, supplemented by a demonstration to illustrate the analytical details of the assessment. The research results are intended to be used as a reference for future engineering practice.

River embankments are important flood prevention facilities. It is necessary to start planning for seismic safety assessment and classification of river embankments that are of high importance (notably in metropolitan areas) and located in areas with severe liquefaction potential. For embankments that have a seismic capacity less than the requirement, it is recommended that the administration should quickly improve their earthquake resistance to avoid the risk of secondary disasters caused by post-earthquake floods. For embankments of major rivers, the administration should conduct a comprehensive preliminary seismic evaluation to identify sections at risk of damage due to earthquake shaking and carry out detailed earthquake resistance evaluation work for the reference of subsequent earthquake resistance reinforcement operations.

References

AIJ (Architectural Institute of Japan), (2001) Recommendations for design of building foundations. (in Japanese)

Idriss, I.M. and Boulanger, R.W. (2008) Soil liquefaction during earthquakes. EERI Monograph MNO-12.

JRA (Japan Road Association) (1996) Design specifications for highway bridges, Part V seismic design. (in Japanese).

Hwang, J.H., Khoshnevisan, S., Juang, C.H., and Lu, C.C. (2021) Soil liquefaction potential evaluation – An update of the HBF method focusing on research and practice in Taiwan. Engineering Geology, 280, 105926. doi:10.1016/j.enggeo.2020.105926

Construction and Planning Agency, MOI (2011) Seismic design specifications and commentary of buildings. (in Chinese)

Public Construction Commission (2000) Rapid diagnosis and reinforcement strategy for port and river embankments after earthquake. Report No. 106. Public Construction Commission, Taiwan.

River Embankment Earthquake-Resistant Measures Emergency Review Committee (2011) Report (draft) on how to proceed with future earthquake resistance measures for river embankments based on the Great East Japan Earthquake. (in Japanese)

Sasaki, Y., Towhata, I., Miyamoto, K., Shirato, M., Narita, A., Sasaki, T., Sako, S. (2012) Reconnaissance report on damage in and around river levees caused by the 2011 off the Pacific coast of Tohoku earthquake. Soils Found., 52(5):1016-1032.

Stark, T.D. and Mesri, G (1992) Undrained Shear Strength of Sands for Stability Analysis. Journal of the Geotechnical Engineering Division, ASCE, 118(GT11):1727-1747.

Tsai, C.C., Hsu, S.Y., Wang, K.L., Yang, H.C., Chang, W.K., Chen, C.H., and Yu-Wei Hwang, Y.W. (2017) Geotechnical reconnaissance of the 2016 ML6.6 Meinong Earthquake in Taiwan. Journal of Earthquake Engineering., 22(9): pp. 1710-1736.

Youd, T.L., Idriss, I.M., Andrus, R.D., Arango, I., Castro, G., Christian, J.T., Dobry, R., Liam, Finn, W.D., Harder Jr., L.F., Hynes, M.E., Ishihara, K., Koester, J.P., Laio, S.S.C., Marcuson III, W.F., Martin, G.R., Mitchell, J.K., Moriwaki, Y., Power, M.S., Robertson, P.K., Seed, R.B., and Stokoe II, K.H. (2001) Liquefaction resistance of soils: summary report from the 1996 NCEER and 1998 NCEER/NSF workshops on evaluation of liquefaction resistance of soils. Journal of Geotechnical and Geoenvironmental Engineering, ASCE, 127(1):297–313.

A Preliminary Study on the Effect of Lowering Groundwater Level on Soil Liquefaction Potential in the Taipei Basin

Yuan-Chang Deng[1] Chih-Chieh Lu[2] Jin-Hung Hwang[3]

Abstract

The purpose of this study is to present a preliminary discussion of the effect of lowering the groundwater level on the soil liquefaction potential in the Taipei Basin for practicable engineering conditions. Soil liquefaction evaluations with different groundwater table settings were conducted to determine the factor of safety against soil liquefaction for each soil layer of the Taipei Basin boreholes by Taiwan soil liquefaction simplified hyperbolic function procedure. The liquefaction potential index (PL) was adopted to evaluate the soil liquefaction effect of a liquefiable soil column. The PL values of the boreholes were spatially interpolated to produce regional PL maps. The PL liquefaction potential levels under different ground water table settings were used to evaluate the effect of lowering the water table on soil liquefaction potential.

Two groundwater level conditions were considered in this study. One was the benchmark groundwater level, which was set as the average water level during the flood season during implementation of "Home Security Plan", also the water level used in the refined soil liquefaction potential map of the Taipei Basin. The results of the benchmark analysis showed that the proportion of area having low potential is 37.4%, that having medium potential is 37.3%, and that having high potential is 25.3%. The second groundwater level examined for the comparative analysis was the benchmark water level dropped by 3 m, based on an anti-liquefaction strategy suggested in the literature. The results of the comparative analysis showed that the proportion of the area having high potential is less than 5%, indicating that the soil liquefaction potential can be significantly reduced. The value of lowering the water level can be used as a starting point for soil liquefaction prevention and disaster mitigation improvement strategies in the Taipei Basin.

Keywords: Soil liquefaction, liquefaction potential index, lowering groundwater table, soil liquefaction potential map.

Introduction

In 1999, the 921 Chi-Chi earthquake struck central Taiwan and caused extensive soil liquefaction. This attracted the attention of researchers and engineers, and the study of soil liquefaction subsequently became mainstream, benefitting from the fact that cases of soil liquefaction, earthquake records, and relevant geological information were well documented. Some Taiwanese researchers developed a local simplified procedure based on standard penetration test blow counts (SPT-N) in light of the framework proposed by Seed et al. (1985), namely the hyperbolic function (HBF) procedure (Hwang et al., 2012).

In 2016, approximately 17 years after the 921 Chi-Chi earthquake, the Meinong earthquake, with a local magnitude (M_L) of 6.6, struck southern Taiwan, causing serious building damage due to soil liquefaction in the Tainan area. Because of the great public concern about the risk of soil liquefaction in urban areas after this event, about one month after the Meinong earthquake the Central Geological Survey disclosed the first version of a soil liquefaction potential map based on data from a limited number of boreholes. This map provided a ranking of liquefaction risk in terms of the liquefaction potential index (P_L). In order to provide the public with a better understanding of soil liquefaction risk, the Construction and Planning Agency Ministry of the Interior (CPA/MOI) then promoted the "Home Security Plan" to produce a refined soil liquefaction potential map for local administrative divisions that contain liquefiable areas. To facilitate the execution of

this plan, the National Center for Research on Earthquake Engineering (NCREE) served as general counselors for Taipei City and New Taipei City to establish a standard operating procedure and supervise the contractor (CECI Engineering Consultants) in executing the plan according to the setting requirements. The working group has been engaged in this project for approximately two years and has accumulated a wealth of experience in its execution.

The refined soil liquefaction potential maps released by the Taipei City Government and the New Taipei City Government show that areas with high liquefaction potential in the Taipei Basin are densely populated, suggesting that the issue of soil liquefaction caused by earthquakes is important with regard to disaster prevention, mitigation strategies, and urban planning in the Taipei Basin Metropolitan Area.

Engineering lower water tables is one of the effective anti-liquefaction strategies being used, but there is little research related to the management of this process for the regional water levels used in the Taipei Basin. Yasuda and Hashimoto (2016) pointed out that the damage to Japanese wooden structures caused by earthquake-induced soil liquefaction could be avoided when groundwater levels were kept to 3 m below the surface.

In order to realize the applications of the work conducted by Yasuda and Hashimoto (2016), this study used their recommendations to examine the differences in the distribution of regional soil liquefaction potential between a benchmark ground water level (set as the average water level during flood season) and a comparative ground water level, which was 3 m lower than the benchmark water level. The results can be used as a reference for the formulation of relevant disaster prevention and mitigation strategies in the Taipei Basin.

Refined Borehole Database of the Taipei Basin

The Taipei Basin is a highly developed region in Taiwan. Many large projects including large-scale land development, public rapid transit systems, freeways, and highways have been completed and have operated over recent decades. This public infrastructure has resulted in the generation of a large geological drilling database distributed throughout the Taipei Basin, which is an essential input for soil liquefaction assessment. The total number of boreholes in the Taipei Basin is currently as many as 12962, which means that there are approximately 53 boreholes per square kilometer assuming a uniform spatial distribution. However, since the quality control of the early geological drilling was not well established, much of the submitted borehole data is not reliable enough for use in liquefaction assessment. Therefore, it is necessary to conduct further inspection and

screening processes before borehole data can be included. In the screening process, the quality of the drilling data was first classified. The classification principle was based on the complete set of the data including the unified soil classification system (USCS) information, SPT-N value, index properties of the soil and the judgement of the authors. The first class included data that required almost no correction nor supplementary data; the second class required some correction and/or supplementary data; the third class included data that were considered unreliable and lacked some essential information; and the fourth class represented data that were considered extremely unreliable and lacked essential information.

In this study, the boreholes belonging to the third and fourth classes were discarded and only borehole data of the first and second classes were used for analyses. For these boreholes, where soil sample data were missing they were supplemented using information from neighboring soil samples with similar USCS characteristics. If there were no suitable nearby references, the missing data were constructed from a statistical analysis of reliable soil sample data. After the above processing, the number of remaining boreholes was 5182. Their distribution in the Taipei Basin is shown in Figure 1. The solid blue circles are boreholes drilled during the "Home Security Plan" project from 2017 to 2018. The purpose of the drilling was mainly for the evaluation of soil liquefaction in the Taipei Basin. In order to reduce operation variability, the automatic drop hammer system was adopted, resulting in improved drilling quality. Based on the energy measurements of selected boreholes, the energy ratio of the automatic drop hammer system in this case was approximately 65~70%. According to the statistical results of the boreholes from the "Home Security Plan", liquefiable sandy soils, including USCS categories SM, ML, CL-ML, and other gravel soils, account for 58.3% of all soils. Among the liquefiable sandy soils, the SM soils are in the majority and account for 53.5% of the liquefiable soils. The SM soils have an average N value of approximately 12 and an average fines content of 25%, the CL soils have an average N value of 5 and an average fines content of 94%, and the ML soils have an average N value of 9 and an average fines content of 75%.
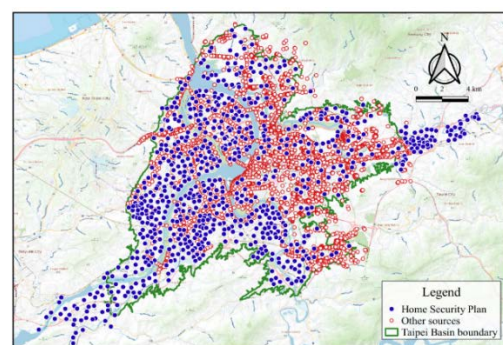

Figure 1. Distribution of boreholes in the Taipei Basin after the screening process was conducted.

Soil Liquefaction Potential Evaluation

Design earthquake parameters and ground water table

The moment magnitude (M_w) and the horizontal peak ground acceleration (PGA) are the earthquake parameters used for the evaluation of soil liquefaction. According to the recommendations of the latest "Seismic design specifications and commentary of buildings", the design earthquake with a return period of 475 years (10% probability of exceedance in 50 years) is required when considering soil liquefaction. In this study, the same concept was used. For a return period of 475 years, the corresponding M_w is 7.3 and its horizontal PGA is 0.24 g. All the boreholes in this study are within or near the Taipei Basin, and both M_w and PGA are consistent throughout.

The ground water table (GWT) is also a critical parameter for soil liquefaction evaluation. However, Since the existing GWT data are insufficient, the ground water table of the boreholes drilled by the "Home Security Plan" was measured during the execution of the plan. Based on the GWT measurements, it can be easily shown that the GWT changes throughout the year, and it can be conservatively stated that the contour of the average ground water table in the Taipei Basin during flood season can be reproduced for use in the soil liquefaction evaluation of all boreholes in this study. In order to examine the influence of lowering the groundwater level on the soil liquefaction potential of the Taipei Basin, a comparative ground water level is used, set as the benchmark water level lowered by 3 m.

Methods to evaluate soil liquefaction potential

To determine the effect of soil liquefaction in areas that experienced severe liquefaction during the design earthquake, the liquefaction potential index (P_L) proposed by Iwasaki et al. (1978) is commonly used. According to this index, sites with $P_L > 15$ are regarded as having high liquefaction potential, sites with $5 < P_L \leq 15$ are regarded as having middle liquefaction potential, and sites with $P_L \leq 5$ are regarded as having low liquefaction potential. P_L is evaluated from the obtained factors of safety (FS) in light of the Taiwan local HBF method (Hwang et al, 2012) to predict the potential of liquefaction to cause damage at the surface. P_L and the spatial coordinates of every borehole are used in spatial ordinary Kriging interpolation to produce regional liquefaction potential maps consisting of all discrete cells in the Taipei Basin.

Effect of Lowering Groundwater Level on Soil Liquefaction Potential

This study compares soil liquefaction between a benchmark groundwater level, which was set using the average ground water table of the Taipei Basin during flood season, and a comparative ground water level, which was set at 3 m lower than the benchmark water level.

Table 1 shows the percentage distribution of each liquefaction potential level (high, medium, and low P_L) among the analyzed boreholes for both ground water levels. The benchmark soil liquefaction evaluation shows that the percentage of boreholes with high, medium, and low liquefaction potential is each approximately one third of the total. The liquefaction potential results for the lowered water table show that the percentage of boreholes with high liquefaction potential is dramatically reduced, those with middle liquefaction potential remains the same at 31.7%, and those with low liquefaction potential increases to 64.9%. This indicates that lowering the groundwater level can substantially reduce the risk of liquefaction.

Figure 2 shows the soil liquefaction potential P_L map using the benchmark groundwater level, and Figure 3 shows the P_L map using the comparative groundwater level. Table 2 shows the percentage distribution of areas affected by each liquefaction potential levels for both ground water levels. The results of the evaluation using the benchmark groundwater level reveal that the area occupied by each liquefaction potential level is also approximately one third of the total. The area with high liquefaction potential is widely distributed over the middle- and down- stream areas of the Danshui and Keelung Rivers. In general, the areas far from the rivers have little soil liquefaction potential. The results of the soil liquefaction evaluation using the comparative (lowered) groundwater level reveal that the area with high liquefaction potential accounts for a very small fraction of the total, while that with low liquefaction potential increases to two-thirds of the total. This indicates that lowering the groundwater level decreases the proportion of high liquefaction potential and increases the proportion of low liquefaction potential area. These values can be used as a preliminary reference for soil liquefaction prevention and disaster mitigation strategies in the Taipei Basin.

Table 1. The percentage distribution of each liquefaction potential level among boreholes for both GWTs

Analysis GWT setting	Borehole proportion (%)		
	Low	Middle	High
Mean GWT during flood season (Benchmark)	38.4	31.7	29.9
Benchmark GWT dropped by 3 m	64.9	31.7	3.4

Table 2. The percentage distribution of areas affected by different liquefaction potential levels for both GWTs

Analysis GWT setting	Area proportion (%)		
	Low	Middle	High
Mean GWT during flood season (benchmark)	37.4	37.3	25.3
Benchmark GWT dropped by 3 m	67.2	32.3	0.5
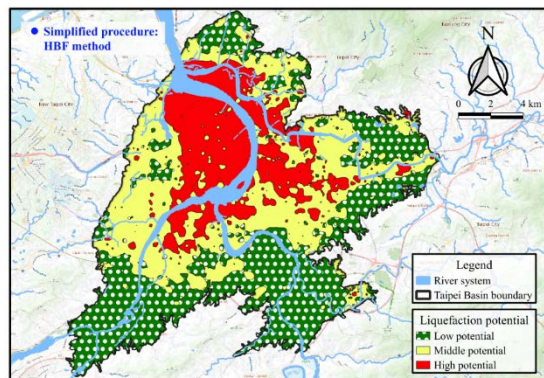
Figure 2. Soil liquefaction potential map of the Taipei Basin (benchmark groundwater level)
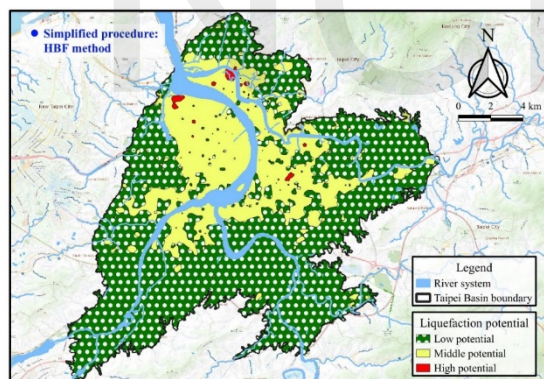
Figure 3. Soil liquefaction potential map of the Taipei Basin (benchmark water level dropped by 3m)

Conclusions

The effect of lowering the groundwater level on the soil liquefaction potential of the Taipei Basin was examined. The results suggest that lowering the groundwater level can significantly decrease the proportion of high potential soil liquefaction area and boreholes. The results can be used as a preliminary reference for soil liquefaction prevention and disaster mitigation strategies in the Taipei Basin.

Acknowledgements

References

Hwang, J.H., C.H. Chen, and C.H. Juang (2012). "Calibrating the model uncertainty of the HBF simplified method for assessing liquefaction potential of soils," Sino-geotechnics, 133, 77-86. (in Chinese)

Iwasaki, T., F. Tatsuoka, K. Tokida, and S. Yasuda (1978). "A practical method for assessing soil liquefaction potential based on case studies at various sites in Japan," Proceedings of the 2nd international conference on microzonation for safer construction—research and application, San Francisco, CA, 885-896.

Seed, H.B., K. Tokimatsu, L.F. Harder, and R.M. Chung (1985). "Influence of SPT Procedures in Soil Liquefaction Resistance Evaluation," J. of Geot.Engr., ASCE, 111(12), 1425-1445, 1985.

Yasuda, S., and Hashimoto, T., "New project to prevent liquefaction-induced damage in a wide existing residential area by lowering the ground water table," Soil Dyn. Earthq. Eng., 91, 246–259, 2016.

Dynamic Properties of Seabed Soil in Offshore Windfarms

Sheng-Huoo Ni[1], Chia-Han Chen[2], and Yu-Jou Hsu[3]

倪勝火 [1]　　陳家漢 [2]　徐羽柔 [3]

Abstract

This study conducts a dynamic triaxial test on soil samples extracted from the seabed offshore of Changhua, Taiwan. For sandy soils, reconstituted specimens were designed based on their fines content (15%, 30%, and 50%), void ratio (0.7, 0.8, and 0.9), and degree of saturation (15%, 30%, 60%, and 100%) using the moist tamping technique. The dynamic triaxial tests were performed at three confining stress levels (20, 80, and 320 kPa) under displacement-controlled conditions. This research investigates the influence of the aforementioned factors on the dynamic shear modulus and the damping ratio of the soil. To obtain complete dynamic property curves of the seabed soils, normalized shear modulus reduction curves and damping ratio curves from dynamic triaxial tests were combined with resonant column tests later. According to the test results, the normalized shear modulus reduction curves are roughly at the upper boundary of the suggested range of Seed and Idriss (1970), while the damping ratio curves trend towards the lower boundary of this range. Void ratio, saturation, effective confining pressure, and fines content all affect the shear modulus and damping ratio, with fines content having a less significant effect. The increase in effective confining pressure, degree of saturation, and void ratio, and the decrease in fines content, move the complete shear modulus reduction curves to higher strain. By increasing the effective confining pressure and decreasing the fines content, the complete damping ratio curves show the same shift.

Keywords: dynamic triaxial tests, shear modulus, damping ratio, dynamic properties

Introduction

The west coast of Taiwan has many wind farms suitable for wind power generation. The wind turbines built in Taiwan must face the mechanical vibration of the wind turbine itself, as well as short-term repeated loads such as typhoons and earthquakes, during which soil on the seabed may also undergo soil liquefaction. Furthermore, the interaction of piles and soil affects the operation of wind turbines. The dynamic properties of the soil are thus particularly important. In addition, research conducted by local scholars indicates that the soil on the west coast of Taiwan has unique mechanical properties. Therefore, this research focuses on determining the dynamic properties of seabed soils using dynamic triaxial tests. The results will be later combined with resonant column test data in an attempt to generate undrained shear modulus reduction curves and damping ratio curves over a wide range of strains.

Test Materials and Methods

Test materials

The soil samples for this test were taken from offshore windfarm sites in Changhua. Soil samples were prepared according to the content of three groups of fine particles, and then physical property tests were carried out on the soil, including a specific gravity test, a sieve analysis test, a hydrometer test, and an Atterberg limits test. The soil samples are classified according to the unified soil classification method (USCS), and the physical properties of the specimens are listed in Table 1. Figure 1 shows the grain size distribution curve of the soil samples.

[1] Professor, National Cheng Kung University
[2] Associate Researcher, National Center for Research on Earthquake Engineering
[3] Graduate student, National Cheng Kung University
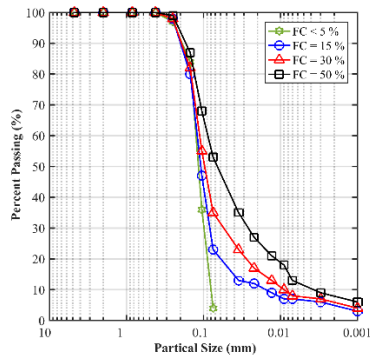
Figure 1. Grain size distribution curve of samples.

This study is based on the wet tamping method of preparing remolded samples for silty soil in the seabed. Deaired water was used to flush and saturate the specimens in these tests.

Table 1. Physical properties of specimens

Properties of Specimens	Specific Gravity	Liquid Limit	Plastic Limit	USCS Class.
FC < 5%	2.650	N.L.	N.P.	SP
FC = 15%	2.715	N.L.	N.P.	SM
FC = 30%	2.720	N.L.	N.P.	SM
FC = 50%	2.727	N.L.	N.P.	ML

Equipment and specimen preparation

In this experiment, the fines content parameters were set as 15%, 30%, and 50%. After the soil emerges from the top of the thin tube, the coarse and fine particles must be separated using the wet sieving method. With a No. 200 sieve (0.074 mm) as the boundary, the soil sample that remains on this sieve is used in this experiment. The coarse particles are dried for later use, while the finest particles are those that have passed through the No. 200 sieve. After drying, the samples must be passed through a No. 200 sieve to ensure that no coarse particles are mixed in them, and stored in an oven. The water content required by each sample is then calculated from the specific gravity of the soil sample. Next, the coarse and fine particle weights and the water weight of the target sample are sequentially added, and the soil sample is mixed evenly, sealed, and placed in a constant temperature and humidity box to ensure that the added water is fully mixed with the soil sample particles.

This study uses the British-made dynamic triaxial test instrument at the National Center for Research on Earthquake Engineering Tainan Laboratory. The body and peripheral equipment of the instrument are shown in Figure 2. A specimen size of 5 cm in diameter by 10 cm in height was used in this study. The experimental program for the specimen included measurements on saturated and unsaturated specimens. All the saturated specimens were required

to achieve B-values greater than 0.95. All specimens were isotropically consolidated to the desired effective consolidation stress before the dynamic tests were performed.
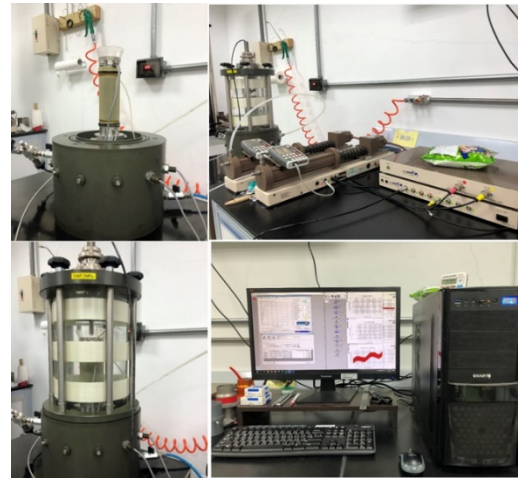
Figure 2. Dynamic triaxial testing apparatus

Testing procedures

Initially, the bender element test was conducted to measure the shear wave velocity after a specimen was consolidated. All dynamic triaxial tests were performed using sinusoidal loading with constant strain amplitude at a frequency within a range of ±0.1 Hz, starting with compression loading. The initial single amplitude was 0.005 mm. The test ended when the amplitude reached 1.28 mm or when the hysteresis loop was deformed in series.

Young's modulus, shear modulus, and damping ratio were calculated from the dynamic triaxial tests following the guidelines provided in the American Society for Testing and Materials (ASTM) D3999 manual.

Results and Discussions

In this study, a saturated specimen and an unsaturated specimen were configured for strain control experiments, and the influence of fines content and void ratio on the dynamic characteristics of the saturated specimen under a variable confining pressure were studied. The effects of fines content, void ratio, confining pressure, and degree of saturation of soils on the dynamic properties were studied.

Effect of confining pressures

A typical result for the effect of effective confining pressures on shear modulus is shown in Figure 3. In the test, three effective confining pressures were used: 20 kPa, 80 kPa, and 320 kPa. Figure 3 shows how shear modulus (both unnormalized and normalized) and shear strain variation relate to the effective

confining pressure of samples with fixed void ratio, saturation, and fines contents. This normalization involves dividing the measured shear modulus (G) by the maximum measured shear modulus (G_{max}) of the bending element under a fixed confining pressure. It can be seen that the maximum shear modulus increases as confining pressure increases, which is consistent with previous work. Figure 4 shows the variation of damping ratio with shear strain for various effective confining pressure.
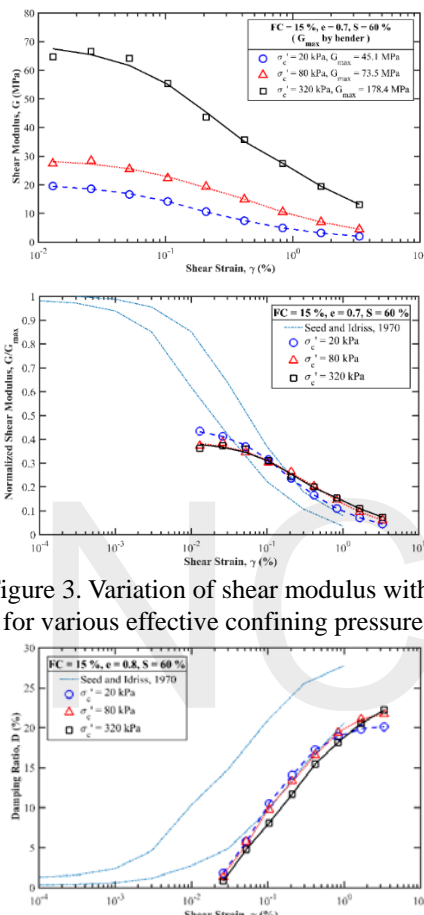
Figure 3. Variation of shear modulus with strain for various effective confining pressures

Figure 4. Variation of damping ratio with strain for various effective confining pressures

Effect of soil saturations

A typical result for 15% fine contents is shown in Figure 5. In the figure, four specimen saturations were used: 15%, 30%, 60%, and 100%. This shows the relationship between normalized shear modulus and shear strain variation with the specimen saturations of samples. Figure 6 shows the variation of damping ratio with shear strain for various degrees of saturation of samples.
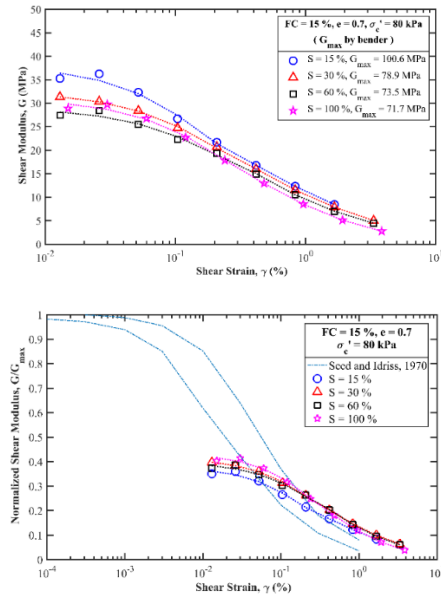
Figure 5. Variation of shear modulus with strain for various saturations
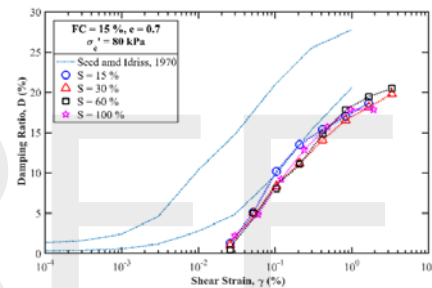
Figure 6. Variation of shear modulus with strain for various degrees of saturation of samples

Effect of Void ratios

A typical result for 20 kPa confining pressure and various void ratios is shown in Figure 7. In the figure, three void ratios of specimen were used: 0.7, 0.8, and 0.9. Figure 7 shows the relationship between the (both unnormalized and normalized) shear modulus and shear strain variation with the void ratios. Figure 8 shows the variation of damping ratio with shear strain for various void ratios.
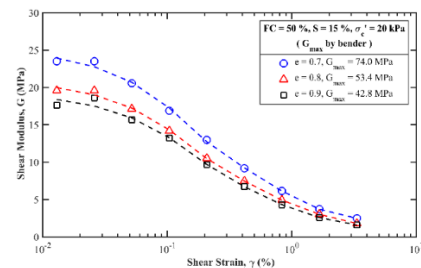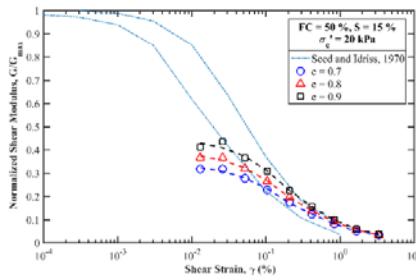
Figure 7. Variation of shear modulus with strain for various void ratios
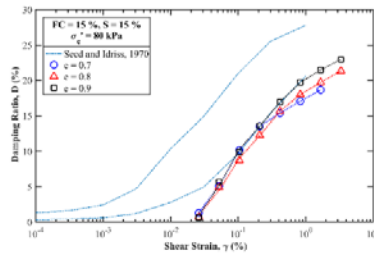
Figure 8. Variation of shear modulus with strain for various void ratios

Effect of fine contents

A typical result for 80 kPa confining pressure and various fine contents is shown in Figure 9. In the figure, three void ratios of specimen were used: 0.7, 0.8, and 0.9. Figure 9 shows the relationship between the (both unnormalized and normalized) shear modulus and shear strain variation with the fine contents. Figure 10 shows the variation of damping ratio with shear strain for various fine contents.

Conclusions

1. The shear modulus of saturated specimens decays more significantly than that of unsaturated specimens.
2. The effect of fines content on the normalized shear modulus reduction curve is less significant than that of void ratio and saturation.
3. An increase in effective confining pressure, saturation, and void ratio, and a decrease in fines content, all lead to a shift towards higher strain in the complete normalized shear modulus reduction curves.
4. An increase in effective confining pressure and a decrease in fines content also results in a shift to higher strain of the complete damping ratio curve.

According to the test results, the normalized shear modulus reduction curves of unsaturated seabed soils decay less when there is large strain.
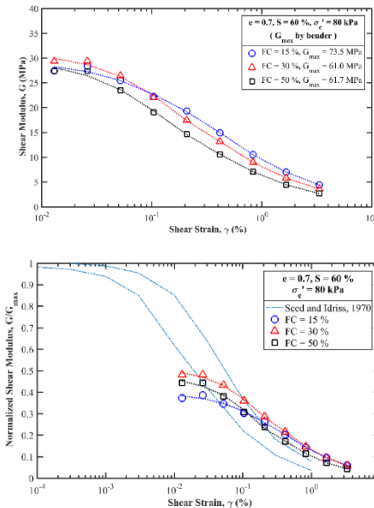
Figure 9. Variation of shear modulus with strain for various fine contents
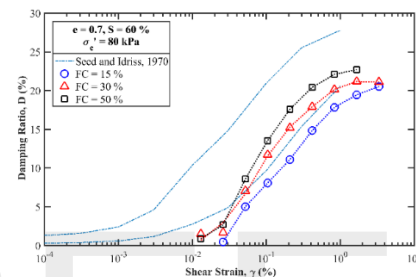
Figure 10. Variation of shear modulus with strain for various fine contents

References

ASTM, "Standard Test Methods for the Determination of the Modulus and Damping Properties of Soils Using the Cyclic Triaxial Apparatus," *ASTM International Standard Methods*, Vol. 91, No. Reapproved, pp. 1–16, 2013.

GDS, "The GDS 2Hz/5Hz/10Hz Dynamic Testing System Hardware Handbook," *GDS Instruments Ltd.*, pp. 1–30, 2006.

Gu, X., Yang, J., Huang, M., and Gao, G., "Bender Element Tests in Dry and Saturated Sand: Signal Interpretation and Result Comparison," *Soils and Foundations*, Elsevier, Vol. 55, No. 5, pp. 951–962, 2015.

Hardin, B.O., and Drnevich, V.P., "Shear Modulus and Damping in Soils: Measurement and Parameter Effects," *Journal of Soil Mechanics and Foundations Division,* Vol. 98, No. SM6, pp. 603–624, 1972.

Seed, H.B., and Idriss, I.M., "Soil Moduli and Damping Factors for Dynamic Response Analyses," *Report* No. EERC 70-10, Earthquake Engineering Research Center, University of California, Berkeley, 1970.

Seismic Performance of Steel Bridge Columns (I)

Hsiao-Hui Hung[1] Kuang-Wu Chou[2] and Chia-Chuan Hsu[3]

洪曉慧 [1]、周光武 [2]、許家銓 [3]

Abstract

The purpose of this research is to study the seismic performance of steel bridge columns through analysis and tests in order to establish a reasonable formula for the plastic hinges of steel columns and to feed them back into the seismic design and evaluation specification. The implementation method of this study is first to investigate the domestic and foreign steel column-related seismic codes and research, including the codes of Taiwan, Japan, and the United States. In addition, the types and design details of common steel bridge columns in Taiwan are investigated, and the design and construction of the specimens are then carried out to confirm and compare their seismic performance through tests. Furthermore, with the structural simulation analysis, the nonlinear model of the steel column is corrected on the basis of the test results, and then the parameter analysis is performed with the corrected analytical model. This year, we study the circular steel column first, and design two specimens. Although the two specimens have the same design, one of them is filled with low-strength concrete and the other is completely hollow to compare the effect of filled concrete on the nonlinear performance of steel columns. In addition, preliminary parameter analysis is conducted to discuss the effect of different plate thicknesses and axial force ratios.

Keywords: steel bride columns, cyclic loading test, nonlinear pushover analysis

Introduction

After the 921 earthquake, bridge authorities in Taiwan such as the Freeway Bureau, the Directorate General of Highways, and several county and city governments all conducted seismic performance assessments and retrofit for existing bridges. Among them, for the bridges with reinforced concrete (RC) columns, there are many relevant studies or regulations both domestic and abroad for reference, so effective and practical design and construction can be carried out. However, for the seismic evaluation and retrofit of bridges with steel columns, because of the lack of relevant domestic test reports and no clear research cases to follow, most of them refer to Japanese cases and studies. Considering that the seismic performance of steel columns is closely related to construction details, foreign research results may not be applicable to domestic engineering environments. In addition, since steel columns have

the advantages of light weight, high strength, good ductility, easy fabrication, and a short construction period, many viaducts in Taiwan are constructed with steel columns, especially for urban viaducts. Therefore, there is an urgent need to study the seismic performance of localized steel bridge columns. This study intends to study the seismic performance of common types of steel bridge columns in Taiwan and to establish a localized plastic hinge property and a seismic evaluation method for steel bridge columns. Relevant tests of steel columns and numerical simulation analysis will also be conducted to verify the accuracy of the evaluation method. The research and development results can provide reference for practical design and evaluation for bridges with steel columns in the future. This study will be implemented over years. This year, it mainly focuses on circular single-column steel piers, and two test specimens are

[1] Research Fellow, National Center for Research on Earthquake Engineering
[2] Associate Research Fellow, National Center for Research on Earthquake Engineering
[3] Assistant Research Fellow, National Center for Research on Earthquake Engineering

designed, laboratory tests are planned, and preliminary simulation analysis is carried out.

Specifications for steel bridge columns

This research will initially focus on steel columns with a circular hollow structure section (HSS); therefore, the follow-up description will also focus on the circular steel column. At present, the seismic design of bridges emphasizes the ductile design, with the purpose of enabling the ductile members to have reliable nonlinear deformation ability during an earthquake. Therefore, there is a newly added chapter related to the design details of steel bridge columns in the current domestic code for the seismic design of highway bridges [1]. It mentions that the detailed design of steel bridge columns should prevent local buckling, weld bead tearing, shear failure, or other brittle failures of the members. To achieve this purpose, the following methods can be adopted: (1) the width–thickness ratio of the wall of the rectangular steel column or the diameter–thickness ratio of the wall of the circular steel column shall be limited; (2) for the corner welding, full-penetration groove welding shall be adopted. However, the design code does not provide the relevant design requirements in detail and only suggests to refer to the latest Japanese specifications for highway bridges, or other relevant specifications published by AASHTO or AISC.

Regarding the setting of plastic hinges for steel bridge columns, the code for seismic evaluation and retrofit design of highway bridges [2] in Taiwan provides relevant calculation formulas. The content mainly refers to the Japanese specifications for highway bridges [3]. The stress–strain relationship of the steel and the filled concrete used for the plastic hinges is shown in Figure 1. Among them, considering the quality variability of domestic steel plate production and the deterioration factor of materials caused by environmental factors, the upper limit of tensile ultimate strain of steel is conservatively adopted as $15\varepsilon_y$, where ε_y is the yield strain of steel. The allowable ultimate compressive strain of steel depends on its geometric conditions and whether it is filled with concrete.

For circular steel columns without filled concrete, the allowable ultimate compressive strain ε_a is calculated according to formula (1)

$$\varepsilon_a = (20 - 140R_t)\varepsilon_y \tag{1}$$

$$R_t = \frac{R}{t}\frac{F_y}{E}\sqrt{3(1-\mu^2)} \tag{2}$$

where R is the radius of the circular steel column, t is the thickness of the steel plate, μ is the Poisson ratio of the steel, F_y is the yield strength of the steel, and E is

the elastic modulus of the steel. The scope of application of formula (1) is as follows:

$$0.03 \le R_t \le 0.08 \,,\, 0.2 \le \bar{\lambda} \le 0.4 \,,\, 0 \le N/N_y \le 0.2 \tag{3}$$

$$\bar{\lambda} = \frac{1}{\pi}\sqrt{\frac{F_y}{E}} \cdot \frac{l}{r} \tag{4}$$

In equation (3), N is the design axial force, N_y is the yielding axial force calculated according to the condition of full section yielding, l is the effective buckling length of the member, r is the radius of gyration of the section.

For circular steel columns filled with concrete, the allowable upper limit of the compressive strain $\varepsilon_a = 7\varepsilon_y$ for the domestic code [2]. This regulation is different from the Japanese code. The Japanese code [3] stipulates that the upper limit of the compressive strain $\varepsilon_a = 7\varepsilon_y$ is only applicable to rectangular columns. For circular columns, the upper limit of the compressive strain $\varepsilon_a = 5\varepsilon_y$, and it only applies to the following situations:

$$0.03 \le R_t \le 0.12 \,,\, 0.2 \le \bar{\lambda} \le 0.4 \,,\, 0 \le N/N_y \le 0.2 \tag{5}$$
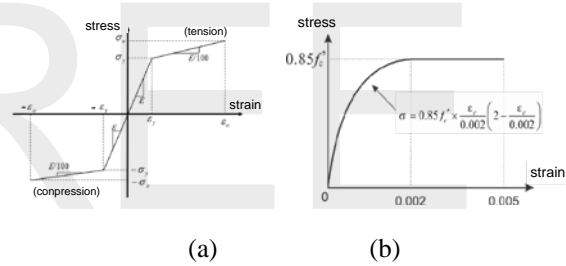
Figure 1. Stress–strain relationship for (a) steel; (b) in-filled concrete

The above provisions of the scope of application also imply that the code requires that the slenderness ratio l/r of the steel column should be less than $1.256\sqrt{(E/F_y)}$, and the axial force ratio N/N_y should be less than 0.2. For circular steel columns without concrete filling, the diameter–thickness ratio D/t should be less than $0.097\,E/F_y$, and for circular steel columns filled with concrete, it should be less than $0.145\,E/F_y$.

After obtaining the stress–strain curves of steel and in-filled concrete according to the above description, the moment–curvature relationship diagram of the cross-section can be obtained by the slicing method, and then the plastic hinge curve of the steel column can be obtained.

The domestic code for seismic evaluation and retrofit design of highway bridges also sets the allowable upper limit for the ductility of bridge columns. Taking important bridges in general earthquake zones as an example, under a level II

earthquake, the allowable ductility of a single column is 3.5, and the same regulations are used for steel columns and concrete columns. In the United States, the California Department of Transportation (Caltrans) has established an independent specification for steel bridges: Seismic design specifications for steel bridges [4]. For ductile members such as bridge piers, this code sets the allowable limiting ductility according to the allowable damage level. For repairable damage level, the allowable displacement ductility is 3 and the rotation ductility is 6; for significant damage level, the allowable displacement ductility is 4 and the rotation ductility is 8. In addition, Caltrans also stipulates the width–thickness ratio requirements for ductile compression members. For the wall of round hollow structural section (HSS) bridge columns, the diameter–thickness ratio D/t must be lower than $0.038E/F_y$. For the wall of the concrete-filled round tube, the diameter–thickness ratio needs to be lower than $0.076 E/F_y$. Both the above limits are stricter than those in the Japanese and domestic codes. For the slenderness ratio, it is required to be less than $2.36\sqrt{(E/F_y)}$. Currently, there is no consistent standard for the design of steel piers worldwide, especially the requirements for their nonlinear behavior after yielding.

Specimen design and construction

According to the above-mentioned domestic design code related to steel columns, two circular steel column specimens were designed in this study, named as specimen A and specimen B. As shown in Figure 2, these two specimens have the same dimensions; the total height of the specimens is 5.3 m, of which the column body is 3.7 m, the column head is 0.6 m, and the foundation height is 1 m. The diameter of the column specimen is $D = 0.8$ m, the thickness of the steel plate is $t = 1.4$ cm, the material of the steel plate is SN490B, and the corresponding diameter–thickness ratio is 57. Specimen A is a hollow column without concrete filling, while specimen B is filled with concrete up to 2 m in the column. The compressive strength of the filled concrete $f'_c = 140$ kgf/cm^2. To make the steel column stably fixed in the RC foundation, the specimen is designed according to the domestic design practice. A steel anchor frame base is designed in the foundation and 16 anchor bolts are adopted to join the steel anchor base and the base plate of the steel column.

This year, the construction of specimen A has been completed. As shown in Figure 3, the steel column and RC foundation were fabricated separately. Among them, the steel anchor frame and anchor bolts were precast in the foundation before grouting, and the column base plate and stiffeners were added at the bottom of the column. Both parts were made in the factory and then shipped to the NCREE for assembly. When assembling, the reserved holes in the base of the steel column were aligned with the pre-embedded anchor bolts and inserted. After adjusting the horizontal positioning, the bolts were tightened. Then, the non-shrinkage cement mortar was poured between the bottom plate of the steel column body and the foundation. After the non-shrinkage cement mortar solidified, the construction was completed.
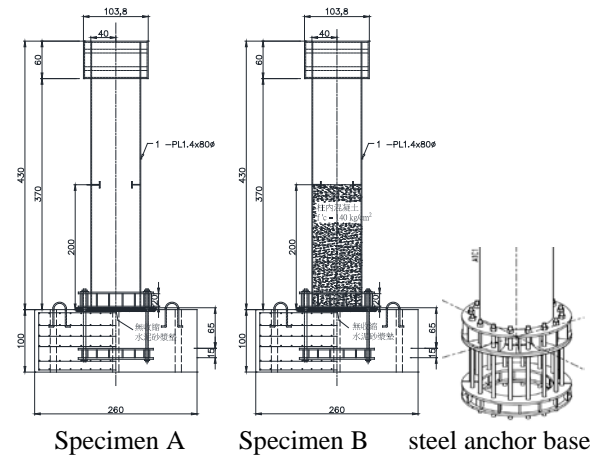
Figure 2. Design diagram of the specimens

Figure 3. Photos of specimen A
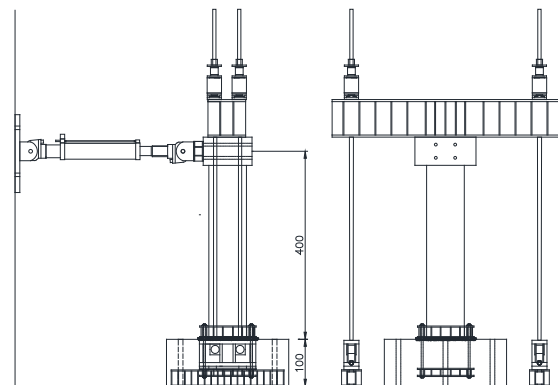
Figure 4. Experimental setup

Parametric study

The structural simulation analysis was carried out for the test in advance. Figure 5 shows the analysis model and the pushover analysis results using Sap 2000 structural analysis software. Three-dimensional shell elements were used to simulate steel plates. The foundation was not included in the simulation model, and the boundary condition for the column base was assumed to be fixed. The analysis considered geometric nonlinearity, including the P-delta effect and large displacement effect. The analysis results are also shown in Figure 5. It can be found that the column bottom is in the shape of an outer drum along the direction of the lateral force, indicating that the bottom of the column has buckled. From the relationship curve between the base shear and the lateral displacement, it can also be found that after the specimen reaches its strength of approximately 80 tf, the base shear gradually decreases with the increase in displacement, which means that its strength degraded with the increase in displacement, and its stiffness also decreases rapidly.
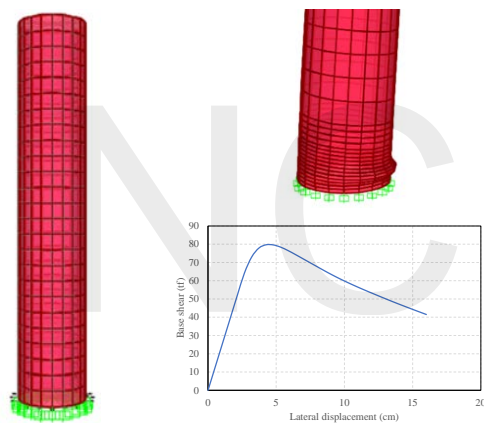
Figure 5. Specimen simulation model and analysis results

To investigate the key parameters affecting the seismic performance of steel bridge columns, a parametric study through nonlinear pushover analysis was also carried out in this study. The variables considered include the thickness of the steel plate and the ratio of the axial force. Figure 6(a) shows the effect of varying plate thickness. The thicknesses of the steel plates considered are 10, 14, and 19 mm, corresponding to the cases where the diameter–thickness ratio D/t is 80, 57, and 42, respectively. As shown in the figure, with the increase in the plate thickness, that is, the increase in the diameter–thickness ratio, in addition to the obvious increase of the strength can be seen, the proportion of the strength degradation of the specimen after yielding is also slightly reduced. Figure 6(b) shows the effect of varying axial force, considering the axial force ratios of 0.1, 0.15, and 0.2. As shown in the figure, with the increase in the axial force, the strength of the specimen

decreases slightly, and the rate of stiffness degradation increases.

(a)

(b)
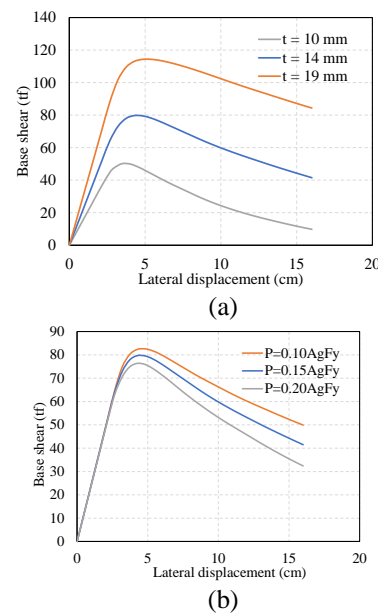
Figure 6. Parametric analysis results: (a) effect of plate thickness; (b) effect of axial force ratio

Conclusions

This study completed the design, fabrication, and preliminary analysis of steel column specimens this year. The analysis results showed that the diameter–thickness ratio and axial force ratio greatly affect the nonlinear behavior of steel columns. By incorporating large displacement effects and P-delta effects into analytical simulations, the buckling of steel columns can be effectively predicted. In the future, the accuracy of the simulation analysis will be verified through cyclic loading tests, and the parameter analysis results will be revised as a reference for specification revisions.

References

1. Ministry of Transportation and Communications (MOTC), Specification for seismic design of highway bridges, 2018. (In Chinese)

2. Ministry of Transportation and Communications (MOTC)，Specification for seismic evaluation and retrofit design of highway bridges, 2021. (In Chinese)

3. Japan Road Association (JRA), Specifications for Highway Bridges V: seismic design, 2012.

4. Caltrans, Caltrans Seismic Design Specifications for Steel Bridges, Second Edition, 2016.

Existing Hospital Structures Seismically Retrofitted by Externally Connecting Viscous Dampers

Wang-Chuen Lin[1], Jenn-Shin Hwang[2], Chung-Han Yu[3], Cho-Yen Yang[4] and Shiang-Jung Wang[5]

林旺春 [1]、黃震興 [2]、游忠翰 [3]、楊卓諺 [4]、汪向榮 [5]

Abstract

To seismically retrofit existing hospitals, it is not only necessary to guarantee that their performance will be superior to that of general structures during and after earthquakes, but it is also very important to minimize the impact on daily operations and on patients during the reconstruction period. A seismic retrofit strategy involving external connections with linear viscous dampers whose damping coefficients can be more efficiently distributed, is investigated in this study. Three damping coefficient distribution methods are discussed and examined. Numerical results show that if inappropriately designed added reaction structures and linked viscous dampers can be precluded by eliminating those that fall within undesired frequency ratio bands, then the adoption of any of the three distribution methods can satisfactorily control the seismic responses of existing hospitals. Furthermore, it is shown that adopting the third distribution method, which is based on the kinetic energy at the more important stories, is the most cost-effective.

Keywords: seismic retrofit, viscous damper, external connection, viscous damping coefficient, distribution method

Introduction

When seismically retrofitting existing hospitals, accommodating the original structural configuration and space, minimizing the impact on daily operations and patients during the reconstruction period, and guaranteeing the functionality of housed critical medical equipment should be taken into consideration along with main goal of achieving the desired seismic performance. This study proposes the use of linear viscous dampers to be externally connected between existing hospital structures and one or more purpose-built reaction structures as a practical and feasible seismic retrofit strategy. This is shown in Figure 1, in which Structure A represents the hospital structure to be retrofitted and Structure B represents the reaction structure. This proposed seismic retrofit strategy is similar in concept to the connection of two adjacent structures using velocity-dependent dampers to simultaneously reduce their wind- or earthquake-induced responses and the probability of collision between them. This concept has been discussed in many past studies (Zhang and Xu, 2000; Bhaskararao and Jangid, 2007; Hwang *et al.*, 2007).
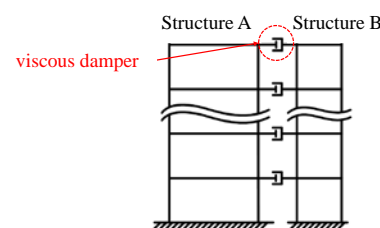
Figure 1. Proposed seismic retrofit strategy.

In this study, the undesired frequency ratio band of two multi-degree-of-freedom (MDOF) structures, is identified considering only their fundamental modal characteristics (Hwang *et al.*, 2007). Two damping coefficient distribution methods for the externally connected dampers are then derived based on the relative kinetic energy at each story divided by the

---

total relative kinetic energy of the hospital structure. Finally, retrofitting examples are numerically examined and compared with their counterparts derived using the conventional uniform distribution method.

Two SDOF Systems Linked by a Viscous Damper

When simplifying an MDOF system to a representative single-degree-of-freedom (SDOF) system, the effective modal mass can be calculated from:

$$M^* = \frac{\left(\sum_i m_i \phi_i\right)^2}{\sum_i m_i \phi_i^2} \tag{1}$$

where M^* is the fundamental modal mass of the MDOF system; m_i is the mass assigned to the ith story; ϕ_i is the normalized mode shape of the first mode at the ith story ($\phi_{roof} = 1$). Two SDOF systems connected by a viscous damper are presented in Figure 2, in which M_a^*, c_a, and k_a are the effective modal mass, damping coefficient, and stiffness of Structure A, respectively, M_b^*, c_b, and k_b are the corresponding parameters of Structure B, and c_d is the damping coefficient of the linked viscous damper. The corresponding equation of motion when adopting a linear viscous damper can be written in matrix form as:

$$[m]\{\ddot{x}\} + [c]\{\dot{x}\} + [k]\{x\} = -[m]\{1\}\ddot{x}_g \tag{2}$$

where $[m] = \begin{bmatrix} M_a^* & 0 \\ 0 & M_b^* \end{bmatrix}$; $[c] = \begin{bmatrix} c_a + c_d & -c_d \\ -c_d & c_b + c_d \end{bmatrix}$; $[k] = \begin{bmatrix} k_a & 0 \\ 0 & k_b \end{bmatrix}$; $\{x\} = \begin{Bmatrix} x_a \\ x_b \end{Bmatrix}$; $\{\dot{x}\} = \begin{Bmatrix} \dot{x}_a \\ \dot{x}_b \end{Bmatrix}$; $\{\ddot{x}\} = \begin{Bmatrix} \ddot{x}_a \\ \ddot{x}_b \end{Bmatrix}$; x_a, $\dot{x}_a$, and $\ddot{x}_a$ are the horizontal displacement, velocity, and acceleration of Structure A relative to the ground, respectively; x_b, $\dot{x}_b$, and $\ddot{x}_b$ are the horizontal displacement, velocity, and acceleration of Structure B relative to the ground, respectively; and $\ddot{x}_g$ is the input ground acceleration.
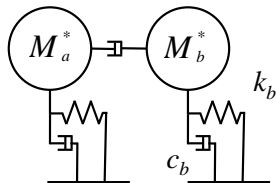
Figure 2. Illustration of two SDOF systems connected by a viscous damper.

Based on the assumption of proportional damping, the effective damping ratios of Structures A and B ($\xi_{eff,a}$ and $\xi_{eff,b}$) are calculated from:

$$\xi_{eff,a} = \frac{c_a + c_d}{2M_a^* \omega_a} = \xi_a + \frac{c_d}{2M_a^* \omega_a} = \xi_a\left(1 + \frac{c_d}{c_a}\right) \tag{3.1}$$

$$\xi_{eff,b} = \frac{c_b + c_d}{2M_b^* \omega_b} = \xi_b + \frac{c_d}{2M_b^* \omega_b} = \xi_b\left(1 + \frac{c_d}{c_b}\right) \tag{3.2}$$

where $\omega_a = (k_a/M_a^*)^{0.5}$; $\omega_b = (k_b/M_b^*)^{0.5}$; $\xi_a = c_a/(2M_a^* \omega_a)$; and $\xi_b = c_b/(2M_b^* \omega_b)$. Based on the study by Hwang *et al.* (2007), the relationship between the phase lag of two adjacent SDOF systems and the actual effect of the linked damper has been established. A way to prevent the frequency ratio of two adjacent structures from falling into the undesired range was proposed to ensure that the linked dampers would in fact enhance the damping ratios of the two structures. With the values of ξ_a, ξ_b, c_d/c_a, and c_d/c_b, the calculated values of $|\xi_n-\xi_{eff,a}|/\xi_{eff,a}$ and $|\xi_n-\xi_{eff,b}|/\xi_{eff,b}$ less than 0.02 are used here to quantitatively define the lower and upper bounds of the undesired frequency ratio band. The undesired frequency ratio bands with $c_d/c_a = 1 \sim 6$ and $c_d/c_b = 1 \sim 12$ for $\xi_a = \xi_b = 5\%$ are presented in Figure 3.
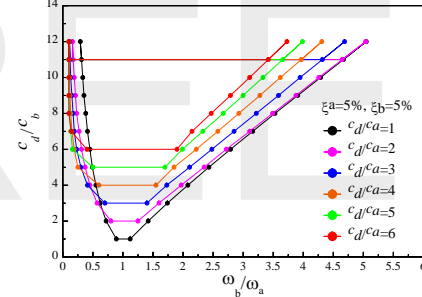
Figure 3. Undesired frequency ratio bands.

Distribution of Damping Coefficients Based on Energy Approaches

Assuming that the mechanical properties and installation schemes of linear viscous dampers at one story are the same, the supplementary damping ratio provided by all the dampers can be calculated from (FEMA 356, 2000):

$$\xi_d = \frac{T\sum_j c_j \cos^2\theta_j \phi_{rj}^2}{4\pi\sum_i m_i \phi_i^2} \tag{4}$$

where T is the fundamental modal period of the structure; c_j is the damping coefficient of the dampers at the jth story; θ_j is the inclination angle of the dampers at the jth story; ϕ_{rj} is the first modal relative displacement between two ends of the dampers at the jth story in the horizontal direction; m_i is the mass assigned to the ith story; and ϕ_i is the normalized mode shape of the first mode at the ith story ($\phi_{roof} = 1$).

The first modal period of the hospital structure to be retrofitted, generally, is much longer than that of the new reaction structure. For simplicity, the latter is ideally assumed to behave as a rigid body during derivation, and since the linked dampers are installed horizontally, the ϕ_{rj} of the dampers installed at the jth story is identical to ϕ_i. Thus, Eqs. (3.1) and (3.2) can be rewritten as:

$$\frac{c_d}{2M_a^* \omega_a} = \xi_d = \frac{T_a \sum_r C_r \phi_r^2}{4\pi \sum_N m_N \phi_N^2} \tag{5.1}$$

$$\frac{c_d}{2M_b^* \omega_b} = \xi_d = \frac{T_b \sum_r C_r \phi_r^2}{4\pi \sum_N m_N \phi_N^2} \tag{5.2}$$

where T_a and T_b are the fundamental modal periods of Structure A and Structure B, respectively; C_r is the damping coefficient of the dampers connected to the rth story of Structure A; ϕ_r is the first modal relative displacement between two ends of the dampers at the rth story in the horizontal direction; m_N is the mass assigned to the Nth story of Structure A; ϕ_N is the normalized mode shape of the first mode at the Nth story of Structure A ($\phi_{roof} = 1$); N is the total number of stories of Structure A; and r is the total number of stories linked by the dampers.

The uniform distribution (UD) method, i.e., that for which the damping coefficients designed for viscous dampers at different stories are the same ($C_r = C$), is simple and convenient, and also well accepted in engineering practice. By using Eq. (5.1), the formula for calculating the damping coefficient of the linear viscous dampers at each story can be calculated from:

$$C = \frac{c_d \sum_N m_N \phi_N^2}{M_a^* \sum_r \phi_r^2} = \frac{4\pi \xi_d \sum_N m_N \phi_N^2}{T_a \sum_r \phi_r^2} \tag{6}$$

The distribution method proposed by Hwang *et al.* (2013), in which the damping coefficients of the viscous dampers at each story are proportional to the relative kinetic energy of each story corresponding to the first mode of vibration, is used in this study. This method is denoted as the story kinetic energy (SKE) method hereafter. Based on this method, the relative kinetic energy at the ith story is proportional to $m_i\phi_i^2$, and the damping coefficients of the viscous dampers installed at the rth story of the hospital structure can be calculated using Eq. (5.1) as follows:

$$C_r = \frac{c_d m_r \phi_r^2 \sum_N m_N \phi_N^2}{M_a^* \sum_r m_r \phi_r^4} = \frac{4\pi \xi_d m_r \phi_r^2 \sum_N m_N \phi_N^2}{T_a \sum_r m_r \phi_r^4} \tag{7}$$

To make the SKE method more effective, viscous dampers should be installed at stories whose relative kinetic energy is larger than the average relative kinetic energy, as follows:

$$m_i\phi_i^2 > \frac{\sum_i m_i \phi_i^2}{N} \tag{8}$$

With the criterion given in Eq. (8) and by substituting Eq (7) into Eq. (5.1), the formula for distributing the total damping coefficients among the linear viscous dampers installed at the appropriate stories can be obtained from:

$$C_r = \frac{c_d m_l \phi_l^2 \sum_N m_N \phi_N^2}{M_a^* \sum_l m_l \phi_l^4} = \frac{4\pi \xi_d m_l \phi_l^2 \sum_N m_N \phi_N^2}{T_a \sum_l m_l \phi_l^4} \tag{9}$$

where l is the number of stories whose relative kinetic energy is larger than the average relative kinetic energy. This method is called the story kinetic energy to efficient stories (SKEES) method hereafter.

Demonstration Examples

An actual three-dimensional model consisting of two structures connected by linear viscous dampers was numerically analyzed, as illustrated in Figure 4. Structure A, being nine by three spans, represents an existing, regular 8-story hospital structure to be retrofitted; the heights of the first story and the other stories are 4 m and 3.5 m, respectively; the calculated fundamental modal period in the X direction is 0.945 s. Structure B represents three separate new reaction structures each designed with one by one spans. The 8-story Structure B has the same total height and story heights as Structure A, as presented in Figure 4. The fundamental modal periods of Structure B in the X direction are calculated as 0.183 s. Both structures are assumed to have an inherent damping ratio of 5%.
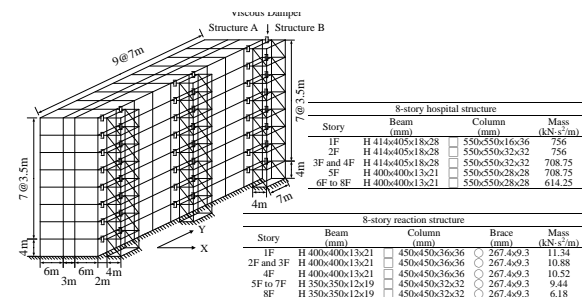
Figure 4. Retrofit example three-dimensional models

A target damping ratio of 15% was set for Structure A. Then, $\omega_b/\omega_a = 5.18$, $c_d/c_a = 2$, and $c_d/c_b = 8.64$. These design parameters do not fall within the undesired frequency ratio bands, as observed from Figure 3. The damping coefficients distributed to different stories of the hospital structure are summarized in Table 1. The original 1940 El Centro N-S earthquake with an intensity of 0.348 g was used

as the ground input. The elastic maximum relative displacements and maximum story drift angles at all stories of the 8-story hospital structure based on the UD, SKE, and SKEES methods are presented in Figure 5. Regardless of whether the UD, SKE, or SKEES method was used, the retrofitted hospital structure showed better displacement control performance than the original, which implies that the externally connected linear viscous dampers are effective in reducing the seismic response of the hospital structure.

Table 1 Distributions of damping coefficients at different stories of the 8-story hospital structure

Story	UD (kN·s/m)	SKE (kN·s/m)	SKEES (kN·s/m)
8	854.3	1156.7	1222.6
7	854.3	1002.1	1059.2
6	854.3	797.3	842.7
5	854.3	653.9	691.1
4	854.3	408.6	-
3	854.3	215.0	-
2	854.3	84.6	-
1	854.3	13.2	-
Total	6834.4	4331.3	3815.5
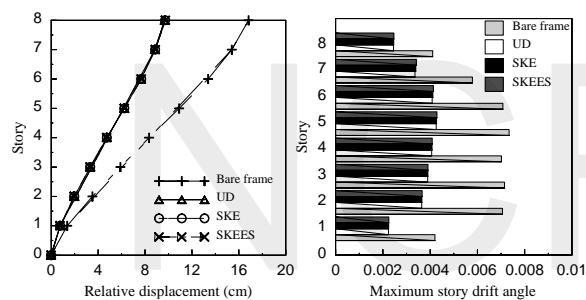
Figure 5. Elastic seismic responses of the 8-story hospital structure

Table 2 Maximum damper forces at each story of the 8-story hospital structure

Story	UD (kN)	SKE (kN)	SKEES (kN)
8	679	903	950
7	624	724	762
6	546	506	533
5	441	339	358
4	338	163	-
3	254	68	-
2	165	17	-
1	72	1	-
Total	3120	2720	2604

The maximum damper forces obtained using the three different distribution methods are listed in Table 2. For all cases, the higher the story linked by the viscous dampers, the larger the damper force required. With almost the same control performances under the El Centro, using the UD method always resulted in a larger required total damper force than using the SKE and SKEES methods. Therefore, using the SKE or SKEES method is more cost-effective than using the UD method for the proposed seismic retrofit strategy.

Furthermore, using the SKEES method always resulted in a smaller required total damper force than using the SKE method. Thus, in addition to verifying the feasibility and effectiveness of the concept of strategic distribution of the total damping coefficients to dampers installed at appropriate stories, it has also been found that using the SKEES method is more economical compared with the SKE method. In summary, the SKEES method is the most attractive option for the proposed seismic retrofit strategy considering both practical and economic considerations.

Conclusions

A seismic retrofit strategy for existing hospitals involving external connection with linear viscous dampers whose damping coefficients can be more efficiently distributed was proposed, analytically discussed, and numerically examined. For the proposed seismic retrofit strategy, the obtained undesired frequency ratio band obtained can be utilized to preclude improper design of the purpose-built reaction structure and the linked dampers. Under El Centro, the higher the story linked by viscous dampers was, the larger was the damper force required, regardless of whether the UD, SKE, or SKEES method was used. Under almost the same control performances, using the UD method resulted in a larger required total damper force than using the SKE and SKEES methods, and using the SKEES method resulted in the smallest required damper force. It can be concluded that using the SKE method offers some economic benefits, but using the SKEES method is the most economical for the proposed seismic retrofit strategy.

References

Zhang, W.S. and Xu, Y.L. (2000). "Vibration Analysis of Two Buildings Linked by Maxwell Model-Defined Fluid Dampers." *J. Sound Vib.* **233**(5) 775-796.

Bhaskararao, A.V. and Jangid, R.S. (2007). "Optimum Viscous Damper for Connecting Ddjacent SDOF Structures for Harmonic and Stationary White-Noise Random Excitations." *Earthq. Eng. Struct. Dyn.* **36**(4) 563-571.

Hwang, J.S., Wang, S.J., Huang, Y.N. and Chen, J.F. (2007). "A seismic Retrofit Method by Connecting Viscous Dampers for Microelectronics Factories." *Earthq. Eng. Struct. Dyn.* **36**(11) 1461-1480.

FEMA 356 (2000). *Prestandard and Commentary for the Seismic Rehabilitation of Buildings*. American Society of Civil Engineers for the Federal Emergency Management Agency, Washington, D.C..

Hwang, J.S., Lin, W.C. and Wu, N.J. (2013). "Comparison of Distribution Methods for Viscous Damping Coefficients to Buildings." *Struct. Infrastruct. Eng.* **9**(1) 28-41.

Experimental Verification of an Eccentric Rolling Isolation System by Small Shaking Table Tests

Cho-Yen Yang[1], Yu-Jen Lai[2], Lap-Loi Chung[3], Shieh-Kung Huang[4], Wang-Chuen Lin[1], and Chung-Han Yu[1]

楊卓諺 [1]、賴煜仁 [2]、鍾立來 [3]、黃謝恭 [4]、林旺春 [1]、游忠翰 [1]

Abstract

Isolation systems have proved to be an effective way to control structural responses by shifting the fundamental frequency from the dominant frequency of earthquakes. However, those conventional isolation systems possessing low fundamental frequency may be invalid under near-fault earthquake conditions, which also possess low-frequency content, and may even fail due to excessive displacement response. Therefore, many researchers have changed their focus to nonlinear isolation systems, one of which is the eccentric rolling isolation system (ERIS). The dynamic behavior of the ERIS has been established by past research; the frequency of the system varies with the rolling angle, which can mitigate the resonance effect when the system is subjected to a near-fault earthquake. In this paper, the feasibility of the ERIS is further investigated by shaking table tests. The prototype specimen also proves that its mechanism has practical applications.

Keywords: nonlinear isolation system, eccentric rolling system (ERIS), shaking table test

Introduction

The issue of long-period structures subjected to near-fault ground motions has attracted more attention after several big earthquakes occurred worldwide; these include the 2008 Wenchuan, 2010 Chile, and 2011 Tohoku earthquakes. Near-fault earthquakes differ from far-field earthquakes in that they possess low-frequency content and the velocity pulse may induce permanent displacement. Conventionally, the isolation period lies between 2 s and 3 s (0.33-0.5 Hz), which is also the dominant frequency range of near-fault ground motions. Issues could arise when an isolated structure has a high probability of being excited by near-fault ground motions, which may make the isolation system invalid due to resonance (Wipplinger 2004; Yegian and Kadakal 2004; Lu et al. 1997). Taking friction pendulum bearings (FPBs) as an example, the isolation period of an FPB is controlled by the radius of the sliding surface, which means that it is fixed when the radius is determined. This also results in a linear restoring force of the FPB, which causes a resonance effect when the isolation system

with FPBs is subjected to near-fault ground motions. To mitigate or avoid this issue, several researchers have indicated that an isolation system with a nonlinear restoring force may be a solution. An isolation system possessing a nonlinear restoring force has an isolation frequency (or period) that is not fixed, thus mitigating the resonance effect. Jangid and Londhe (1998) proposed an elliptical rolling isolation system, in which an elliptical rolling rod was installed in a five-story shear building. From simulation results, the absolute acceleration at the roof after isolation was reduced from 13.26 m/s^2 to 2.54 m/s^2. Butterworth (2006) proposed a similar concept by combing two half circles non-concentrically. Another study improved the friction pendulum bearing by suggesting a variable curvature of the sliding surface (Pranesh and Sinha 2002). Chung et al. (2009) and Yang et al. (2010) proposed an eccentric rolling isolator. In this study, the mass is fixed to a circular isolator eccentrically; the restoring force is therefore also nonlinear and the frequency varies with the rolling angle. The effectiveness of this particular nonlinear rolling isolation system under near-fault ground motions was

[1] Associate Researcher, National Center for Research on Earthquake Engineering
[2] Graduate Student, National Taiwan University
[3] Adjunct Emeritus Advisor, National Center for Research on Earthquake Engineering
[4] Assistant Professor, National Chung Hsing University

numerically verified. The resonance effect was significantly mitigated compared with a linear isolation system. Such types of nonlinear isolators usually possess a stiffness softening effect to guarantee good acceleration reduction. However, a softer stiffness also results in a larger isolation displacement. A well-developed design method is necessary for nonlinear isolators. Otherwise, the isolation system may be ineffective due to the excessive displacement response.

To further study and examine the eccentric rolling isolation system (ERIS), a shaking table test was conducted and results are presented in this paper. The theoretical model and the feasibility of the proposed mechanism are both verified by experimental results.

Mathematical Model

A schematic diagram of the ERIS is presented in Figure 1. The mass m representing the isolation object is pinned to the circular isolator. The radius of the circular isolator is R, and the distance between the pin and the center of the isolator is αR where the α is eccentricity ($0 \leq \alpha < 1$). Only one degree of freedom θ is adopted to describe the response of the system. To derive the equation of motion for the ERIS subjected to seismic excitation, the coordinate X_g representing the ground displacement is introduced. The position vector of the mass is obtained from:

$$\vec{X} = [(R\theta - \alpha R \sin\theta) + X_g]\mathbf{i} + (R - \alpha R \cos\theta)\mathbf{j} \tag{1}$$

To derive the equation of motion, Lagrange's equation (Eq. (2)) is introduced.

$$\frac{d}{dt}\left(\frac{\partial L}{\partial \dot{\theta}}\right) - \frac{\partial L}{\partial \theta} = Q^{N} \tag{2}$$

where Q^{N} is the non-conservative force for the corresponding degree of freedom. Lagrangian L is the difference between the kinetic and potential energy of the system. In this paper, the friction force is considered for energy dissipation (Eq. (3)):

$$Q^{N} = -f_r \alpha R \tag{3}$$

Taking the time derivative of Eq. (1) and substituting the result and Eq. (3) into Eq. (2), the equation of motion as shown in Eq. (4) can be obtained after reordering.

$$m\left(R^2 + \alpha^2 R^2 - 2\alpha R^2 \cos\theta\right)\ddot{\theta} + m\alpha R^2 \sin\theta \cdot \dot{\theta}^2 + mg\alpha R \sin\theta + f_r \alpha R = -m\left(R - \alpha R \cos\theta\right)\ddot{X}_g \tag{4}$$

Shaking Table Test

The prototype of the ERIS mechanism is designed to be effective in only one direction. The uniaxial shaking table test was planned and conducted accordingly. The setup of the specimen is illustrated in Figure 2. The total weight of the specimen excluding the racks was 18.78 kg. The weight of each circular isolator (spur gear) was 2.06 kg, and the weight of the superstructure was 10.54 kg. The radius of the circular isolator and eccentricity were 7.5 cm and 0.3, respectively. The friction due to rolling and rotation of the bearing at the center of the gear were considered for the friction damping. For the sensor allocation, a total of six channels were used to measure the acceleration and displacement responses (Figure. 3). Two accelerometers were installed at the center of the platform to measure the horizontal (parallel to the loading direction) and vertical accelerations, and one accelerometer was installed at the corner of the platform to check whether or not torsion occurs. A laser displacement transducer was installed on the shaking table to measure the isolation displacement.

Different types of input excitations are used in experiments, including sinusoidal, white noise, and seismic excitation. In this paper, only sinusoidal and seismic excitations were introduced. In sinusoidal cases, various frequencies with a fixed displacement amplitude equal to 30 mm were considered (displacement control), and the hysteresis is compared in Figure 4. Figure 4 shows that the isolation displacement increases with decreasing frequency of excitation, and the nonlinear behavior of the ERIS also becomes more obvious. The softening effect in stiffness was observed when the isolation displacement was roughly equal to 100 mm. This phenomenon conforms with the simulation results in a previous study.

In the case of seismic excitation, three earthquakes, Kobe, Chi-Chi (TCU068), and El Centro in two horizontal directions (i.e., a total of six ground motions) with various amplitudes were adopted. The seismic performances in acceleration and displacement after isolation are summarized in Figure 5 and 6. In Figure 5, the acceleration ratio in the Y direction is defined as the maximum absolute acceleration after isolation divided by the peak ground acceleration (PGA), which can thought of as an acceleration reduction. For the cases shown in Figure 5, the ERIS is effective as all acceleration ratios are smaller than 100%. On the other hand, the isolation displacement lies within the range 10-120 mm (Figure 6). The cases of the El Centro earthquake in the north-south and Chi-Chi (TCU068) earthquake in the east-west directions are examples discussed in detail.

The seismic performance of the ERIS under the El Centro N-S ground motion is tabulated in Table 1. Within the PGA range 0.240-0.434 g, the acceleration

ratio increased from 38% to 54%, which indicates that the ERIS is effective in reducing the ground acceleration transmitted to the superstructure. The isolation displacement corresponding to the same PGA range increased from roughly 19 mm to 59 mm. The seismic performance under the Chi-Chi (TCU068) earthquake excitation is shown in Table 2. In this case, experiments with a displacement amplitude smaller than 300% cannot be conducted due to the stroke limitation of the actuator. For the two PGA cases, the acceleration ratios were 70% and 67%, respectively. The maximum isolation displacement for an amplitude of 300% case was only 28.3 mm.

Conclusions

Past research on the eccentric rolling isolation system (ERIS) has focused on theoretical or numerical analysis. To address the lack of experimental studies on the ERIS, a uniaxial shaking table test was conducted to verify the accuracy of numerical simulation and the feasibility of the prototype mechanism. Based on the experimental results, the ERIS indeed shows its effectiveness under seismic excitations. The mechanism is also proven to have possible practical applications in design of isolation systems.

References

Wipplinger, L.A., "Dynamic testing of a masonry structure on a passive isolation system," Journal of Architectural Engineering; 10:15-21 (2004).

Yegian, M.K., Kadakal, U., "Foundation isolation for seismic protection using a smooth synthetic liner," Journal of Geotechnical and Geoenvironmental Engineering, 130:1121-1130 (2004).

Lu, L.Y. and Yang, Y.B., "Dynamic Response of Equipment in Structures with Sliding Support," Earthquake Engineering and Structural Dynamics; 26(1): 61-76 (1997).

Jangid, R.S., Londhe, Y.B., "Effectiveness of elliptical rolling rods for base isolation," Journal of Structural Engineering 124:469-472 (1998)

Butterworth JW. Seismic response of a non-concentric rolling isolator system. Advances in Structural Engineering; 9:39-54 (2006).

Pranesh M. and Sinha R., "Earthquake Resistant Design of Structures using the Variable Frequency Pendulum Isolator", Journal of Structural Engineering, Vol. 128, No. 7, July 1(2002)

Yang, C.Y., Hsieh, C.H., Chung, L.L., Chen, H.M., and Wu, L.Y., "Effectiveness of Eccentric Rolling Isolation System with Friction Damping", Journal of Vibration and Control, DOI:10.1177/1077546311428633 (2010).

L.L. Chung, C.Y. Yang, H.M. Chen, L.Y. Lu. "Dynamic behavior of nonlinear rolling isolation system", Structural Control and Health Monitoring, Vol. 16, pp. 32-54 (2009).

Table 1. Seismic performance (El Centro)

El Centro N-S					
Amplitude (%)	300	400	500	600	700
PGA (g)	0.240	0.273	0.330	0.384	0.434
max. abs. acc. (g)	0.091	0.128	0.167	0.224	0.235
max. isolation disp. (mm)	19.35	28.15	37.89	49.58	58.61

Table 2. Seismic performance (Chi-Chi TCU068EW)

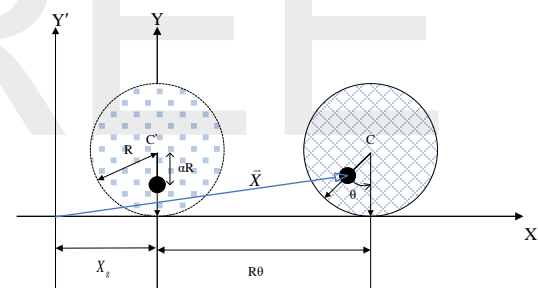| Chi-Chi TCU068 E-W		
Amplitude (%)	200	300
PGA (g)	0.124	0.170
max. abs. acc. (g)	0.087	0.114
max. isolation disp. (mm)	15.12	28.30

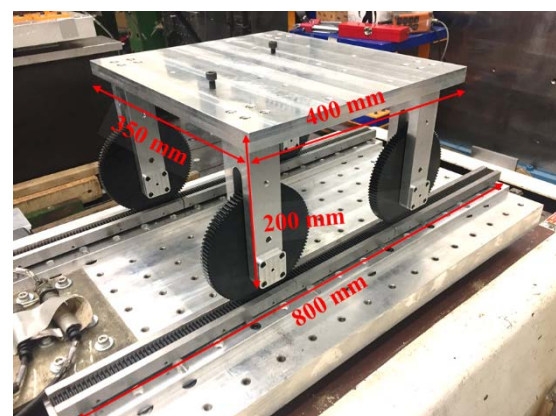Figure 1. Schematic diagram of the eccentric rolling isolation system (ERIS)
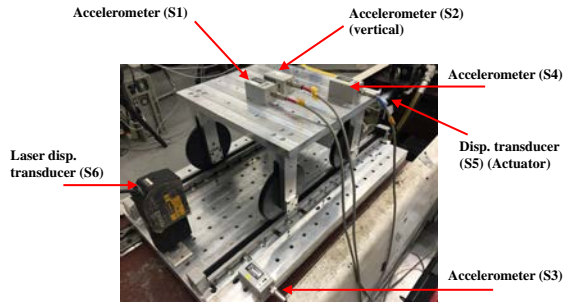

Figure 2. Specimen setup
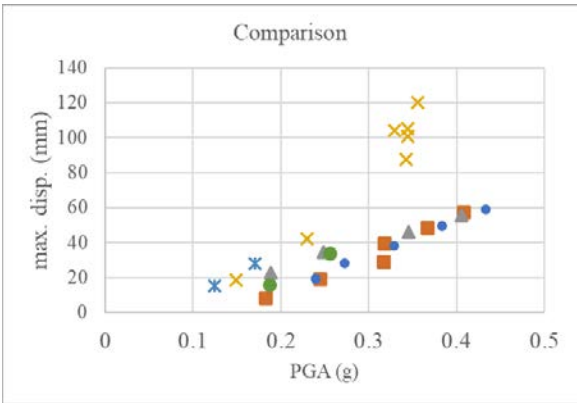
Figure 3. Sensor layout

Figure 6. Comparison of isolation displacement under seismic excitation
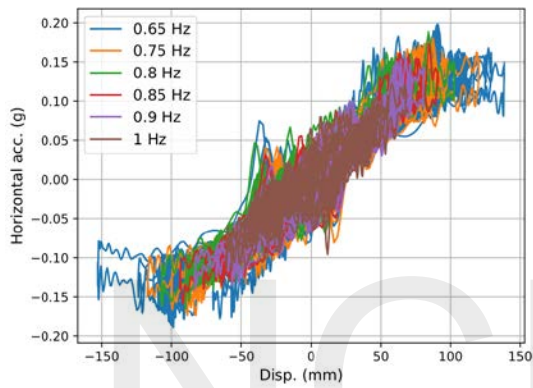
Figure 4. Comparison of hysteresis under sine wave excitation
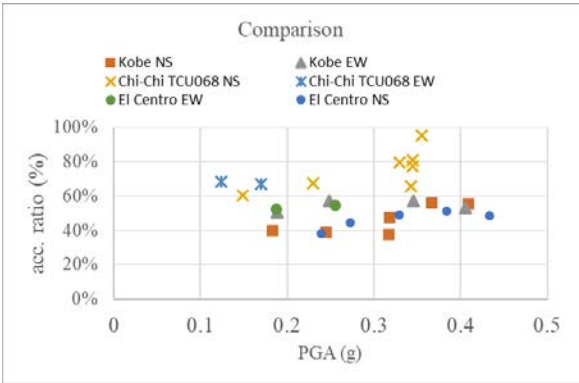
Figure 5. Comparison of acceleration reduction under seismic excitation

Experimental Studies of Seismic Evaluation and Strengthening Strategies for Small-bore Piping

F.-R. Lin [1], C.-Y. Chen[2], J.-F. Chai [3], Z.-Y. Lin [4]

Abstract

In recent years, due to the vigorous development of performance design concepts, the seismic resistance of building structures has been improved, and the main disasters and economic losses caused by earthquakes have shifted from structural to non-structural systems. This study takes a hospital as an example to explore the seismic performance of pipelines subjected to different types of earthquakes, damage to ceilings, water leakage, partial collapse, and other failure modes. The results of shaking table tests and numerical model analysis are used to verify the simplified evaluation methods.

Keywords: non-structural components, fire protection sprinkler system, shaking table tests, seismic strengthening devices, numerical analysis, simplified evaluation

Introduction

During small- and medium-scale earthquakes, a fire-protection sprinkler system might be damaged and cause leakage of small-bore piping, and sprinkler heads might impact ceiling boards resulting in falling dusts and debris. In large-scale earthquakes, anchorage or supports of sprinkler piping systems might lose seismic capacity. Damage related to sprinkler piping may cause interruption of the normal medical functions of hospitals and fail to prevent secondary disasters such as fires after earthquakes. Therefore, improvement of seismic performance designs of fire-protection sprinkler systems is necessary.

In this study, a full-scale fire-protection sprinkler piping system with an area of approximately 10 m x10 m was suspended on the shaking table in the Tainan Laboratory of the National Center for Research on Earthquake Engineering. Shaking table tests were carried out to compare the effects of different seismic strengthening configurations. Floor responses of two kinds of buildings under far-field or near-fault earthquakes were adopted as input motions. Numerical models simulating the seismic response of the hospital pipeline system were established to verify the simplified evaluation method. The research contents are briefly described as follows:

1. Taking the fire-protection sprinkler piping system of a hospital damaged during the 2010 Jiaxian earthquake as an example, a full-scale fire-protection sprinkler piping system was recreated and hung by a rigid test frame in the laboratory. As shown in Figure 1, the tested sprinkler piping specimen covered two sickrooms and an outside corridor. The part of the sprinkler piping damaged during the Jiaxian earthquake was tested. The real main pipe of the sprinkler system along the corridor exceeds the range of the shaking table. Therefore, the boundary condition of the tested partial main pipe was designed according to initial simulation results of moment distribution under earthquakes. In addition to the original configuration, three types of seismic strategies were adopted: braces of the main pipe, diagonal cables for branches or sprinkler heads, and flexible hoses for small-bore piping at wall penetrations.

2. The seismic behavior of the sprinkler piping system covering the entire floor plan was evaluated by numerical analysis with SAP2000 software. Comparing numerical analysis and shaking-table test results of part of the piping system, the accuracy or conservativism of analysis parameters of nonlinear dynamic analysis were verified and then applied to the complete numerical model of the sprinkler piping system covering the entire floor plan. Component parameters of seismic devices including bracing

---

attachments, wire cables, and flexible hoses were set according to the results of specific cyclic-loading tests.

3. In order to enable engineers to design sprinkler piping conservatively without complex numerical analysis, the seismic behavior of the sprinkler piping observed in shaking table tests was used to adjust parameters of the simplified evaluation method (Tsai, 2018) and thus improve its effectiveness and accuracy, as shown in Figure 2.
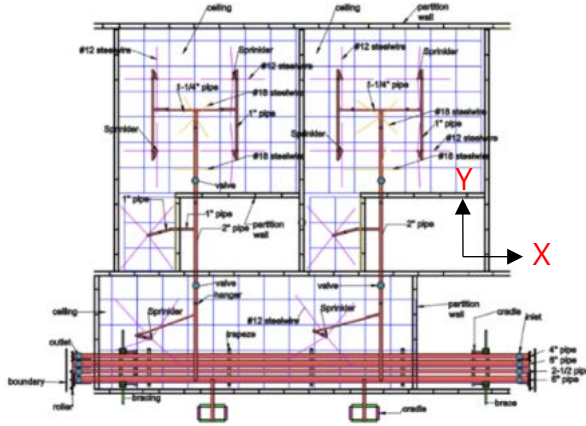
Figure 1. Test specimen of sprinkler piping (Su, 2020)
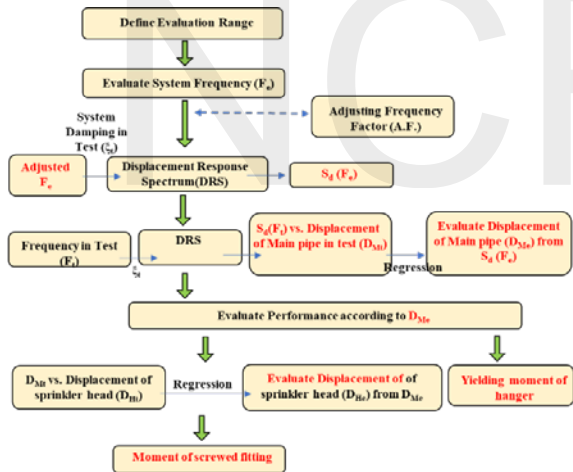
Figure 2. Simplified evaluation flowchart

Effectiveness of Seismic Improvement Strategies For Sprinkler Piping

Seismic strategies

Based on the National Fire Protection Association NFPA13 standard, this research proposes four seismic improvement strategies for the example case. Table 1 lists the strengthening devices of each strategy. Strengthening devices used are main pipe bracing, flexible hose, and diagonal steel-wire cables.

Seismic performance of sprinkler piping with strengthening devices

1. Axial force of main pipe bracing

As shown in Fig. 1, based on the damaged example case, the main source of inertia force is from the main pipe along the corridor in the *X* direction. Therefore, the seismic response of the piping system in the *Y* direction is controlled by the fundamental mode of lateral movement of the main pipe, which can be evaluated by the corresponding spectral acceleration of input motion in the *Y* direction. Figure 3 depicts the comparison of axial forces of the diagonal braces of the main pipe due to the floor spectral acceleration for three configurations: SBH, AXX, and AXF cases. The spectral acceleration values corresponding to the piping system frequency in the *Y* direction were obtained from the response spectrum of the test frame. The axial forces of the braces on both sides were derived from the measured maximum strain values under each shaking table test. Comparing the SBH and AXF cases indicated in Figure 3, due to the smaller frequency of the AXF system, both the spectral acceleration value and axial force of braces were amplified under the same input motion (3DNDL40). On the other hand, the flexible hoses decreased the effects of the partition walls on the response of piping, so that both the displacement response of the pipeline system and the axial force of the diagonal brace were amplified. From test results, it can be seen that more consideration should be given to the seismic capacity of diagonal braces while installing flexible hoses arranged near wall penetrations.

Table 1 Test configurations

	Seismic brace of main pipe (A、S)	Restraint of branch lines (B)		Restraint of sprinkler heads (H)		Flexible pipe (F)
		Left room	Right room	Left room	Right room	
Case 1 (SBH)	V	V	V	V	V	
Case 2 (AHLABR)	V		V	V		
Case 3 (AXX)	V					
Case 4 (AXF)	V					V
Original (XXX)						

V: installed devices
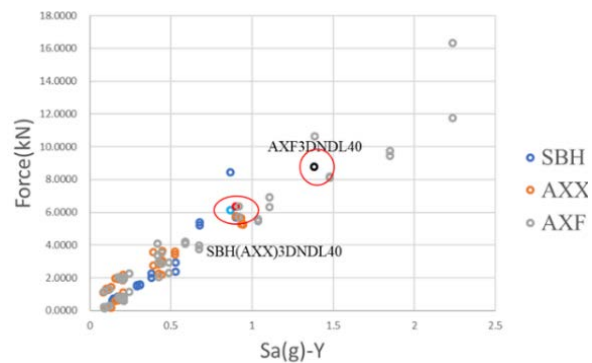
Figure 3. Comparison of axial forces of braces

2. Leakage situation

The example case shows that the damaged threaded joint of the one-inch drop could easily cause leakage in the hospital. Therefore, the seismic capacity of the threaded joint of the one-inch branch pipe is also one of the important factors in the design of the fire sprinkler system. Table 2 depicts a comparison of the bending moment and water pressure of the one-inch pipe when each test configuration was damaged or reached the maximum input motion. Table 2 also shows that there was no leakage in terms of the SBH and AXF tests. The test results verify the effectiveness of the steel-wire cables to branches and drops. In addition, the use of small-bore flexible hoses near wall penetrations increases the displacement response of the piping system during earthquakes, but it can reduce the damage at the threaded joints of the one-inch branch pipes.

Table 2 Bending moment of one-inch pipe and leakage situation

Configuration	Input motion	Water pressure (kgf/cm2)	1" pipe moment (kgf-cm)
AXF	3DNDL60 no leakage	no leakage	338
			-410.3
AXX	Left room	3DNDL40	no leakage	3110
			-3179
SBH	3DFDH60 no leakage	no leakage	547.6
			-110.5
XXX	1YNDL10	6.87	5540
		6.996	-5061

Configuration	Input motion	Water pressure (kgf/cm2)	1" pipe moment (kgf-cm)
AXF	3DNDL60 no leakage	no leakage	606.4
			-436.7
AXX	Right room	3DNDL40	6.758	3851
		6.77	-2898
SBH	3DFDH60 no leakage	no leakage	565.4
			-277.4
XXX	1YNDL10	no leakage	5504
			-2264

3. Effects on adjacent ceiling systems

For commercial buildings, sprinkler heads of the fire protection system are generally arranged at the center of ceiling boards. Therefore, excessive relative movement between sprinkler piping and suspended ceiling systems could easily result in impacts between ceiling boards and sprinkler heads. From previous studies and component tests of ceiling boards (Tsai, 2018), when the displacement of a sprinkler head is equal to or greater than 16.6 mm, it is judged that the mineral-fiber ceiling board was torn and damaged. Figure 4 compares the sprinkler head displacement of each configuration due to the spectral floor acceleration to evaluate the ceiling failure situation. The displacement of the sprinkler head in the original configuration (XXX) greatly exceeds 16.6 mm. It can

be seen that under the same spectral acceleration, the displacement of the sprinkler head in the SBH configuration is small. Therefore, the seismic steel-wire cables and braces of the main pipe are verified to decrease effects on the adjacent ceiling system. On the other hand, from the comparison between the AXX case and the AXF case, although the installation of the flexible hoses reduces the bending moment of the one-inch branch pipe, it also causes an increase of sprinkler head displacement due to the lower displacement limitation offered from the partition wall. Therefore, the displacement response of sprinkler heads in the AXF case was larger than that in the AXX case.
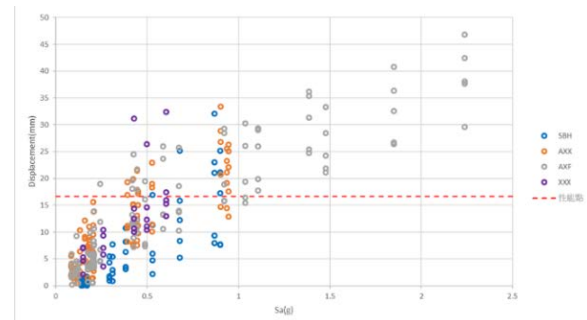
Figure 4. Comparison of sprinkler head displacement

Numerical Model Analysis

In this study, SAP2000 software was used to establish numerical models of each test configuration (Figure 5). The parameter settings of the numerical models were verified with shaking table tests, and these were extended to the numerical model of the complete hospital pipeline system (Figure 6).
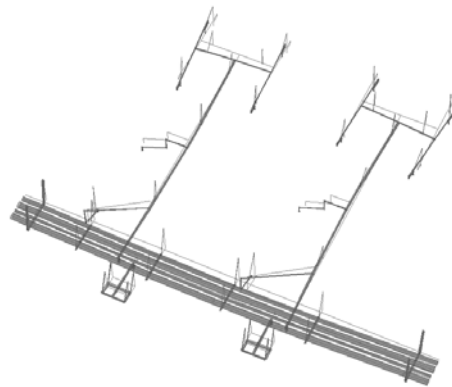
Figure 5. Numerical model of partial pipeline system
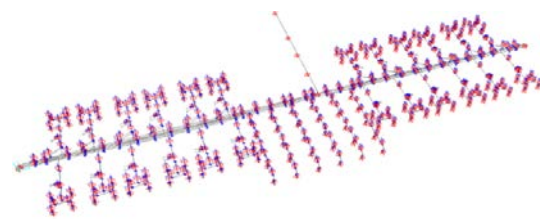
Figure 6. Numerical model of whole pipeline system

Figure 7 depicts displacement responses of the main pipe of the tested AXX case (blue line), the corresponding numerical model (red line), and the numerical model covering the whole floor plan (black line). It can be seen that due to the nonlinear response of sprinkler piping under large-scale floor motion, the numerical peak value (red line) and the tested value (blue line) are different. Numerical responses of the main pipe of partial (red line) and complete (black line) models are quite similar due to the boundary condition of the partial main pipe; this boundary condition was carefully designed based on the location of the inflection point of the main pipe shown in the initial numerical modal analysis of the complete piping system. Figure 8 depicts the comparisons of maximum main pipe displacement of tests and numerical results for four tested cases. Most of the numerical results are smaller than test results; this unconservative tendency requires attention. According to test and analysis results, a safety factor for numerical analysis is proposed to bring the numerical analysis results closer to the real response of the main pipe.
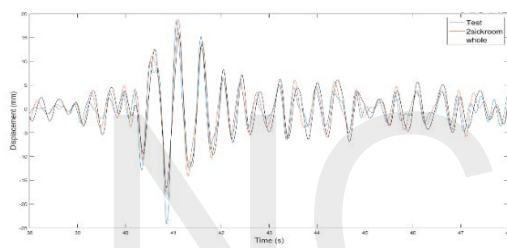
Figure 7. Displacement response of the main pipe in the AXX case
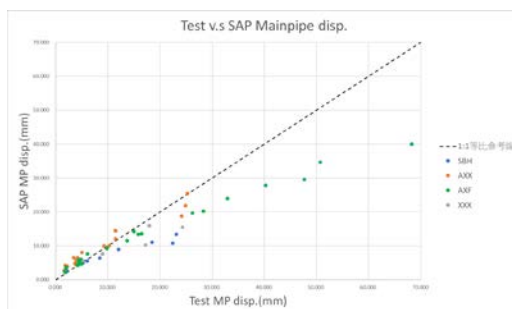
Figure 8. Maximum displacement of the main pipe

Simplified Evaluation And Verification

The third part of this study uses the floor spectral displacement to evaluate the displacement response of the main pipe along the corridor, and then estimates the dynamic response of related branch lines covering sickroom systems from the displacement response of the main pipe. As shown in Figure 9, the relationship between spectral displacement and the displacement response of the main pipe is adopted to evaluate the displacement response of the main pipe.
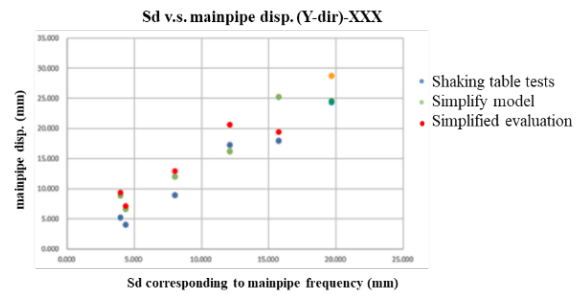
Figure 9. Relationship between responses of main pipe and spectral displacement

Conclusions

The effectiveness of three types of seismic restraint device were tested: braces with well-designed attachments for the main pipe, steel cables for branch lines, and flexible hoses for penetrations. Braces on main pipes with well-designed attachments were found to be most critical in controlling the majority of inertial forces acting on the piping system. Steel cables restrain displacements of sprinkler heads but effectiveness is decreased due to the necessity of maintaining slack to keep the piping level with the ceiling system. Flexible hoses were effective in decreasing local impact forces near wall penetrations. While bracing can reduce damage from impacts onto adjacent ceiling systems and architectural components, the optimum strategy to avoid leakage is to strengthen the main pipe with braces and to use flexible hoses near wall penetration to decrease demands on screwed fittings, or to use braces and steel cables to limit the movements of the main pipe and branch lines, respectively.

References

1. National Fire Protection Association (NFPA), Standard for the Installation of Sprinkler Systems, NFPA 13, U.S, 2019.

2. Yung-An Tsai, Seismic Performance Assessment of Strengthened Fire Protection Sprinkler Piping Systems in Hospitals, 2018.

3. Pei-Ru Wu, Seismic Performance of Flexible Hose of Fire Protection Sprinkler Piping Systems, 2020.

4. Shao-Chun Tseng, A Study on Seismic Behavior of Fire Protection Sprinkler Piping Systems in Hospital, 2020

5. Cheng-Yen Su, A Study on Seismic Displacement-Limiting Devices of Fire Protection Sprinkler Piping System, 2020

Experimental Study on Sloshing Modes and Frequencies of Storage Liquid in Rectangular Tanks

Wei-Hung Hsu[1], Juin-Fu Chai[2], Fan-Ru Lin[3] and Yi-Jun Kao[4]

徐瑋鴻[1]、柴駿甫[2]、林凡茹[3]、高翊鈞[4]

Abstract

Storage tanks are often used to store various liquids, such as water, petroleum, liquefied natural gas, and chemicals. They can be vertical or horizontal tanks. Liquid storage tanks are important facilities in industry, and their seismic capacity is often an important performance objective in tank design. When the storage tank is subjected to an earthquake, it will cause sloshing behavior of the liquid within. The liquid oscillation mode (also known as the convective mode) and its frequency affect liquid sloshing behavior as well as the seismic response of the storage tank, which may cause damage to the tank body and roof, even cause liquid overflow. Therefore, the convective modes and their frequencies are important bases for exploring the liquid sloshing behavior.

The sloshing behavior of the liquid caused by an earthquake is quite complex, often being a combination of multiple convective modes. Moreover, breaking waves are generated when the liquid hits the wall of the storage tank. In this study, a small-scale storage tank shaking table test is performed to understand the seismic response of the liquid. To explore the convective modal responses at different liquid levels, an impulse input motion with a frequency bandwidth of 0.3–2 Hz is used in the test such that free oscillation of the liquid is induced. Therefore, the fundamental and higher convective modes and frequencies could be extracted from the shaking table test. Based on this, the relationship between convective modes and the liquid sloshing behavior is discussed further.

Keywords: shaking table test, storage tank test, convective mode, fluid–structure interaction

Introduction

Past earthquakes have had a great impact on storage facilities of oil and natural gas. The damage to such facilities is often accompanied by secondary disasters such as fire. An earthquake affecting the liquid storage tank in the petrochemical industry may not cause a large number of casualties but has a wide range of influence. The failure of the function of the critical facilities will affect the needs of various industries and people's livelihood, which may in turn cause social and economic shutdown. It may also cause damage to the environment and lead to huge economic losses. Therefore, the failure of the critical facilities may have a greater impact than the failure of building structures. In view of this, it is necessary to deeply understand the causes of secondary disasters due to the seismic response of liquid storage tanks. For Taiwan, which is located in the earthquake zone, it is an urgent research topic.

The purpose of this study is to investigate the sloshing behavior of the liquid in a storage tank when it is affected by an earthquake. The convective modes and frequencies of the liquid can be analyzed from the liquid oscillation. Based on the results, the relationship between the convective modes and the liquid sloshing behavior is discussed. For this purpose, a small-scale rectangular storage tank was used in this study to conduct a shaking table test. During the test, a storage tank with various water levels was tested by an impulse input motion with a frequency bandwidth of 0.3–2 Hz. The design of the storage tank and impulse input motion are described below.

[1] Assistant Researcher, National Center for Research on Earthquake Engineering
[2] Deputy Director General & Division Director, National Center for Research on Earthquake Engineering
[3] Associate Researcher, National Center for Research on Earthquake Engineering
[4] Master Student, Department of Civil and Construction Engineering, National Taiwan University of Science and Technology

Hydrodynamic Model

According to the linear sloshing model proposed by Housner (1957), the hydrodynamic pressure can be divided into two parts: impulsive pressure and convective pressure. The impulsive pressures are generated by the impulsive movement of the wall of the storage tank. The convective pressures are generated by the oscillation of the liquid. To study the effect of hydrodynamic pressure on the storage tank, Housner (1957) simplified the complex sloshing behavior into an equivalent hydrodynamic model to consider pressures caused by the impulsive mode and the asymmetric convective mode. In the model, the impulsive mass M_0 is connected rigidly to the wall of the tank, and the convective mass Mn ($n = 1, 3, 5,…$) is spring mounted on the wall, as shown in Figure 1. In the figure, only two asymmetric modes are shown. The author used the approximate method to derive the formula for calculating the frequency of the asymmetric convective mode in the rectangular tank, as follows:

$$\omega_n^2 = \sqrt{\frac{5}{2}}\frac{g}{(l/n)}\tanh\left(\sqrt{\frac{5}{2}}\frac{h}{(l/n)}\right) \qquad (1)$$

where ω_n is the nth ($n = 1, 3, 5,…$) convective frequency, g is the gravitational acceleration, l is the half length of the tank parallel to the shaking direction, and h is the liquid level. Graham and Rodriguez (1952) derived the formula using Laplace transform, as follows:

$$\omega_m^2 = g(2m+1)\frac{\pi}{2l}\tanh\left((2m+1)\pi\frac{h}{2l}\right) \qquad (2)$$

where ω_m is the asymmetric convective frequency ($m = 0, 1, 2,…$), $m = 0$ is for the first asymmetric mode, $m = 1$ is for the second asymmetric mode, etc. Figure 2 shows that the frequencies obtained from Eq. (1) are slightly higher than those from Eq. (2), with a difference of less than 1%. Furthermore, Ibrahim (2005) mentioned that the formulae for the symmetric and asymmetric convective modes in the rectangular tank are as follows:

$$\omega_{symm\,(k)}^2 = g(2k)\frac{\pi}{2l}\tanh\left((2k)\pi\frac{h}{2l}\right) \qquad (3)$$

$$\omega_{asymm\,(k)}^2 = g(2k-1)\frac{\pi}{2l}\tanh\left((2k-1)\pi\frac{h}{2l}\right) \qquad (4)$$

where $\omega_{symm(k)}$ is the kth symmetric convective frequency and $\omega_{asymm(k)}$ is the kth asymmetric convective frequency ($k = 1, 2, 3,…$). By comparison, Eq. (2) is equal to Eq. (4).
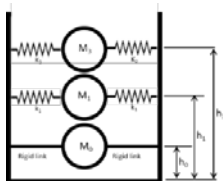
Figure 1. Illustration of the equivalent hydrodynamic model
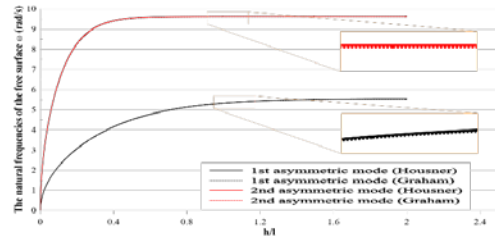
Figure 2. Comparison of the first two asymmetric convective frequencies from Eq. (1) and Eq. (2)

Test Configuration and Input Motion

In the study, two square and two rectangular storage tanks were designed to be installed on the shaking table simultaneously for testing. The tanks can be considered as rigid tanks considering their high frequencies. The dimensions of the tanks are shown in Table 1. Outside each tank is a water-receiving tank to avoid water splashing to the shaking table. Figure 3 is the design model and Figure 4 is the tank configuration on site. Table 2 lists various design water levels for testing. The corresponding convective frequencies fall in the range of 0.3–2 Hz. In the test, magnetostrictive linear-position sensors (Temposonic transducers) were used to capture the oscillation of the free surface. The sensors were installed at positions 5 cm away from the tank wall as shown in Figure 5. All positions in Figure 5 are numbered; for example, TRL1 represents the measurement point No. 1 of the low rectangular tank and TSH12 represents the measurement point No. 12 (corner point) of the high square tank. Figure 6 shows the sensor configuration on site.

The input motion was designed as an impulse wave with a frequency bandwidth of 0.3–2 Hz to stimulate free oscillation of the water surface for various water levels. Because the oscillation amplitude is related to the spectral acceleration, the acceleration response spectrum of the impulse wave is roughly maintained at a constant value between 0.3 Hz and 2 Hz to ensure the amplitude is similar. Figure 7 shows the time history and frequency spectrum of the impulse wave. Figure 8 shows the acceleration response spectrum of the impulse wave.

Table 1. Dimensions of the tanks

Square Tanks (LxWxH)		Rectangular Tanks (LxWxH)	
Low	High	Low	High
1 m x 1 m x 0.7 m	1 m x 1 m x 1.5 m	1 m x 0.5 m x 0.7 m	1 m x 0.5 m x 1.5 m

Table 2. Design water levels

Design water levels (cm)	
Square	8, 14, 20, 24, 28, 32, 36, 40, 50, 60, 80, 100
Rectangular	8, 12, 16, 20, 24, 28, 32, 36, 40, 50, 60, 80
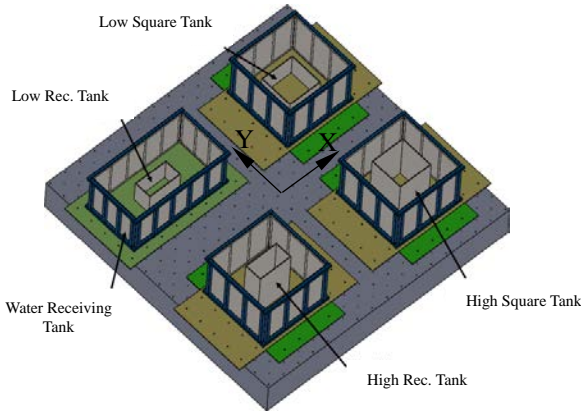
Figure 3. Design model

Figure 4. Tank configuration on site

(a) Low square (b) Low rectangular
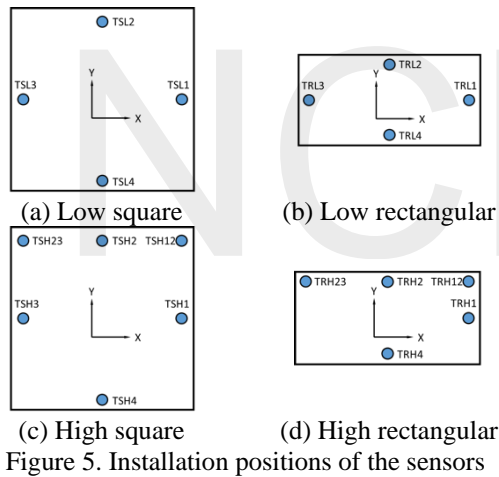
(c) High square (d) High rectangular
Figure 5. Installation positions of the sensors
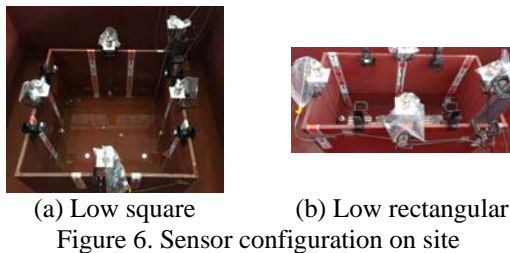
(a) Low square (b) Low rectangular
Figure 6. Sensor configuration on site
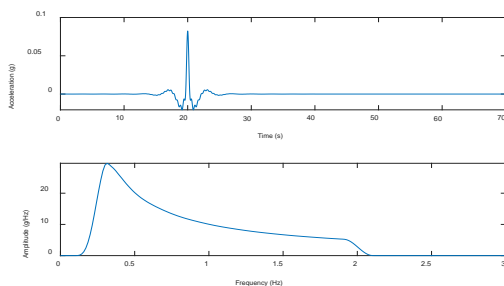
Figure 7. Time history and frequency spectrum of the
impulse wave
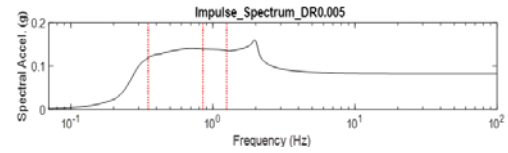
Figure 8. Acceleration response spectrum of the
impulse wave

Test Results and Discussions

The test results of the impulse wave only in a single direction, X- or Y-direction, were discussed. Figure 9 shows the test results of the X-direction oscillation of the water surface of the rectangular tank with $h = 36$ cm, and Figure 10 shows the test results of the Y-direction oscillation of the water surface of the square tank with $h = 60$ cm. The figures indicate that the oscillation frequency for the specific water level and tank length is fixed, and the oscillation frequency varies with the depth of water.

The measured oscillation of the water surface can be converted to the signal of the frequency domain by Fast Fourier transform (FFT) to obtain frequency contents of the oscillation. Therefore, the fundamental and higher convective mode frequencies of the water in the storage tank can be obtained. The following only shows frequency spectra of two cases for explanation. Figure 11 and Figure 12 show the FFT of the X-direction measured data of TRH1 for the rectangular tank with $h = 20$ cm and $h = 50$ cm, respectively. The two figures are marked with the first four convective frequencies, calculated by Eqs. (3) and (4). The figures indicate that there exists an unknown mode between the second mode and third mode or the third mode and fourth mode. The same result also appeared in other water levels and oscillation directions. Figure 13 and Figure 14 show the relationship between the first four convective frequencies and the ratio of h/l for the X- and Y-direction of the rectangular and square tanks, respectively. The figures contain the theoretical and the experimental results. It can be observed that the convective frequency increases with increasing h/l and then converges toward a constant value. The figures also show that the experimental results are close to the theoretical results except for the fourth mode in the Y-direction of the rectangular tank. The main reason for this difference is that the Y-direction dimension of the rectangular tank is too small, and the fourth mode is not significant because of the boundary effects. It can be observed that the unknown mode frequency is between the second and the third mode frequencies when $h/l < 0.64$, while it is between the third and the fourth mode frequencies when $h/l > 0.64$.
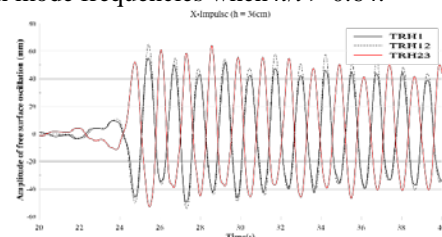
Figure 9. X-direction oscillation of the water surface
of the rectangular tank with $h = 36$ cm
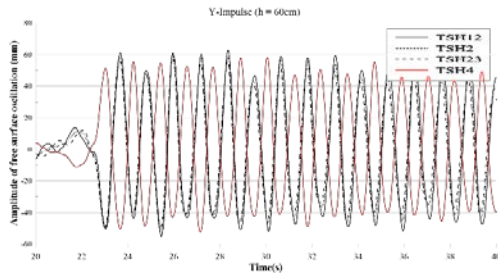
Figure 10. Y-direction oscillation of the water surface of the square tank with $h = 60$ cm
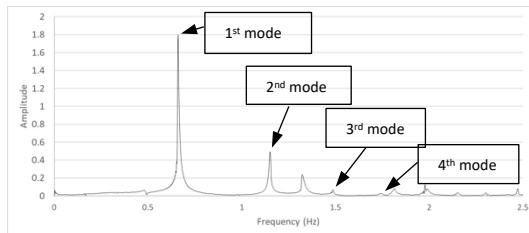
Figure 11. FFT of X-direction measured data of TRH1 for the rectangular tank with $h = 20$ cm
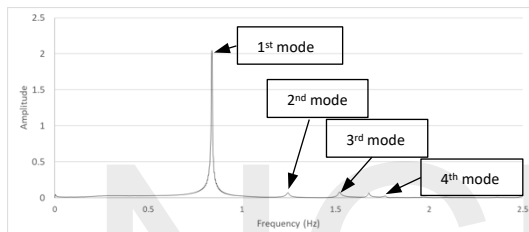
Figure 12. FFT of X-direction measured data of TRH1 for the rectangular tank with $h = 50$ cm
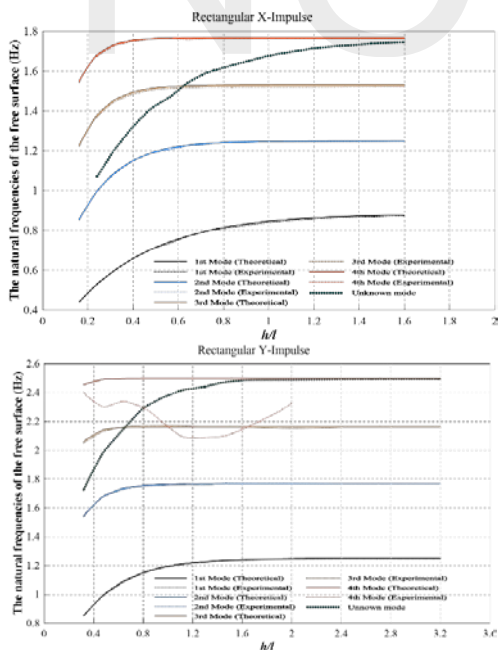
Figure 13. Relationship between the first four convective frequencies and the ratio of h/l for the rectangular tank
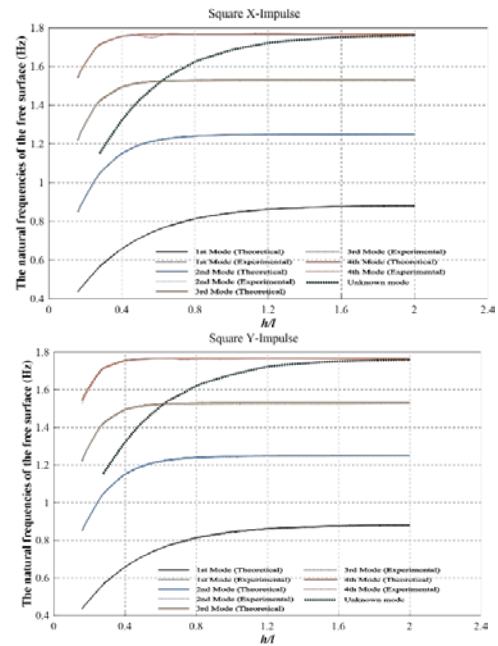
Figure 14. Relationship between the first four convective frequencies and the ratio of h/l for the square tank

Conclusions

In this study, a small-scale rectangular storage tank was used to conduct a shaking table test. The first four convective frequencies for various water levels were obtained and compared with the theoretical values. The test results indicated that the experimental frequency results are close to the theoretical values except for the fourth mode in the Y-direction of the rectangular tank. The main reason for the difference is that the Y dimension of the rectangular tank is too small, and the fourth mode is not significant because of the boundary effects. In addition, an unknown mode was observed from the test results, and its frequency was between the second and fourth modes. Its physical meaning needs to be further studied and analyzed.

References

Housner, G. W., (1957). "Dynamic pressures on accelerated fluid container", *Bulletin of the Seismological Society of America*, 47(1), 15-35.

Graham, E. W., Rodriguez, A. M. (1952). "The characteristics of fuel motion which affect airplane dynamics", *ASME Journal of applied mechanics*, 19(3), 381-388.

Ibrahim, R. A., (2005). "Liquid sloshing dynamics", *Cambridge University Press*.

Numerical Analysis of Mechanical Performance for Buried Ductile Iron Pipes for Water Transmission

Hsuan-Chih Yang,[1] Che-Yu Chang,[2] and Gee-Yu Liu[3]

楊炫智 [1]、張哲瑜 [2]、劉季宇 [3]

Abstract

Current water pipelines commonly use controlled low strength material (CLSM) as the backfill. The backfill material increases the safety of the pipeline. If it is plausible to reduce the depth of cover, the construction process would be easier, faster, and more economical. Finite element numerical analysis on ductile iron pipe with CLSM backfill is conducted in this study. The mechanical behavior for pipes of different diameters with different depths of cover under vehicle loading are studied. Results of this study summarize possible depth of cover to reduce the construction time and cost while maintaining the safety of the pipeline.

Keywords: Ductile iron pipe, Controlled low strength material, Depth of cover, Finite element analysis

Introduction

Most fundamental civil facilities have been established in Taiwan. The priority tasks are nowadays facility maintenance and replacement of aged pipelines. In particular, the latter task is complex to perform in a city in terms of the construction method, range, and cost. In light of such difficulties and to reduce public construction cost, Japan has already evaluated the possibilities and issued new guidelines in 1999 for a smaller depth of cover required for buried pipelines.

In recent years, controlled low strength material (CLSM) has been used as backfill owing to its high flowability, self-compacting, and self-leveling characteristics. This type of backfill material solves the problem of subsidence of roads. In addition, the Taiwan Water Company has switched to using higher strength ductile iron pipes (DIP). Based on the abovementioned two enhancements, research on the possibility of reducing the required depth of cover for buried pipelines is necessary. With a reduced depth of cover, the underground area could be better utilized. Moreover, the construction time, cost, and range would be considerably lower.

This study focuses on the buried DIP with CLSM as the backfill. Finite element numerical analyses are conducted to better understand the mechanical behavior of the DIP of different diameters and depths of cover under vehicle load.

Finite Element Model of the Buried Ductile Iron Pipe

This study performs finite element numerical analysis with the commercial program ABAQUS. Various diameters of DIPs are currently used. The minimum and maximum diameters, 100 mm and 2600 mm, of the DIPs are selected for this research to analyze their mechanical behavior under vehicle load. The model dimensions, material properties, and boundary conditions are described in this section. To present the interaction between the pipe, the backfill, and the soil, the model consists of three portions: the DIP, the CLSM, and the soil.

Figure 1 shows the model dimensions. The DIP diameter is denoted as D, while the distance from the pipe edge to the trench edge is denoted as B. The entire trench width would be $D+2B$. For the DIP diameters of 100 mm and 2600 mm, the lengths B are 20 cm and 50 cm, respectively. The model length in the pipe axial direction is 6 m, which is the general pipe length

between connections.

Four depths of cover are considered in this study, namely 30, 60, 90, and 120 cm. Subtracting the 10 cm pavement thickness, the depths of the CLSM above the pipe in the analysis model are 20, 50, 80, and 110 cm, respectively. In addition, the CLSM is only used as the backfill in the trench, and the surrounding soil is still the support of the trench. Therefore, the surrounding soil is also considered in the analysis model.

As for the soil width, based on the pile foundation design, the interval of piles should be twice the pile diameter to avoid pile group effects. When possible, the interval should be larger than three times the pile diameter. In terms of the soil depth, according to the theory of bearing capacity of foundation, failure usually occurs at a depth of 1–1.5 times the foundation width.
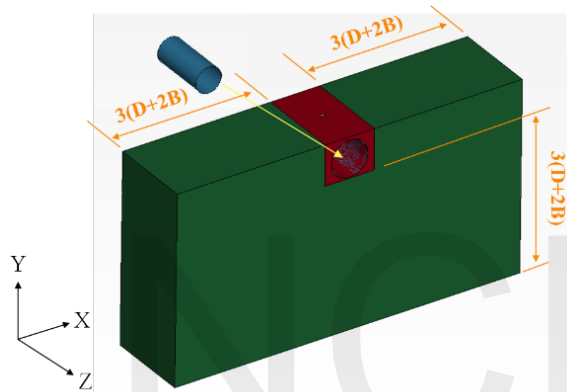
Figure 1. Analysis model dimensions for DIP Φ2600

Given the above-mentioned effecting range, the soil dimensions of this study are defined as three times the trench width on both sides of the trench as well as the depth below the trench bottom. Taking the DIP with a diameter of 100 mm as an example, the trench width is 50 cm, and therefore, the soil width is 150 cm on each side, and the soil depth is 150 cm measuring from the bottom of the trench.

Figure 1 shows the model dimensions for the DIP with a diameter of 2600 mm (DIP Φ2600) and the depth of cover of 30 cm. The DIP is shown in blue, while the CLSM is in red and the soil is in green.

Table 1 shows the material properties used in this study, including the density, Young's modulus, and Poisson ratio.

Because the surrounding soil has been considered in this study, the boundary conditions are applied at the soil outer edges. The contact between the DIP and the CLSM and between the CLSM and the soil are tied together. No sliding or collision is expected during the analysis.

As for the loading, the DIP under vehicle load

without water pressure inside the pipe is first analyzed, followed by the case when water pressure is present inside the pipe, which could reflect the effect of the water pressure on the DIP.

The vehicle load is determined on the basis of the AASHTO-20 recommendation of a single wheel load as 7.3 ton with an impact factor of 1.35. Therefore, the vehicle load used in this study is 10 ton. This load is then applied on an area of 20 cm × 30 cm at the center of the trench top in the form of uniform loading.

Table 1. Material properties of the analysis model

	Density (tonne/mm^3)	Young's modulus (N/mm^2)	Poisson ratio
DIP	7.15e-9	1.6e5	0.28
CLSM	1.80e-9	8.7e2	0.25
Soil	1.80e-9	20.0	0.30

Analysis Results

This section presents the mechanical behavior of the DIP with diameters of 100 mm and 2600 mm under 10 ton vehicle load. Results of the four different depths of cover, namely 30, 60, 90, and 120 cm, are summarized in Tables 2, 3, 4, and 5, respectively for DIP Φ100, and in Tables 6, 7, 8, and 9, respectively for DIP Φ2600.

The maximum von Mises stress, axial stress, and hoop stress of the DIP are summarized along with their locations. The cases with vehicle load only and with both vehicle and water pressure inside the DIP are both presented in these tables.

The results show that the maximum von Mises, axial, and hoop stresses for DIP Φ100 occur at the pipe bottom despite the depth of cover. As for the DIP Φ2600, the maximum von Mises, axial, and hoop stresses occur at the pipe top right underneath the vehicle load for the depths of cover of 30 cm and 60 cm, and occur at the pipe bottom for the depths of cover of 90 cm and 120 cm.

With only vehicle load, DIP Φ100 showed decreased stress when the depth of cover was increased. As for DIP Φ2600, stress was less sensitive to the depth of cover when such was higher than 50 cm. This phenomenon is assumed to be related to the stress distribution and loading area.

When the pipe underwent vehicle load and water pressure, DIP Φ100 was not sensitive to water pressure. The stresses did not increase considerably. The trend

was still the same as that without water pressure, i.e., the stress reduced with the increase of the depth of cover.

However, DIP Φ2600 showed significantly different behavior from that of DIP Φ100. The stresses were notably higher with the presence of water pressure. For DIP Φ2600, water pressure seemed to be more critical than the vehicle load.

Table 2. Maximum stresses of DIP Φ100 with a depth of cover of 30 cm (MPa)

DIP von Mises Stress		DIP Axial Stress		DIP Hoop Stress	
Without water	With water	Without water	With water	Without water	With water
91.90 (Pipe bottom)	84.60 (Pipe bottom)	76.02 (Pipe bottom)	80.20 (Pipe bottom)	4.90 (Pipe bottom)	19.92 (Pipe bottom)

(Note: positive stress = tension; negative stress = compression; von Mises stress is always positive since it is a square root of the sum of stress values squared.)

Table 3. Maximum stresses of DIP Φ100 with a depth of cover of 60 cm (MPa)

DIP von Mises Stress		DIP Axial Stress		DIP Hoop Stress	
Without water	With water	Without water	With water	Without water	With water
42.00 (Pipe bottom)	39.00 (Pipe bottom)	38.06 (Pipe bottom)	42.24 (Pipe bottom)	1.02 (Pipe bottom)	16.03 (Pipe bottom)

(Note: positive stress = tension; negative stress = compression; von Mises stress is always positive since it is a square root of the sum of stress values squared.)

Table 4. Maximum stresses of DIP Φ100 with a depth of cover of 90 cm (MPa)

DIP von Mises Stress		DIP Axial Stress		DIP Hoop Stress	
Without water	With water	Without water	With water	Without water	With water
26.00 (Pipe bottom)	26.50 (Pipe bottom)	23.76 (Pipe bottom)	27.94 (Pipe bottom)	0.46 (Pipe bottom)	15.47 (Pipe bottom)

(Note: positive stress = tension; negative stress = compression; von Mises stress is always positive since

it is a square root of the sum of stress values squared.)

Table 5. Maximum stresses of DIP Φ100 with a depth of cover of 120 cm (MPa)

DIP von Mises Stress		DIP Axial Stress		DIP Hoop Stress	
Without water	With water	Without water	With water	Without water	With water
17.90 (Pipe bottom)	21.00 (Pipe bottom)	15.94 (Pipe bottom)	20.12 (Pipe bottom)	0.31 (Pipe bottom)	15.32 (Pipe bottom)

(Note: positive stress = tension; negative stress = compression; von Mises stress is always positive since it is a square root of the sum of stress values squared.)

Table 6. Maximum stresses of DIP Φ2600 with a depth of cover of 30 cm (MPa)

DIP von Mises Stress		DIP Axial Stress		DIP Hoop Stress	
Without water	With water	Without water	With water	Without water	With water
20.60 (Loading point)	60.80 (Loading point)	-2.10 (Loading point)	13.48 (Loading point)	7.27 (Loading point)	56.01 (Loading point)

(Note: positive stress = tension; negative stress = compression; von Mises stress is always positive since it is a square root of the sum of stress values squared.)

Table 7. Maximum stresses of DIP Φ2600 with a depth of cover of 60 cm (MPa)

DIP von Mises Stress		DIP Axial Stress		DIP Hoop Stress	
Without water	With water	Without water	With water	Without water	With water
5.30 (Loading point)	58.90 (Loading point)	-0.48 (Loading point)	14.51 (Loading point)	-0.81 (Loading point)	56.71 (Loading point)

(Note: positive stress = tension; negative stress = compression; von Mises stress is always positive since it is a square root of the sum of stress values squared.)

Table 8. Maximum stresses of DIP Φ2600 with a depth of cover of 90 cm (MPa)

DIP von Mises Stress		DIP Axial Stress		DIP Hoop Stress	
Without water	With water	Without water	With water	Without water	With water
1.37 (Loading point)	51.13 (Loading point)	-0.19 (Loading point)	14.75 (Loading point)	-0.25 (Loading point)	56.88 (Loading point)
6.00 (Pipe bottom)	60.50 (Pipe bottom)	-0.47 (Pipe bottom)	15.72 (Pipe bottom)	-1.89 (Pipe bottom)	62.75 (Pipe bottom)

(Note: positive stress = tension; negative stress = compression; von Mises stress is always positive since it is a square root of the sum of stress values squared.)

Table 9. Maximum stresses of DIP Φ2600 with a depth of cover of 120 cm (MPa)

DIP von Mises Stress		DIP Axial Stress		DIP Hoop Stress	
Without water	With water	Without water	With water	Without water	With water
0.70 (Loading point)	51.20 (Loading point)	-0.14 (Loading point)	14.86 (Loading point)	-0.28 (Loading point)	56.99 (Loading point)
6.80 (Pipe bottom)	61.60 (Pipe bottom)	-0.54 (Pipe bottom)	15.77 (Pipe bottom)	-2.07 (Pipe bottom)	62.69 (Pipe bottom)

(Note: positive stress = tension; negative stress = compression; von Mises stress is always positive since it is a square root of the sum of stress values squared.)

Conclusions

In this study, the DIPs of the minimum and maximum diameters usually used, i.e., DIP Φ100 and DIP Φ2600, were analyzed for their behavior under vehicle load. The DIP was located in a trench with four different depths of cover using the CLSM as the backfill. The surrounding soil is also taken into consideration in the analysis, as well as the water pressure in the pipes.

The results show that DIPs of four different depths of cover with and without water pressure all met the safety factor requirement of 2.

With only vehicle load, DIP Φ100 showed decreased stress when the depth of cover was increased. On the other hand, stress of DIP Φ2600 was less sensitive to the depth of cover when such was higher than 50 cm. This phenomenon is assumed to be related to the stress distribution and loading area.

When the pipe underwent vehicle load and water pressure, DIP Φ100 was not sensitive to water pressure. The stresses did not increase considerably. The trend was still the same as that without water pressure, i.e., the stress reduced with the increase of the depth of cover.

However, DIP Φ2600 showed significantly different behavior from that of DIP Φ100. The stresses were notably higher with the presence of water pressure. For DIP Φ2600, water pressure seemed to be more critical than the vehicle load.

Under four different depths of cover and different loading conditions, with and without water pressure, the maximum stresses for DIP Φ100 and DIP Φ2600 were only 91.90 and 62.76 MPa, respectively. These are less than half of the yield stress of 210 MPa. The safety factor of 2.0 was satisfied.

References

Abaqus Analysis User's Manual (6.12), 2012, Dassault Systèmes Simulia Corp.

DIRPA (Ductile Iron Pipe Research Association), 2016. Design of Ductile Iron Pipe.

日本延性鐵管協會，2000，「ダクタイル管の浅層埋設について」。

台灣自來水公司，2020，「自來水管埋設施工說明書」。

Seismic Damage Assessment of Large Water Treatment Plants in a Near-Fault Scenario

Gee-Yu Liu[1]

劉季宇 [1]

Abstract

The objective of this study is to assess the damage to large water treatment plants in a near-fault earthquake scenario. The Feng-Yuan First and Second Water Treatment Plants were selected as subjects as they were the only plants located in the near-fault area that suffered substantial damage in the 1999 Chi-Chi Taiwan earthquake. The actual and simulated ground shaking and failure at the two plants have been either specified or computed. The actual and simulated damage states of their critical components have also been determined based on documents and photographs and on fragility models, respectively. The damage states of the two plants themselves were simulated through systems analysis and were compared with the actual damage states. It was found that the method employed in this study provided the best damage estimation. However, the "actual hazards" data needed for simulation would be unavailable unless an earthquake has taken place. As a result, an improved near-fault ground failure prediction model is needed to better predict ground failure due to fault rupture.

Keywords: lifeline systems, near-fault, seismic damage, water treatment plant, 1999 Chi-Chi Taiwan earthquake

Introduction

Earthquake hazards in near-fault regions involve complicated and unpredictable ground failure due to fault rupturing and have dire effects on critical infrastructure. Large water treatment plants, electric power substations and switchyards play a pivotal role in the serviceability of lifeline systems. They usually occupy a wide area with many critical and distributed components. Once they experience earthquake hazards, the damage can be tremendous and very complicated. It is an oversimplification to assess these merely as pointwise entities. Instead, it is more appropriate to assess such facilities based on a component-to-system approach, which is the investigatory approach introduced here.

In this study, the Feng-Yuan First and Second Water Treatment Plants (FY1 and FY2) were analyzed. They are both very large and were substantially damaged in the 1999 Chi-Chi, Taiwan earthquake. In fact, they are the only water treatment plants to sustain substantial damage in recent earthquake events in Taiwan. It is fortunate that documents and photographs of their damage are still available, albeit in very limited numbers, and can be employed to approximate what actually happened not only to the two plants as a whole but also to their components individually.

Earthquake Experiences of the Feng-Yuan Water Treatment Plants

As depicted in Figure 1, FY1 and FY2 are located in the vicinity of the Chelungpu fault. FY1 in particular experienced fault rupturing at its north-western corner. In the Chi-Chi earthquake, many of the component water basins and tanks of these plants suffered damage, which resulted in failure of the two plants and a severe water outage in Taichung City following the earthquake. FY1 became inoperable due to collapse of its clear water tanks and critical water pipelines, which took years to restore. FY2 was operable, but at a reduced capacity and with poor quality water output. With this damage and reduction in functionality, the damage states of FY1 and FY2 following the earthquake can be classified as extensive (but almost complete) and moderate, respectively (台灣自來水公司，2000；葉純松，2002).

The inventory and damage data of FY1 and FY2, including the associated documents and photographs, were collected and examined in this study. In the case of FY1, whose layout is depicted in Figure 2, the critical components consisted of raw water intake stations, flocculation basins, sedimentation basins, rapid sand filters, and clear water tanks. All of these were reinforced concrete water-containing structures, and the classification of their damage states can be carefully determined according to the definitions given in Table 1, which follows the methodology of HAZUS (FEMA, 2010). Their damage states were carefully classified as well. For example, the sedimentation basin of the first water treatment unit (Figure 3) and the 15,000-ton clear water tank (Figure 4), both at FY1, were extensively and completely damaged, respectively.

Figure 1. Chelungpu fault traces around FY1 and FY2 water treatment plants
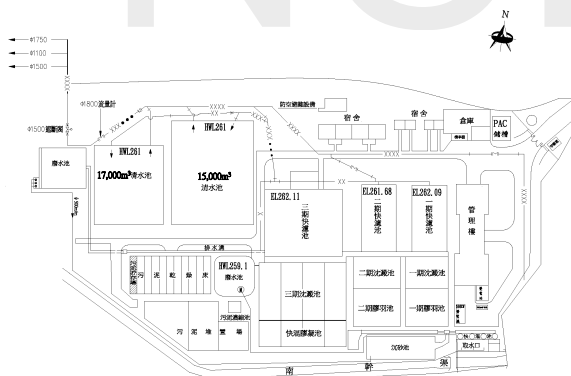
Figure 2. The layout of FY1, depicting its critical components for water treatment

Table. 1. Classification of damage states and definitions for reinforced concrete water basin/tank structures

Damage state	Definition
None	No damage
Slight	Minor cracks in structural elements, no loss of contents or functionality
Moderate	Moderate cracks in structural elements, minor loss of contents or functionality
Extensive	Severe structural damage, out of service
Complete	Collapse of structure, loss of all content or functionality

Figure 3. Damage to one of the three sedimentation basins of FY1 during the Chi-Chi earthquake

Figure 4. Damage to one of the two clear water tanks of FY1 during the Chi-Chi earthquake

Hazard

We first considered the actual hazards that occurred at FY1 and FY2 due to the Chi-Chi earthquake. Concerning ground failure, the field reconnaissance report by the Central Geological Survey indicated that ground displacements of 3.5 m vertically and 5.0 m horizontally were observed at the site directly next to the two collapsed clear water tanks of FY1 (經濟部中央地質調查所，1999). Otherwise, our observations indicate that the rest of the components of FY1 and the entirety of FY2 suffered minor or no ground displacement. Consequently, the two clear water tanks of FY1 were assumed to sustain permanent ground deformation (PGD) of 5 m, and the rest of the water basins and tanks of FY1 and FY2 were all assumed to sustain a PGD of 40 cm. The peak ground acceleration (PGA) in the neighborhood of FY1 and FY2 was found to be 354.7 gals according to the interpolation of observed data from the strong

motion stations of the Central Weather Bureau.

The simulated hazards at FY1 and FY2 can be achieved via the Taiwan Earthquake Loss Estimation System (TELES), given the adequate seismic source parameters reflecting the Chi-Chi earthquake. As a result, the simulated PGA is 593 gals, and the PGD caused by the fault rupture is 72.27 cm. The hazard of soil liquefaction can be ignored.

Fragility

Recently, the National Center for Research on Earthquake Engineering (NCREE) developed the software "Twater" for scenario-based seismic assessment of water supply systems. Twater is a sub-system of the TELES software. The damage to the water pipelines and facilities of a system can be simulated using the adequate fragility models proposed in Twater. These facilities include water treatment plants and basin and tank structures (經濟部水利署，2019). Although both are spatially assumed to be point objects for analysis, a water treatment plant is particularly specified with an "equivalent circle", according to its scale, as depicted in Figure 5. The size of the circle is used in Twater to decide how likely it would be to encounter a fault rupture.

The fragility models can predict the probabilities of exceeding the damage states of a facility as S (slight), M (moderate), E (extensive), and C (complete), given the hazard of either ground shaking or ground failure to which the facility is exposed. The parameters defining the fragility curves for ground shaking and ground failure, which are assumed to be of a cumulative log-normal functional form defined by medium (M) and standard deviation (SD), are summarized in Tables 2 and 3, respectively. The curves for ground shaking employ PGA as the variable and a medium M of unit g, while the curves for ground failure employ PGD as the variable and a medium M of unit cm.
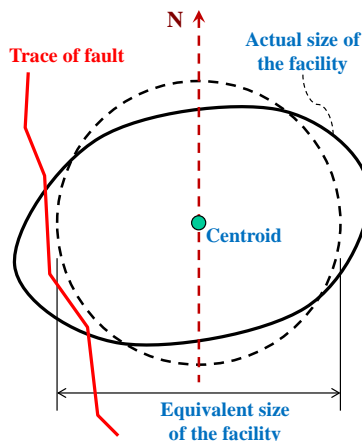
Figure 5. The spatial relationship between a water

supply facility and a fault trace considered in Twater

Table. 2. The parameters defining the fragility curves of a water treatment plant (WTP) and various basin/tank structures (BTS) in this study due to ground shaking

	Slight		Moderate		Extensive		Complete	
	M	SD	M	SD	M	SD	M	SD
WTP	0.432	0.55	0.576	0.50	0.720	0.45	1.080	0.40
BTS1	0.552	0.55	0.736	0.50	0.920	0.45	1.380	0.40
BTS2	0.504	0.55	0.672	0.50	0.840	0.45	1.260	0.40
BTS3	0.456	0.55	0.608	0.50	0.760	0.45	1.140	0.40

Table. 3. The parameters defining the fragility curves of a water treatment plant (WTP) and various basin/tank structures (BTS) in this study due to ground failure

	Slight		Moderate		Extensive		Complete	
	M	SD	M	SD	M	SD	M	SD
WTP	22	0.60	30.8	0.50	44	0.45	66	0.45
BTS1	44	0.60	61.6	0.50	88	0.45	132	0.45
BTS2	37	0.60	51.8	0.50	74	0.45	111	0.45
BTS3	24	0.60	33.6	0.50	48	0.45	72	0.45

Analysis Method

In this study, the damage state of each basin or tank structure in FY1 and FY2 was simulated using the actual and simulated hazards at these two plants. The results were further employed to compute the simulated damage states of the two plants. In this computation, only the critical components of a water treatment plant were included in the analysis. FY1 for example, which was constructed and extended in three phases, consists of three independent water treatment units in a parallel connection. Each unit consists of three components, a flocculation basin, a sedimentation basin, and a set of rapid sand filters, in series connection. The treated water from each unit is fed into either of the two clear water tanks, which are connected in parallel, and is then ready for transmission to the downtown areas. Components such as waste water basins, sludge thickening tanks, and sludge drying beds are not essential to the water treatment process and do not have to be included in analysis. Accordingly, the logic diagrams showing the water treatment processes of FY1 and FY2, together with the critical components involved, can be plotted as in Figures 6 and 7. As a result, a systems analysis was performed to determine the damage states of FY1

and FY2 from the damage state of their critical components, which were assessed via the fragility model.
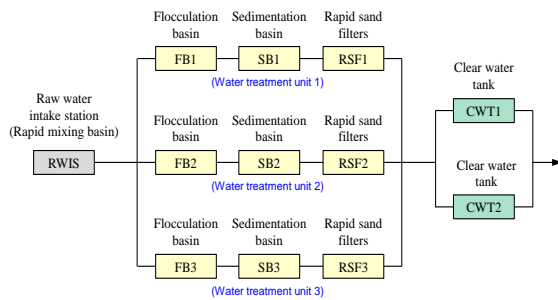
Figure 6. Logic diagram of FY1
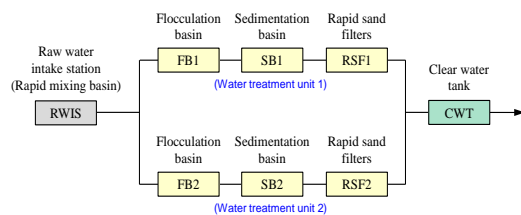
Figure 7. Logic diagram of FY2

Comparison between Actual Damage and Assessed Result

Various damage results are summarized in Table 4 for comparison. They are:

(1) The actual damage states of FY1 and FY2 and their critical components;

(2) The assessed damage states of FY1 and FY2 using the Twater fragility model and simulated hazards;

(3) The assessed damage states of FY1 and FY2 using the Twater fragility model and actual hazards;

(4) The assessed damage states of all critical components using the Twater fragility model and actual hazards and the damage states of FY1 and FY2 determined through a component-to-system approach used in this study.

Table. 4. Damage states of FY1 and FY2 and their critical components using the four methods

	(1)	(2)	(3)	(4)
FY1	E/C	E	C	C
Critical components of FY1	M~C	-	-	M~C
FY2	M	E	M	M
Critical components of FY2	M	-	-	M

It appears that Twater is able to provide reasonable, if not ideal, estimations of the damage sustained by FY1 and FY2. The method employed in this study provided the best damage estimation, including that of the critical components. However, the limitation was that the "actual hazards" data would not be available unless the earthquake took place.

Conclusions

In this study, the systems analysis method has been applied to large water treatment plants to assess their damage in a near-fault earthquake scenario. It was found that this method, a bottom-up approach covering all critical components organized in a logic diagram representing the actual water treatment process, provided the best damage estimation if the "actual hazards" are available. However, ground failure in a near-fault area following earthquakes is, so far, unpredictable, meaning that a precise distribution of permanent ground displacement over a very large water treatment plant cannot be prescribed, unless an earthquake actually occurs. An improved model for prediction of ground failure in near-fault areas due to fault rupture still needs to be developed.

References

FEMA (Federal Emergency Management Agency) (2010). Multi-Hazard Loss Estimation Methodology: Earthquake Model, Hazus-MH MR5, Department of Homeland Security, US.

台灣自來水公司 (2000)，九二一集集大震自來水搶修(復舊)紀實，台中。

經濟部中央地質調查所 (1999)，九二一地震地質調查報告，台北。

經濟部水利署 (2019)，公共給水系統地震災害影響評估之研究，研究報告，計畫編號 MOEA-WRA-1080314，台北。

葉純松 (2002)，九二一地震大臺中地區供水危機處理，都市防救災研討會論文集，台北。

Establishment of a Smart Building Management System

Ren-Zuo Wang[1] and Chih-Shian Chen[2]

王仁佐 [1]、陳志賢 [2]

Abstract

Many smart building management systems have been developed in Taiwan, but they have limited expansion capability, and the real building appearance cannot be accurately displayed. Therefore, the National Center for Research on Earthquake Engineering developed a new smart building management system that can import different types of 3D objects. This system also uses the TWD97 coordinate reference system, which can immediately integrate GPS coordinates of outdoor hardware devices. Sensors installed in a building can transmit real-time electricity consumption data to the system, and the monthly electricity bill can be calculated using the information provided by the Taiwan Power Company. In this way users can clearly understand the electricity usage of each room.

Keywords: Smart building management system, real-time monitoring, power usage information

Introduction

Most smart building management systems in Taiwan have been developed using commercial software, and so they are often limited by their software functionality and ability to expand. In addition, only simple color systems are used and it is not easy for them to display real construction materials. Building information modelling (BIM) models only use indoor local Cartesian coordinate systems, which are difficult to integrate with geodetic coordinate systems.

The smart building management system examined in this study has a better expansion capability that can import different types of data. Moreover, the system uses real world TWD97 coordinate information, which can immediately integrate the GPS coordinates of outdoor hardware devices. The advantage of a single 3D GIS graphic console is that it can visually display all management data, which is different from traditional web pages that display information across multiple pages. The system also adopts technology developed by the National Center for Research on Earthquake Engineering (NCREE) that can help to avoid maintenance issues caused by expansion of the system functions. Therefore, this system can operate continuously and can be upgraded through innovative research and technology from the NCREE year by year.

The Smart Building Management System

Using the technology developed by the NCREE, sensors in the Taiwan Car Lab, in an outdoor environment, and in the Information Security and Smart Technology R&D Building were all incorporated into a smart building management system. This structure is shown in Figure 1. The positions of the equipment corresponding to the information points are marked in the BIM model so that the system can be used to achieve daily maintenance with visual management, reduce maintenance costs, and increase maintenance management speed.
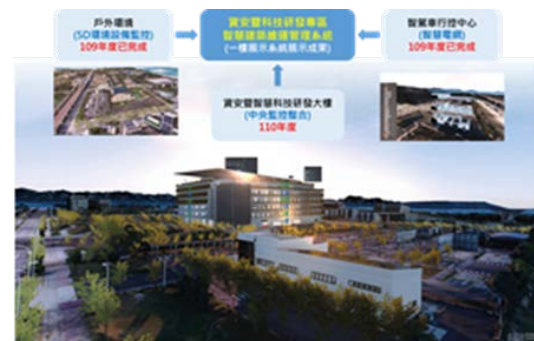
Figure 1. Architecture of the smart building management system

[1] Research Fellow, National Center for Research on Earthquake Engineering
[2] Assistant Researcher, National Center for Research on Earthquake Engine3ering

This system collects and counts data from various environmental sensors located in the Information Security and Smart Technology R&D Building, builds models of various equipment and sensors in the building, and edits the BIM model of the electromechanical and pipeline structures, as shown in Figure 2.

Figure 2. Information Security and Smart Technology R&D Building-BIM model

System Functions of the Smart Building Management System

The BIM model was modified according to an as-built drawing of the building, including the various main systems: power system, fire system, air conditioning system, illumination system, monitoring system, renewable energy system, charging pile system, etc. In addition, the sensor specification files and appearance pictures were organized. An equipment model was drawn of the real size and appearance as each real sensor and integrated into the building model to more accurately map the real world.

In order to allow managers to control the spatial location data of the sensors and equipment, the NCREE team integrated equipment models with IoT real-time monitoring data and integrated them into a high-efficiency visual 3D GIS map. This enabled the smart building maintenance system to identify abnormal signals from the equipment in the building and improved maintenance speed and management convenience. At present, the solar energy system, charging pile system, monitoring system, illumination system, power system, and environmental monitoring system of the Smart Technology R&D Building have been connected. The interface information is described as follows:

1. Solar system (Figure 3): (1) Power generation information: (A) Total real work; (B) Total virtual work; (C) Gross generation; (D) State of solar panels; (2) Power inverter information of solar energy: (A) State; (B) Work; (C) Voltage; (D) Current; (E) Frequency (F) Cumulative power generation; (G) Updating time.
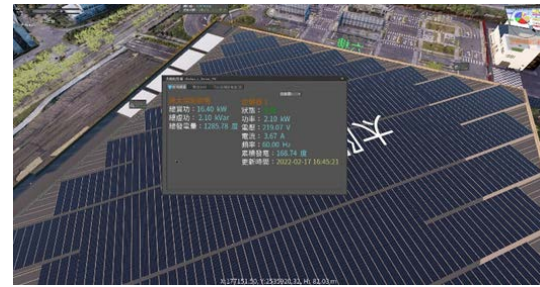
(a) Solar system panel information
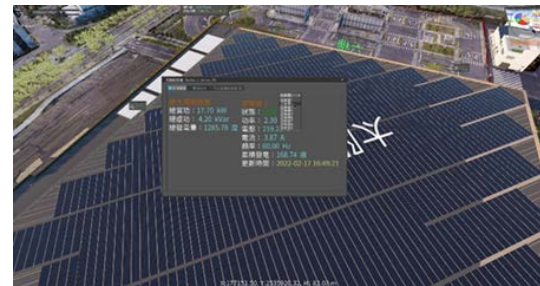
(b) Solar inverter information
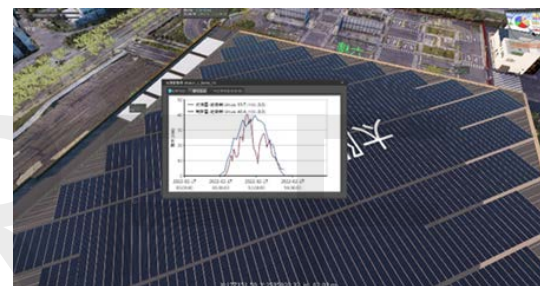
(c) Solar system real work information
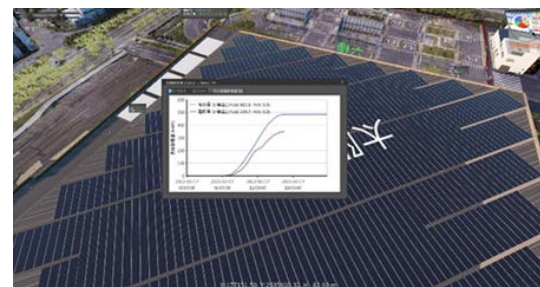
(d) Solar system cumulative power generation information

Figure 3. Solar system

2. Charging pile system (Figure 4): (1) State; (2) Voltage; (3) Current; (4) Work; (5) Start time for charging; (6) End time for charging; (7) Cumulative charge; (8) Admission time; (9) Departure time; (10) Updating time.
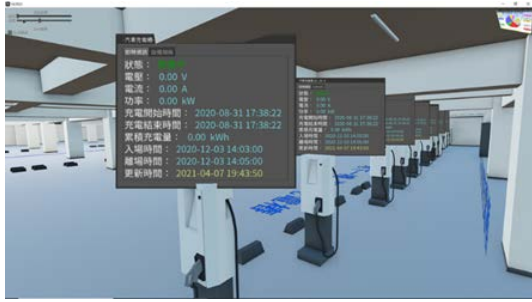
Figure 4. Charging pile system

3. Monitoring system (Figure 5): (1) Monitoring screen; (2) Updating time.

Figure 5. Monitoring system-1F

4. Illumination system (Figure 6): (1) Electric circuit information; (2) Control loop information; (3) Room information.

(a) Illumination system model
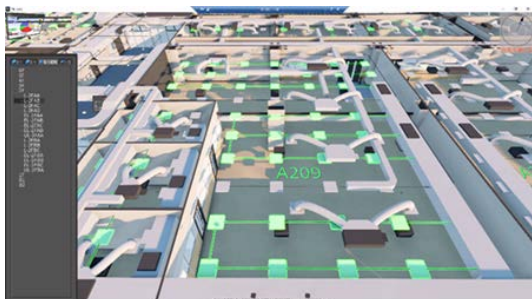
(b) Illumination system electric circuit L-2FAB
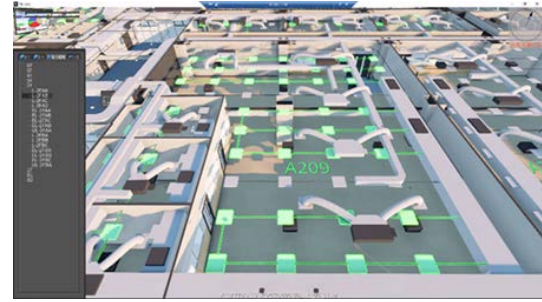
(c) Illumination system electric circuit EL-2FAB
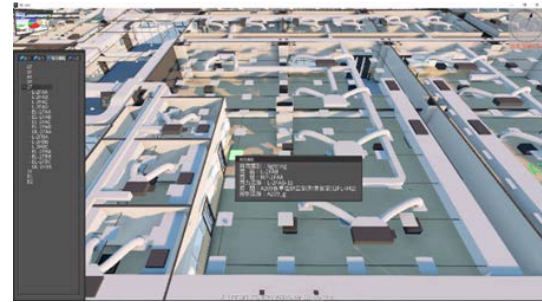
(d) Lighting equipment panel information

Figure 6. Illumination system

5. Electric power system (Figure 7): (1) Cumulative power information; (2) Power statistical analysis graphs.

(a) Cumulative power information based on floor

(b) Cumulative power information based on category

(c) Cumulative power information-1F

Figure 7. Electrical power system

6. Environmental monitoring system (Figure 8): (1) Micro weather station: (A) Air temperature; (B) Relative humidity; (C) Air pressure; (D) Wind speed; (E) Wind direction; (F) Precipitation; (G) Radiation value; (H) Updating time; (2) Air quality billboard: (A) CO_2 concentration; (B) Temperature; (C) Humidity; (D) Particulate matter concentration; (E) Updating time.
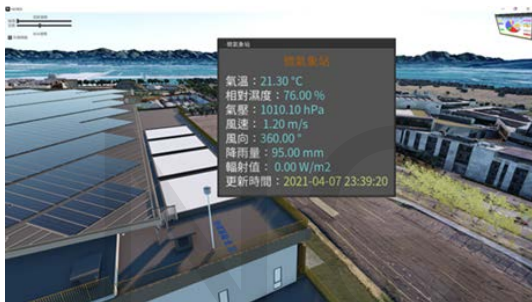
(a) Micro weather station panel information

(b) Air quality billboard information

Figure 8. Environmental monitoring system

Integration of the BIM, Rental Space, and Electricity Billing

The platform is divided into an illumination system, socket system, emergency power supply system, light current system, and an air conditioning system based on the type of electricity consumption. The building space is divided into three types: (1) public space (space that everyone can use, such as toilets or computer rooms); (2) rental space; and (3)

non-rental space (space used by the management unit). The Taiwan Power Company sends electricity from a high voltage electrical panel to a low voltage electrical panel and equipment. Based on this hierarchical relationship, the electricity consumption corresponds to the space where different circuits are located. Five types of electricity consumption, namely the illumination system, socket system, emergency power supply system, light-current system, and the air conditioning system are distributed to different users in both public space and non-public space. The color floor plan of the second floor is shown in Figure 9.

The electricity consumption of each space is obtained through the method outlined above. The contracted capacity of the Smart Technology R&D Building is 1280 kW. The electricity price table of the Taiwan Power Company is divided into a basic charge or energy charge, summer or non-summer months, and peak or off-peak times, etc., and it is used to calculate the electricity pricing of each space. The integration diagram of the BIM, rental space, and electricity pricing is shown in Figure 10.

Figure 9. Color floor plan of the second floor
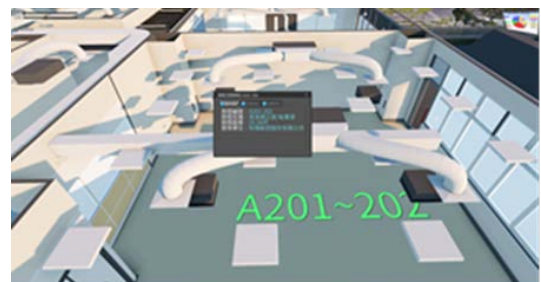
Figure 10. Integration diagram of the BIM, rental space, and electricity pricing

Conclusions

This research developed a smart building management system. This system relies on sensors installed in a building that transmit data to it, by which it can update electricity consumption in real-time and calculate electricity pricing per month. As a result, users can clearly know the electricity consumption of each room.

Multi-Degree-of-Freedom Force–Displacement Mixed Control Analysis for a Structure under Multi-axial Loading

Ming-Chieh Chuang[1], Kung-Juin Wang[2], An-Chien Wu[1], and Keh-Chyuan Tsai[3]

莊明介 [1]、王孔君 [2]、吳安傑 [1]、蔡克銓 [3]

Abstract

To mimic the complex behavior of a structure subjected to multi-axial loading, a method for the multi-degree-of-freedom (MDOF) force–displacement mixed control analysis is proposed by the researchers of the Taiwan National Center for Research on Earthquake Engineering (NCREE). Conceptually, the MDOF force–displacement mixed control analysis of a structure can be analyzed with the solutions for constraint problems in the finite-element method. However, this is difficult to implement in an existing structural analysis program. Thus, NCREE researchers propose a novel method that can offer a convenient and fast solution by using the existing elements. In the proposed method, a substitute model with artificial supports is intentionally added for solving the constraint problem with the penalty function. In particular, the existing zero-length element, SixDJoint element in PISA3D, is utilized to represent the substitute model. Thus, the MDOF force–displacement mixed control analysis can be conducted by using the existing element. The effectiveness of the proposed method is demonstrated via the simulation of the steel panel damper substructure of the hybrid simulation in 2019.

Keywords: MDOF displacement control analysis, hybrid simulation, online model updating, steel panel damper

Introduction

In a hybrid simulation (HS), the target structure can be divided into components whose behavior can be modelled numerically with confidence and those that should be tested physically. Therefore, the target structure under investigation can be partitioned into multiple substructures. These substructures can be divided into two categories including the numerical substructure (NS) and the physical substructure (PS). Hybrid simulations allow the numerical and physical substructures to be integrated such that the interactions between them can be considered in the evaluation of seismic performance. As a result, hybrid simulations can provide a cost-effective alternative to the shaking table test for investigating large-scale target structures.

Recently, the researchers of Taiwan's National Center for Research on Earthquake Engineering (NCREE) (Chuang *et al.*, 2018; Wang *et al.*, 2019) developed online model updating (OMU) to advance such hybrid simulations (Figs. 1 and 2). While the OMU is conducted, parameter identification for model updating can be resolved with an auxiliary numerical model (ANM). For an ANM, it is crucial to mimic the complex behavior of a specimen (PS) subjected to uniaxial or multi-axial loading in an advanced hybrid simulation. However, difficulties arise due to the lack of a convenient method for the multi-degree-of-freedom (MDOF) force–displacement mixed control analysis. To address this challenge, NCREE researchers propose a novel method using the existing elements in this study. The effectiveness of the proposed method was verified via the simulation of a steel panel damper (SPD) (Tsai *et al.*, 2018) substructure in the hybrid simulation conducted in 2019 (Fig. 2).
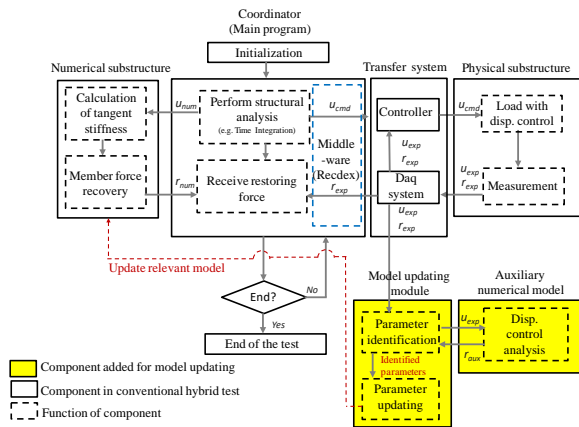
Fig. 1. Framework of advanced hybrid simulation
with online model updating.

PI: Prof. Keh-Chyuan Tsai
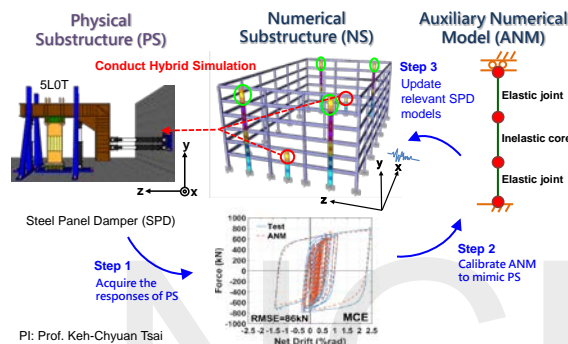
Fig. 2. Hybrid Simulation with an SPD substructure
in 2019

Advanced Hybrid Simulations of a Six-Story SPD–MRF

An SPD (Fig. 3) is an energy dissipation device that promotes the shear yielding mechanism of a steel wide-flange section to dissipate the earthquake-induced input energy.
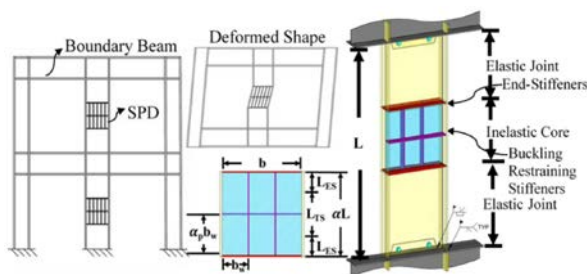
Fig 3. Schematics and stiffener locations of the SPDs in a moment-resisting frame

To experimentally investigate the performance of an SPD and a moment-resisting frame (MRF) equipped with SPDs during seismic events, NCREE researchers conducted a series of hybrid simulations performed on an SPD specimen. In the hybrid simulation (Fig. 2), a 2.8-m-tall SPD specimen made of low-yield-strength steel was tested using the reaction wall and strong floor

with actuators at the NCREE. The SPD specimen remained at zero axial (or vertical) load while it was subjected to the loads for displacement controls for the in-plane translational and rotational degrees of freedom. With OMU technologies, the researchers utilized the SPD specimen as a PS to conduct the six-story SPD–MRF hybrid simulation that was performed in 2019 (Fig. 2).

MDOF Force–Displacement Mixed Control Analysis Method

To mimic the complex behavior of a structure subjected to multi-axial loading, a simulation method for the MDOF force–displacement mixed control analysis was proposed in this study. Conceptually, the MDOF force–displacement mixed control analysis of a structure can be analyzed with the solutions for problems of constraint on movement in the finite-element method. However, this is difficult to implement in an existing structural analysis program. Thus, NCREE researchers proposed a novel method (Chuang *et al.*, 2021) that can offer a convenient and fast solution by using the existing elements. In the proposed method (Fig. 4), the target model is constructed to represent the simulated structure. Subsequently, the substitute model with artificial supports is constructed and located on the identical node of the target model according to the controlled degrees of freedom (DOFs). In general, an artificial support comprises a boundary node and one or more fictitious springs. The fictitious springs with relatively large stiffness are set according to the controlled degree of freedom such as u_z and θ_x (Fig. 4). The substitute model is intentionally added for solving the constraint problem relating to MDOF displacement with the penalty function. As shown in Fig. 4, the combined model comprises the target model and the substitute model. Both the target and substitute models work in parallel to conduct the MDOF force–displacement mixed control analysis of the combined model.

Obviously, the structural responses of the combined model are dominated by the linear elastic substitute model. In other words, to achieve the desired displacements, the required external loads can be straightforwardly determined (or estimated) from the specified stiffness of the artificial supports. Thus, the MDOF force–displacement mixed control analysis of the target model can be conducted by imposing the estimated external loads on the combined model.
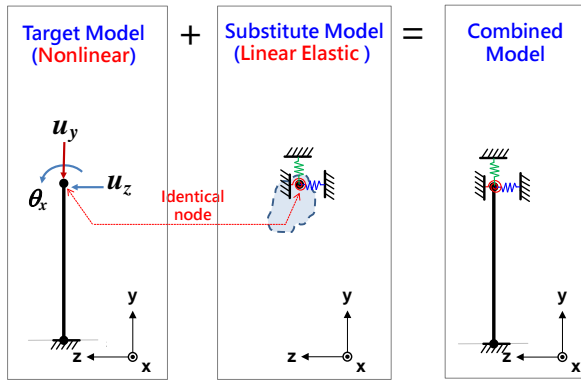
Fig. 4. Schematics of the proposed method for the MDOF force–displacement mixed control analysis

Verification

The measured experimental data (i.e., the histories of displacement and rotation of the SPD top end) of the SPD specimen obtained from the 2019 SPD–MRF hybrid simulation are used to verify the effectiveness of the proposed method.

Based on the proposed MDOF force–displacement mixed control analysis method, the three-segment SPD, which comprises one inelastic core and two elastic joints, is represented using three beam–column elements as the target model. The two-surface plasticity model (Dafalias and Popov, 1975) that combines isotropic and kinematic hardening effects is the constitutive model adopted for the beam–column element used for the IC segment. Fortunately, PISA3D (Lin *et al.*, 2009), the nonlinear structural analysis program developed by the NCREE researchers, provides both the beam–column element and the two-surface model, which is called the hardening material model in PISA3D. Hence, PISA3D is used to construct the target model.

Moreover, the zero-length element, which is called SixDJoint element in PISA3D, is utilized to represent the substitute model with artificial supports. Moreover, two fictitious springs of artificial supports with relatively large stiffness are specified for the in-plane translational and rotational degrees of freedom, respectively. With the proposed method, the loading histories of the combined model were determined from the specified stiffness of the fictitious springs of the substitute model according to the measured and desired displacement histories for the in-plane translational and rotational degrees of freedom. Figures 5 and 6 compare the experimental results with the target model hysteresis, obtained using parameter values that are previously identified from the test results. Figures 5 and 6 show that the responses of the target model and the SPD are in good agreement.

Figures 7 and 8 present the variation of errors for the in-plane translation and in-plane rotation of the top the SPD specimen, respectively. It is evident that at any time instance, the errors are very small. Thus, the effectiveness of the proposed method can be verified.
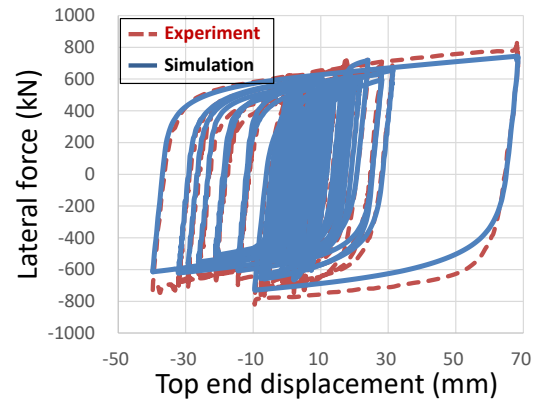
Fig. 5. Shear vs. drift relationships for the SPD specimen and the target model
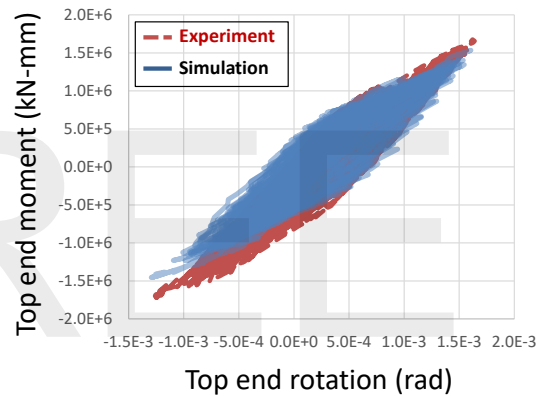
Fig. 6. Moment vs. rotation relationships for the SPD specimen and the target model
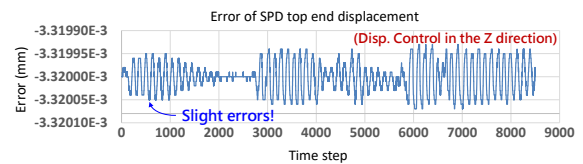
Fig. 7. Time histories of errors of displacement control in the Z direction
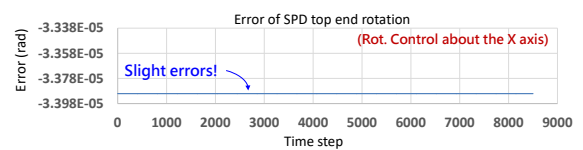
Fig. 8. Time histories of errors of rotation control about the X axis

Conclusions

With the proposed method, the MDOF force–displacement mixed control analysis for the SPD specimen that exhibits the complex nonlinear behavior can be conducted. Through OMU with the proposed method, a high-fidelity ANM for OMU could be constructed during hybrid simulations. Furthermore, the proposed method could allow MDOF force–displacement mixed control analyses be conducted by using not only PISA3D but also other commonly used analysis programs such as OpenSees, SAP2000, and ETABS.

References

Chuang MC, Hsieh SH, Tsai KC, Li CH, Wang KJ, Wu AC. (2018). Parameter identification for on-line model updating in hybrid simulations using a gradient-based method. *Earthquake Engineering and Structural Dynamics*, **47**(2): 269-293.

Wang KJ, Chuang MC, Tsai KC, Li CH, Chin PY, Chueh SY. (2019). Hybrid testing with model updating on steel panel damper substructures using a multi-axial testing system. *Earthquake Engineering and Structural Dynamics*, **48**(3): 347-365.

Tsai KC, Hsu CH, Li CH, Chin PY. (2018). Experimental and analytical investigations of steel panel dampers for seismic applications in steel moment frames. *Earthquake Engineering and Structural Dynamics*, **47**(6): 1416-1439.

Chuang MC, Tsai KC, Wang KJ. (2021). Multi-Degree-of-Freedom Force-Displacement Mixed Control Analysis via a Novel Use of the Zero-Length Elements, *Proceedings of the 45th National Conference on Theoretical and Applied Mechanics*, New Taipei, Taiwan.

Dafalias YF, Popov, EP. (1975). A model of nonlinearly hardening materials for complex loading. *Acta Mechanica*, **21**(3): 173-192.

Lin BZ, Chuang MC, Tsai KC. (2009). Object-oriented development and application of a nonlinear structural analysis framework. *Advances in Engineering Software*, **40**(1): 66-82.

Prediction of Landslides Using Machine Learning Techniques Based on Spatio-Temporal Factors and InSAR Data

Yan-Ting Lin[1] Hsiao-Ying Yen[2] Nai-Hsuan Chang[2] Hung-Ming Lin[2] Jen-Yu Han[3] Kuo-Hsin Yang[3] Chuin-Shan Chen[3]

林彥廷 [1] 顏筱穎 [2] 張乃軒 [2] 林宏明 [2] 韓仁毓 [3] 楊國鑫 [3] 陳俊杉 [3]

Abstract

Taiwan's mountainous areas feature steep terrain and broken geological environment. With the invasion of typhoons or heavy rain events, slope disasters such as landslide and debris flow can occur frequently. As a result, how to effectively apply multiple spatial data to predict landslide has become a forward-looking topic for current disaster management. The development of remote sensing detection technology, such as satellite spectral images and interferometric synthetic aperture radar (InSAR) collected in a fixed period is able to help obtain information on earth surface properties and geometric changes. Through the spatial analysis of the slop units, this research quantifies a total of 14 spatio-temporal factors. The correlation analysis is employed to detect factors that significantly cause landslides, and then artificial intelligence machine learning is used to construct a landslide prediction model. Finally, the confusion matrix verifies the prediction results and evaluates the quality. The research shows that the landslide prediction is better than 80% correct and points out the spatio-temporal factors that affect the slope unit collapse in the survey area. This result also suggests clearer conservation sites and potential assessment for land conservation. The overall study will be effectively used as the application for project site selection, slope protection, and disaster prevention management.

Keywords: landslide prediction; machine learning; the displacement gradient of InSAR; correlation analysis; spatio-temporal factors

Introduction

High rainfall intensity usually causes serious landslide events in mountainous areas. It is necessary to predict landslide occurrence and behavior and adopt appropriate prevention policies and methods in order to improve disaster relief effectiveness and reduce casualties and property loss during and after disasters. Landslide prediction aims to predict the possibility of the occurrence of landslides in a specific area using the available data, which include conditional factors and historical landslides. These data are collected from landslide inventories and static instruments.

In recent years, remote sensing technology has effectively identified large-scale landslide-sensitive areas and generated landslide inventories, which are crucial for predicting landslides before they occur or recur, especially in remote or inaccessible areas. Compared with optical sensors, synthetic aperture radar (SAR) sensors use longer wavelength microwaves. Having all-weather and all-day operational capability, SAR sensors can penetrate cloud cover and reduce the limitations imposed by the atmosphere to remotely evaluate the accurate range and severity of landslide disasters in almost real time. Although some particular meteorological situations, such as thick rain cells, may disturb the backscattering coefficient, SAR remains more powerful than optical sensors for long-term landslide observation. SAR sensors also provide high spatial resolution and can clearly observe target objects in full-time and in almost all weather conditions. Long-term interferometric SAR (InSAR) observations are calculated as the deformation-induced phase shift through the backscattered microwave signal between several coherent acquisitions. The landslide behavior of time-series information, which depends on millimeter measurement accuracy and meter spatial resolution, is obtained under most atmospheric conditions. Nowadays, SAR technology is widely used in morphological monitoring [1].

Recently, machine learning and data mining

techniques have been applied to landslide susceptibility modeling. These methods incorporate different factors that might cause landslides in order to evaluate the probability of a landslide occurrence. Machine learning algorithms enrich the quality and accuracy of the generated susceptibility maps. Researchers use and compare various machine learning models on the basis of different data and integrate different machine learning models to improve accuracy. In the field of civil engineering, the combination of artificial intelligence technology and spatial data has considerable benefits for environmental monitoring [2]. At the same time, it assists people in making decisions and judgments, such as in the safety assessment of structures [3], river flooding levels [4], and landslide warnings [5]. The method proposed in this study is to combine spatial-temporal data, including InSAR observables, as a landslide susceptibility factor with other traditional geological and land cover factors into a model that can improve the accuracy of landslide prediction.

Segmentation of Slope Units

This study used the slope unit as the basis of analysis to show the topographic characteristics of each slope. These slope units served as a framework for the subsequent geographical interpretation of the environmental spatial factors. The method of slope unit segmentation refers to the catchment overlap concept proposed by Xie et al. [6], as shown in Figure 1. First, the water catchment area in a digital elevation model (DEM) is identified through the hydrology module in ArcGIS software, and the water line is converted into a ridge line by flipping the DEM, which is divided into two slope units (left and right). When the hydrology module identifies a small catchment area, the default flow accumulation value is set to 500 as the threshold value for dividing the river area. Then, the slope units are cut out, and each area becomes less than 30 ha. With the aid of a shadow map, an aspect map, a slope map, a river map, and a satellite orthophotograph overlay, the overlap between each slope unit is confirmed.
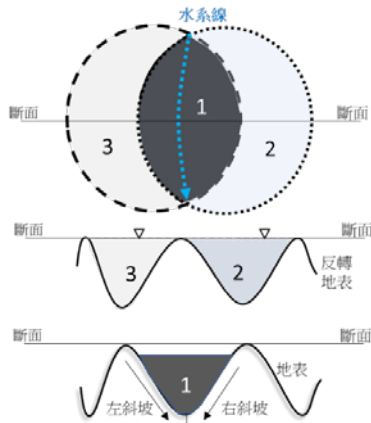
Figure 1. Schematic diagram showing division of slope units using the overlap method for catchment areas

Numerical Indexing of Related Spatial Factors and Annual Displacement Velocity Gradient of InSAR

The spatial factors were divided into four categories: terrain, location, geological, and driving. The terrain category represents the geometric changes in surface elevation and coverage distribution, including elevation, slope, aspect, terrain roughness, profile curvature, and vegetation index. The location category shows the distance of influencing factors, including roads, rivers, and geo-faults. The geological category reflects the strength, folds, and dip slopes of rock formations. The driving category is the rainfall factor (Figure 2).

InSAR technology calculates the phase difference to estimate the displacement of the ground through more than two periods of SAR observations. In order to reduce the periodic or systematic noise caused by any uncontrollable factors and to extract a meaningful index for evaluating the ground stability, the annual velocity gradients derived from InSAR displacement fields were used. First, the annual displacement information of InSAR was placed in the range −1 to 1 by mean normalization, as shown in Equation (1), to unify the scale and reduce the systematic error of the In-SAR data:

$$Z_{norm} = \frac{Z - \mu}{Z_{max} - Z_{min}} \tag{1}$$

where Z_{norm} is the normalized InSAR displacement value, Z is the annual displacement of InSAR, and μ is the average annual displacement.

The annual displacement velocity of InSAR was obtained as the slope value in first-order linear fitting (Equation (2)). These discrete observation points were interpolated with a regular grid size of 20 m to present the field of annual displacement velocity. For highlighting the displacement positions, the field gradient was calculated using a 3×3 moving window, the same as for computing the profile curvatures. The index calculation was expressed as in Equation (3):

$$\Delta Z = V \Delta t + dZ \tag{2}$$

$$\nabla_V \mathbf{f}(V) = \begin{bmatrix} \partial \mathbf{f}(V_a) & \partial \mathbf{f}(V_b) & \partial \mathbf{f}(V_c) \\ \partial \mathbf{f}(V_d) & \partial \mathbf{f}(V_e) & \partial \mathbf{f}(V_f) \\ \partial \mathbf{f}(V_f) & \partial \mathbf{f}(V_g) & \partial \mathbf{f}(V_i) \end{bmatrix} \tag{3}$$

where V is the annual displacement speed of InSAR, Δt is the annual observation time, and ΔZ is the difference in annual displacement.

(a) annual displacement velocity gradient of InSAR

(b) elevation

(c) slope

(d) aspect

(e) terrain roughness

(f) profile curvature

(g) vegetation index

(h) water distance

(i) road distance

(j) fault distance

(k) rock mass strength

(l) folds

(m) dip slope

(n) annual rainfall
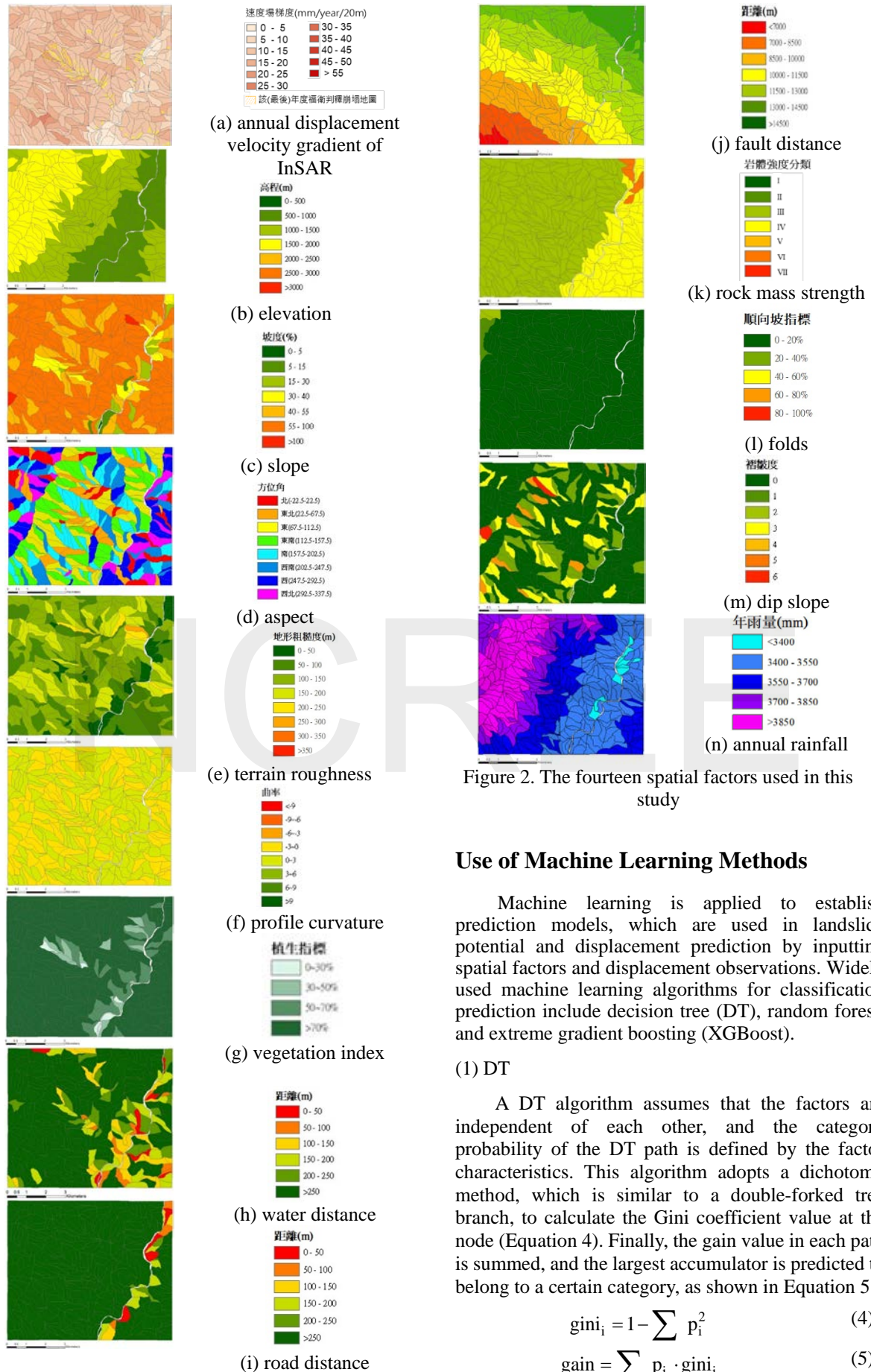
Figure 2. The fourteen spatial factors used in this study

Use of Machine Learning Methods

Machine learning is applied to establish prediction models, which are used in landslide potential and displacement prediction by inputting spatial factors and displacement observations. Widely used machine learning algorithms for classification prediction include decision tree (DT), random forest, and extreme gradient boosting (XGBoost).

(1) DT

A DT algorithm assumes that the factors are independent of each other, and the category probability of the DT path is defined by the factor characteristics. This algorithm adopts a dichotomy method, which is similar to a double-forked tree branch, to calculate the Gini coefficient value at the node (Equation 4). Finally, the gain value in each path is summed, and the largest accumulator is predicted to belong to a certain category, as shown in Equation 5:

$$gini_i = 1 - \sum p_i^2 \qquad (4)$$

$$gain = \sum p_i \cdot gini_i \qquad (5)$$

where P_i is the probability. If the node has only one category, P_i will be 0. If the numbers of two categories are the same, P_i will be 0.5.

(2) Random forest

Random forest is a collection of multiple DTs and adds the use of bagging. The observation data are taken out of the number of samples and trained as *n* types of classifiers. The random uncertainty of the data is considered according to the sample difference in each DT. Under the same weight, the classifier uses the summed majority as the best classification tree to predict the classification. Equation (6) represents the probability of the cth factor in the tth DT, and the average probability value *gc* of the category is obtained according to the sum of multiple DTs. Finally, the category of the slope unit *x* is determined according to the maximum g_c value (Equation (7)):

$$P(c|v_i(x)) = \frac{P(c|v_i(x))}{\sum_{l}^{n=1} P(c_l|v_i(x))} \quad (6)$$

$$g_c(x) = \frac{1}{t}\sum_{i=1}^{t} P(c|v_i(x)) \quad (7)$$

where P is the probability, c is the category, *v* is the node, *l* is the number of categories, *t* is the number of DTs, and g_c is the average probability of the cth category.

(3) XGBoost

The XGBoost function is composed of two components: the prediction error of boosting and the complexity of DT. The feature factors are combined and branched into a DT, and a new boost function is learned from the previous calculation residuals. In Equation (8), the first component calculates the error between the prediction and actual observation, and the other component indicates the complexity of the regularized DT, which covers the number of nodes and the node probability value.

$$f = \sum_{i=1}^{n} E(y_i, y_{k_i}) + \sum_{k=1}^{K} \Omega(f_k) \quad (8)$$

where E is the error between the prediction and actual observation and $\Omega(f_k)$ is the complexity of the DT.

Discussion and Conclusions

This study was implemented for Putunpunas River (Kaohsiung City, Taiwan). The experiment collected four years of spatial data and then these data were used to construct the 14 spatial factors through an indexed analysis. A common timescale (year) was established for the analysis to resolve the differences in timescales of the various spatial factors. The spatial factor datasets from 2007 to 2009 served as the input for the machine learning, and the 2010 spatial factor data were used to calculate the output of potential evaluation.

The machine learning algorithms used in this research achieved accuracies of 70% to 80% in landslide classification. Of the three algorithms, the random forest method exhibited the best calculation, yielding a prediction accuracy rate of 80.50% (Figure 3). The random forest method effectively performed independent training for high-dimensional, multi-feature factors. In addition, the random forest algorithm exhibited strong anti-interference capabilities, such as an imbalance in the number of classifications and missing parts of the feature data, so it could avoid excessive parameter setting and reduce overfitting problems.

Future research will test the slope unit area to define the interval scale of the predicted landslide seriousness. In addition, the error units (near the river channel) will consider fluid movement behaviors to solve the error prediction. Finally, the current annual observation time scale will be refined into months or days to further improve the prediction accuracy.
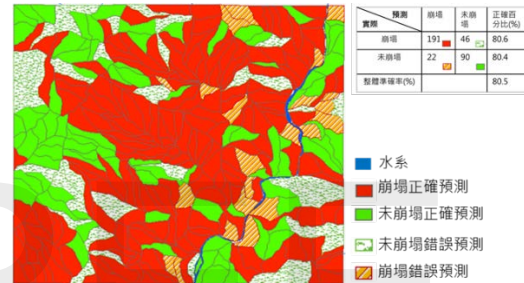
Figure 3. Visual illustration of the landslide prediction results

References

1. Hooper, A., Segall, P., and Zebker, H. (2007), "Persistent scatterer interferometric synthetic aperture radar for crustal deformation analysis, with application Volcán Alcedo, Galápagos", *Journal of Geophysical Research, 112*(B7), pp. 407.

2. Reich, Y. (1997), "Machine learning techniques for civil engineering problems", *Computer-Aided Civil and Infrastructure Engineering*, *12*(4), pp. 295-310.

3. Flah, M., Nunez, I., Chaabene, W. B., and Nehdi, M. L. (2020), "Machine learning algorithms in civil structural health monitoring: a systematic review", *Archives of Computational Methods in Engineering*, pp. 1-23.

4. Lin, Y. T., Yang, M. D., Han, J. Y., Su, Y. F., and Jang, J. H. (2020), "Quantifying Flood Water Levels Using Image-Based Volunteered Geographic Information", *Remote Sensing, 12*(4), pp. 706.

5. Thirugnanam, H., Ramesh, M. V., and Rangan, V. P. (2020), "Enhancing the reliability of landslide early warning systems by machine learning", *Landslides, 17*(9), pp. 2231-2246.

6. Xie, M., Esaki, T., and Zhou, G. (2004), "GIS-Based Probabilistic Mapping of Landslide Hazard Using a Three-Dimensional Deterministic Model", *Natural Hazards, 33*(2), pp. 265-282.

Applicability of the Ground Motion Prediction Equations for Wide-area Seismic Damage Assessment

Chin-Hsun Yeh[1], Lee-Hui Huang[2]

葉錦勳 [1]、黃李暉 [2]

Abstract

The National Center for Research on Earthquake Engineering has been developing the Taiwan Earthquake Loss Evaluation System (TELES) for many years. It is necessary to explore the applicability of the new ground-motion prediction equations in wide-area seismic damage assessment to enhance the accuracy of estimation results. The new ground-motion prediction equations use the moment magnitude and consider seismic source types and fault rupture mechanisms. The ground-motion prediction equation (GMPE) Chao19 is based on the strong-motion records, including attributes of seismic source characteristics, various distance measures, and local site conditions of individual records in Taiwan over the past two decades. Chao19 should be suitable for wide-area seismic damage assessment in Taiwan. However, significant differences exist between the ground-motion intensity estimates from different GMPEs within 10 km of fault ruptures. In addition, Chao19 generally underestimates the ground-motion intensity near the rupturing fault. This systematic inconsistency is owing to the lack of strong-motion records near the active faults of large earthquakes. Chao19 may be one of the built-in GMPEs in TELES in the near future. Therefore, it is necessary to carefully review the critical factors that affect the ground-motion intensity near the rupture fault area to avoid underestimating the damage and be consistent with the historical earthquake records.

Keywords: wide-area seismic damage assessment, ground-motion prediction equation, seismic source type, fault rupture mechanism, site condition

Background

The Taiwan Earthquake Loss Assessment System (TELES), developed by the National Center for Research on Earthquake Engineering, has been widely used in disaster reduction planning and risk management (Yeh, 2003). For example, disaster prevention agencies are assisted in developing regional disaster reduction and rescue plans based on seismic disaster simulations. The real-time and automated early seismic loss estimation information after an earthquake can help quickly activate emergency responses. Probabilistic seismic risk assessment models have been proposed and the Taiwan Residential Earthquake Insurance Fund was assisted in developing its risk assessment model TREIF-ERA.

When conducting seismic disaster simulations, the predicted ground-motion intensities in each region, including the peak ground acceleration (PGA) and the 0.3-second-period and 1.0-second-period structural response accelerations, are used to estimate the soil liquefaction probability and settlement, and the structural damage state probabilities. Therefore, the accuracy and rationality of ground-motion prediction models plays a critical role in disaster reduction.

New Ground-Motion Prediction Equations

In 2019, the National Center for Research on Earthquake Engineering assisted the Taiwan Power Company in completing a high-level seismic hazard analysis of nuclear power plants. The project collected Taiwan's strong-motion records from 1990 to 2016. Each record includes attributes related to the seismic source characteristics, the local site conditions, and the various distance measures between the station and the fault rupture surface. Because all features are recorded

---

in a single table, it is called a flat file of strong-motion records. Using the flat file of strong-motion records, Chao et al. (2019) developed a new GMPE (Chao19), which can be applied to both crustal and subduction earthquakes. Chiou and Lin (2019) referred to the new GMPEs in the United States, Japan, and Europe and integrated the above-mentioned flat file of strong-motion records in Taiwan to establish revised GMPEs suitable for Taiwan. There are seven revised GMPEs for crustal earthquakes and two for subduction earthquakes. The suffix adj is added after the original name to show the differences. This paper only discusses the GMPEs for crustal earthquakes, as listed in Table 1.

Referring to Table 1, all new GMPEs consider the seismic source parameters, the path, and the local site effects. The new GMPEs can estimate any period of structural response accelerations. However, individual GMPE use different parameters.

In the source column of Table 1, all new GMPEs adopt the definition of moment magnitude (M_w). Some GMPEs directly input the fault rupture mechanism (F_{FT}), which can be roughly divided into normal, reverse, or strike-slip faults. Some GMPEs take the rake angle of the hanging wall relative to the footwall as the input parameter. However, it is still converted to the corresponding fault rupture mechanism before calculation. In addition, some GMPEs include the focal depth (Z_{hyp}) or the depth of the fault rupture top (Z_{tor}) to distinguish the difference in ground-motion intensity caused by different rupture depths.

slowly on the hanging wall of minor dip angle thrust faults.

As listed in Table 2, some GMPEs consider the hanging wall effect and require inputs of dip angle (δ) and width (W) of the fault rupture surface. These GMPEs may use additional distance measures, namely R_{jb}, R_x, R_1, and R_{y0}, to model the attenuation of the hanging wall effect. The definitions of these distance measures are shown in Figure 2. R_x is the horizontal distance from the top edge of the rupture surface, measured perpendicular to the fault strike. R_1 is the value of R_x at the bottom edge of the rupture surface. R_{y0} is the horizontal distance off the end of the rupture surface measured parallel to strike.
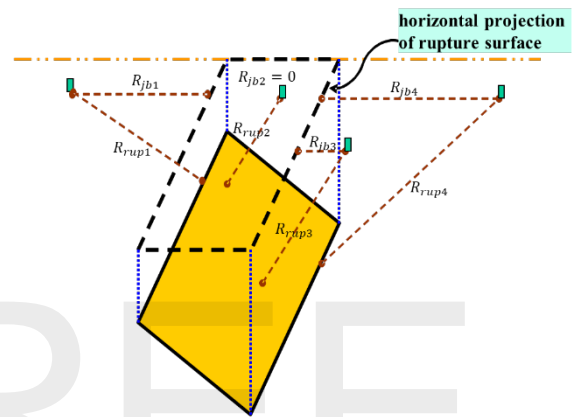
Figure 1. Schematic diagram for definitions of R_{rup} and R_{jb}

Table 1 Parameters in GMPEs for crustal earthquake

GMPE	Source	Path	Site
ASK14adj	M_w, Z_{tor}, λ	R_{rup}	$V_{s30}, Z_{1.0}, F_{VS}$
ASB14adj	M_w, F_{FT}	R_{jb}	V_{s30}
Bi14adj	M_w, F_{FT}	R_{jb}	V_{s30}
BSSA14adj	M_w, F_{FT}	R_{jb}	$V_{s30}, Z_{1.0}$
CB14adj	M_w, Z_{hyp}, λ	R_{rup}	$V_{s30}, Z_{2.5}$
CY14adj	M_w, Z_{tor}, λ	R_{rup}	$V_{s30}, Z_{1.0}, F_{VS}$
I14adj	M_w, Z_{tor}, F_{FT}	R_{rup}	V_{s30}
Chao19	M_w, Z_{tor}, F_{FT}	R_{rup}	$V_{s30}, Z_{1.0}, F_{VS}$

In the path column of Table 1, most GMPEs use the closest distance from the site to the fault rupture surface (R_{rup}) or the closest distance from the site to the horizontal projection of the fault rupture surface (R_{jb}), as shown in Figure 1. If R_{jb} is used without considering the depth of the fault rupture surface, it may not be suitable for estimating the ground motion intensity caused by deep earthquakes. Using R_{rup} can indicate that the ground-motion intensity decays

Table 2 Parameters in GMPEs to consider the hanging wall effect

GMPE	Source	Path
ASK14adj	δ, W	R_{jb}, R_x, R_1, R_{y0}
CB14adj	δ, W	R_{jb}, R_x
CY14adj	δ, W	R_{jb}, R_x

In the site column of Table 1, all GMPEs use the average shear wave velocity within 30 m of the ground surface (V_{s30}) as the parameter for the site effect. The parameter F_{VS} is an indicator to distinguish the estimation method of V_{s30}. Some GMPEs consider the effect of the thickness of the soil layer under the site. The soil layer thickness is the depth at which the shear wave velocity reaches 1000 m/s or 2500 m/s and is designated by $Z_{1.0}$ and $Z_{2.5}$, respectively.

GMPE for Wide-Area Seismic Damage Assessment

Most structures subject to earthquake damage assessment can be roughly divided into buildings, bridges, facilities, and buried pipelines. The seismic response behavior and the failure modes of different structure types have unique characteristics, which results in the slight variation in the required ground-motion parameters. Ground-motion parameters such as PGA and peak ground velocity (PGV) are commonly used in literature. However, since the structural response spectrum can reflect the maximum response of the structure under a given earthquake, it is the best ground-motion parameter for estimating the structural damage state probabilities. Because there are no actual measurements under scenario earthquakes and the ground-motion intensity estimates from the GMPEs contain significant uncertainties; therefore, we use a simplified standard form of the structural response spectrum to represent the seismic demand in each region. The entire structural response spectrum is constructed using the short-period (S_{a03}) and one-second period (S_{a10}) structural response accelerations, as shown in Figure 3.

Figure 2. Schematic diagram for definitions of R_x and R_{y0}

The ground-motion attenuation law used in TELES adopts the research results from Jean (2001). Since the complete seismic source characterization, path, and site-effect attributes were not available in the strong motion records, the only seismic source-related parameter used in Jean (2001) was the Richter magnitude, which was commonly used by the Central Weather Bureau. It did not distinguish the source types, fault rupture mechanisms, depth, etc. Although many source parameters were not considered in Jean's model, it can still reasonably provide PGA and short-period (S_{a03}) and one-second period (S_{a10}) structural response accelerations required in seismic damage assessment. When the simulation results are compared with the actual number of disasters over the past years, the error is within a reasonable range.

Applicability of GMPEs

In Figure 4, building damage during the Chi-Chi earthquake in 1999 was concentrated in the hanging wall or within 10 km of the fault line. Therefore, the estimated ground-motion intensity within 10 km is crucial and can seriously affect the estimation result of disaster damage. If the GMPEs cannot reasonably predict the ground-motion intensity in the near-fault area, they may seriously overestimate or underestimate the amount and distribution of the resulting disasters.

Figure 3. Standard form of structural response spectrum

Figure 4. Distribution of building damage in the Chi-Chi earthquake in 1999

We compared the estimation results of Jean (2001) with new GMPEs listed in Table 1 at the footwall site

under an earthquake magnitude of 7.5. Figure 5 shows that the closer the distance, the more significant the difference in estimations from different GMPEs. The difference is reduced when the closest distance to the fault rupture line exceeds 10 km. The differences were due to a lack of data and model uncertainties. The estimated value of Jean (2001) within 10 km of the fault is too large, while the estimated value of Chao19 within 10 km of the fault is too small. More near-fault strong-motion records are required to reduce the model error.

When applying Jean (2001) in TELES, the concept of a seismogenic rupture zone was adopted to increase the closest distance and avoid overestimating the ground motion intensity near the fault. In other words, the distance to the seismogenic rupture zone was substituted into the distance parameter of the GMPE.

Chao19 distinguished the source type and the fault rupture mechanism and was based on the strong-motion records of Taiwan. Therefore, the Chao19 GMPE should better reflect the characteristics of local ground motions in Taiwan. In the future, if Chao19 is the built-in GMPE of TELES, it is necessary to explore the method further to avoid underestimating the ground motion intensity within 10 km of the fault and integrate the existing site effect modification model of TELES.
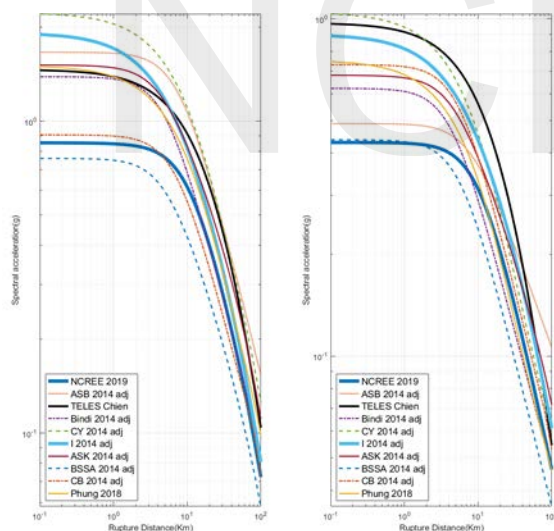
Figure 5. Comparison of S_{a03} (left) and S_{a10} (right) from GMPEs at footwall side under the scenario of an earthquake with magnitude 7.5

References

1. Chiou, B. and P.-S. Lin, 2019, "Adjusted Foreign GMPEs for Taiwan."
2. Chao, S.-H., B. Chiou, C.-C. Hsu, P.-S. Lin, 2019, "Development of Horizontal and Vertical Ground Motion Models for Crustal Earthquakes and Subduction Earthquakes in Taiwan," NCREE-19-003.
3. Yeh, C.-H., 2003, "Taiwan Earthquake Loss Estimation System (TELES)," NCREE-03-002 (in Chinese).
4. Jean, W.-Y., 2001, "Seismic Hazard Analysis Considering Characteristic Earthquakes and Site Effects," NCREE-01-036 (in Chinese).

Post-earthquake Patient Flow Simulation for Multiple Emergency Departments

Chi-Hao Lin[1] and You-Xuan Lin[1]

林祺皓 [1]、林祐萱 [2]

Abstract

After a massive earthquake, the supply of emergency medical care may fall short of the rising demand for treatment, leading to congestion in emergency departments (EDs). Located in the Circum-Pacific seismic belt, Taiwan is under threat of disastrous earthquakes. Emergency medical systems play a critical role in supplying immediate medical aids to casualties and suppressing the impact of an earthquake on society. Estimating potential problems emergency medical systems may encounter in the face of the sudden increase in casualties induced by an earthquake can help practitioners of relevant fields as well as decision-makers formulate response measures and improve preparedness for seismic disasters. Therefore, in this study, we propose a model for patient flow simulations among multiple EDs that constitute an entire emergency healthcare system. Simulation results of a case study with eight hospitals involved under a seismic scenario (magnitude 6.6) show the reduced capacity of an emergency medical system to offer timely treatment.

Keywords: discrete event simulation, emergency department, patient flow simulation, post-earthquake patient surge

Introduction

Resilience refers to the ability of a community in the face of a disaster to "resist, absorb, accommodate, adapt to, transform and recover from the effects of a hazard in a timely and efficient manner (United Nations International Strategy for Disaster Reduction, 2009)." To put it simply, a resilient community is one that mitigates the impact of a disaster as much as possible and resumes its normal state as quickly as possible. Of the vital factors that determine resilience, hospital emergency departments (EDs), whose function is to offer emergency healthcare and accommodate patients, play a critical role in minimizing fatalities and relieving the suffering of victims.

A flood of patients into EDs after an earthquake may risk collapse of the emergency healthcare service, thus causing less effective healthcare and even unnecessary loss of lives. A failure to contain the impact of an earthquake then violates the principle of resilience. Previous studies have found that as the patient number grows over 1.4 times the normal level in one single hospital, a significant delay in treatment after earthquakes results (Lin, Lin, & Lin, 2021). Instead of having only one hospital to manage all seismic casualties, commonly after a seismic disaster where the mass casualty is caused, a region will have several hospitals to collaborate and accommodate the large patient volume together. To estimate the collaborative performance of EDs, a model that enables simulations of multiple hospitals in each of which the inner patient flow can be operated simultaneously should be built.

In literature, the estimation of multiple hospitals is usually conducted with little variability in the patient in-to-out sojourn time, and the throughput is simply modeled as an interval of time without details about the queueing for various medical services (Ceferino, Mitrani-Reiser, Kiremidjian, Deierlein, & Bambarén, 2020). The drawback of this model design is that in reality, patients of different categories undergo different procedures in the ED. Congestion occurring in any medical service will impede the ED performance. Moreover, where a long queue is formed in the ED provides different information in terms of its ability to provide basic emergency care function, resource arrangement, and the critical capacity to treat

[1] Associate Researcher, National Center for Research on Earthquake Engineering
[2] Research Assistant, National Center for Research on Earthquake Engineering

patients of different acuity levels.

In this study, we applied the discrete event simulation based on SimPy to model the phases of input, throughput, and output in the emergency department (Asplin et al., 2003). According to the casualty estimate by TELES (Yeh, Loh, & Tsai, 2006), the five districts of Taipei City having the most casualties induced by a seismic scenario of a magnitude 6.6 earthquake caused by the Shanchiao Fault were chosen as the research target, and the eight first-aid hospitals located in these five districts were included for patient flow simulations. The result shows that supposing the seismic casualties visit hospitals within 4 days, on the third day, the ED crowdedness will reach the peak and will be suppressed as soon as the casualty visits terminate.

Details of the Scenario

The simulation was conducted under a seismic scenario of a magnitude 6.6 earthquake caused by the Shanchiao Fault where the max peak ground acceleration is 0.58g. According to the estimate by TELES, in the daytime, Taipei City may have 5,675 persons injured in total excluding those without the need of medical care in hospitals. The five districts having the largest medical demand were selected for analyses. Details of the five districts and hospitals located in the region are provided in Table 1.

Table 1. Information of the target research area and hospitals for simulation.

District	Medical Demand (daytime)	First-aid Hospitals	Daily ED Patients
Beitou Dist.	578	Taipei Veterans General Hospital	231
		Cheng Hsin General Hospital	120
Zhongshan Dist.	544	MacKay Memorial Hospital	350
Shilin Dist.	419	Shin Kong Wu Ho-Su Memorial Hospital	151
		Taipei City Hospital-Yangming Branch	63
Datong Dist.	418	Taipei City Hospital-Zhongxing Branch	72
Zhongzheng Dist.	402	National Taiwan University Hospital	307
		Taipei City Hospital-Heping Fuyou Branch	115

Note: The column, Medical Demand (daytime), refers to earthquake-induced casualties; the column, Daily ED Patients, refers to regular patient visits.

Patient Flow Model

Patient flow in the ED was modeled as a series of independent events. Upon arrival, each patient is triaged first to determine the degree of urgency and complete registration. After treatment, the patient path diverges into three: leaving the ED for discharge or for further medical care (e.g., to undergo an operation), being put under observation, and undergoing laboratory tests before observation. Figure 1 displays the patient flow and paths used in our study, and Table 2 shows the percentage of patients being distributed to

each path. The time patients spend at each service is determined by random sampling from the corresponding time distributions. The time distribution of each medical service at the ED and corresponding parameters are listed in Table 3. The parameters shown in Table 3 are for less urgent patients having no need to undergo emergency surgery. Patients in an emergency for surgery should spend less time in the ED; therefore, parameters of time distributions for this type of patients will be adjusted to make the total length of sojourn around half that of other patients. To represent the queuing behavior, each service relies on a limited number of sources.

Each of the eight hospitals share the same patient flow models. What distinguishes them is the resource number available for every service to represent the capacity of hospitals, which is directly related to the average daily patient counts (as presented in Table 1).
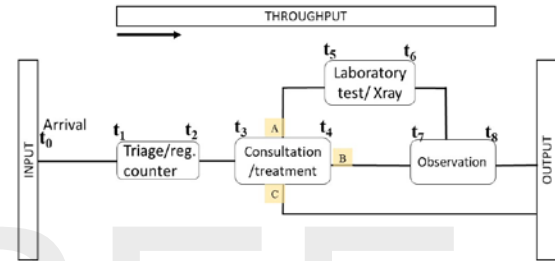

Figure 1. Patient flow models from input to output.

Table 2. Percentage of patients taking different paths in the ED

Path	AL3		AL4		AL5		AL1+AL2	
	Seismic	Normal	Seismic	Normal	Seismic	Normal	Seismic	Normal
A	12%	12.5%	7.2%	7.68%	0%	0%	3.3%	5.28%
B	38%	39.5%	22.8%	24.32%	1%	1.5%	3.3%	5.28%
C	0%	0%	0%	0%	3%	4.5%	3.4%	5.44%
SUM	50%	52%	30%	32%	100%	6%	10%	16%

Note: AL stands for Acuity Level. AL1 is the patient of the highest level of emergency and AL5 the lowest

Table 3. Time distributions of each medical service at the ED

Service	Probability distribution	Source
Triage/registration	Gamma(4.5, 0.7)	Favier et al. (2019)
Ttreatment	[1]Tri(15, 45, 90)	Favier et al. (2019)
Observation	Tri(0, 15, 60)	Adapted from Favier et al. (2019)
Lab/X-ray	Gamma(2.5, 9.2)	Côté (1999)
Operation	Tri(60, 240, 480)	#
Bed	$Tri(avg - 2880, {}^2avg, avg + 2880)$	#

Note: 1. triangular distribution; 2. the average length of stay of inpatients

Simulation Setup

The simulation covers 99 days in which the beginning 65 days are in the normal state, followed by

the 4-day seismic period and ended with 30 days in the normal state. The simulation before the earthquake is to reach the stable state approximate to the real-world observations, and that after the 4-day seismic period is for recovery. Since after the earthquake, patient arrival patterns will change, in the simulation we distinguish arrival rates on normal days and on the 4 days in the seismic period. As illustrated in Figure 2, after an earthquake hits, patients arrive at the ED in a pattern different from that on normal days. The patterns were adapted from [6]. It is assumed that the impact of an earthquake on the ED patient visits lasts for four days. After the four days, the normal pattern will be resumed.
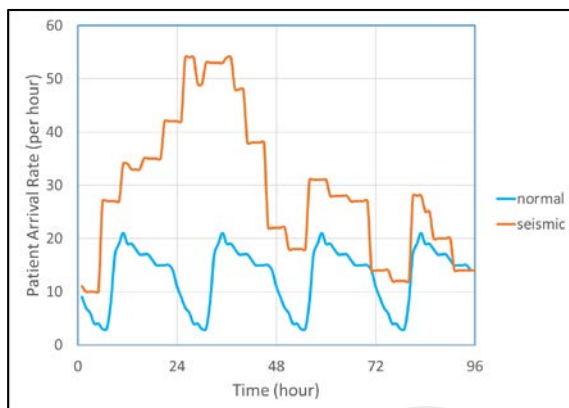

Figure. 2. Patient arrival rates on normal days and after an earthquake.

In addition to earthquake-induced patients, ordinary patients may seek emergency treatment in the four days. Therefore, in this study, the total number of patients after the earthquake strikes includes both the earthquake-induced patients and ordinary patients. The relevant patient numbers to compute the post-earthquake casualty number are as presented in Table 1. During the four days, each hospital will be assigned patients against the patient proportion of the eight hospitals on normal days. This manipulation is to simulate the situation of emergency healthcare systems without deliberate diversion strategies. Instead, the patient transportation/arrival follows the patterns on normal days.

All simulations were repeated 300 times to average out the potential overlying data caused by sampling from time distributions as well as the patient distribution between hospitals.

Results

According to the guide issued by the Ministry of Health and Welfare, patients of different acuity levels can tolerate waiting times of different lengths. The most severe patients with acuity levels 1 and 2 should receive treatment by 10 minutes, while patients with acuity levels 3, 4, and 5 should receive treatment within 30, 60, and 90 minutes, respectively. Beyond the suggested time, patients will be placed at risk of

deterioration and even death. Therefore, the time from arrival to treatment serves as an insightful index reflecting the capacity of the emergency healthcare system to supply timely and effective treatment. In our model, the duration of time is t3-t0 (see Figure 1), named door-to-doctor henceforth. Figure 3 shows the average door-to-doctor of the eight hospitals under the defined scenario. For the sake of readability, Figure 3 displays only results on the 60th day to the 75th day where the critical information is captured. It can be found that on the 66th day when the earthquake strikes, the door-to-doctor starts to surge and hits the peak on the 68th day, or the 3rd day after the earthquake. After that, it starts to drop and resumes normality on the 70th day; that is, the emergency healthcare system is able to recover as soon as the seismic casualties stop visiting.
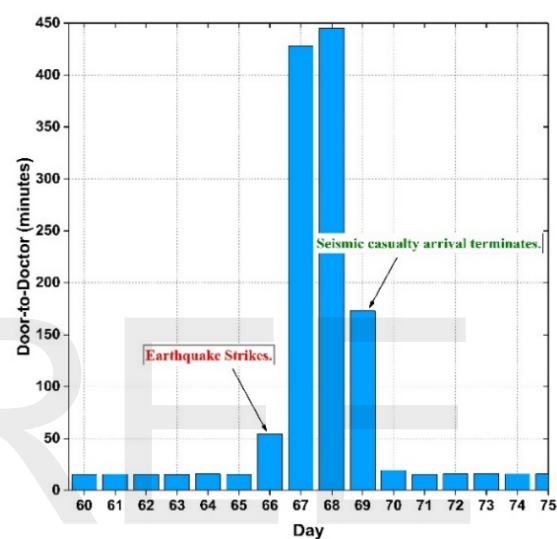

Figure 3. Impact of the patient surge on the performance of the emergency healthcare system after an earthquake.

Conclusions

In this study, we have presented a case study of the patient flow simulation with multiple hospitals. The methodology leveraged in our model design allows greater flexibility for researchers and practitioners to examine emergency care performance for different services in the EDs. In this paper, we have also provided the performance measure, door-to-doctor, which can serve as an index about the capacity of the emergency care system for timely treatment. In addition to door-to-doctor, information about the overall stay of patients in the ED can also be computed to reflect the efficiency of the EDs. Moreover, our method allows simultaneous simulation of multiple hospitals, enabling regional simulations. Last but not least, the modeling with the resource number of each services specified enables the integration of the failure probability estimation to the simulation to represent capacity decline caused by the functionality loss of hospitals.

References

Asplin, B.R., Magid, D.J., Rhodes, K.V., Solberg, L.I., Lurie, N. and Camargo, C.A. (2003), "A conceptual model of emergency department crowding", Annals Emergency Medicine, 42, 173-80.

Ceferino, L., Mitrani-Reiser, J., Kiremidjian, A., Deierlein, G. and Bambarén, G. (2020), "Effective plans for hospital system response to earthquake emergencies", Nature Communications, 11, 4325.

Côté, M.J. (1999) "Patient flow and resource utilization in an outpatient clinic", Socio-Economic Planning Sciences, 33, 231-245.

Favier, P., Poulos, A., Vasquez, J.A., Aguirre, P., de la Llera, J.C. (2019) "Seismic risk assessment of an emergency department of a Chilean hospital using a patient-oriented performance model", Earthquake Spectra, 35, 489-512.

Lin, Y.-X., Lin, C.-H. and Lin, C.-H. (2021), "A challenge for healthcare system resilience after an earthquake: The crowdedness of a first-aid hospital by non-urgent patients", PLOS ONE, 11 (4), e0249522.

United Nations International Strategy for Disaster Reduction. 2009 UNISDR Terminology on Disaster Risk Reduction [cited 2020 Dec 24]. Available from: https://www.preventionweb.net/files/7817_UNISDRTerminologyEnglish.pdf

Yeh, C.-H., Loh, C.-H. and Tsai, K.-C. (2006), "Overview of Taiwan Earthquake Loss Estimation System", Natural Hazards, 37(1-2), 23-37.

Experiments of BRBs with Varying Section Truss Restrainers

An-Chien Wu [1], Ming-Chieh Chuang [1], Keh-Chyuan Tsai [2]

吳安傑 [1]、莊明介 [1]、蔡克銓 [2]

Abstract

Buckling-restrained braces (BRBs) can effectively improve the stiffness, strength, and energy dissipation capacity of building structures. The key feature of the truss-confined BRB (TC-BRB) is attaching an additional truss system outside the steel casing. The truss system is composed of several steel open-web truss frames, thereby providing overall restraining rigidity and reducing steel casing section size and infilled mortar. The overall self-weight is reduced as compared to the conventional BRB, especially in the cases of long-span and large axial capacity BRB applications. An experimental program was conducted using cyclically increasing loads on two 1/3-scale TC-BRB specimens, each of 850kN nominal yield strength and 6.3m long with a varying depth of the truss frame. Test results show that both specimens have a very stable hysteretic response, meeting the AISC acceptance criteria. The two specimens eventually failed at a very large axial strain either with a global flexural buckling of the restraining system or a tensile fracture of the steel core. A simplified method for estimating the elastic buckling strength of the TC-BRB is then developed, and its accuracy is verified through finite element model analysis. Recommendations on the seismic design and analysis of the TC-BRB are being prepared in a separate paper.

Keywords: buckling-restrained brace, truss-confined restrainer, effective rigidity, buckling load

Introduction

Recently, a novel type of buckling-restrained brace (BRB) called a truss-confined BRB (TC-BRB), with a varying cross-sectional depth, has been investigated. As shown in Figure 1, the restraining system of the proposed TC-BRB is fabricated using several truss frames attached to a common steel casing [Chen et al. 2021, Chen 2021]. Each truss frame is symmetric to its mid-span and composed of several truss segments in series. Each of the truss segments consists of a chord near-parallel to the BRB longitudinal axis, a diagonal, and a pair of posts approximately in the BRB transverse direction. Most of the flexural rigidity of the truss system is provided by the chord, while the diagonal and posts mainly contribute to the overall shear rigidity of each segment. In order to improve the out-of-plane stability of the truss confining system,

transverse components are distributed at a certain distance along the BRB longitudinal axis to connect the truss frames. The flexural and shear rigidities contributed by the transverse components are negligible.

Test Program

In order to represent the TC-BRB as a part of the mega braced frames adopted in a tall building Figure 2), a diagonal brace inclined at approximately 45 degrees across four stories, each with a story height of 4m, was considered. Due to the limitations of the test facility, the prototype TC-BRB in the mega braced frame was scaled down by approximately 1/3. The two specimens, 2VT and 4VT, were designed with a total length of approximately 6.3m (L_{BRB} in Figure 1). Both specimens had a nominal yield capacity of 850kN with a cruciform core cross-section made from 25-mm-thick CNS SN490B steel plate. Each end of

the steel core was connected to an end plate welded by a pair of lug plates with the pin connection details. The steel casings were made from 139.6×4mm CNS STK490 steel tubes and infilled with 56MPa mortar. The chord of the truss confining system was shaped to have the center-to-center distance between the steel casing and the chord varied along the BRB. The shape agrees with a function of $h(x) = h_0\cos(a\pi x/L_{sc})$, where L_{sc} is the casing length, a controls the curvature of the chord, h_0 is the central height of the truss frame, and $x = 0$ and $x = L_{sc}/2$ are the locations of the casing midspan and end, respectively. For the case $a = 0$, the TC-BRB would have a constant cross-sectional depth truss system. This type of TC-BRB has been investigated by other researchers [Guo et al. 2017a, Guo et al. 2017b]. Specimens 2VT and 4VT were constructed with h_0 equal to 290 mm and 330 mm and corresponding a values of 0.85 and 0.89, respectively. The nominal cross-sectional dimensions of the chord and the post in Specimen 2VT were 48.4×3.2mm, while they were 48.4×3mm in Specimen 4VT. The sizes of the diagonal and transverse tubes were 33.8×2.8mm for both specimens. The truss frames of both specimens were divided into twelve truss segments with equal spacing L_s between adjacent posts.
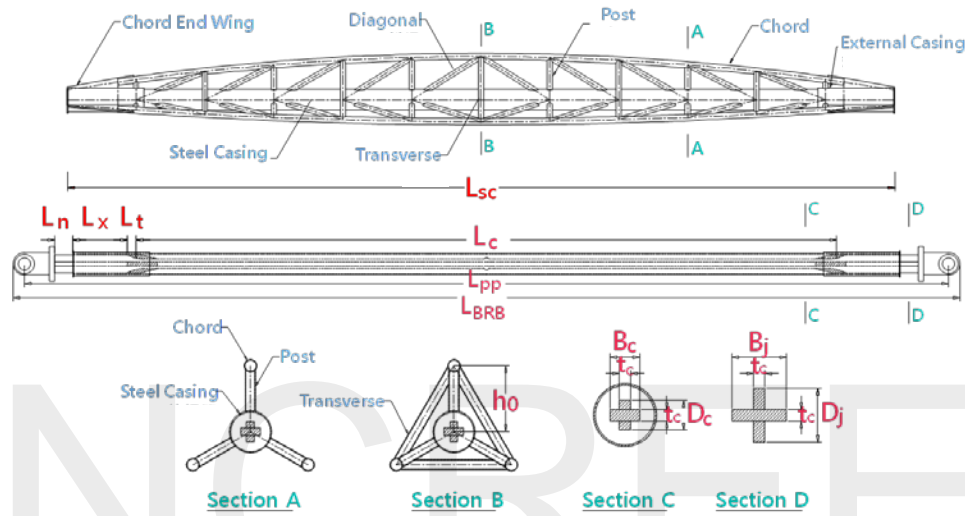

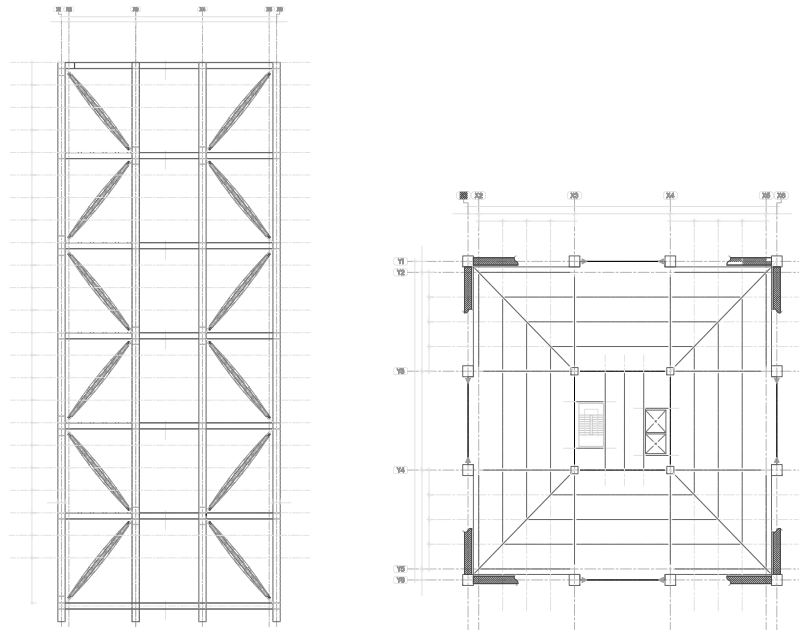Figure 1. Cross-sectional details of the proposed TC-BRB.

Figure 2. Elevation and floor framing plan of the prototype tall building.

The specimens were tested using the multi-axial testing system (MATS) at the Taiwan National Center for Research on Earthquake Engineering [Lin et al. 2017] by applying cyclically

increasing displacements as prescribed in the AISC specifications [AISC 2016]. Two steel connectors were made to anchor the pin ends of the specimens to the reaction wall or MATS platen and to provide end boundary conditions for the gussets. A pair of displacement transducers was mounted at each brace end to measure the axial deformations. A motion capture system was adopted in order to record the in-plane and out-of-plane deformations along the specimens. The standard loading proceeded with increasing axial deformations, considering inter-story drift ratios (IDRs) ranging from 0.5% to 2% for two cycles at each deformation level. The extended loading was continued with five cycles of 2% IDR to achieve an index of 200 cumulative plastic deformation (CPD), as prescribed by the specifications [AISC 2016]. In order to trigger potential instability of the specimens, axial deformations corresponding to 3% to 5% IDRs were applied following the last cycle of 2% IDR until failure occurred.

Test Results

The BRB's initial imperfection can result from the fabrication error and self-weight. Figure 3 shows the initial crookedness of the specimens, where the negative in-plane values are toward the gravity direction and the positive out-of-plane values are toward the east. It can be found that the fabrication error and self-weight had significant effect on the in-plane initial crookedness of the specimens. As shown in Figure 4, both specimens exhibited stable and repeatable hysteresis behavior with a maximum core strain larger than 1.4% throughout the standard loading and the first five cycles of the extended loading without any observable instability or damage. During the abovementioned loadings, the over-strength ratios due to the strain hardening effect (ω) were 1.28 and 1.48, while the peak compression-to-tension ratios (β) were 1.14 and 1.10 for Specimens 2VT and 4VT, respectively, when the 2% IDR cycle was completed. Specimen 2VT buckled with the obvious in-plane flexural deformation developed along the restraining system (Figure 5) at the first cycle of 3% IDR loading, and the axial compressive strength dropped drastically after reaching 1647kN with a CPD value of 236. Specimen 4VT sustained the subsequent 3% to 5% IDR loadings and its steel core eventually fatigue fractured at the 5th cycle in the 5% drift loadings. During the entire test, the developed maximum tension and compression of 1480 and 1971kN in Specimen 4VT was recorded. The maximum ratios of ω and β calculated were 1.66 and 1.36, respectively, and the gained CPD value was 625. In addition, from the axial force versus deformation relationships given in Figure 4, it can be seen that the axial stiffness and compressive strength rose slightly when Specimen 4VT was compressed to axial deformations larger than 100mm. This kind of phenomenon is likely caused by the effects of severe high-mode buckling developed along the core, or when the compressible spacing at any one end of the inelastic core was exhausted.
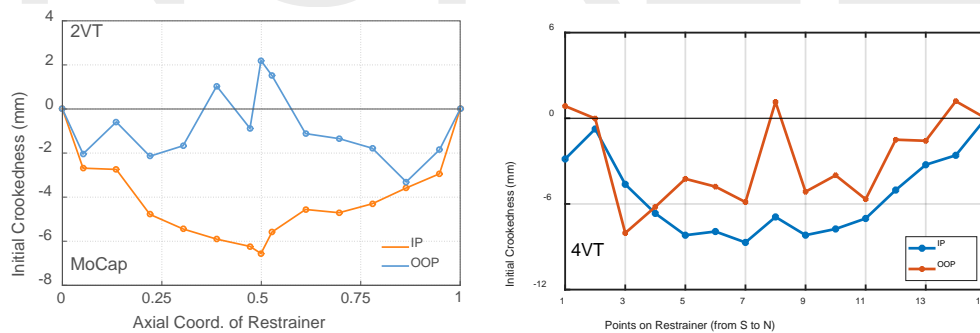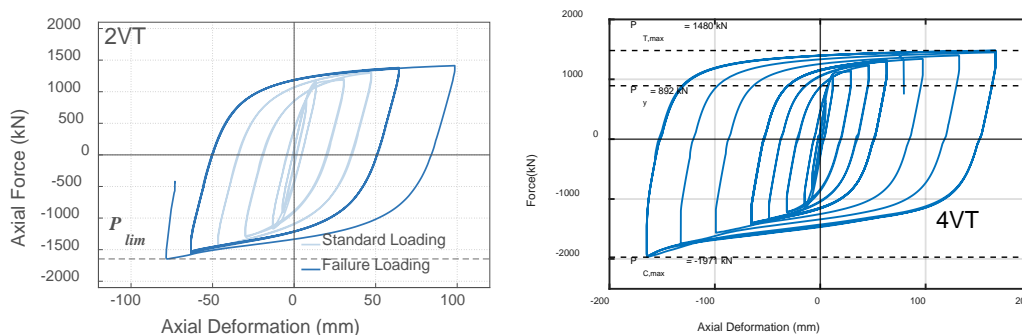

Figure 3. Initial crookedness of specimens.

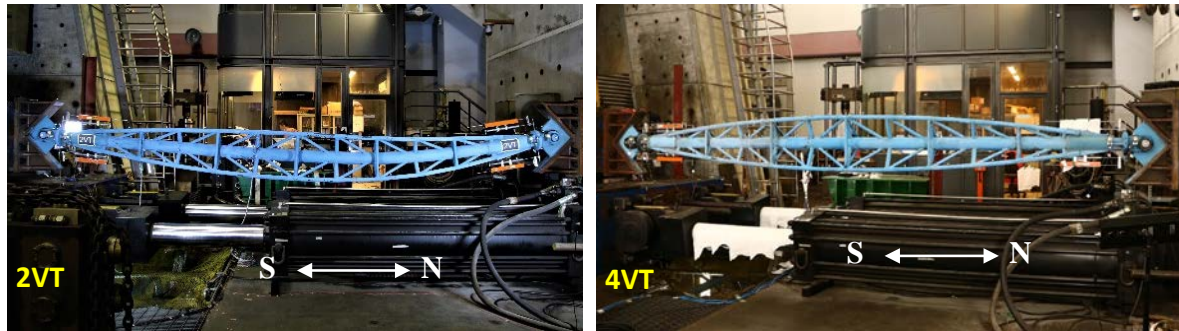Figure 4. Hysteresis behavior of specimens.

Figure 5. Damage conditions of specimens at the end of testing.

Conclusions

The proposed TC-BRB with a varying cross-sectional depth truss confining system appears feasible and practical for long-span BRBs. Its novel restraining system may have remarkable advantages on the efficient flexural rigidity, less self-weight, and the associated architectural appearance when it is adopted as a large load-carrying and long-span brace in mega braced frame structures. The two 1/3-scale TC-BRBs, with different mid-span heights of the truss frame of their restraining systems, represent a brace length of approximately 20m and a nominal yield capacity of 7650kN in the prototype mega braced frame, were investigated. Their experimental performance demonstrates satisfactory hysteretic behavior complying with the requirements prescribed in the model specifications. Test results indicate that a properly fabricated TC-BRB specimen designed with a stiffer truss confining system is able to sustain a larger CPD without flexural buckling. It is confirmed that the proposed TC-BRB can be designed and fabricated to achieve excellent seismic performance. A simplified method in estimating the elastic buckling strength of the TC-BRB has been developed. Its accuracy was verified through finite element model analysis. Recommendations for the seismic design and analysis of the TC-BRB will be introduced in a subsequent paper.

References

Chen C, Lin YC, Wu AC, Chen LA, Tsai KC. Long-span buckling-restrained braces using truss-confined restrainers. Structural Engineering 2021; 36 (2): 5-50. (in Chinese)

Chen LA. A Study of BRBs using Varying Section Steel Truss Restrainers. Master Thesis, National Taiwan University: Taipei, Taiwan, 2021. (in Chinese)

Guo YL, Zhou P, Wang MZ, Pi YL, Bradford MA. Numerical studies of cyclic behavior and design suggestions on triple-truss-confined buckling-restrained braces. Engineering Structures 2017a; 146: 1-17.

Guo YL, Zhou P, Wang MZ, Pi YL, Bradford MA, Tong JZ. Experimental and numerical studies of hysteretic response of triple-truss-confined buckling-restrained braces. Engineering Structures 2017b; 148: 157-174.

Lin TH, Chen PC, Lin KC. The multi-axial testing system for earthquake engineering researches. Earthquakes and Structures 2017; 13 (2): 165-176.

American Institute of Steel Construction (AISC). Seismic Provisions for Structural Steel Buildings (AISC 341-16). AISC: Chicago, Illinois, 2016.

Effect of Soil Nonlinearity on High-frequency Spectral Decay at High Strains for Site Response Analysis

Norman Abrahamson,[1] Ellen Rathje,[2] Yu-Wen Chang,[3] Domniki Asimaki,[4] Chih-Wei Chang,[5] Hsun-Jen Liu,[6] Shang-Yi Hsu,[7] and Chiun-Lin Wu[8]

Norman Abrahamson、Ellen Rathje、張毓文、Domniki Asimaki、張志偉、
劉勛仁、許尚逸、吳俊霖

Abstract

This study demonstrates that equivalent-linear (EQL) analysis is necessary to correct the results of the EQL method, owing to its known deficiencies related to overdamping of the high-frequency components of motion when induced strains are large. A steep slope at the high-frequency components of the Fourier amplitude spectrum (FAS) is computed at the surface from EQL analysis. This difference is informed by numerical site response simulations using the EQL and nonlinear (NL) approaches, as well as by recorded ground motions. This study presents EQL and NL site response analyses that are used to support the adjustment for correcting the high-frequency components of the EQL FAS.

Keywords: equivalent-linear, site response analyses, kappa, high strain.

Introduction

A well-known drawback of equivalent-linear (EQL) site response analysis is that it attempts to approximate the nonlinear (NL) response of a soil through a linear, viscoelastic solution with frequency-independent properties. By doing so, the method disregards the small-amplitude, high-frequency components of deformation that involve hysteresis loops with little modulus degradation or damping (*i.e.*, nearly elastic secondary loops). By assigning uniform NL properties independent of frequency, EQL analyses result in surface ground motions that exhibit unrealistically low amplitudes at high frequencies when the induced strains are large (Kausel and Asimaki, 2002). Various adjustments to EQL analysis have been proposed to address this issue, including an approach that scales the high-frequency components of the EQL Fourier amplitude spectrum (FAS) to match a target kappa (κ) (Xu and Rathje, 2021).

To quantify the high-frequency energy that is artificially damped by EQL analyses, the empirical FAS and analytical FAS for high strain are used. To capture the intensity dependency of the high-frequency attenuation by EQL and NL analyses, the rock-outcrop ground motions scaled to amplitudes from small to large were used.

Empirical FAS for High Strain

In order to indicate the NL site response behavior at high strain, the Next Generation Attenuation (NGA) West2 data set (Ancheta *et al.*, 2014) and the Taiwan NGA data set (National Center for Research on Earthquake Engineering (NCREE), 2019) were searched to find data likely to have very high strains. Ground motions in soft soil sites (with a averaged shear-wave velocity to a depth of 30 meters $V_{S30} < 220$ m/s), of magnitude $M > 6.0$, and the closest distance to the rupture surface $Rrup < 10$ km were selected. Using these selection criteria with the TNGA data set yielded twelve recordings. For this set, the high-frequency slope of the geometric mean normalized spectrum is

[1] Professor, University of California at Berkeley, USA

[2] Professor, University of Texas at Austin, USA

[3] Associate Researcher, National Center for Research on Earthquake Engineering

[4] Professor, California Institute of Technology, USA

[5] Assistant Technologist, National Center for Research on Earthquake Engineering

[6] Assistant Researcher, National Center for Research on Earthquake Engineering

[7] Associate Researcher, National Center for Research on Earthquake Engineering

[8] Deputy Director General, National Center for Research on Earthquake Engineering

0.068 s (Figure 1). For the NGA-West2 data set, there were 47 recordings that fell in the magnitude, distance, and V_{S30} ranges. For this set, the high-frequency slope of the geometric mean normalized spectrum corresponds to a high-frequency κ of 0.065 s (Figure 2), which is consistent with the slope from the TNGA data set.

Based on the consistency of the flat slope at high frequencies for high strain from the empirical data, the NL site response behavior of large ground motion should be present in the EQL site response analysis.
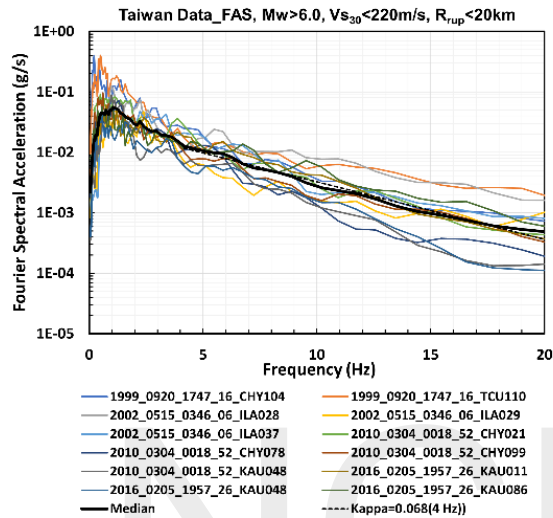

Figure 1. FAS for TNGA data with $M > 6.0$, $V_{S30} < 220$ m/s, and $R_{rup} < 20$ km.
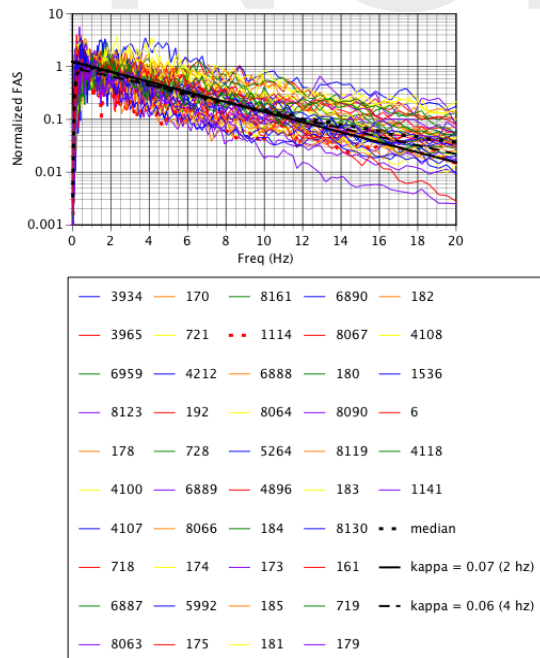

Figure 2. FAS for NGA-West2 data with $M > 6.0$, $V_{S30} < 220$ m/s, and $R_{rup} < 20$ km. The numbers in the legend are the record sequence numbers in the NGA-West2 data set.

Analytical FAS for High Strain

The two NL codes yielded identical results for frequency-domain EQL analyses using time series as input motions for all levels of ground shaking. Two independent NL site response codes, Deepsoil (Hashash *et al.*, 2018) and Py-Seismosoil (Shi and Asimaki, 2020), and two NL constitutive laws were used, the modified hyperbolic model (MKZ; Kondner and Zelasko, 1963), which was implemented in both codes, and the hybrid-hyperbolic model (HH; Shi and Asimaki, 2017), which was implemented in Py-Seismosoil. For low-intensity ground motions (peak ground acceleration PGA < 0.15 g), EQL and NL analyses were nearly identical (Figures 3(a) and (b)). For input ground motions with PGAs between 0.15 g and 0.65 g, the NL and EQL analyses started diverging, but the two NL constitutive models predicted the same response because the soil strength had not yet been reached. For the strongest input ground motion, PGA = 1.34 g, both NL constitutive models (MKZ simulated in Deepsoil and HH simulated in Py-Seismosoil) showed a flatter high-frequency decay in the FAS than for The EQL results (Figures 3(c) –(e)).

Figure 4 shows the computed surface EQL and NL FAS in a log-linear plot for input intensities of PGA = 0.067 g, 0.33 g, and 1.34 g. At PGA = 0.067 g, the EQL and NL results are similar and indicate κ = 0.045 s. The EQL and NL results deviate at high frequencies, with the NL results displaying a flatter slope. This flatter slope at high frequencies takes on similar values for PGA = 0.33 g and 1.34 g (κ = 0.060–0.065 s). These κ values are only slightly larger than the low-strain κ of 0.045 s, indicating that, even at large strains, the high frequencies are associated with damping that is close to its small strain value.

Spectral Shapes for High Strain

The computed surface FAS from the EQL and NL analyses for the three input intensity levels are plotted in Figure 5. The EQL and NL results are essentially the same for the smallest input intensity of 0.005 g, and the high-frequency slope of the FAS represents the small-strain κ for the site (κ = 0.065 s). For the two higher intensity motions, the EQL and NL FAS are similar at lower frequencies but deviate at higher frequencies. Here the FAS from NL analysis continuously flattens and between 20 Hz and 30 Hz becomes essentially horizontal. The high-frequency κ between 5 Hz and 15 Hz for the NL analyses ranges from 0.044 s to 0.053 s. This smaller κ, which indicates lower decay at high frequencies and less damping than at small strains, is due to additional high frequencies introduced in the NL analysis by the instantaneous stiffness increase that occurs at shear stress reversals when large strains are induced. The EQL analyses for the three higher intensity levels reveal much larger κ values (between 0.21 s and 0.59 s) owing to the significantly reduced stiffness and

increased damping associated with the induced strain levels. The strain-compatible properties are imposed uniformly throughout the time history in the EQL analyses, as opposed to the instantaneous stiffness reduction of the NL response. Figure 6 plots the surface acceleration response spectra for the EQL and NL analyses for the four input intensity levels. For the two largest intensity levels (PGA = 0.94 g and 4.06 g), the response spectra from the EQL analysis are consistently larger than those from the NL analysis, although the peak in the response spectra generally occurs at the same periods (T ≈ 2 s). One noticeable difference in the spectral shapes of the EQL and NL responses is the flat response at shorter periods (up to 0.3 s–0.5 s) in the EQL spectra, which is not observed in the NL spectra. This difference is more clearly seen in the normalized response spectra (Sa/PGA), which are shown in Figure 5 for the two highest intensity levels. The spectra from the NL analysis remain flat only to 0.06–0.1 s, and then start to increase moderately between 0.1 s and 0.8 s. This spectral shape at high frequencies for the NL analysis is a result of the shape of the FAS at high frequencies (Figure 5(a)) and can be incorporated into the EQL analyses through the adjustment method.

The results in Figure 3 indicate not only differences in frequency content between the EQL and NL analyses, but also differences in amplitude. The PGA from NL analysis is 40% to 60% smaller than that from EQL analysis for the two largest intensity levels, implying that the EQL analysis may be overestimating the site amplification. However, both NL and EQL analyses underpredict observed site amplifications at high frequencies when large strains are induced in the analysis, and the underprediction is more significant for NL analyses. This underprediction is likely a result of the assumption of one-dimensional wave propagation, in which layers are assumed to extend infinitely in the horizontal direction in the site response analysis. Under this condition, when large strains are induced and the shear strength is mobilized on a horizontal plane, shear stresses cannot be transmitted and the peak acceleration and short period response at the ground surface are bounded. This effect is more significant when the fully NL stress–strain response of the soil is modeled. As a result, it is likely that the true amplification is somewhere between those predicted by the EQL and NL analyses.

Conclusions

Based on the consistency of κ at high frequencies obtained from the equivalent-linear (EQL) and nonlinear (NL) analytical models and from the available empirical data, it is seen that the spectral values of the short-period response for the strong-motion recordings using the EQL method are higher than those using the NL method even though the EQL method overdamps the high frequencies. These larger

spectral values of the short-period response are due to the peak in the response spectrum in the 1.5–2 s period range. Therefore, the short-period Sa values do not reflect the amplitudes of the short-period Fourier amplitude spectrum.

(a) PGA = 0.067 g   (b) PGA = 0.134 g

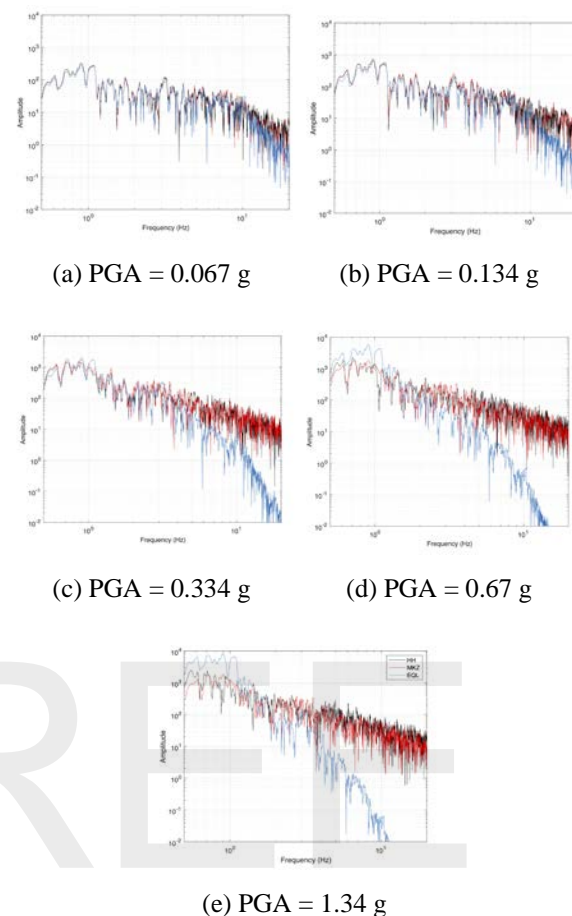(c) PGA = 0.334 g   (d) PGA = 0.67 g

(e) PGA = 1.34 g

Figure 3. Comparison of EQL method and two NL constitutive models: (a)-(b) for low levels of shaking, EQL and NL analyses yield almost identical results; (c)–(e) for moderate to strong motions, the EQL method underestimates the high-frequency content.
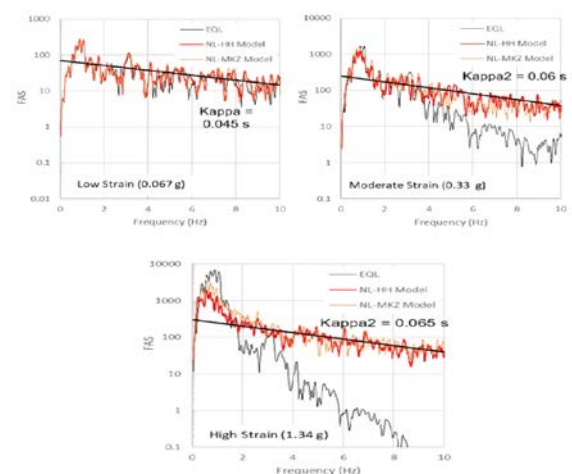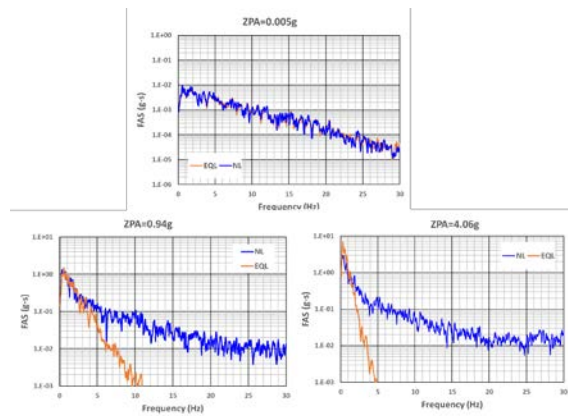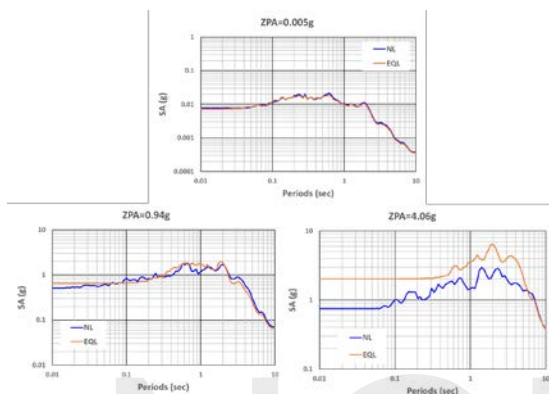

Figure 4. Comparison of FAS and κ for EQL and NL models for three shaking levels.

(a) Surface FAS

(b) Surface acceleration response spectra

Figure 5. Surface FAS and acceleration response spectra from EQL and NL analysis for the three input intensity levels.
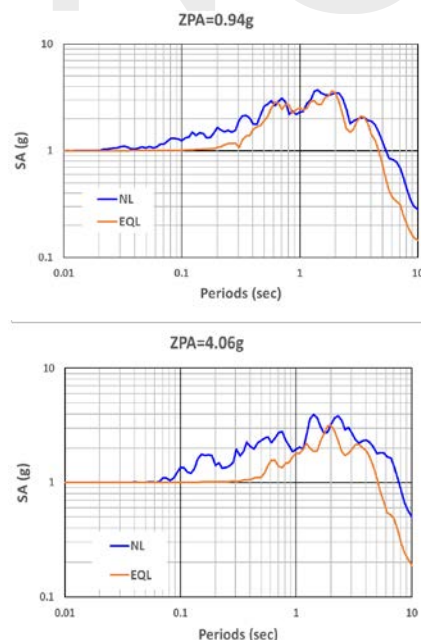

Figure 6. Normalized surface acceleration response spectra from EQL and NL analyses for input intensity levels of PGA = 0.94 g and PGA = 4.06 g.

References

Hashash, Y. M., Dashti, S., Musgrove, M., Gillis, K., Walker, M., Ellison, K., and Basarah, Y. I. (2018). Inuence of tall buildings on seismic response of shallow underground structures. Journal of Geotechnical and Geoenvironmental Engineering, 144(12), 04018097.

Kausel, E. and Assimaki, D. (2002). Seismic simulation of inelastic soils via frequency-dependent moduli and damping. Journal of Engineering Mechanics, 128(1), 34-47.

Kondner, R. L. and Zelasko, J. S. (1963). A hyperbolic stress strain formulation for sands. 2nd Pan. Am. Conference in Soil Mechanics Foundation Engineering. Vol. 1: 289-394. Brazil.

National Center for Research on Earthquake Engineering (2019). Development of the Hazard Input Document for Taiwan Using SSHAC Level 3 Methodology: Summary Report, prepared for Taiwan Power Company, 203pp.

Shi, J. and Asimaki, D. (2020). jsh9PySeismoSoil: (Version v0.3.6). Zenodo. http://doi.org/10.5281/zenodo.3711582.

Timothy D. Ancheta, Robert B. Darragh, Jonathan P. Stewart, Emel Seyhan, Walter J. Silva, Brian S.J. Chiou, Katie E. Wooddell, Robert W. Graves, Albert R. Kottke, David M. Boore, Tadahiro Kishida, and Jennifer L. Donahue (2014). NGA-West2 database. Earthquake Spectra. 30. 10.1193/070913EQS197M.

Xu, B. and Rathje, E. (2021). The Effect of Soil Nonlinearity on High Frequency Spectral Decay and Implications for Site Response Analysis, Earthquake Spectra, https://doi.org/10.1177/ 8755293020981991.

Seismic Potential and Velocity Structure
of Hengchun Peninsula

Yu-Chih Huang, Che-Min Lin[2], Hung-Hao Hsieh[3], Chih-Wei Chang[4]

黃有志[1]、林哲民[2]、謝宏灝[3]、張志偉[4]

Abstract

Taiwan is located at a convergent plate boundary and is characterized by intense seismicity and complex tectonics. The Hengchun Peninsula is an accretionary prism formed by plate collision and it is dominated by fold-and-thrust belts. The Hengchun Fault is an eastward-dipping thrust fault that is located near the intersection of the foothills and the plains, with both ends suspected to extend into the sea. Based on the data from historical earthquakes, the Hengchun Peninsula is generally considered to have a high risk for seismic hazards. Recently, a temporary seismic network was operated by the National Center for Research on Earthquake Engineering with twelve broadband seismometers along the Hengchun Fault with an interstation spacing of approximately 5 km. Some nearby broadband stations were also included to monitor the seismic activity and to study shallow crustal velocity structures underneath the Hengchun Peninsula. The seismicity mainly occurs in the offshore regions of the Hengchun Peninsula and is caused by plate tectonics. The magnitudes for most past events are less than 3, with focal depths of more than 20 km to the west of the Hengchun Peninsula and approximately 10–30 km to the east. In addition, intense seismicity occurs to depths of 10 km in the Jiupeng area, namely in the vicinity of Fengkanghsi Fault. In this research, time domain empirical Green's functions are obtained from the cross-correlation of daily ambient seismic noise signals with long-term stacking. The 0.5–15 s Rayleigh-wave phase-velocity dispersion curves are found and then 1–5 s Rayleigh-wave phase-velocity maps are constructed. The lateral resolution is determined through a checkerboard resolution test and shallow crustal S-wave velocity structures within 3 km depths of the surface are derived. High velocities may imply the presence of Miocene strata or mud diapirs. More detailed velocity distributions are compared with the information for geological structures, groundwater distribution, and other associated phenomena.

Keywords: Hengchun Peninsula, seismicity, ambient seismic noise, tomography, velocity structures

Tectonic Setting and Geological Structure

Taiwan is located at a convergent plate boundary where the Eurasian Plate interacts with the Philippine Sea Plate and is characterized by complex tectonics and intense seismicity (Tsai et al., 1977; Tsai, 1986). The Hengchun Peninsula is located on the southernmost tip of Taiwan and connects to the Hengchun Ridge to the south. It is an accretionary prism formed by plate tectonics and is dominated by fold-and-thrust belts, that is, Hengchun Peninsula may be regarded as representative of the early stage of the Taiwan orogen.

Figure 1 shows that the strata are generally older in the middle of the accretionary prism and gradually young on both sides, and the accretionary prism thickens and widens toward the north. In principle, the geodynamics are that the Eurasian Plate subducts eastward along the Manila Trench at 21°N, and the Eurasian Plate collides with the Luzon Arc at 22°N; these tectonic styles are approximately demarcated by 21.5°N (Chen et al., 2005). Furthermore, the deformation front, out-of-sequence thrust, and Hengchun Fault are major tectonic structures from west to east, among the fold-and-thrust belts. The deformation front connects to the Manila Trench in the south and may extend to the geological boundaries between the Western Foothills and the Western Coastal Plains on the Taiwan Island in the north. The out-of-

sequence thrust may connect with the Shoushan and Chishan Faults on land, and the Hengchun Fault may connect with the Chaochou Fault (Figure 2; Lin et al., 2009).
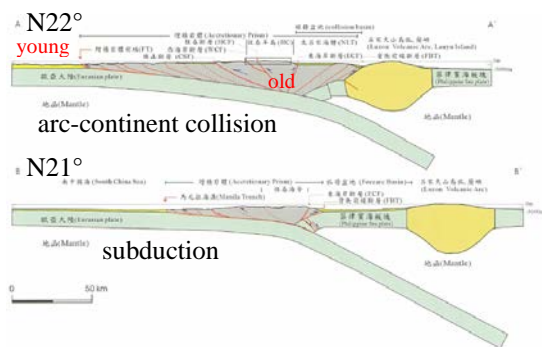

Figure 1. The Hengchun Peninsula is an accretionary prism (gray areas) and is dominated by fold-and-thrust belts (Chen et al., 2005).
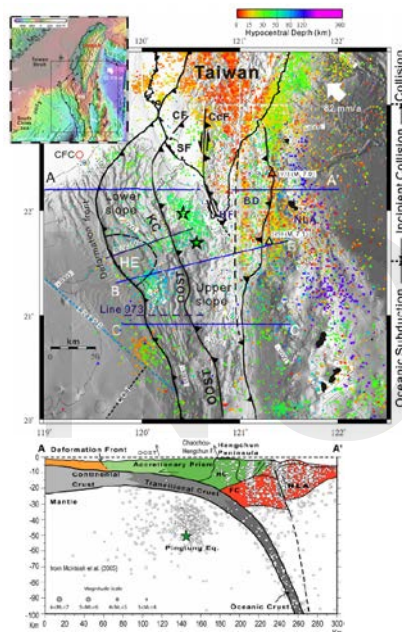

Figure 2. The tectonic setting and seismic activity of the Hengchun Peninsula and its surroundings (Lin et al., 2009).

According to the map of Taiwan's active faults released by the Central Geological Survey (CGS) in 2021, the Hengchun Fault is categorized as a late Pleistocene active fault. The Hengchun Fault is an eastward-dipping thrust fault, located along the intersection of the foothills and the plains, with both ends suspected to extend into the sea (Figure 3; Giletycz et al., 2017). Therefore, the Taiwan Earthquake Research Center (TEC) and CGS announced the Hengchun Fault has a high probability of more than 20% for earthquakes with magnitudes greater than 6 to occur within 50 years. Hence, the Hengchun Peninsula is considered to have high seismic risk. However, in the historical earthquake in 1959 and the sequence of two main shocks in 2006, the epicenters were located in the offshore regions of the Hengchun Peninsula. Although the magnitudes were

greater than 7 and tsunamis were triggered with heights of tens of centimeters, these events were caused by plate tectonic interaction, rather than activity along the Hengchun Fault.

Moreover, many mud volcanoes and mud diapirs have been discovered in the southwest offshore regions of Taiwan after detailed surveys over many years. They could be connected to similar onshore structures and be correlated with geological structures, such as anticlines, faults, and tablelands (Chen et al., 2016; Ching et al., 2016). The mud diapirs are still active and are characterized by high gravity anomalies, which may be related to high pore pressures caused by plate tectonic processes (Doo et al., 2015).
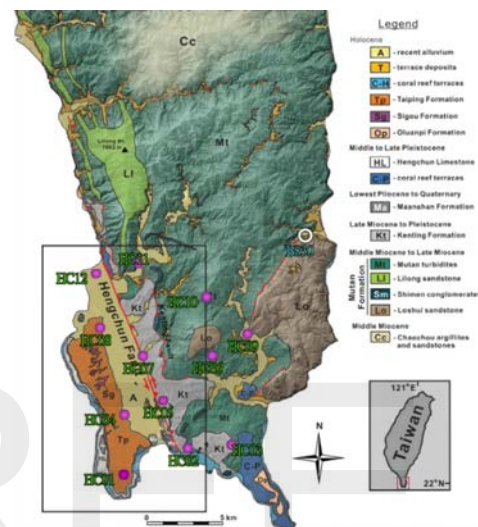

Figure 3. The geological structure (Giletycz et al., 2017) and broadband seismic stations operated by the NCREE along the Hengchun Fault (purple solid circles) and other networks (white circles).

Seismic Stations and Activity

Recently, a temporary seismic network was operated by the National Center for Research on Earthquake Engineering (NCREE) to monitor the seismic activity in the Hengchun Peninsula. The network used twelve broadband seismometers along the Hengchun Fault with an interstation spacing of approximately 5 km (Figure 3). Some nearby broadband stations were also included and the program for relocating earthquakes more accurately with the double-difference algorithm (hypoDD; Waldhauser and Ellsworth, 2000) was applied. The seismicity was predominately located in the offshore regions of the Hengchun Peninsula, similar to findings of Lin et al. (2009) (Figure 2), and this was caused by plate tectonic processes (Figure 4). The magnitudes for most events were less than 3, with focal depths of more than 20 km to the west of the Hengchun Peninsula and approximately 10–30 km to the east. Furthermore, intense seismicity was detected to depths of 10 km of the surface in the Jiupeng area, that is, in the vicinity of Fengkanghsi Fault.
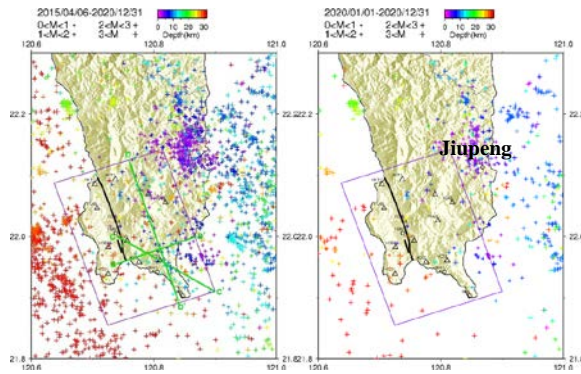
Figure 4. Detected seismicity from 2015-04-06 to 2020-12-31 (left) and from 2020-01-01 to 2020-12-31 (right).

Shallow Crustal Velocity Structures Beneath the Hengchun Peninsula

Since the basic theorem of ambient seismic noise analysis has been generally verified, investigations of subsurface velocity structures have provided important insights for various parts of the world. Ambient seismic noise contains diffuse wavefields with passive structural signals. The propagation is similar to that of surface waves, hence exhibiting dispersion properties related to underground velocity structures. The time domain empirical Green's functions (TDEGFs) can be obtained from the cross-correlation of station pairs with simultaneous and continuous ambient seismic noise signals (Weaver, 2005). Relatively stable and representative TDEGFs could be enhanced after long-term stacking. Then, the tomographic method was applied to construct phase-velocity maps and a checkerboard resolution test (CRT) was used to assess the lateral resolution of the obtained phase velocities. The S-wave velocity (Vs) structures were constructed, and it was shown that the depth range is positively related to the aperture of the seismic network and its lateral resolution is positively related to the density of seismic stations. Figure 5 shows the data analysis procedures for processing ambient seismic noise in this study; they are similar to those of Huang et al. (2018).
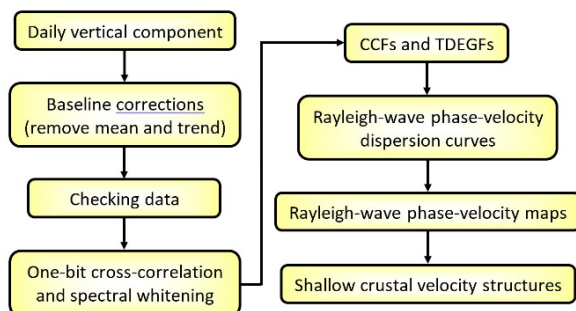

Figure 5. Data processing of ambient seismic noise in this study.
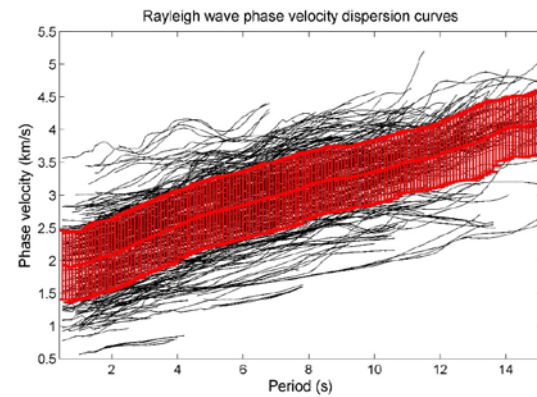
The daily vertical-component data from 2018 to

Figure 6. Measured 0.5–15 s Rayleigh-wave phase-velocity dispersion curves. Black lines indicate individual dispersion curves and the red band represents the average with standard deviation.
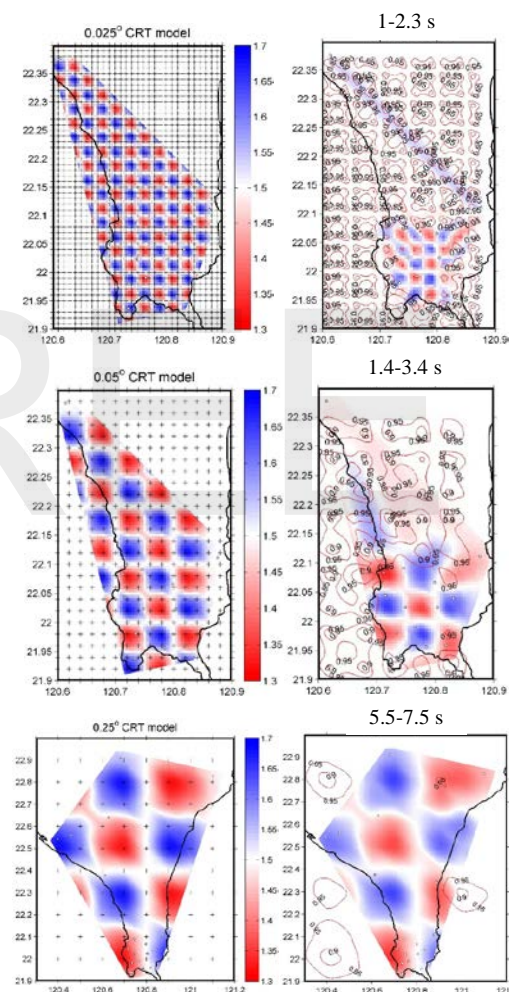
Figure 7. The 0.025°, 0.05°, and 0.25° CRT input models (left; + mark positions of the tomographic grid points) and the recovery results (right).

2020 were first assessed for quality and then downsampled from 100 Hz to 20 Hz. Daily cross-correlation functions (CCFs) were calculated using a 100-s lag time in the 0.5–15 s period band. Figure 6 shows the measured Rayleigh-wave phase-velocity dispersion curves, including the averages and standard deviations. Figure 7 displays CRT input models for a

velocity contrast of 1.5 ± 0.2 km/s at 0.025°, 0.05° and 0.25° anomalies and 0.01°, 0.02°, and 0.1° grid spacing, respectively. The recovery results indicate that the regions with high station densities near the Hengchun Fault were recovered with 0.025° and 0.05° anomalies. In contrast, for other regions with low station densities on the Hengchun Peninsula, the CRT could only be recovered with a 0.25° anomaly.

Based on CRT recovery results, a 0.02° grid spacing was applied for the construction of 1–5 s Rayleigh-wave phase-velocity maps around the Hengchun Fault. At every grid point, the Rayleigh-wave phase-velocity dispersion curves were extracted from the phase-velocity maps. An initial velocity model with related physical parameters was provided, and the SURF program (Herrmann, 2013) was then employed to derive 1-D Vs structures. Figure 8 presents three 2-D Vs profiles within 3 km depths near the Hengchun Fault. Small-scale, near-surface high velocities anomalies were found to be distributed near the surface expression of the Hengchun Fault, and large-scale high velocity anomalies occur below the hills on the north and east sides of the Hengchun Fault. Hence, it is speculated that the high velocities may indicate the locations of Miocene strata or mud diapirs (which produce high gravity anomalies).
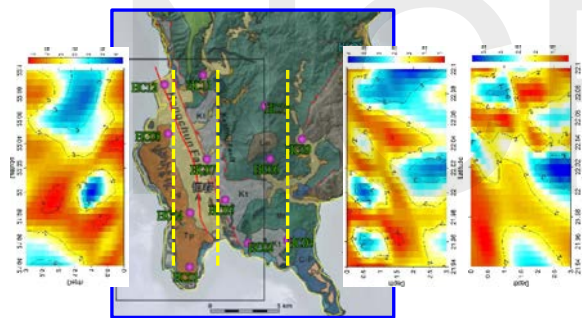

Figure 8. Three 2-D Vs profiles to depths of 3 km near the Hengchun Fault.

Future Studies

In the near future, more detailed shallow crustal Vs structures beneath the Hengchun Peninsula will be obtained to provide comparisons with the information derived from geological structures, groundwater distribution, and associated phenomena. Based on these observations, the earthquake probabilities of seismogenic structures such as the Hengchun Fault can be evaluated with more confidence. The parameters are important for constructing strong ground motion, assessing seismic hazards, and numerically simulating potential seismic risks. Some of the results in this study were published in academic conferences or the project reports of the Ministry of Science and Technology.

References

Chen, S. C., Hsu, S. K., Tsai, C. H., Wang, Y., Horng, C. S., and Kuo, F. W. (2016), "The Influence of mud diapirism on the tectonic evolution in nearshore and onshore areas of the West Hengchun Hill", *Min. Metal.* 60, 7-22. (in Chinese with English abstract)

Chen, W. S., Lee, W. C., Huang, N. W., Yen, I. C., Yang, C. C., Yang, H. C., Chen, Y. C., and Sung, S. H. (2005), "Characteristics of accretionary prism of Hengchun Peninsula, southern Taiwan: Holocene activity of the Hengchun Fault", *Western Pacific Earth. Sci.* 5, 129-154. (in Chinese with English abstract)

Ching, K. E., Gourley, J. R., Lee, Y. H., Hsu, S. C., Chen, K. H., and Chen, C. L. (2016), "Rapid deformation rates due to development of diapiric anticline in southwestern Taiwan from geodetic observations", *Tectonophys.* 292, 241-251.

Doo, W. B., Hsu, S. K., Lo, C. L., Chen, S. C., Tsai, C. H., Lin, J. Y., Huang, Y. P., Huang, Y. S., Chiu, S. D., and Ma, Y. F. (2015), "Gravity anomalies of the active mud diapirs off southwest Taiwan", *Geophys. J. Int.* 203, 2089–2098.

Giletycz, S. J., Chang, C. P., Lin, A. T. S., Ching, K. E., and Shyu, J. B. H. (2017), "Improved alignment of the Hengchun Fault (southern Taiwan) based on fieldwork, structure-from-motion, shallow drilling, and levelling data", *Tectonophys.* 721, 435-447.

Herrmann, R. B. (2013), "Computer Programs in Seismology: An Evolving Tool for Instruction and Research", *Seismol. Res. Lett.* 84, 1081-1088.

Huang, Y. C., Ohkura, T., Kagiyama, T., Yoshikawa, S., and Inoue, H. (2018), "Shallow volcanic reservoirs and pathways beneath the Aso caldera revealed using ambient seismic noise tomography", *Earth Planets Space* 70, 169.

Lin, A. T., Yao, B., Hsu, S. K., Liu, C. S., and Huang, C. Y. (2009), "Tectonic features of the incipient arc-continent collision zone of Taiwan: Implications for seismicity", *Tectonophys.* 479, 28-42.

Tsai, Y. B. (1986), "Seismotectonics of Taiwan", *Tectonophys.* 125, 17-37.

Tsai, Y. B., Teng, T. L., Chiu, J. M., and Liu, H. L. (1977), "Tectonic implications of the seismicity in the Taiwan region", *Mem. Geol. Soc. China* 2, 13-41.

Waldhauser, F., and Ellsworth, W. L. (2000), "A double-difference earthquake location algorithm: method and application to the northern Hayward fault, California", *Bull. Seism. Soc. Am.* 90, 1353-1368.

Weaver, R. L. (2005), "Information from seismic noise", *Science* 307, 1568-1569.

Discussion of the Activity of the Tatun Volcano Group from Recent Monitoring Results

Hsiao-fen Lee[1], Ya-chuan Lai[1], Min-Hung Shih[1], Cheng-Horng Lin[1,2], Chin-hsing Liu[1] and Chia-Jui Teng[1], Teng-Yang Shao[1]

李曉芬 [1]、賴雅娟 [1]、史旻弘 [1]、林正洪 [1,2]、劉進興 [1]、鄧嘉睿 [1]、邵騰揚 [1]

Abstract

According to survey and monitoring results over many years, the Tatun Volcano Group (TVG) is identified as an active volcano. Taiwan Volcanic Observatory-Tatun (TVO) was established in 2011 to monitor the volcanic activity using various methods, including seismic activity, fluid geochemistry, and ground deformation. According to recent monitoring data, the volcano was relatively quiet from 2017 to 2018. However, based on an increasing level of hydrogen chloride in fumarolic gas, magmatic or deep hydrothermal fluid might have upwelled at the end of 2018. The seismic activity in the TVG increased in 2019 to approximately 1.5 times the background value. In 2020, it increased to as much as twice the background value. In addition to the significant increase in the number of microseisms, earthquakes with ML greater than 3.0 have also increased. Geochemical results have shown another anomaly, with a significant increase in helium content. The hot spring cation concentration in the Dayoukeng area also increased sharply. This increase in cation concentration might be due to a large amount of upwelling deep hydrothermal fluid. In 2021, the geochemical anomalies continued, but seismic activity steadied as pressure was released. These anomalies indicate that the TVG has become more active. The current monitoring work will continue to focus on whether there are more magmatic signals and on possible disasters caused by hydrothermal activities, such as phreatic eruptions.

Keywords: Tatun Volcano Group, volcano monitoring, micro-earthquake, geochemistry

1. Introduction

Hot springs and other geothermal activities of the Tatun Volcano Group (TVG) are still quite evident. The results of investigations over recent decades, including high helium isotopic ratios (~5–7 R_A) and increased seismicity, emission of volcanic gases, geothermal activity, and occurrence of hot springs, indicate that volcanic activity may not have stopped. Moreover, such observations imply that a magma reservoir exists beneath the TVG (Song *et al*., 2000; Yang *et al*., 1999). The last eruption at the TVG was 5–6 thousand years ago, as determined from ash dating (Belousov *et al*., 2010). It has been concluded that the TVG is an active volcano. Furthermore, the magma reservoir has been identified by seismic signal analysis and located in the Wanli area (Lin, 2016; Huang *et al*., 2021). A conduit with clustered seismicity was found beneath the Dayoukeng area, which is one of the strongest fumaroles in the TVG, and is connected to a fracture zone. Such clustered seismicity may be triggered by volcanic gases and fluids ascending from a deep magma reservoir and would be the likely pathway for ascending magma for a TVG eruption in the future (Pu *et al*., 2020).

The magmatic system of the TVG is stable overall, and no immediate eruption can be expected. However, the possibility of future eruption must still be considered, and, given the substantial hydrothermal activity of the TVG, eruption may be phreatic. Hence, detailed monitoring must be continued in order to detect significant volcanic activity. Recent monitoring data, especially important geochemical indicators, show that the activity in the TVG has changed. This study reports these unusual observations of the TVG, and the corresponding changes in various data.

2. Monitoring Methods

The Tatun Volcano Observatory continues to employ a variety of monitoring methods, including seismic monitoring, geochemical analysis, study of surface deformation, and geothermal measurements.

[1] National Center for Research on Earthquake Engineering
[2] Institute of Earth Sciences, Academia Sinica

The results of seismic and geochemical monitoring are presented here.

2-1 Geochemical analysis

The geochemical methods used by the Tatun Volcano Observatory include direct sampling and continuous soil gas monitoring. The method used in the present study is direct sampling. The sampling locations are shown in Figure 1. Water temperature, conductivity, and other parameters were measured *in situ* at each site and filtered water samples were brought back to the laboratory for analysis. The analyses included determination of concentrations of chloride (Cl^-), sulfate (SO_4^{2-}), sodium (Na^+), potassium (K^+), magnesium (Mg^{2+}), calcium (Ca^{2+}), and other main anion and cation components. Fumarolic gas was sampled using a Giggenbach bottle, which is commonly used by volcanologists. The volume of the Giggenbach bottle was approximately 170 mL, with 50 mL of alkali hydroxide solution in the bottle, and the following gases were analyzed: H_2O, CO_2, H_2S, SO_2, HCl, CH_4, N_2, H_2, He, Ar, and CO. Iodine was used to obtain SO_2/H_2S ratios. Helium isotopic value was collected and stored in another vacuum glass bottles equipped with stopcocks at both ends and analyzed in the laboratory.

2.2 Seismic monitoring

When magma rises or a hydrothermal fluid migrates, many micro-earthquakes may be triggered along the path due to changes of stress in the rocks. This means that seismicity can be used to obtain important information. A dense seismic network was established for monitoring and investigating the seismicity of the TVG. To date, forty seismic broadband stations have been installed in the TVG, with the majority distributed southeast of the Shanjiao fault (Figure 1). With good network coverage of the Mount Cising, Dayoukeng, and Bayan areas, micro-earthquakes can be readily detected.
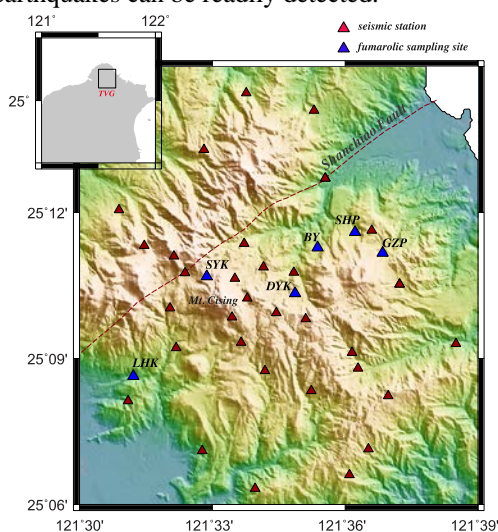

Figure 1. Distribution map of seismic stations and fumarolic sampling sites. DYK: Dayoukeng; SYK:

Shiaoyoukeng; BY: Bayen; LHK: Liaohuangkuo; SHP: Sihuangping; GZP: Gengziping. Hot spring samples were collected in DYK ares.

3. Results and Discussion

Between the end of 2018 and 2021, the geochemical signatures have changed dramatically. This study focuses on changes in fumarolic gas and water composition, and compares them with seismic monitoring results.

The variation of fumarolic gas composition is a very important and useful index when discussing volcanic activity. In gas composition, the ratio of hydrogen chloride to carbon dioxide (HCl/CO_2) is one of the parameters often used to distinguish between magmatic and hydrothermal activity. Figure 2 shows the variation of the HCl/CO_2 ratio at each sampling site from 2016 to 2021. The red dotted line is the international empirical threshold separating hydrothermal from magmatic activity. From 2016 to 2018, which was a relatively stable period, the HCl/CO_2 ratio did not change significantly, except in the Dayoukeng (DYK) area. At the end of 2018, however, there was a sudden and significant increase in HCl in the whole area, and this trend continued until 2021. This means that, during this period, although the volcanic system was still dominated by a hydrothermal environment, more magmatic material was added into the system.
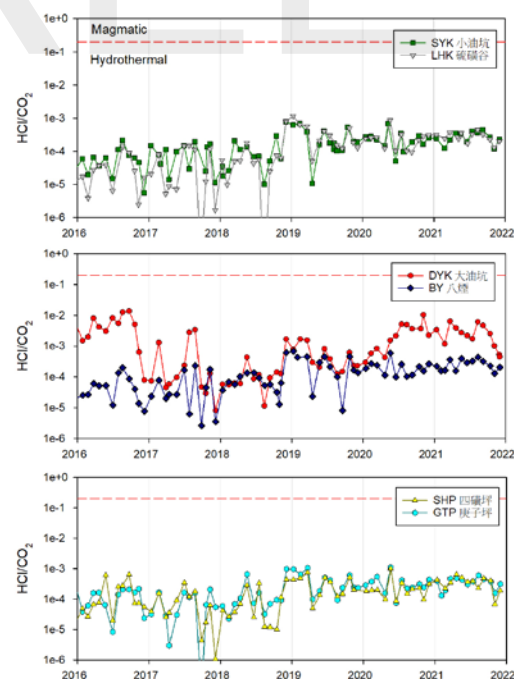

Figure 2. Variations of the HCl/CO2 ratio in the fumarolic gas with time.

Two earthquakes, with ML larger than 3, occurred in the TVG area in January and February of

2019. A significant increase in the concentration of helium was observed after the earthquakes, especially in the Bayan area. The ratio of helium to argon (He/Ar) is also a parameter that determines the relative importance of a magmatic source. The atmosphere is the main source of argon, while the sources of helium are ^{4}He in the crust and ^{3}He in the mantle. Figure 3 shows the variation of the He/Ar ratio in the fumarolic gas with time over 2016 to 2021. There are significant differences between the values before and after 2019 caused by increase in helium. It is noted that, during this period, the helium isotopic ratio (^{3}He/^{4}He) did not change significantly, indicating that both ^{3}He and ^{4}He concentrations increased. One of the possible reasons for this phenomenon is that the pathway for the gas became smoother, so helium could escape more easily than before 2019. It also means that the magma might have a chance of rising up through the smoother path. It is also worth noting that, if the original magma reservoir is not supplemented by other new substances, then the helium isotope ratio might not change significantly when the magma rises. However, the upwelling of magma might release more helium. The increase in helium continued into 2021, but the most dramatic changes were in 2019 and 2021.
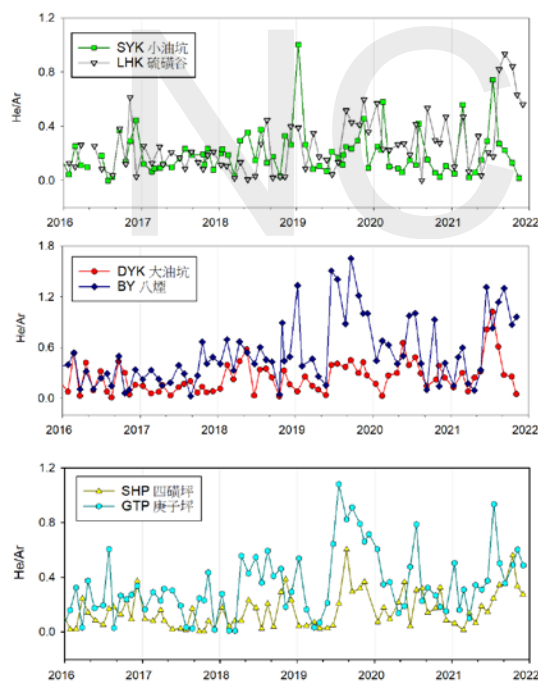

Figure 3. Variation of the He/Ar ratio in the fumarolic gas with time.

The DYK area has the highest helium isotopic ratio (~6.7RA) in the TVG. Such a high helium isotopic value indicates that (1) the DYK area may be closer to the magma reservoir or (2) the pathway of the fluid is smoother than at other sites. From other studies (Lin *et al*, 2016; Huang *et al*, 2021) , it is known that the location of the magma reservoir is still some distance from the DYK area, so it can be inferred that

the pathway of fluid under this area is much smoother than at other sites.

There are two stages of variation displayed in the monitoring results of hot springs in the DYK area (Figure 4). First, the chloride concentration began to increase since 2019, which is consistent with the abnormal trend of fumarolic gas. The second phase of variation began in the second half of 2020, when a greater number of cations were detected and the anions also changed drastically. However, the anomaly in cation concentration does not correspond exactly in time to the anomaly in fumarolic gas composition. In summary, both the fumarolic gas and hot spring compositions indicate the relative importance of magmatic or hydrothermal activity.
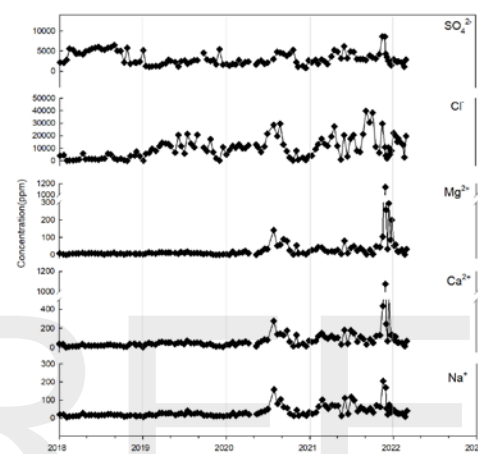

Figure 4. Variation of the major ion concentration of hot springs in Dayoukeng with time.
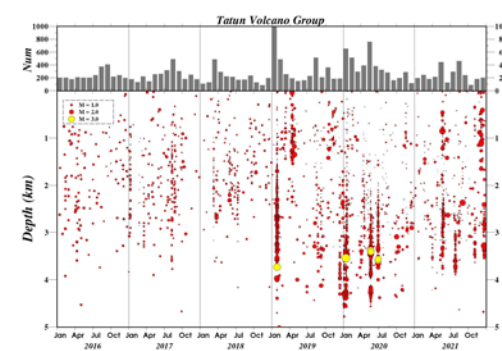
Figure 5. Distribution of the number, scale, and depth of microseisms in the TVG area.

A large number of seismic events was observed in 2019, and this increased significantly in 2020 (Figure 5). In 2020, the number of microseisms was as high as 4,550 which is twice the background micro-seismic activity level in the TVG area, approximately 2,000 to 2,500 each year. Moreover, the epicentral depth was deeper than previously. The number of earthquakes decreased slightly in 2021. It is worth noting that the seismic activity in 2020 was mainly concentrated in the first half of the year, and the cation

anomaly happened just after the most intense period of seismic activity.

Pu *et al.* (2021) established a volcanic activity model by comparing the focal mechanism of the DYK earthquake with observations of volcanic gas eruptions (Figure 6). When deep material, such as magma, begins to rise, it squeezes the formation, causing pressure in the deep surrounding rock to increase. At this time, the seismic activity indicates thrust faulting (compression). Due to the impermeable cap rock, only part of the fumarolic gas escapes. Shallow earthquakes then occur primarily as extensional normal faults when material moves upward and begins to be released near the surface. After the release is complete, seismic activity decreases. Therefore, the peaks of fumarolic gases do not exactly coincide with the peaks of seismic activity.
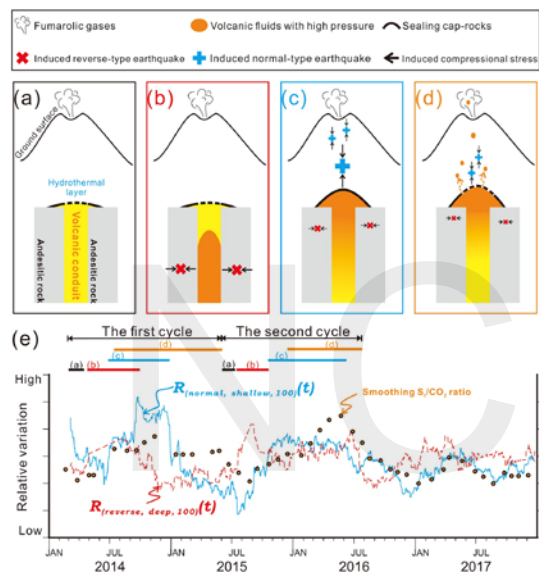

Figure 6. A volcanic activity model established by earthquake and fumarolic gas observations (Pu et al., 2021).

By comparing recent anomalies of fumarolic gas, hot springs, and seismicity, the chronological order of these anomalies is similar to this volcanic activity model. The changes can be divided into several stages. 1) At the end of 2018, high concentrations of hydrogen chloride in fumarolic gas were detected. Upwelling of a magmatic or deep hydrothermal fluid should have commenced during this stage. Due to the blockage caused by caprock, the fumarolic gas exhibited the characteristics of deep material, but the amount had not yet reached its peak value. 2) After several larger and deeper earthquakes in early 2019, helium concentration also increased. At the same time, the anion concentration of the hot springs was affected by the escaping acidic gas composition. 3) The seismic activity peaked in 2020. Significant changes in cations were observed after the seismic activity. This might be due to the rupture of the cap rock causing large

amounts of deep fluid to be added to the original system. Based on the model, the peak of the fumarolic gas anomaly should follow the seismic event. However, the anomalies in fumarolic gas were observed before the seismic events. It is unclear whether the anomaly in 2021 is a follow-up event to that in 2019 or another new event. This means that the model of volcanic activity in the TVG could be more complex. In any case, these unusual phenomena suggest that the TVG is currently in a stage with more activity than previously. The observatory will continue to pay attention to whether there are more magmatic signals in the future and to the possible disaster that could be caused by hydrothermal activity, such as a phreatic eruption.

Reference

1. Belousov, A., Belousova, M., Chen, C. H., Zellmer, G. F., 2010. Deposits, character and timing of recent eruptions and gravitational collapses in Tatun Volcanic Group, Northern Taiwan: Hazard-related issues. J. Volcanol. Geotherm. Res., 191, 205-221.

2. Huang, HH., Wu, ES., Lin, C.H., Ko, J. Y.−T., Shih M.H., Koulakov, I., 2021. Unveiling Tatun volcanic plumbing structure induced by post-collisional extension of Taiwan mountain belt. Scientific Reports, 11, 5286.

3. Lin, C.H., 2016. Evidence for a magma reservoir beneath the Taipei metropolis of Taiwan from both S-wave shadows and P-wave delay, Scientific Reports, Vol. 6, 39500.

4. Pu, H. C., Lin, C. H., Lai, Y. C., Shih, M. H., Chang, L. C., Lee, H. F., Lee, P.T., Hong, G.T., Li, Y.H., Chang, W.Y., Lo, C. H., 2020. Active Volcanism Revealed from a Seismicity Conduit in the Long-resting Tatun Volcano Group of Northern Taiwan, Scientific Reports, 10.

5. Pu, H. C., Lin, C. H., Lee, H. F., Lai, Y. C., Chang, L. C., Shih, M. H., 2021. Ascending Volcanic Fluids Portended by Spatiotemporal Variations of the Earthquake Mechanisms in the Tatun Volcano Group in Northern Taiwan, Geophysical Research Letters 48(9).

6. Song, S.R., Yang, T.F., Yeh, Y.H., Tsao, S.J., Lo, H.J., 2000b. The Tatun volcano group is active or extinct? J. Geol. Soc. China, 43, 521–534.

7. Yang, T. F., Sano, Y., Song, S. R., 1999. ^{3}He/^{4}He ratios of fumaroles and bubbling gases of hot springs in Tatun Volcano Group, North Taiwan. Il Nuovo Cimento Soc. Ital. Fisica C, 22, 281-286.

Geochemical Field Surveys of Geothermal Areas in the Ilan Region of Northeast Taiwan

Vivek Walia[1], Shih-Jung Lin[2], Arvind Kumar[3], and Ching-Chou Fu[4]

瓦里亞[1]　林世榮[2]　亞耳文[3]　傅慶州[4]

Abstract

This study reports on geochemical field surveys of some geothermal areas in the Ilan region of northeast Taiwan. Samples from different water bodies present in the Ilan area were collected and analyzed. Soil-gas field surveys in Qingshui Geothermal Park were undertaken for radon, CO_2, and CH_4 measurement. Based on the results of these surveys, a suitable site was selected for installing a continuous radon monitoring station. A temporary radon monitoring station was built at this site using RADEX MR107 advanced radon gas detectors.

Keywords: geochemical field survey, geothermal area, monitoring station, northeast Taiwan

Introduction

The Ilan Plain, shown in Figure 1, is situated at the southwestern tip of the back arc basin of the Okinawa Trough, which spreads westward into the Taiwan orogen. A long-debated issue is whether the opening of normal-fault system of the Okinawa Trough propagates and transforms into the thrust-fault system of the Taiwan orogen. Inverted resistivity profiles obtained from a series of surveys conducted in the 1970s around the Chingshui-Sanshing-Hanchi area of southwestern Ilan County (Ho, 1975; Hu et al., 2001; Angelier et al., 2008). The 2D and 3D inverted resistivity images have revealed the regional structures A substantial conductive structure dipping toward the northwest at an angle of 30-40° is associated with the Niudou Fault, which separates the early Miocene Szeleng and Kangkou Formations from the Lushan Formation in the Sanshing area. Two conductive structures in the Sanshing area have a dip angle of 50-70° and a dip direction associated with normal faults observed in different surveys (Ho, 1975; Hu et al., 2001; Angelier et al., 2008). In addition, three high-angle discontinuities, dipping toward the north with an angle of 60-80° can be recognized in the resistivity profile along Hanchi. It is proposed that these structures be recognized as continuations of normal faults found under unconsolidated sediments in the Ilan Plain. Resistivity profiles from the Chingshuichi area indicate the presence of the vertical Chingshuichi, Dachi, and Xiaonanauo Faults. Hot springs are found in the junction area of the Chingshuichi and the Xiaonanauo Faults. The Chingshui geothermal field, which has geothermal fluid originating from substantial depth, is located at the junction of these two fault systems.
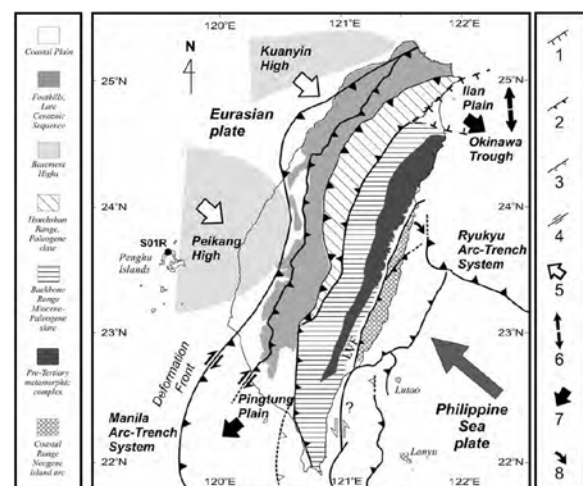

Figure 1. Tectonic framework and main structural units of the Taiwan collision zone (adapted from Ho, 1975; Hu et al., 2001; Angelier et al., 2008; and geological maps).

[1] Research Fellow, National Center for Research on Earthquake Engineering, walia@ncree.narl.org.tw
[2] Assistant Research Fellow, National Center for Research on Earthquake Engineering, sjlin@ncree.narl.org.tw
[3] Associate Research Fellow, National Center for Research on Earthquake Engineering, kumar@ncree.narl.org.tw
[4] Associate Research Fellow, Institute of Earth Sciences, Academia Sinica, ccfu@earth.sinica.edu.tw

Analysis of groundwater samples from different water bodies for hydro-geochemical and isotopic parameters are helpful in understanding the tectonic setting and its implications. Most of the hot springs in the areas can be related to active faults (Curewitz and Karson, 1997). The changes in nearby stream flow, yield of springs, and water table are due to the changes in the permeability of active faults. Reported changes have occurred both during pre-seismic (Roeloffs, 1988) and post- and co-seismic events (Muirwood and King, 1993; Rojskczer et al., 1995). It is expected that hot springs from deep reservoirs are superior for earthquake precursory studies as compare to artesian springs and groundwater from shallower reservoirs. Artesian springs from smaller subsurface water bodies are preferable to the groundwater from larger reservoirs.

In geochemical measurements, fault zones filled with fluids and weathered gouge will result in very conductive responses. Earth degassing is controlled by gas origins, routes of gas transfer, and the underlying force for degassing, which is tectonic stress (Tamburello et al., 2018). Fault blocks in the investigating area are under the influence of various tectonic stresses; therefore the gases emitted in different regions have different geochemical characteristics. The interrelationship among earth degassing and active tectonic units at various scales (local, regional, and continental) have been broadly examined in volcanic regions (Werner and Cardellini, 2006; Mazot et al., 2014), seismic regions (Tamburello et al., 2018), and fault zones (Li et al., 2013; Dupré et al., 2015). The soil gas observations from various studies have shown anomalous values of gas concentrations and flux that can be related to active fault zones (Tamburello et al., 2018; Li et al., 2013). The results of field investigations (Yang et al., 2006; Li et al., 2013; Yuce et al., 2017), statistical phenomena (Martinelli and Dadomo, 2017), and dynamic experiments on rocks (Martinelli and Plescia, 2005) have also shown that the stress related to crustal deformation influences earth degassing. Moreover, atmospheric CO_2 and CH_4 irregularities linked to fault zones and the build-up of tectonic stress, have been recorded in satellite hyperspectral data (Cui et al., 2017.

In order to better understand the tectonic setting of the Ilan region geochemical field surveys of geothermal areas have been undertaken.

Methodology

Radon monitoring in water

250 ml samples of water were collected in glass bottles from different hot springs and subsurface water bodies in Ilan and the northern part of the Hualien area for radon concentration analysis (Figures 2-4). As the gas is quickly released from water during sampling,

water samples were collected such as to avoid bubbling and out-gassing. Samples were analyzed using a RAD 7 radon detector (Durridge Company, USA). This technique uses a closed loop aeration process, through which the air volume and water volume are sustained independent of the flow rate. Air recirculates through the water and is continuously extracted until a state of equilibrium is reached. The equilibrium process takes approximately 5 minutes;. Thereafter, no more radon can be extracted from the water. The detail of this technique is already published by the authors in their previous study (Kumar et al., 2009).

Radon monitoring in soil

Soil gas sampling was also carried out in the study area. In soils, gases are commonly sampled at depths of 0.7–1.0 m (Walia et al., 2010) with steel probes. For this study, a hollow steel probe 3 cm in diameter and 130 cm long was selected and a disposable sharp awl was attached to the bottom of the steel probe, which made the steel probe capable of drilling into the soil and prevented soil from blocking it. This steel probe was pounded into the ground to a depth of 0.8–1.0 m using a hammer and a drive-in-head (Figure 5).

A hand-pump, through a specially designed rubber tube (with two filters, one for dust and the other for mist) connected to the hollow steel probe was used to collect gas in sample bags. If the flux was good, the hand-pump was replaced by an alpha-pump (an automatic pump having a pumping rate of 1 L/min) to collect soil–gas in vacuum sample bags having a capacity of 3 L. Before collecting the soil gas in the sample bags, the tube and the probe were flushed to remove any air that might be present by pumping for about 1 min. Tedlar standard sample bags (manufactured by SKC Limited United Kingdom) were used for collecting soil–gas samples. These bags utilize two fittings of inter polypropylene that combine the hose/valve and the septum holder, which allow the sample bag to be used in closed circuit for radon analysis. The soil–gas samples collected in the 3 L sample bags were analyzed for radon using the RAD 7 radon detector.

CO_2 and CH_4 measurement in soil

For CO_2 flux measurement in soil, LI-850 CO_2 Analyzers has been used. It has CO_2 measurement range from 0-20,000 ppm. It is a high-performance monitoring system that give accurate, stable reading. Easy-to-use software and minimal maintenance provide hassle-free measurements for a wide range of applications and system integration options.

For CH_4 flux measurement in soil, Guardian NG Gas Monitor has been used. The 'Guardian NG' gas monitor range provides high accuracy detection and measurement of CH_4 gases, where detection level ranges of between 0 – 3000 ppm and 0 – 100% by

volume are required.

Results and Discussions

The collection and analysis of groundwater samples from different hot springs and subsurface water bodies were carried out in the Ilan area. Figure 2 shows the location of water sampling sites in Ilan, and Figure 3 shows photographs of the water sampling sites. Table 1 gives a summary of recorded radon, temperature, pH, conductivity, and oxidation-reduction potential (ORP) of different water bodies in the Ilan area.

Field surveys in Qingshui Geothermal Park were also undertaken for radon, CO2, and CH4 measurements. Figure 4 shows the sampling locations in Qingshui Geothermal Park, and Figure 5 shows photographs of the collection of soil gas samples and monitoring of fluxes during the surveys.
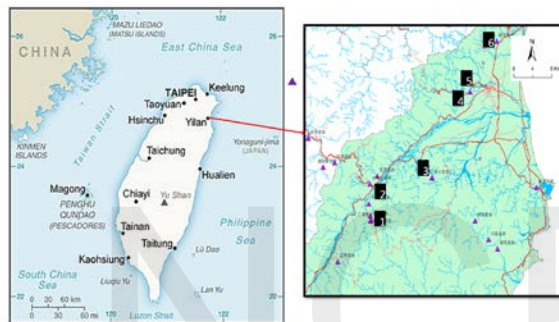
The recorded radon values in the Qingshui thermal area varies from 562 ± 100 Bq/m3 to 11700 ± 400Bq/m3 whereas the recorded slope of CO2 flux varies from 0.1746 to 1.2092. The CH4 flux value recorded at the Qingshui thermal area was very low (Table 2). At two sites (5 and 10) radon values were higher than those recorded at the other sites; therefore, site 5 was selected for installing a continuous radon monitoring station. A temporary radon monitoring station has been built at this site (Figure 6) using RADEX MR107 advanced radon gas detectors as tested above.

Figure 4. Map showing sampling locations in Qingshui Geothermal Park.

Figure 5. Collection of soil gas samples and monitoring of fluxes.

Figure 2. Location of water sampling sites in Ilan.

Table 1. Summary of results obtained from the water samples of the Ilan area.

S. No.	Name	Type	Temperature (°C)	Radon (Bq/m³)	pH	Conductivity (ms/cm)	Oxidation Reduction Potential (mv)
1	Jiou-Jhih-Ze	Well	84.2	0	8.2	4.42	-277
2	Pai-Gu-Shi	River	60.8	141	6.6	0.91	30
3	Qing-Shui Geothermal Park	Pool	70.0	60	8.2	4.20	-19
4	Bubble Crab	Pool	22.6	27300	7.3	0.20	145
5	Yuan-Shan	Well	45.0	11200	7.6	1.90	-70
6	Jiao-Si	Well	32.0	252	8.1	0.93	109

Figure 3. Photographs of water sampling sites in Ilan.

Table 2. Recorded radon, CO_2 flux, and CH_4 flux in Qingshui Geothermal Park.

Sample No.	Position & Description	Rn (Bq/m³)	E	N	CO₂ flux slope	CH₄ flux slope (%)
1	Qingshui_1	6960 ±360	24.60531	121.63933	0.9865	0
2	Qingshui_2	4720 ±320	24.60581	121.63925	0.9193	0
3	Qingshui_3	5830 ±340	24.60616	121.63913	1.2092	0
4	Qingshui_4	4390 ±310	24.60662	121.63913	0.8288	0
5	Qingshui_5	11700 ±440	24.60681	121.64018	0.3358	0
6	Qingshui_6	2370 ±210	24.60687	121.64049	0.4327	0
7	Qingshui_7	562 ±100	24.60813	121.6386	0.3192	0
8	Qingshui_8	969 ±160	24.60984	121.64069	0.6729	0
9	Qingshui_9	7120 ±410	24.60944	121.6395	0.2256	0
10	Qingshui_10	11600 ±510	24.60887	121.63847	0.5595	0
11	Qingshui_11	679 ±150	24.61099	121.63619	0.7261	0
12	Qingshui_12	3230 ±240	24.60908	121.63763	0.6122	0
13	Qingshui_13	3180 ±250	24.6071	121.63889	0.1746	0

The aim of the temporary monitoring station is to test the RADEX MR107 advanced radon gas detectors for soil gas measurement as well as the sensitivity of this temporary station to seismicity and meteorological parameters. If this station is found to be suitable for further study, then a continuous radon monitoring station will be built at the location. This will further aid earthquake precursor studies.

Figure 6. Setting up a temporary radon monitoring station using the RADEX MR107 advanced radon gas detector at Qingshui Geothermal Park.

References

Angelier, J., et al., Does extrusion occur at both tips of the Taiwan collision belt? Insights from active deformation studies in the Yilan Plain and Pingtung Plain regions, Tectonophysics (2008), doi:10.1016/j.tecto.2007.11.015

Cui, Y., Ouzounov, D., Hatzopoulos, N., Sun, K., Zou, Z and Du, J., "Satellite observation of CH_4 and CO_2 anomalies associated with the Wenchuan MS 8.0 and Lushan MS 7.0 earthquakes in China," Chemical Geology, vol. 469, pp. 185–191, 2017.

Curewitz, D., and Karson, J.A., Structural settings of hydrothermal outflow: fracture permeability maintained by fault propagation and interaction. J. Volcanol. Geotherm. Res., 79, 149-168, 1997

Dupré, S., Scalabrin, C., Grall, C., et al., "Tectonic and sedimentary controls on widespread gas emissions in the sea of marmara: results from systematic, shipborne multibeam echo sounder water column imaging," Journal of Geophysical Research: Solid Earth, vol. 120(5)2891–2912, 2015.

Ho, C.-S. An introduction to the geology of Taiwan: explanatory text of the geologic map of Taiwan. Ministry of Economic Affairs, R.O.C. 153 pp, 1975.

Hu, J.-C., Yu, S.-B., Angelier, J., Chu, H.-T. Active deformation of Taiwan from GPS measurements and numerical simulations. J. Geophys. Res. 106, 2265–2280, 2001.

Kumar A, Singh S, Mahajan S, Bajwa BS, Kalia R, Dhar S. Earthquake precursory studies in Kangra valley of north-west Himalayas, India, with special emphasis on radon emission. Appl Radiat & Isot 67:1904–191, 2009.

Li, Y., Du, J., Wang, X., Zhou, X., Xie, C., and Cui, Y., "Spatial variations of soil gas geochemistry in the Tangshan area of Northern China," Terrestrial Atmospheric and Oceanic Sciences, 24(3)323–332, 2013.

Martinelli, G and Plescia, P. "CO_2 and CH_4 emissions from calcareous-marly rock under stress: experimental tests results," Annals of Geophysics, 48(1)167–173, 2005.

Martinelli, G and Dadomo, A. "Factors constraining the geographic distribution of earthquake geochemical and fluidrelated precursors," Chemical Geology, vol. 469, pp. 176–184, 2017.

Mazot, A., F. M. Schwandner, F.M., Christenson B. et al., "CO_2 discharge from the bottom of volcanic Lake Rotomahana, New Zealand," Geochemistry Geophysics Geosystems, 15(3)577–588, 2014.

Muirwood, R., and G.C.P. King, Hydrologic signatures of earthquake strain, J. Geophys. Res., 98, 22,035-22,068, 1993.

Roeloffs, E. A., Hydrologic precursors to earthquakes: a review, Pure Appl. Geophys., 126, 177-209, 1988

Rojstaczer, S., S. Wolf, and R. Michel, Permeability enhancement in the shallow crust as a cause of earthquake-induced hydrological changes, Nature, 373, 237-239, 1995.

Tamburello, G., Pondrelli, S., Chiodini, G., and Rouwet, D. "Global-scale control of extensional tectonics on CO_2 earth degassing," Nature Communications, 9(1) 4608, 2018.

Werner C., and Cardellini, C. "Comparison of carbon dioxide emissionswith fluidupflow,chemistry,andgeologicstructures at the Rotorua geothermal system, New Zealand," Geothermics, 35(3)221–238, 2006.

Yang, T.F., Fu, C. C., Walia V., et al., "Seismo-geochemical variations in SW Taiwan: multi-parameter automatic gas monitoring results," Pure and Applied Geophysics, 163(4)693–709, 2006.

Yuce, G., Fu, C.C., W. D'Alessandro et al., "Geochemical characteristics of soil radon and carbon dioxide within the Dead Sea Fault and Karasu Fault in the Amik Basin (Hatay), Turkey," Chemical Geology, 469,129–146, 2017.

Tamburello G, Pondrelli S, Chiodini G, Rouwet D Global-scale control of extensional tectonics on CO_2 earth degassing. Nat Commun. 2, 9(1), 4608, 2018.

Walia, V., Lin,S.J., Ching Fu, C.-C., Yang, T.F., Hong, W.-L., Wen, K.-L., Chen, C.-H. "Soil–gas monitoring: A tool for fault delineation studies along Hsinhua Fault (Tainan), Southern Taiwan", Applied Geochemistry 25(4), 602-607, 2010.

Construction of Fourier Phase Spectrum Database for Horizontal Ground Motions in Taiwan Region

Jyun-Yan Huang[1], Shu-Hsien Chao[1] and Che-Min Lin[2]

黃雋彥 [1]、趙書賢 [1]、林哲民 [2]

Abstract

A phase spectrum database derived from a Fourier transform for both horizontal components of ground motions in Taiwan is constructed. The two horizontal components were rotated into radial and transverse components to understand the basic physics of the frequency domain for Taiwan. The database used was based on the original work of Taiwan's Senior Seismic Hazard Analysis Committee (SSHAC) level 3 Probabilistic Seismic-Hazard Analysis project, as documented by the National Center for Research on Earthquake Engineering. The SSHAC database is useful for understanding the phase behavior corresponding to seismic source, path, and site effects because it contains very complete information regarding earthquake location, magnitude, and epicentral distance range. It could also be applied as a substitute for the use of random phases in stochastic simulation for engineering purposes. The preliminary results suggest that a slight bias in the phases of the radial and transverse components might occur for larger magnitudes, near-field distances, and harder rock sites, but there is no significant trend at this stage of the analysis.

Keywords: database of Fourier phase spectrum, Taiwan

Introduction

High frequency ground motion prediction methods are very important in engineering seismology. Most cases use the existing ground motion model (GMM) to evaluate the intensity level of target sites from certain magnitudes, distances, and site conditions. However, it is still very difficult to take into account the finite-fault effect in the GMM owing to the complexity involved in considering the distance from a large rupture fault, especially in the case of near-fault events. The stochastic finite-fault method (Boore, 2009; Motezedian and Atkinson, 2005) plays an important role in the provision of high frequency ground motion simulations and has been practically applied in Taiwan (Huang et al., 2016, 2017); however the limitations of the stochastic ground motion simulation technique are obvious in that the uncertainty of the acceleration time history is immense under random phase assumptions. Therefore, we have tried to build a database to further check on the applicability of the phase spectrum with strong ground motions.

The existing ground motion database in the Senior Seismic Hazard Analysis Committee (SSHAC) project in Taiwan documented by the National Center for Research on Earthquake Engineering (NCREE, 2016) provides a series of high-quality strong ground motions from 1991 to 2016 with a M_w magnitude range of 2.2 to 7.6, a range of rupture distances from 0.05 km to 610 km, and site condition ranges from class A to E according to the National Earthquake Hazards Reduction Program (NEHRP). The database has created a very good opportunity to study seismic behavior in the Taiwan region. In this study, we built an add-on database derived from this original dataset by further calculating the Fourier phase spectrum of two horizontal components for whole records in the SSHAC database. Several indexes were then checked for phase differences of the radial (R) and transverse (T) components of ground motion to evaluate the relation of the phase spectrum with seismic source, path, and site effects.

---

[1] Associate Research Fellow, National Center for Research on Earthquake Engineering
[2] Research Fellow, National Center for Research on Earthquake Engineering

Methodology and database

In order to extend the ground motion database from its main focus on pseudo spectral acceleration (PSA), peak ground acceleration (PGA), and peak ground velocity (PGV) to include the Fourier phase spectrum (FAS), the Fourier amplitude spectrum for each record must first be calculated by following the procedures of the next-generation attenuation project of Eastern North-America (NGA-East, Kottke et al., 2021). To prevent further uncertainty in the use of random-vibration theory on account of the down-sampling and smoothing processes that were suggested by Kottke et al. (2021), the sampling frequency was initially not small in the whole frequency range. This generally influences the calculation of the phase spectrum for a target record.

Figure 1 shows a sample phase spectrum from the 1999 ChiChi Taiwan earthquake, which is the largest recent event in Taiwan. It seems that there was not sufficient definition in the phase angle of the R and T components or the difference between them, owing either to the large selected frequency interval or to cut-off of the time windows for the shear wave by the variances. Therefore, we tried to line up the Fourier phase angles from the unwrapping process of the continuous frequency series for the entire database. We applied a windowed time history from the manually picked P-wave arrivals to the end of the records and padding zeros to a time-window length of 2^{16} points. After taking the fast Fourier transform from a specific time window after the P arrival, the Fourier phase spectrum carries information of the time interval between the P and S wave arrivals, implying that the seismic information related to the source, path, and site effect would generally reflect the dominant frequency of the FAS first, before it would show on the Fourier phase spectrum.

We also applied the unwrapping procedure to each phase spectrum to continuously check the phase change from clockwise rotated angles to a continuous series of the phase spectrum (Fig. 2). Specifically, the large phase change in the overall trend of the continuous series of the phase spectrum implies that the dominant frequency difference between the P and S waves occurs in a certain frequency band. Therefore, unwrapping processes were carried out for all records of the two horizontal components in the whole data set for Taiwan.

Results and Discussions

The difficulty of directly predicting the phase spectra meant that we tried to check the difference between the two horizontal components first. In this study, in order to understand the preliminary features

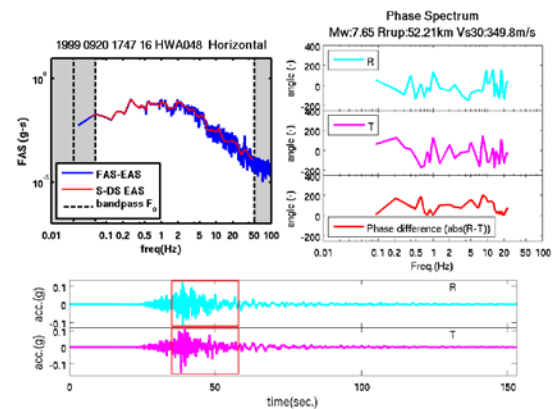of the phase spectrum seismic behavior (such as the

Figure 1. Sampled FAS, phase spectrum, and acceleration time history of the R and T components of station HWA048 during the 1999 Chi-Chi Taiwan earthquake.
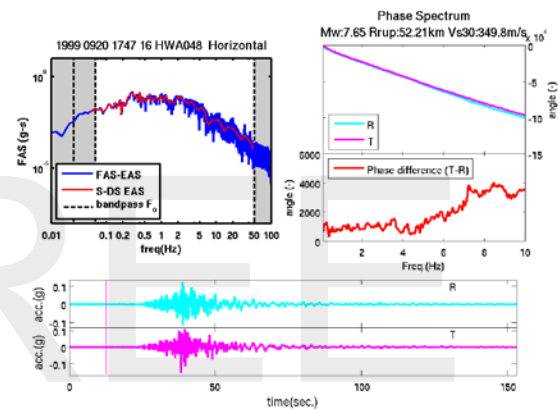

Figure 2. Sampled FAS, unwrapped phase spectrum, and acceleration time history of the R and T components of station HWA048 during the 1999 Chi-Chi Taiwan earthquake.

source, path, and site effects), we further investigated the scaling relation between the magnitude M_w, rupture distance R_{rup}, and site-class related index V_s30 (the mean velocity of top surface down to 30 m depth), compared to the phase difference between the R and T components. The preliminary results for different magnitudes (M_w) are shown in Fig. 3 and indicate that there is no significant frequency dependent feature in the phase spectrum with regard to the source effect. A slight trend can be seen at magnitude M_w greater than 6, but it is not significant, and this implies that larger variance occurs during larger magnitude events.

The distance scaling relations are shown in Fig. 4, which suggests that there is no significant trend for distance scaling with respect to phase differences between the R and T components. This implies that there is not a large difference in the seismic waves passing through similar materials for both horizontal components. The results also suggest that it may be

appropriate to use an assumption of homogeneity in the underground structure for investigation of the path effect in large scale seismology.

Finally, the V_s30 scaling (Fig. 5) shows a slight trend at sites characterized by hard rock (e.g., where V_s30 is greater than 600 m/s), and there is the implication that local site responses at soft soil sites may show a similar response in both horizontal components and generate similar phase angles in certain frequency bands related to the site response; this would cause a smaller trend in the phase difference when V_s30 is small. It is worth pointing out that some of the phase differences during the unwrapping procedure could be even larger (reaching as much as plus or minus 3000 degrees for low frequency and over 10000 degrees for high frequency), being generated from a continuous phase series at each frequency step in the unwrapping procedure. This could be caused by a large degree of variance in the seismic effects in certain frequency ranges.

Larger high frequency variance in the phase difference and a higher overall range of the phase difference number were discovered in the following situations: $M_w > 6.0$, $R_{rup} < 15$ km, and $V_s30 < 300$ m/s. This indicates that the main variance of the seismic waves was concentrated at large, near-field, and softer sites; however, there was generally a lack of control in the engineering seismology conducted and so this needs further evaluation.
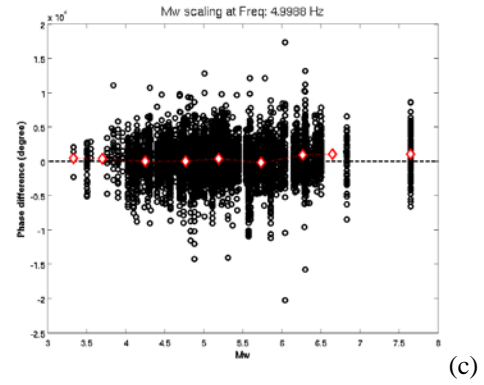

(c)

Figure 3. Source (M_w) scaling relation of the phase difference between the R and T components (T degrees minus R degrees) in the Taiwan data set: (a) 0.2 Hz; (b) 1 Hz; and (c) 5 Hz.
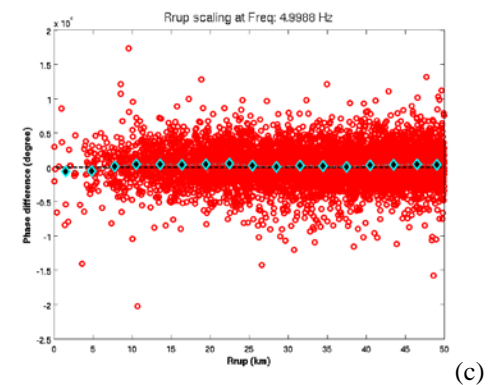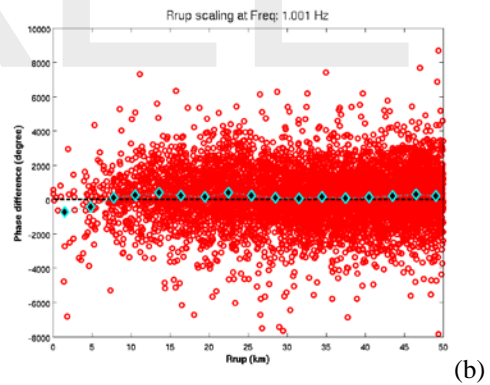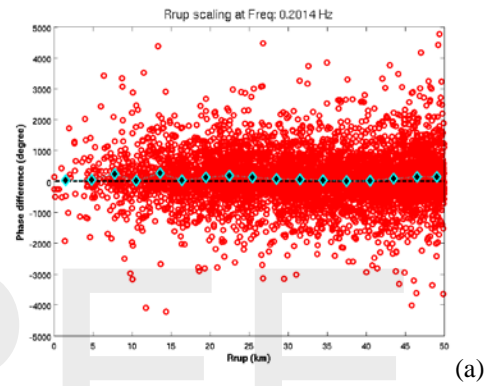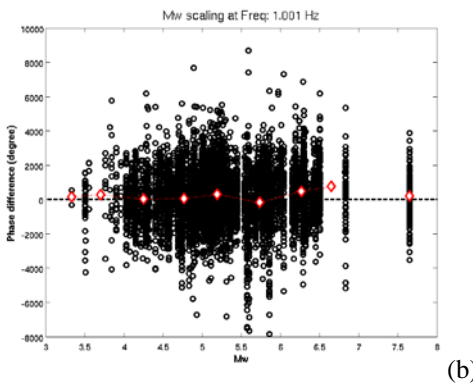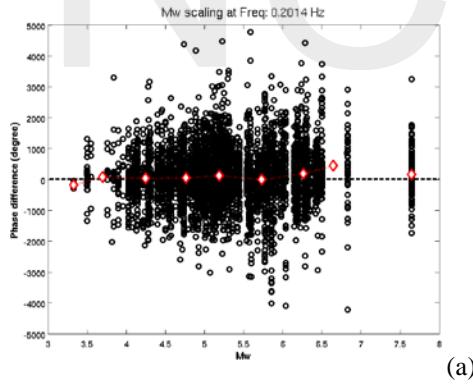

(a)

(b)

(c)

(a)

(b)

Figure 4. Distance (R_{rup}) scaling relation of the phase difference between the R and T components in the Taiwan data set: (a) 0.2 Hz; (b) 1 Hz; and (c) 5 Hz.
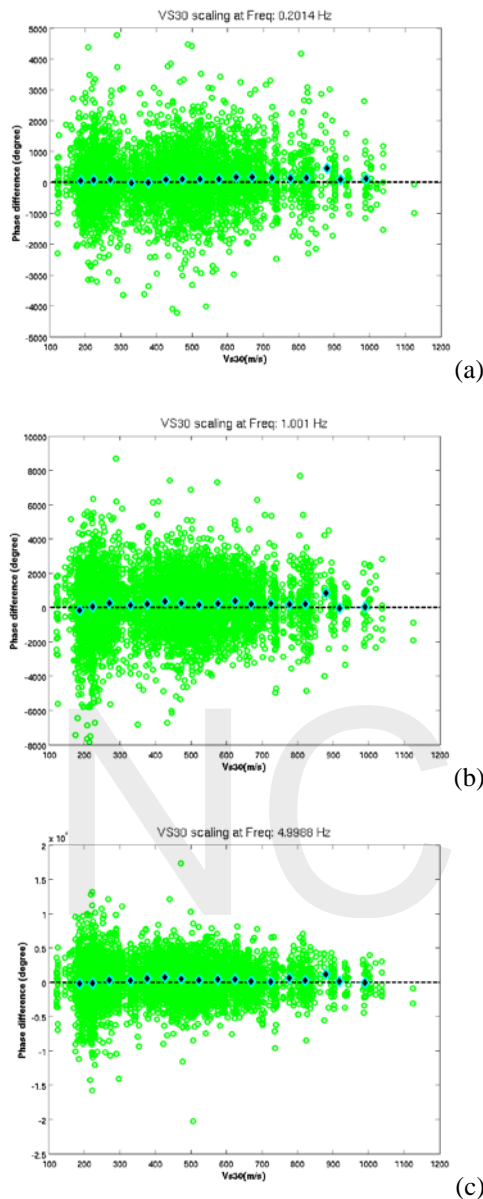

(a)

(b)

(c)

Figure 5. V_s30 scaling relation of the phase difference between the R and T components in the Taiwan data set: (a) 0.2 Hz; (b) 1 Hz; and (c) 5 Hz.

Conclusions

In this study we constructed an add-on data set for the ground motion database in the Taiwan Senior Seismic Hazard Analysis Committee level 3 Probabilistic Seismic-Hazard Analysis project by calculating the Fourier phase spectrum for each record in the data set for the whole of Taiwan. The unwrapped phase spectrum was generated because it was prohibitively difficult to directly use or predict the Fourier phase spectrum for the wide frequency range ground-motion simulation technique (Hisada and

Bielak, 2005), and this permits the continuous series of phase angles to be connected to the seismic effects in engineering seismology studies much more simply. We investigated the source, path, and site scaling relations between the radial and transverse components of ground motion, which indicated a slight trend for M_w and V_s30 scaling, but no significant trend for R_{rup} scaling relations. Further evaluation is needed, specifically about the relationship between individual components of the phase spectrum and its effects.

References

Boore, D.M., (2009). "Comparing stochastic point-source and finite-source ground-motion simulations: SMSIM and EXSIM", Bull. Seismol. Soc. Am. 99(6), 3202-3216.

Hisada, Y., and Bielak, J. (2005). "An extension of the stochastic Green's function method to long-period strong ground-motion simulation(abstract)", Seismol. Res. Lett. 76(2), 242.

Huang, J.Y., Wen, K.L., Lin, C.M., Kuo, C.H. and Chen, C.T., (2016). "Various fault slip asperity models for the ETF-based high frequency strong motion simulation of the Sanchiao fault", Taiwan. In Proc. of The 5th IASPEI / IAEE International Symposium: Effects of Surface Geology on Seismic Motion (ESG5), 15th- 17th Aug., Taipei, Taiwan.

Huang, J.Y., Wen, K.L., Lin, C.M., Kuo, C.H., Chen, C.T., and Chang, S.C., (2017). "Site correction of a high-frequency strong-ground-motion simulation based on an empirical transfer function", J. Asian Earth Sci. 138, 399-415.

Kottke, A.R., Abrahamson, N.A., Boore, D.M., Bozorgnia, Y., Goulet, C.A., Hollenback, J., Kishida, T., Ktenidou, O.J., Rathje, E.M., Silva, W.J., Thompson, E.M., and Wang X., (2021). "Selection of random vibration theory procedures for the NGA-East project and ground-motion modeling", Earthq. Spectra 37(S1), 1420-1439.

Motezedian, D. and Atkinson, G.M., (2005). "Stochastic finite-fault modeling based on a dynamic corner frequency", Bull. Seismol. Soc. Am. 95(3), 995-1010.

NCREE, (2016). Web page for reevaluation of probabilistic seismic hazard of nuclear facilities in Taiwan using SSHAC level 3 methodology project, available at http://sshac.ncree.org.tw.

Development of Site-specific Seismic Response Spectra for Nuclear Power Plants in Taiwan – Project Overview

Hsun-Jen Liu[1], Chiun-Lin Wu[2], Shyh-Jiann Hwang[3], and Chung-Che Chou[4]

劉勛仁 [1]、吳俊霖 [2]、黃世建 [3]、周中哲 [4]

Abstract

Following the accident at the Fukushima Dai-ichi Nuclear Power Plant in Japan, the nuclear energy-producing countries have thoroughly reviewed their current regulatory systems for nuclear safety; the conclusion of these reviews was that the first and most urgent action is to update seismic hazard assessment and re-evaluate the basis of seismic design. In Taiwan, the National Center for Research on Earthquake Engineering, commissioned by the Taiwan Power Company, developed up-to-date seismic response spectra for Taiwan nuclear power plants starting from early 2018. This project specially introduced the key elements of the SSHAC Level 3 process, a novel approach for site response analysis, high-quality *in situ* and laboratory testing data, and excellent project team members. After resolving the particular seismicity and geology issues of Taiwan and the limited site-specific characterization data, and despite the COVID-19 pandemic, all of the project outcomes were approved by the Participatory Peer Review Panel by the end of 2021. The outstanding results of this project not only help Taiwan to become a model for the international nuclear industry, but also lay a foundation for further technological advancement of domestic earthquake engineering.

Keywords: seismic hazard reevaluation, ground motion response spectra, site response analysis, SSHAC Level 3 process, nuclear power plant.

Motivation and Purpose

In light of the accident at the Fukushima Dai-ichi Nuclear Power Plant in Japan, resulting from the 2011 Tōhoku earthquake with a moment magnitude of 9.0 and the subsequent tsunami, the Near-Term Task Force (NTTF) was established to conduct a systematic review of US Nuclear Regulatory Commission (US NRC) processes and regulations and to make recommendations for the Commission's policy direction. The Recommendation 2.1 for seismic review, or "NTTF 2.1: Seismic", which requests to perform a reevaluation of site-specific seismic hazard using up-to-date data, methods, and models for seismic sources, ground motion equations, and site amplification.

In line with international action for nuclear safety, the Atomic Energy Council of Taiwan required the Taiwan Power Company (TPC) to carry out "NTTF 2.1: Seismic" to determine whether nuclear power plants should make additional improvements. In response, the National Center for Research on Earthquake Engineering, Taiwan,

commissioned by the TPC, developed the new site-specific seismic response spectra for the target sites. This seismic reevaluation was conducted through the following two projects:

1. ***Reevaluation of Probabilistic Seismic Hazard of Nuclear Facilities in Taiwan using SSHAC Level 3 Methodology*** (or the Taiwan SSHAC Level 3 PSHA Models Project): The objective of this project was to develop up-to-date seismic source and ground motion models to characterize regional and site-specific seismic hazards and to complete the hazard input document (HID). Both the characterization models were constructed using a process that is appropriate for a Level 3 study defined by the Senior Seismic Hazard Analysis Committee (SSHAC). This project was conducted from June 2015 to December 2018 and mainly dealt with issues of geology and seismology.

    Based on the outcomes of the Taiwan SSHAC Level 3 PSHA Models Project, the probabilistic

seismic hazard analysis (PSHA) was performed to calculate the hazard curves and the uniform hazard response spectra for a reference-rock site condition ($\text{UHRS}_{refrock}$) with an average shear-wave velocity (V_S) for the upper 30-m depth (V_{S30}) of 760 m/s. In addition, deaggregation was used to calculate the controlling magnitudes and distances at eleven annual exceedance frequencies (AEFs).

2. ***Development of GMRS and FIRS for Nuclear Power Plants in Taiwan*** (or the Taiwan GMRS/FIRS Project): The objectives of this project were to develop both the site-specific ground-motion response spectra (GMRS, defined to be at the ground surface) and the foundation-input response spectra (FIRS, defined to be at the basement of reactor building), which present horizontal and vertical components, and to document the Seismic Hazard and Screening Report. The input motions and site characterization models for site response analysis were constructed following the key elements of the SSHAC Level 3 process. This project was conducted from March 2018 to December 2021 and mainly dealt with issues of geotechnical engineering and earthquake engineering.

An overview of the procedure, key activities, and achievements of the Taiwan GMRS/FIRS Project is presented in the following section.
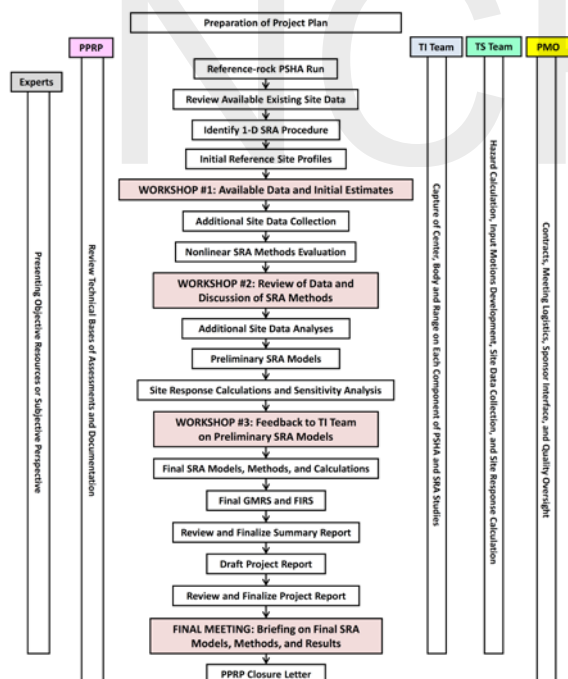

Figure 1. Schematic overview of the project activities.

Actions and Achievements

As described in the NUREG-2117, the fundamental goal of a SSHAC process is to properly carry out and completely document the activities of evaluation and integration. For evaluation, the complete set of data, methods, and models proposed by the larger technical community that are relevant to the analysis of a seismic hazard or site response should be fully considered. For integration, the center, body, and range of technically defensible interpretations (the CBR of the TDI) in light of the evaluation process should be duly represented. For documentation, the technical basis of the data, methods, and models that were used in the assessment should be well recorded.

The sequence of steps for the Taiwan GMRS/FIRS Project, which is in accordance with the key elements of the SSHAC Level 3 process, is illustrated in Figure 1. The project tasks and achievements are described below.

1. Project Plan Development

The project execution plan was the first document compiled at the beginning of the project and identified the study scope, roles and responsibilities of participants, main activities, schedule, milestones, and products to be delivered. All the target sites adopted identical operation procedures, which were carried out and completed simultaneously after 46 months (nearly 4 years).

2. Organization of Project Participants

The five major teams in the project organization were: (1) Project Management Office (PMO) with four members, which was responsible for running and facilitating project activities; (2) Technical Integrator (TI) Team with four members, which had the most important role of undertaking the processes of evaluation and integration to develop the site-specific GMRS and FIRS; (3) Technical Support (TS) Team with eighteen members, who conducted all calculations and assisted with *in situ* tests; (4) Experts with twelve members, who provided their data, methods, and models to the TI Team, and were involved in technical assessments; and (5) Participatory Peer Review Panel (PPRP) with two members, who independently conducted both procedural and technical reviews.

The TI Team was led by Prof. Norman Abrahamson and included Prof. Ellen Rathje, Prof. Kuo-Liang Wen, and Dr. Joseph Sun; every member had extensive experience in PSHA, site response analysis, and SSHAC process in the nuclear industry. In addition, an internationally recognized expert in the area of geotechnical engineering, Prof. Kenneth Stokoe, in the team of Experts was fully engaged in collection and analyses of the data necessary for developing high-quality site characterization models.

3. Convening Workshops and Meetings

There were four formats of interaction between the TI Team, Experts, TS Team, and the PPRP: 51 regular meetings, 16 working meetings, 8 workshops, and 2 final meetings (one for NPPs #1-3, and the other for mothballed Lungmen NPP). Although the COVID-19 pandemic imposed restrictions on in-person activities after early 2020, the project team ably adjusted to the restrictions, successfully convened workshops and meetings via video conference, and finalized the site-specific GMRS and FIRS, which met quality and scheduling requirements of the project.

4. Selecting Site Response Methodology

One-dimensional (1-D) equivalent-linear (EQL) analyses adopting the random vibration theory (RVT) approach were employed to compute site response for horizontal shaking. Compared with the time-history approach, the RVT approach is not only one of the methods accepted by regulatory guidance, but also efficiently deals with intensive calculations involving numerous cases (parametric uncertainties, eleven AEFs of hazard levels).

The ground motion model used in the PSHA was developed for a reference-rock site condition with a V_{S30} of 760 m/s and implies a linear site amplification function. To be consistent with the assumption and to estimate the site amplification factor (AF) of the horizontal component, this project used a comprehensive approach that accounts for the difference in site amplification between the reference-rock V_S profile and the site-specific V_S profile. This V_S profile correction approach involves two separate site response analyses: (1) a linear analysis assuming the reference-rock V_S profile for calculating an output motion at the hypothetical outcrop ($SA_{ref'}$) of the profile, and (2) a nonlinear analysis addressing the site-specific V_S profile for calculating an output motion at the surface of the profile ($SA_{site'}$). The AF is the ratio of $SA_{site'}$ to $SA_{ref'}$. Figure 2 illustrates how the AF is calculated using the V_S profile correction approach.

The reference-rock V_S profile was developed based on the Taiwan Generic Rock (TWGR) profile which represents a site condition with a V_{S30} of 760 m/s used in the PSHA. Both the reference-rock V_S profile and site-specific V_S profile were set with a depth of 5 km for reaching the geological bedrock condition with a V_S of 3 km/s to fully capture potential nonlinear behavior due to increased damping in the rock under large amplitudes of the input motions.
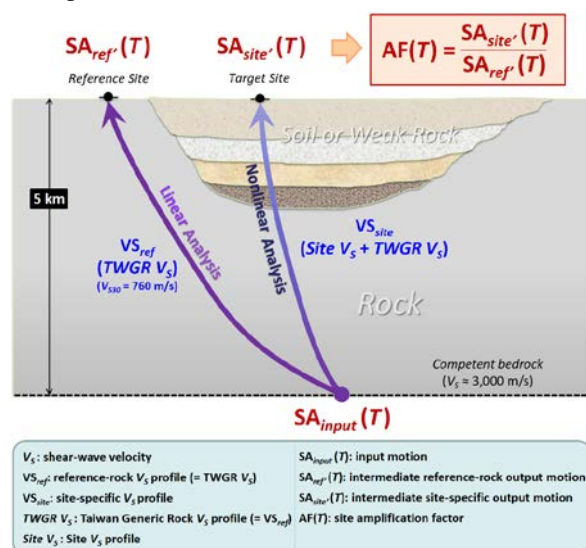

Figure 2. Illustration of the V_S profile correction approach.

To address the overdamping at high strains in the EQL method, in this project the change in the slope of the Fourier amplitude spectra (FAS) was modeled by setting a maximum kappa value of 0.065 s for the high frequencies, and a ratio-based approach was considered by using the three connection ratios, 0.05, 0.11, and 0.17 of the peak FAS. This adjustment to the high-frequency content is called the kappa2 correction (Figure 3). The values of the kappa2 approach judged by the TI Team are based on ranges from empirical data and nonlinear analytical modeling results.
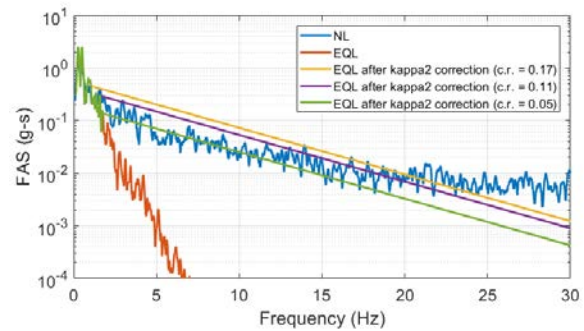

Figure 3. Example of kappa2 correction.

5. Developing Input Motions

The input motion (SA_{input}) is defined at a depth of 5 km that when a seismic wave propagates through the reference-rock V_S profile to the hypothetical outcrop, it produces a response spectrum similar to the $UHRS_{refrock}$ from the PSHA in terms of both the spectral amplitude and the spectral shape and leads to a total kappa value close to 0.044 s. At a depth of 5 km, the V_S of the reference-rock profile is approximately 3 km/s, the mechanical behavior of which is expected to be linear elastic.

For the RVT approach, the input motion is specified as an FAS, which is constructed using a point-source model for high-frequency content and a deconvolution analysis for low-frequency content. For soil hazard calculation, a suite of eleven input motion amplitudes are developed to be consistent with the $UHRS_{refrock}$ for hazard levels of 10^{-1} to 10^{-6} AEF for each target site.

6. Collection of Additional Site Data

In addition to the compilation of existing data such as P-S suspension logging, this project collected new *in situ* and laboratory data to develop high-quality site characterization models for the target sites.

The new *in situ* data are the subsurface V_S results from 1) nineteen test arrays of the spectral-analysis of surface waves (SASW), 2) three arrays of microtremor-array measurements (MAM), 3) three sets of the crosshole seismic test results, and 4) one set of downhole seismic test results. The new laboratory data specify the dynamic material properties from the shallow layer of the target sites, and nearly 85 laboratory test reports for core specimens are documented.

7. Developing Site Characterization Models

The majority of input models used for site response

analysis are V_S profiles and nonlinear material properties. These site characterization models cover a depth range of 0-5 km and capture uncertainties by utilizing three base-cases: best estimate, upper range, and lower range.

For the V_S profile, first the shallow and deep V_S profiles were constructed and then these two profiles were integrated into a complete site V_S profile. The connection points were judged by the TI Team according to criteria such as the compatibility of the merged velocity gradient and the V_S at 5-km depth expectedly close to 3 km/s. The shallow V_S profile was developed using the integrated dispersion curves from *in situ* V_S data and the 3-D iterative forward modeling procedure. The deep V_S profile is taken from the TWGR profile.

The nonlinear material properties, which include strain-dependent shear modulus reduction and damping (MRD) curves, are classified into three categories based on depth: 1) surficial soil-like material, 2) a transition zone, and 3) rock. The boundary between layers 1 and 2 is the depth indicated by reliable *in situ* data (such as local geological and borehole data) and the boundary between layers 2 and 3 is the depth at which V_S approaches 1,000 m/s. The MRD curves for surficial materials used the Darendeli model with adjusted parameters based on site-specific data. The MRD curves for the transition zone and rock were developed by Prof. Kenneth Stokoe, who has been testing rock specimens using the dynamic torsional resonant column method for more than thirty years.

8. Performing Site Response Analysis

All uncertainties were fully characterized using a logic tree (for alternative models of V_S profiles, MRD curves, and kappa2 correction), probability distribution (for weights allocation), and profile randomization (for aleatory variability of the V_S profile). With 54 branches in the logic tree, 200 randomized V_S profiles of each base-case profile, and eleven hazard levels of input motions, a total of nearly 120,000 site response cases were calculated. In addition, the weights assigned to logic-tree branches were judged by the TI Team with empirical data, professional knowledge, and experience.

9. Finalizing GMRS and FIRS

The final GMRS and FIRS comprise both horizontal and vertical components. Because of the original plant design basis, a Safe Shutdown Earthquake (SSE) is defined at the foundation of the reactor building, and the FIRS is defined as a control-point motion to have a consistent comparison with the SSE for screening purposes.

The horizontal motion was developed using the 1-D RVT-based EQL site response analysis (to find site amplification functions), the Approach 3 as described in the NUREG/CR-6728 (to find soil hazard curves and UHRS$_{soil}$ at AEFs of 10^{-4} and 10^{-5}), and the performance-based ground-motion approach described in the RG 1.208 (to find GMRS and FIRS).

The vertical motion used vertical-to-horizontal (V/H) spectral ratios to scale the horizontal motion in place of a site response calculation. The V/H models used two Taiwan-based models (Chao19 and Phung19) and one global model (GA11). This empirical V/H ratio approach was decided by the TI Team in order to achieve a higher site nonlinearity effect and shear-wave domination observed in the vertical ground-motion data of Taiwan.

10. Completion of the Final Project Report

The processes, technical bases, and results produced throughout the project and the PPRP reviews of key outcomes and activities were fully documented in the final Project Report, which comprises three volumes. Volume I contains one report and gives an overview of the project. Volume II contains eight reports and gives a detailed description of the methodology used, technical judgements by the TI Team, and the resulting GMRS and FIRS. Volume III contains eighteen reports and gives a compendium of calculations. In addition, all information of the formal meetings was well documented, with agendas, participant lists, presentation files, summaries of discussions, and video recordings.

11. Participatory Peer Review

The PPRP attended 29 project meetings and workshops during the project period and issued four consensus letters after review of the project plans, the summary report, and the final Project Report. In the end, the PPRP concluded that the project fully meets the intent of a SSHAC Level 3 process and the objective of developing site-specific GMRS and FIRS as stated in the "NTTF 2.1: Seismic". Moreover, PPRP confirmed that the site characterization models capture uncertainty related to the CBR of the TDI in characterizing local site effects at the target sites.

Summary

The Taiwan GMRS/FIRS Project developed up-to-date site-specific seismic response spectra for Taiwan nuclear power plants and created several frontier techniques such as site response analysis via the V_S profile correction approach, kappa2 correction, a standard procedure for *in situ* and laboratory testing, and the data-driven vertical ground motion models. These pioneering and localized achievements will promote innovation in the field of earthquake engineering and geotechnical engineering in Taiwan.

References

Hsun-Jen Liu and Chiun-Lin Wu (2021). "Project Overview", the Final Report of Development of GMRS and FIRS for Nuclear Power Plants in Taiwan, Volume I, Version 1.0, prepared for Taiwan Power Company, October 29, 2021.

Norman Abrahamson, Ellen Rathje, Joseph Sun, Kuo-Liang Wen, Yu-Wen Chang, Hsun-Jen Liu, Domniki Asimaki, Shu-Hsien Chao, Chun-Hsiang Kuo, Wen-Jong Chang, and Kenneth Stokoe (2021). "Technical Report", the Final Report of Development of GMRS and FIRS for Nuclear Power Plants in Taiwan, Volume II, Version 1.0, prepared for Taiwan Power Company, October 29, 2021.

Platform of Input Motion Selection for Taiwan (INMOST)

Hsun-Jen Liu[1], Xue-Min Lu[2], and Wen-Yu Jean[3]

劉勛仁 [1]、呂學敏 [2]、簡文郁 [3]

Abstract

In order to address the key issue of how to select and modify recorded input motions when executing time-history analysis, this study develops a platform for input motion selection for Taiwan, or INMOST. Specific features of INMOST are: (1) meeting the requirements of Taiwan seismic design specifications; (2) generic applications for wider local sites in Taiwan (including Taipei Basin sites); (3) an interactive website with a graphical user interface; (4) provision of suitable seismic records and complete seismic information. INMOST not only succeeds in providing a useful reference for generating horizontal input motions for time-history analysis, but also has reliable practical applications in seismic analysis and design.

Keywords: ground motion selection, time-history analysis, seismic design, INMOST

Introduction and Conception

In recent decades, rapid progress has been made in earthquake engineering, which has led to new and more efficient structural systems, greatly improved quality and quantity of seismic data recordings, significantly improved performance in hardware and software, and more detailed requirements for seismic design regulations. Response history analysis using seismic time series has therefore gradually become the mainstream approach for evaluating the seismic behavior of structures.

Compared with the simple methods of response spectrum analysis and nonlinear static pushover analysis, the advantages of detailed time-history analysis are as follows. First, the structural response over time during and after the application of a real earthquake load can be fully obtained. Second, the higher mode effects and inelastic redistribution can be specifically predicted. Third, since seismic records preserve the properties of ground motions, the structural response not only directly reflects the three primary characteristics of a seismic excitation, *i.e.*, amplitude, frequency content, and duration, but also evaluates structural response uncertainties by various load paths.

However, the most practical issues of time-history analysis are how to select and modify recorded input motions from a huge amount of ground-motion data for satisfying the requirements of a seismic design code. In this context, the National Center for Research on Earthquake Engineering (NCREE) developed a platform for input motion selection for Taiwan, or INMOST (http://seaport.ncree.org/inmost). The main objectives of INMOST are (1) to facilitate local application, (2) to provide a user-friendly interface, and (3) to promote time-history analysis. The strategies of creating INMOST are (1) using Taiwan's ground-motion data and seismic design specifications, (2) supporting wider local sites and broader structural periods, and (3) designing an easy-to-use website.

Platform Development

The first stage in platform development was establishing the Taiwan Recorded Ground-Motion Database for Structural Response-History Analysis for integrating the selected seismic records that correspond to the level of a design basis earthquake in Taiwan (Liu *et al.*, 2021). Next, INMOST was developed as an intuitive and interactive website based on the above database.

The database at the back-end of INMOST is based on Taiwan seismic design specifications and contains nearly 100,000 local seismic records from 1991 to 2018. Ten datasets are grouped in this database, including seven general sites and three Taipei Basin sites. Each dataset includes thirty selected ground-motion records based on a target design spectrum that reflects one of

the representative site characterizations in Taiwan. These selected ground motions are sorted according to goodness-of-fit of spectral shape within a specific range of periods. All parameters of the seismic source, the strong-motion station, ground motion, and ranking are listed in the metafile of each dataset. These support the powerful display and application functions at the front-end of the INMOST website.

Platform Navigation

The structure of INMOST is a one-page-website (Figure 1), so users can have an excellent experience in terms of visual effects, operation efficiency, and data acquisition. In the layout of the webpage, the right side is the welcome area and the feedback entry; the middle is the main operation area for selecting input motions; and the left side is the navigation area for the seven function tabs, which are: (1) About INMOST, (2) Selection Criteria, (3) Results Map, (4) Results Table, (5) Response Spectra, (6) Results Export, and (7) References. The contents and features of each function tab are described below.

Figure 1. INMOST webpage header.

About INMOST

The initial screen of INMOST (Figure 2) adopts the input overlay mode, and the content includes an introduction to the platform, a disclaimer, and two necessary inputs for users to provide basic information (service unit and professional title) and to agree to website usage rules. Through About INMOST, it is possible to review the development basis, service features, and usage principles on the initial screen.

Figure 2. INMOST initial screen.

Selection Criteria

There are two basic principles for the input motion of time-history analysis in the Taiwan seismic design specifications (CPAMI, 2011), Section 3.6.1 for a seismic structure, Section 9.3.7 for an isolated structure, and Section 10.4.1 for a damped structure) as follows:

(1) the input motion must be consistent with magnitudes and fault distances as they control the target design spectrum and (2) the input motion must have a similar spectral shape to the target design spectrum in a specific period range regarding the fundamental period of the structure. In addition, owing to the different requirements of individual analysis projects, such as two- or three-dimensional analysis and average or maximum structural response, the input motion has other project-specific requirements to suit the local circumstances.

Therefore, the criteria for input motion selection provided by INMOST (Figure 3) meet three basic requirements: site-specific, structure-specific, and project-specific. Selection Criteria has two areas for parameter settings, Target Spectrum and Input Motion Conditions. The former has two simple options, selection of general sites or Taipei Basin sites; the latter has five items for selecting the structure-specific requirements (period range, limit of the lowest spectral value) and project-specific requirements (component of ground motion, number of records, limited number of records from one earthquake event).

Considering the practical applications, INMOST has presets for several criteria. For the target design spectra of the three Taipei Basin seismic micro-zonations, a corner period for spectral acceleration (S_a) being proportional to T^{-1} and T^{-2} is given as 4.0 s with reference to a recent study (Jean *et al.*, 2020), and the selected ground motions are focused on both the Chi-Chi (1999) and 331 (2002) earthquakes and the strong-motion stations located in the Taipei Basin area. These presets can be used to appropriately determine spectral shape similarity at long periods. For the lowest value of the scaled recorded spectrum, this criterion is for an individual input motion rather than the mean of all the input motions. For the number of selected input motions, the upper limit is 30 to facilitate the display and operability of Response Spectra.

Figure 3. INMOST Selection Criteria.

Results Map

The results of input motion selection are visualized in the three modes on INMOST: map, table, and plot, with intuitive and interactive functions that are easy to use (Figure 4).

The geographic information map provided by INMOST displays the distribution of all epicenters and strong-motion stations of the selection results. Advanced information is shown when clicking an icon for an epicenter (　) or a strong-motion station (📍). Taking strong-motion stations as an example, details include the earthquake time, the code of the strong-motion station, the epicentral distance, the hypocentral distance, and the average shear-wave velocity (V_S) for the upper 30-m depth (V_{S30}). In addition, for a single event or all earthquake events, the epicenters and the strong-motion stations on the map can be displayed in either decluster (🗺) or cluster (🗺) modes. Users can interact with the map to zoom, pan, and array, then snapshot the current plot (📷).
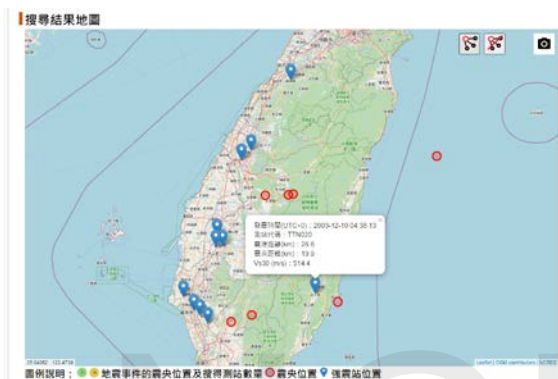
Figure 4. INMOST Results Map.

Results Table

Results Table (Figure 5) lists the parameters of the selected input motions, and its usefully interactive functions are described as follows. (1) The default sorting is according to goodness-of-fit of the spectral shape (*i.e.*, mean-squared error), but users can sort data by any parameter item. (2) The tip for a parameter appears when a cursor is positioned over this parameter item in the table header. (3) When selecting a row of ground motions, the map pans to the location of the strong-motion station. (4) The accelerograms based on original recorded data display when clicking the ACC button. (5) The show-or-hide checkboxes lead to the follow-up functions of Response Spectra and Results Export.

The tabular parameters are adequate for practical application, and can be classified into four categories:

1. *Ranking*: This includes mean-squared error (MSE), scale factor (SF), and component of ground motion. These parameters are the critical references for selecting the applicable input motion suite and scaling the motion amplitude. When three-dimensional analysis is required, it is suggested that both horizontal ground-motion components be applied with an identical scale factor based on the geometric-mean (GM) spectrum of both horizontal components.

2. *Seismic Source*: This includes earthquake time (UTC+0), epicentral coordinates, moment magnitude (M_w), focal depth, epicentral distance, and hypocentral distance. With these parameters, the diversity of the earthquake events can be confirmed, and the correspondence with the characteristics of the target-site controlling earthquake can also be checked.

3. *Strong-Motion Station*: This includes the code of the strong-motion station, station coordinates, V_{S30} value, and the depth for V_S of 1.0 km/s ($Z_{1.0}$). With these parameters, the correspondence with the site conditions between target-site and strong-motion station can be checked, and the degree of basin effect or soft layer depth can also be evaluated.

4. *Ground Motion*: This includes peak ground acceleration (PGA, A), peak ground velocity (PGV, V), strong-motion durations (5%–75% and 5%–95% Arias intensity), pulse period (T_p), and S_a at fifty specified periods. These parameters not only provide the characteristics of the ground-motion energy in terms of amplitude, frequency content, and duration, but also assist in selecting the special ground motion with long-period effects or pulse-like velocity.
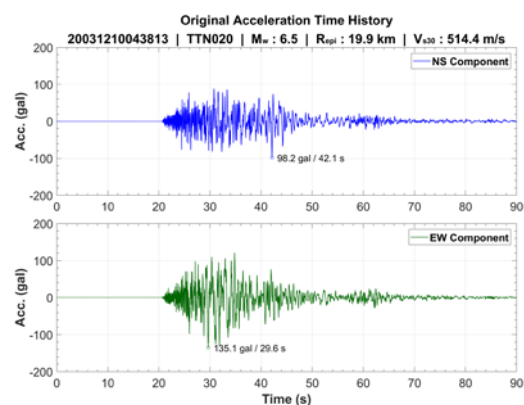

Figure 5. INMOST Results Table and accelerograms.

Response Spectra

Response Spectra (Figure 6) shows the scaled recorded spectra (colored lines), the mean of the scaled recorded spectra (black dashed line), and target spectrum (black dotted line). Users can quickly examine the suitability of the spectral shapes of the selected input motions over the period range of interest.

The interactive functions are described below. (1) The scale (arithmetic or logarithmic) and limits

(minimum and maximum) of both axes of the period and S_a are easily changed. (2) The legend option allows four corner positions for its position to create the best visual effect. (3) Users can hide or show a spectrum when clicking the corresponding label in the plot legend. (4) The values of the period and S_a for a single spectrum (◄) or all spectra (≡) appear when the cursor is positioned on the plot. (5) Users can arrange any spectra style then snapshot the current plot (📷).
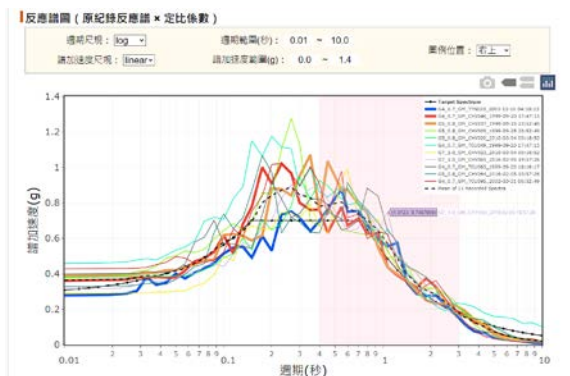

Figure 6. INMOST Response Spectra.

Results Export

All parameters displayed in the Result Table, S_a of the recorded ground motions and S_a of the target spectrum displayed on INMOST, are available to export directly as comma-separated values (CSV) files (Figure 7). Digital acceleration time-history data of earthquake events observed at the strong-motion stations in Taiwan, except for the six disastrous shocks, need to be purchased from the Central Weather Bureau. In this regard, for user convenience, INMOST provides a hyperlink to download or purchase the official earthquake records.

Figure 7. INMOST Results Export.

References

Documents and information on the development of the INMOST database, such as the Taipei Basin design response spectra with T_L, the site amplification factors following a semi-logarithmic empirical model, the procedure of ground-motion selection of the ten datasets, and the sources of pulse-like records and geological data of the strong-motion stations, are presented in full in both Technical Documents and Related Links (Figure 8).

Study reports related to INMOST will be placed in References one after another.

Figure 8. INMOST Results Export.

Summary

The intention behind developing INMOST is to solve procedural problems encountered by local engineers when selecting recorded input motions to comply with a target design basis earthquake. INMOST is a one-page website with intuitive, graphical, and interactive features. It not only succeeds in providing useful records and parametric information for generating horizontal input motions for time-history analysis, but also has reliable practical applications in seismic analysis and design.

For subsequent applications in selecting results with INMOST, users must consider the target-site characteristics such as seismic hazard (magnitude and fault distance), site conditions (*e.g.*, soft or hard layers), ground motion (*e.g.*, velocity pulses), and the followed standards, and then finally determine the appropriate earthquake records and scale factors.

The platform of Input Motion Selection for Taiwan was launched on December 30, 2021, and is available at the following URL: http://seaport.ncree.org/inmost. All are welcome to use, give feedback, and promote it.

Acknowledgments

The author would like to thank the Central Weather Bureau, Taiwan, for providing the recorded acceleration data from the Taiwan Strong Motion Instrumentation Program (TSMIP) for developing the INMOST database.

References

CPAMI, (2011). "Seismic Design Code for Buildings in Taiwan", Construction and Planning Agency, Ministry of the Interior, Taiwan. (In Chinese)

Hsun-Jen Liu, Wen-Yu Jean, and Yu-Wen Chang, (2021). "Taiwan Recorded Ground Motion Database for Structural Response History Analysis," 2020 NCREE Research Programs and Accomplishments Report, pp. 204-207.

Wen-Yu Jean, Hsun-Jen Liu, Chih-Wei Chang, and Yu-Wen Chang, (2020). "A Study on the Design Basis Earthquake for Taipei Basin", *15NCSE*, paper no. 104, Tainan, Taiwan. (In Chinese)

A Taiwan Seismic Microzonation Map—Construction of a Geometric Model of the Hsiaokangshan Fault

Kuan-Yu Chen[1], Chiu-Ping Fan[2], Yu-Wen Chang[3], Hsun-Jen Liu[1], Chih-Wei Chang[4], You-Chia Lee[5]

Abstract

An applicable fault geometric model for PSHA and a hazard map of Taiwan are currently in the process of development. We separated Taiwan into five study areas: central, southwestern, southern, eastern and northern, and plan to integrate and evaluate these areas sequentially in subsequent stages of the project. At present, the geometric model of the active faults of southern Taiwan has been completed. The Hsiaokangshan fault is used here as an example to briefly describe how the geometric model was established and evaluate its uncertainty using integrated data of its surface geological surveys, bore holes, balanced cross sections and seismic reflection profiles.

A thrust-Hsiaokangshan fault lies on the western limb of the Takangshan anticline with a known length of 8 km. The fault geometric model shows that the fault plane extends down to a depth of 10 km with a dipping angle between 50 to 70 degrees. The suggested rupture model of the Hsiaokangshan fault is that of "entire rupture" due to the short fault length.

Keywords: PSHA, Hazard map, Hsiaokangshan fault, reflection seismic data, geometric model

Introduction

The NCREE is conducting a project to create a hazard map of Taiwan with the objective to review and construct a fault model of the land mass to facilitate seismic hazard calculations and other long term programs in the future.

We separated Taiwan into five study areas: central, southwestern, southern, eastern and northern Taiwan and completed the preliminary geometric model of the active faults in central, southwestern and southern Taiwan last year (2021). Models of the active faults in eastern and northern Taiwan are scheduled to be constructed later this year (2022).

As the construction of the fault model of southern Taiwan has been completed, we would like to give the Hsiaokangshan fault (HKSF) (Figure 1) as an example to briefly describe how the fault geometric model was constructed and evaluate its uncertainty using integrated data of its surface geomorphic features, geological surveys, bore holes, balanced cross sections and seismic reflection profiles. Furthermore, because diapirism significantly contributes to the form of the Takangshan anticline, the relationship between the diapir and the adjacent tectonic structure needs to be discussed despite the limited data available.

Fault Features

There are two hills that are distributed from north (Takangshan mount) to south (Hsiaokangshan mounts) in the Kaohsiung area of southern Taiwan, both of them are considered as an single anticlinal form due to a same age limestone layers overlaid.

A topographic lineament located along the west flank of Hsiaokangshan mount can be recognized in aerial photographic images (Sun, 1964; Shen et al., 2006). On the eastside of the lineament, the higher vertical uplift has led to the lineaments (six fault scarplets) being considered, confirming the faulting of the HKSF with an eastern dip (Hsu & Chang, 1979).

Lineaments are clear geographic features of the HKSF that are considered to be one of the potential sources of earthquakes in southern Taiwan. The HKSF

---

is a reverse fault with an NNE trend that extends eight km through Alien to Yanchao (Lin et al., 2009) (Figure 2). Radiocarbon (C14) dating has determined the age of the last faulting event to within the last 13 660 ~ 23 500 years (Yen, 2020), which is classified as a late Pleistocene active fault (Lin et al., 2012; Lin *et al.,* 2021).
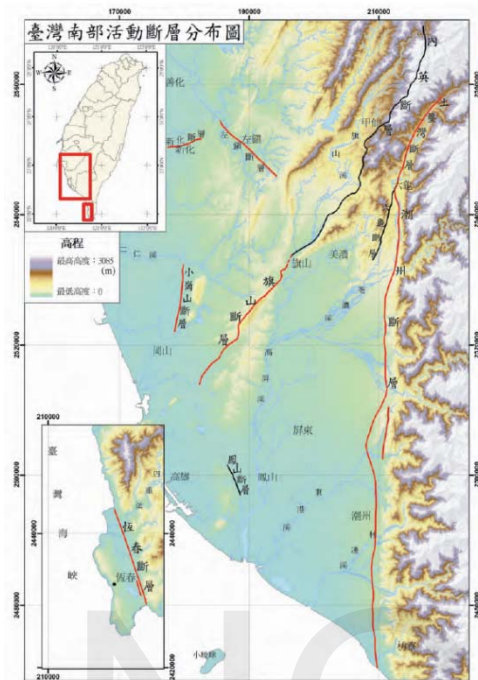

Figure 1. Distribution of active faults in southern Taiwan. The Hsiaokangshan fault located on the left side is described in this report (Lin *et al.,* 2009).
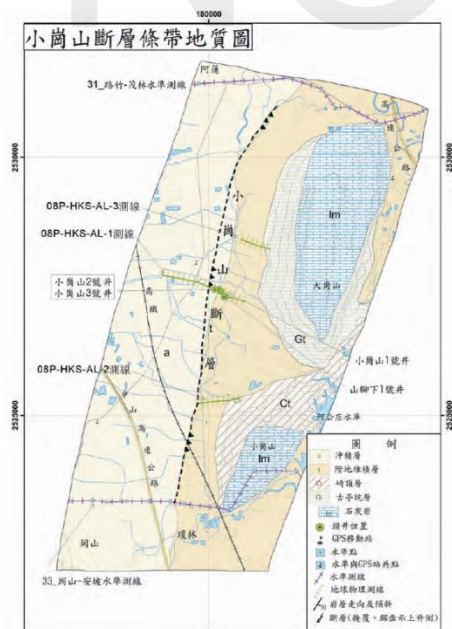

Figure 2. Strip map of the HKSF, which lies on the western limb of the Takangshan anticline, 8 km in length (Lin *et al.,* 2009).

Geological and Geophysical Investigation

The balanced cross-section (Cheng, 2000) shows

the fault plane of the HKSF exhibits 70° dipping from the surface and then changes to 33° dipping until it contacts the decollement at a depth of 10 km (Figure 3).
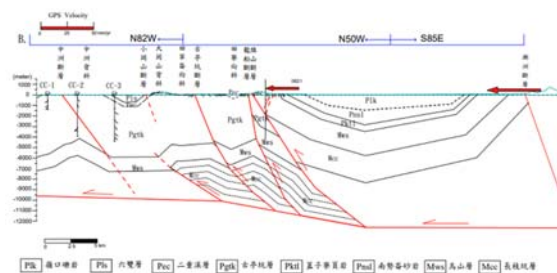

Figure 3. Balanced cross-section showing the dip of the HKSF changes from steep in shallow to gentle in deep (Cheng, 2000).

Four boreholes in a row (Figure 4) that cross perpendicularly to the trace of the HKSF from west to east are named respectively the HKS-1, HKS-2, HKS-3 and SCS-1 (Lin et al., 2009). Intensive shear zones in the mud layers (Gutingkeng (GTK) formation) with 30 - 70° dips (primary dip is 50 - 70°) can be observed in lower HKS-3 and SCS-1 but not in HKS-1 and HKS-2. A geological cross-section based on these boreholes shows that the location has been placed between HKS-1 and HKS-2 (Chen, 2009). According to the interpretation of the seismic reflection profile with the four boreholes, the HKSF comprises an intensive shear zone within a GTK formation, having a 45° dipping fault plane that may lie on the western part of HKS-1 as its major fault (Chen, 2010)
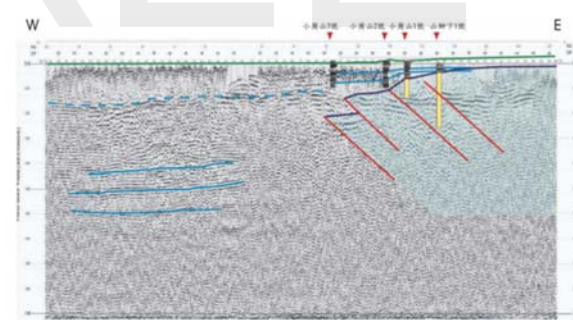

Figure 4. The 45° dipping angle was estimated from analysis of the boreholes and seismic reflection data (Chen *et al.,* 2010).

According to the latest borehole data, the GTK formation has been identified at the 3A site at depth of 26.5 m, but is the top boundary of GTK formation could not be determined at the 3B site (50.6 m total). The isochronous marks on both sites in the P3 geological section (red dots in Figure 5) were helpful for determining the chronostratigraphic correlation, which shows that the top of the GTK formation is at least 25 m higher at 3A, leading to the lack of the lower parts of the Holocene sediment of the same age at the 3B site. Therefore, the location of Hsiaokangshan fault was estimated to be between 3A and 3B, and the dipping angle to be 37° at the surface location of the

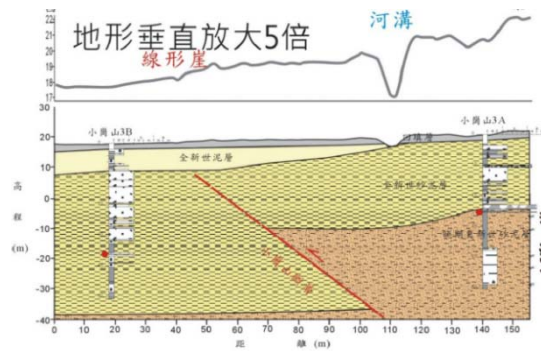lineament (fault) scarp (red line in Figure 5) (Yen, 2020; CGS, 2021).

Figure 5. The location and dip of the HKSF was estimated from the offset of the GTK formation between Borehole 3A and 3B at the surface location of the lineament (fault) scarp (Yen, 2020; CGS, 2021).

Diapirism

Although the Takangshan anticline is regarded as a fault-propagation fold of the Hsiaokangshan fault, several published studies have pointed out that its formative mechanism was mud diapirism.

A PsInSAR image (Chen & Wang, 2019) and the residual gravity anomaly (Doo *et al*., 2015) demonstrate that the Takangshan anticline is an isolated fold of extremely small size, which is different from general anticlines that have elongated and wide fold shapes. The results of Geodetic and GPS data and leveling analysis have revealed that the Takangshan fold gradually uplifts in the inter-seismic period (Chen *et al.,* 2019).

In the seismic reflection profile, the presence of chaotic seismic facies beneath the western limb of the Takangshan anticline indicate that the material is composed of disordered mud layers (Shih *et al*., 2008), and intensive shear zones in the mud material can also be observed in the boreholes (gray sections in HKS-3 and SCS-1 in Figure 6) (Chen *et al*., 2008). Some reflectors near the lower boundary of the chaotic facies area show the upward drag of adjacent sediment suggesting that the underlying mechanism could be diapirism (Weng, 2001; Shih *et al.,* 2008; Fu, 2009).
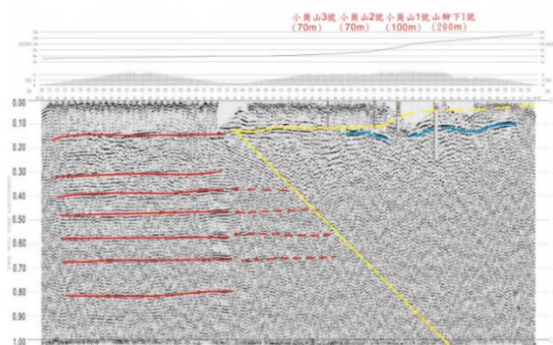

Figure 6. The chaotic facies of the seismic reflection profile indicate the Takangshan anticlinal form may

have resulted from mud diapiric intrusion (Shih *et al*., 2008; Fu, 2009).

Logic Tree Structure

Due to the limitations of the available relevant geological and geophysical data, more expert discussion is needed for specific evaluation of the model. Therefore, we here describe only the preliminary structure of the HKSF logic tree.

As mentioned above, there are two possible scenarios of seismogenic probability, Seismogenic structure and Diapirism, and both are considered. For the node of style of faulting, although the relevant rake information was not yet available, the fault mechanics were based on the assumption that the rake was distributed over a certain range. The fault segmentation features could not be observed in any existing references or data, especially for short faults (<= 8 km). Consequently, only an entire rupture could be considered as a rupture source for our rupture model node. The angle of the shear zone in the boreholes was determined by seismic interpretation and the geological sections, which indicate the dipping angle of the fault plane as ranging between 30 - 70˚. According to an analysis of the integrated data, the median value of the dipping angle was between 45 to 50˚. It was difficult to determine the seismogenic depth from the spatial distribution of earthquakes in SW Taiwan where very few historical earthquakes have occurred in shallow crust. We therefore assumed a 10km depth for our seismogenic depth node based on one balanced cross-section only (Cheng, 2000).

The preliminary structure of the HKSF logic tree is presented in Figure 7 for the convenience of future expert discussion aiming to update and finalize the model with specific values, ranges and weights for each branch of nodes.
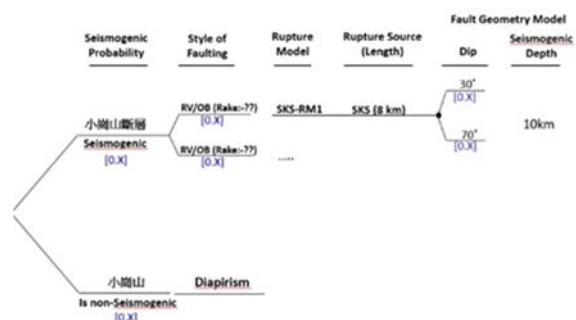

Figure 7. The preliminary structure of the HKSF logic tree.

Future Work

The path forward for this project is to sequentially progress through each planned partition zone to complete the reference collection, integrate and evaluate the remaining active faults (seismogenic structures), as well as three new faults (announced in

January of 2022 by the CGS), the Chushiang fault, the Kouhsiaoli Fault and the Chekualin fault. Our ultimate goal is to construct the logic trees of the active faults of Taiwan to describe their geometric model and activity (slip rate) for the Taiwan Seismic hazard map.

References

1. Central Geological Survey, CGS (2021) 小崗山斷層地質敏感區。中央地質調查所活動斷層地質敏感區畫定計畫書，共 24 頁。

2. Chen Chih-Hao (2009) The Postglacial Marine Environment of the Northern Kaohsiung Coastal Plain－its implications for slip rate of the frontal fold-and-thrust belt. Department of Geoscience, National Taiwan University, Master Thesis Pp.108

3. Chen, Song-Chuen and Wang, Chin-Ch'ang (2019) 台灣西南海域泥貫入體與陸上地質構造關係之研究(V)。科技部補助專題研究計畫成果報告，共 16 頁。

4. Chen, Wen-Shan, Nobuhisa Matsuta, Shih, Ruey-chyuan, Yang, Chih-Cheng, Yu, Neng-ti, Chu, Yao-Guo, Chen, Chih-Hao, Lin, Chii-Wen, Liu, Huan-Chi, Lu, Shih-ting, Liu, Yen-Chiu, Lin,Yen-Hui, Chen, Po-Tsun (2010) Concealed Active Structures beneath the Holocene Marine Sediments in the Western Coastal Plain Using Taiwan as an Example for the Hsiaokangshan Fault. Special Publication of the Central Geological Survey,No.24, P75-91.

5. Cheng Horng-chi (2000) Structural geology of the Tainan to Pingtung area of southwestern Taiwan. Graduate Institute of Applied Geology, National Central University Master Thesis,Pp.92.

6. Doo, W.-B., Hsu, S.-K., Lo, C.-L., Chen, S.-C., Tsai, C.-H., Lin, J.-Y., Huang, Y.-P., Chiu,S.-D. and Ma, Y.-F. (2015) Gravity anomalies of the active mud diapirs off southwest Taiwan. Geophysical Journal International, 203, 2089–2098.

7. Fu Chao-Ming (2009) Subsurface Structure of the Suspicious Hsiaokangshan Fault in Southern Taiwan from Seismic Reflection Images and Core Borings. Department of Earth and Environmental Sciences, National Chung Cheng University, Master Thesis pp.62

8. Hsu, T.L. and Chang, H.C. (1979) Quaternary faulting in Taiwan. Mem. Geol. Soc. China, no.3, p.155-165.

9. Huang Shiun-Tsann (2004) Analysis of Geological Structure for Fold-and-Thrust Belt, Centraland Southern Taiwanthe Chelungpu Fault. Institute of Geophysics, National Central University, Doctoral dissertation, Pp.129.

10. Lin, Chii-Wen, Chen, Wen-Shan, Lin,Yen-Hui, Rau, Ruey-Juin, Liu, Yen-Chiu (2010) A Study of the Xiaogangshan and Fengshan Lineaments in Southern Taiwan. Special Publication of the Central Geological Survey;No.24,P.39-60.

11. Lin, Chii-Wen, Chen, Wen-Shan,Liu, Yen-Chiu,Chen, Po-Tsun (2009) Active faults of eastern and southern Taiwan: explanatory text for the strip maps of active faults scale 1:25,000 = Active faults of eastern and southern Taiwan: explanatory text for the strip maps of active faults scale 1:25,000. Central geological survey special publication, No.23,pp122.

12. Lin, Chii-Wen, Lu, Shih-ting, Chen, Wen-Shan (2012) Active Fault Map of Taiwan: An Explanatory Text (2012 Edition). Special Publication of the Central Geological Survey,No.26, p.1-30.

13. Lin, Qi-Wen, Liu, Yen-Chiu, Chou, Pin-Shan, Lin,Yen-Hui (2021) Recent development of active fault investigations of Taiwan. Bulletin of the Central Geological Survey, No,34,p.1-40.

14. Martín-Martín, J. D., Vergés, J., Saura, E., Moragas, M., Messager, G., Baqués, V. Hunt, D. W. (2017). Diapiric growth within an Early Jurassic rift basin: The Tazoult salt wall (central High Atlas, Morocco). Tectonics, 36(1), 2–32. https ://doi.org/10.1002/2016T C004300

15. Shen, Su-Min, Chang, Jui-Chin, Yang, Guey-San, Lin, Hsueh-Mei, Lin, Tsung-Yi. (2006) 地震地質調查及活動斷層資料庫建置計畫：活動構造地形判釋及資料庫建置分析(2/2)。經濟部中央地質調查所報告，95-13。

16. Shih, Ruey-chyuan, Wang, Wei-Hao, Lee, Yuan-His, Chen, Tai-Shan (2008) 地震地質與地變動潛勢分析－斷層帶地下構造調查研究（2/4），中央地質調查所報告，共 127 頁。

17. Sun, S.C. (1964) Photogeologic study of the Tainan-Kaohsiung coastal plain area, Taiwan. Petrol. Geol. Taiwan, no.3, p.39-51.

18. Weng ChiunPing (2001) Detecting the Hsiaokangshan Fault and Its Neighboring Structures Using the Shallow Seismic Reflection Method. Institute of Geophysics, National Central University Master Thesis Pp.84

19. Yen, Yi-Ching（2020）109 年度活動斷層調查補充地質調查報告書。經濟部中央地質調查所研究報告，共 854 頁